5-2010

Tectonic evolution of the west-central portion of the Newton window, North Carolina Inner Piedmont: Timing and implications for the emplacement of the Paleozoic Vale charnockite, Walker Top Granite, and mafic complexes

Heather Elizabeth Byars
University of Tennessee - Knoxville, hbyars1@utk.edu

To the Graduate Council:

I am submitting herewith a thesis written by Heather Elizabeth Byars entitled "Tectonic evolution of the west-central portion of the Newton window, North Carolina Inner Piedmont: Timing and implications for the emplacement of the Paleozoic Vale charnockite, Walker Top Granite, and mafic complexes." I have examined the final electronic copy of this thesis for form and content and recommend that it be accepted in partial fulfillment of the requirements for the degree of Master of Science, with a major in Geology.

Robert D. Hatcher, Jr., Major Professor

We have read this thesis and recommend its acceptance:

Harry Y. McSween, Theodore C. Labotka

Accepted for the Council:
Dixie L. Thompson

Vice Provost and Dean of the Graduate School

(Original signatures are on file with official student records.)

To the Graduate Council:

I am submitting herewith a thesis written by Heather Elizabeth Byars entitled "Tectonic evolution of the west-central portion of the Newton window, North Carolina Inner Piedmont: Timing and implications for the emplacement of the Paleozoic Vale charnockite, Walker Top Granite, and mafic complexes." I have examined the final paper copy of this thesis for form and content and recommend that it be accepted in partial fulfillment of the requirements for the degree of Master of Science, with a major in Geology.

Dr. Robert D. Hatcher, Jr., Major Professor

We have read this thesis and recommend its acceptance:

Dr. Harry Y. McSween

_____

Dr. Theodore C. Labotka

_____

Acceptance for the Council:

Carolyn R. Hodges

_____

Vice Provost and Dean of the Graduate School

(Original signatures are on file with official student records)

TECTONIC EVOLUTION OF THE WEST-CENTRAL PORTION OF THE NEWTON WINDOW, NORTH CAROLINA INNER PIEDMONT: TIMING AND IMPLICATIONS FOR THE EMPLACEMENT OF THE PALEOZOIC VALE CHARNOCKITE, WALKER TOP GRANITE, AND MAFIC COMPLEXES

A Thesis
Presented for the
Master of Science
Degree
The University of Tennessee, Knoxville

Heather E. Byars
May 2010

DEDICATION

This thesis is dedicated to my parents,
Glenn and Mary Byars,
for their unconditional love and support.

ACKNOWLEDGMENTS

The successful completion of this thesis is attributed to the gracious help and support of many people over my three year stint at the University of Tennessee. Completion of this research would not have been possible without my adviser Dr. Robert D. Hatcher, Jr., who has supported me morally, academically, and financially throughout this project. I am very grateful for the many opportunities I've had during my time here, such as Appalachian field trips and GSA conferences, to expand my knowledge of and love for geology. I would also like to extend my appreciation to my other thesis committee members, Drs. Harry Y. McSween, Jr. and Theodore C. Labotka, for their patience, input, and contributions to my education and thesis. A special thanks goes to all who have provided me assistance with collecting and interpreting analytical data, including: Dr. Lawrence A. Taylor and Allan Patchen in the University of Tennessee Electron Microprobe Facility; Drs. Brendan R. Bream and Arthur J. Merschat for assistance with zircon separation and SHRIMP analyses; Drs. Joe Wooden, Frank Mazdab, and others at the Stanford-U.S.G.S. SHRIMP Lab for training and use of the SHRIMP; and Drs. Paul D. Fullagar and Drew S. Coleman at the University of North Carolina – Chapel Hill's Isotope Geochemistry Lab for providing additional isotopic analyses. Additional thanks is extended to Carl Merschat, Bart Cattanach, and Nick Bozdog at the North Carolina Geological Survey for their assistance with the TRIMBLE GeoXT units and ArcPAD form, for participating in my field review, and feedback on my geologic map.

Where would I be without all those (past and present) in the "Hatchery," or the "Hatcher Mafia" (as a few so named ourselves) who are taking the southern Appalachians by storm, one quadrangle at a time! To my field "partner in crime" and fellow Kentuckian, William Gilliam, who was constantly outsmarting the rocks in my field area with a sledge hammer, it was a pleasure doing field work to the south of you, discussing Newton winder geology, and sharing trips to Boone for some good ole North Carolina BBQ at Woodlands. Mary Varnell Jubb, thank you for your lunacy, friendship, passing along "good karma," and keeping me company during our many late nights at the office. Brittany Davis, thank you for your encouragement, friendship, and the many Cat Square terrane discussions we've had. Arthur Merschat, thank you for your

guidance, willingness to discuss Appalachian geology when needed, and for doing your Ph.D. research in the Blue Ridge so I could have this project in the Inner Piedmont. Andrew Wunderlich, our cartographic lab director and ArcGIS guru, thank you for your endless patience and help with ArcGIS and for always fixing my computer problems. Shawna Cyphers, thank you for the best and worse traverse of my life in the Blue Ridge my first summer here that steered me to Inner Piedmont geology. Jonathan Evenick, thank you for helping me get my feet wet my first year here and teaching me the dos and don'ts of graduate school. Crystal Wilson, thanks for passing on the desk of Inner Piedmont insanity and "hurry up and finish your thesis because you have a job waiting on you." And to the lady who holds the "Hatchery" together and keeps "the family" in line, Nancy "Damama" Meadows, I am forever indebted to you for all that you have done for me including, but not limited to, proofreading papers and abstracts, having awesome birthday celebrations, providing constant prayers, support, and encouragement, lending a compassionate ear, and giving me breathing exercises of "In with the good, out with the bad."

My experience at the University of Tennessee would not have been complete without the faculty, staff, undergraduates, and other graduate students in the Department of Earth and Planetary Sciences. Thanks to everyone who contributed to my education and graduate school experience. A special thanks goes to those whose friendship helped me keep me sane including Karina Cheung, Ian McGlynn, Peter Knappett, Richard Donat, Lizzie Johnson, Kevin Thaisen, Christiana Viviano, Andrew Beck, Jackie Langille, Matt Chojnacki, Eric Hogan, and most importantly, my housemates Megan Carr, Liz Lee, and Aubrey Modi who were constantly encouraging me until the completion my thesis.

A field-based project like mine wouldn't have been possible without the unsuspecting residents of western Lincoln County North Carolina, who gave me, a random stranger, permission to tromp around on their property through the woods, corn fields, cow pastures, and creeks to study rocks. A special thanks goes to Bryan Rollins, Ed Jeranek, and Ken Hovis, for allowing us to have field trip stops on their property for the 2008 SEGSA Inner Piedmont Traverse Field Trip. I would especially like to extend my gratitude to the family of Larry and Beverly Cagle for adopting me and allowing me to move in and "work for wine, room, and board" for my second field season. Also, thank you for introducing me to great people, such as

your family, Cathy and Anthony Davis, Gary and Diane Poovey, and the Woodmill Winery employees, who made my time in North Carolina a wonderful experience.

Finally, I would like to extend a heartfelt thanks to all of my family members and friends who provided endless encouragement, love, and support. Mom and dad, thank you for always believing in me and for being the best parents anyone could ever ask for. Rachel, thank you for your advice on my résumé and interviewing that helped me get a great job. Susan, thanks for the motivation, care packages, and for being an awesome sister. A special thanks to my little sister, Natalie, who was the best field assistant ever and earned her keep by fighting through the briar thickets and carrying my rocks. You helped me more than you know! Thanks to all of my friends who are not in Knoxville; I appreciate all of the encouraging phone calls, emails, and visits during my time here. Amy, thank you for your constant friendship and always being there for me no matter what. Justin, thank you for the countless motivational and pep talks, wake up calls, and your continued friendship. Most importantly, I thank God for his grace, mercy, guidance, and love, and for blessing me with the opportunities I have had and people I have met during my time at the University of Tennessee.

ABSTRACT

Detailed geologic mapping of portions of the Banoak, Reepsville, Lincolnton West, and Cherryville 7.5-minute quadrangles has confirmed the easternmost exposure of the Brindle Creek fault, which frames the Newton window. The Brindle Creek fault is a terrane boundary that separates the overlying Siluro-Devonian assemblage of metasedimentary rocks and Devonian-Mississippian anatectic plutons of the Cat Square terrane from the Neoproterozoic(?)-Ordovician metasedimentary and igneous rocks of the Tugaloo terrane.

Structures related to six deformational events have been identified in this portion of the Inner Piedmont. The Brindle Creek fault has been folded multiple times, resulting in a sinuous outcrop pattern and the formation of the Newton window and smaller Howards Creek window. Portions of three map-scale sheath folds have been identified by map patterns and orientation of dominant mineral lineations, fold axes, and shear-sense indicators. The discontinuity of map-scale bodies of metagraywacke, mafic complexes, and amphibolite is attributed to extension during sheath fold formation. Dominant foliation, mineral lineation, and fold-axis orientations suggest north-northwest directed flow occurred in this portion of the Inner Piedmont.

Zircon geochronology data indicate crystallization of the Vale charnockite at 366.4 ± 3.1 Ma and the enclosing Walker Top Granite at 356.5 ± 5.3 Ma. Zircon saturation thermometry estimates minimum magmatic temperatures for the granitoids at 800-840° C. Whole-rock geochemical and isotopic data indicate the Vale charnockite and Walker Top Granite are genetically related and were derived from deep crustal melting of largely Proterozoic-affinity metasediments in an arc environment. Both granitoids crystallized from the same parent magma; the Vale charnockite is an autolith, or early crystallization of the melt, incorporated into the later crystallizing Walker Top Granite.

Geochemical analyses of Cat Square terrane mafic complexes west of the Newton window suggest these bodies represent vestiges of oceanic crust formed in a back-arc basin setting or from both MORB and volcanic-arc sources as characterized by mixed N-MORB and calc-alkaline volcanic-arc signatures. This back-arc basin likely formed from east-dipping subduction during the development of Ordovician volcanic arcs outboard of Laurentia.

TABLE OF CONTENTS

LIST OF FIGURES

Chapter 1

Chapter 2

Chapter 3

Chapter 4

Chapter 5

Chapter 6

LIST OF TABLES

LIST OF ATTACHMENTS

CHAPTER 1

INTRODUCTION

The grandeur of mountain chains across the world has a timeless appeal to geologists as they are awed by the expansive ranges of peaks rising high above sea level, the significant variety in rock types and compositions, and their sudden termination at the ocean's edge or beneath a coastal plain. These with other intriguing finds, such as economically valuable resources, ignite within geologists the desire to tackle some of the great mysteries of mountain chains: How did they form? How old are they? What processes occurred during their formation? And so on. As technology advances and ideas evolve and build on one another, more questions arise. It becomes a constant search for more data, more answers, and better models to explain observed phenomena in mountain chains, ultimately providing an atmosphere for collaboration, discussions, and disagreements between other scientists.

Over its history, the Appalachian Mountains have been explored by Native Americans, European settlers, Americans, and geologists alike in search of food, economic resources, solitude, and answers for understanding the mountains' existence. From a geologic perspective, the discovery and development of economically valuable resources in America, and across the world, has had the most significant impact on society. Within the region of this study, in the southern Appalachians in west-central North Carolina, there are several examples of this economic impact: gold mining in the South Mountains (Burke, McDowell, and Ruherford Cos.) and Kings Mountain belt (Cleveland, Gaston, Lincoln, and Catawba Cos.), mica mining in the Shelby pegmatite district, emerald mining in Hiddenite (Alexander Co.) and Patterson Springs (Cleveland Co.), and iron ore mining in the Kings Mountain belt for production of metallic iron (Stuckey, 1965; Presnell, 1999). Additional resources, such as spodumene, marble, barite, manganese, and pyrite, are located in the Kings Mountain belt (Horton, 2008). Mica and iron ore mining in west-central North Carolina played key roles during the Revolutionary, Civil, First and Second World Wars (Stuckey, 1965; Presnell, 1999).

Geologic study of the Appalachian Mountains has also had considerable impact within the geologic community for understanding crustal-scale tectonic processes related to the development of mountain chains. Reconnaissance and detailed geologic mapping provide a contextual framework for understanding other data sets, such as geochronology, geothermobarometry, and geochemistry, from which models explaining the formation of orogens are built and developed. These models are modified and refined piecewise as studies are conducted in different areas to address specific problems, forming "islands" of data and information. One such "island" is located in the Columbus Promontory and South Mountains of west-central North Carolina, encompassing approximately 3400 km^2 of the southern Appalachian Inner Piedmont (Fig. 1-1). Two terranes (Tugaloo and Cat Square) and four ductile thrust faults (Tumblebug Creek, Sugarloaf Mountain-Six Mile, Mill Spring, and the western exposure of the Brindle Creek, have been identified and mapped in this region. This study will extend the eastern edge of this island of information, focusing on the rocks in both the Tugaloo and Cat Square terranes, separated by the easternmost known exposure of the Brindle Creek fault. Research was conducted to answer questions raised prior to and during detailed geologic mapping. Results were compared to previous studies and regional tectonic models, adding another piece to the larger puzzle of understanding the formation of the southern Appalachians.

Objectives

The primary goals of this study are to:

1.) Create a detailed 1:24,000-scale geologic map and cross sections of portions of the Banoak, Reepsville, Lincolnton West, and Cherryville 7.5-minute quadrangles adjacent to the previous detailed geologic mapping in the South Mountains and Columbus Promontory (Fig. 1-2; Plate 1).

2.) Define and study the extent and nature of the easternmost known exposure of the Brindle Creek fault, the west-central boundary of the Newton window.

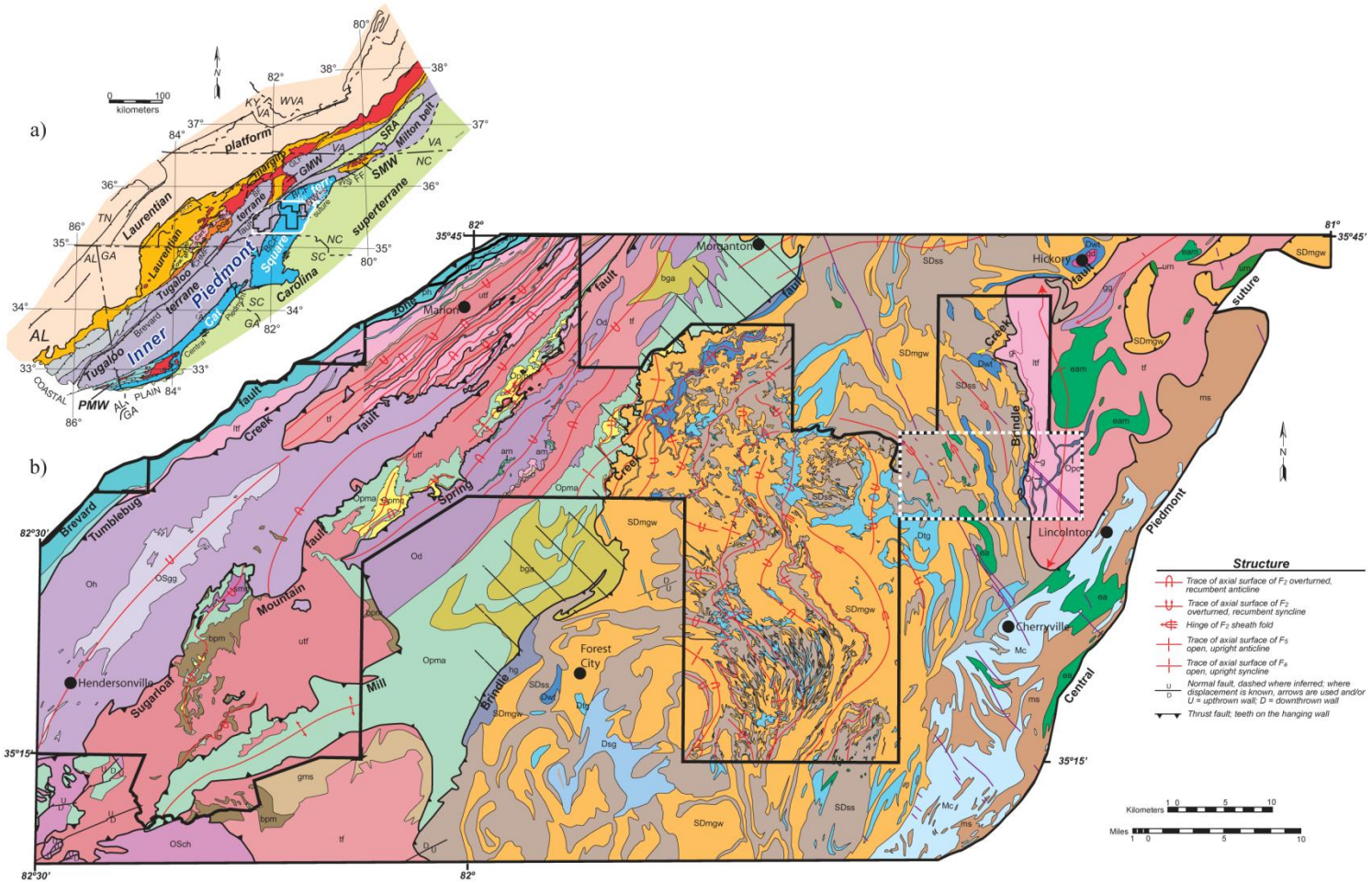

Figure 1-1. Geologic map of the Columbus Promontory, South Mountains, Hickory-Cherryville area in the North Carolina Inner Piedmont. a) Simplified tectonic map showing location of map area in part b (modified from Merschat and Hatcher, 2007). White polygon outlines map area in part b. Black polygon outlines compiled area of detailed geologic mapping. b) Simplified geologic map of the Columbus Promontory, South Mountains, Hickory-Cherryville area in the North Carolina Inner Piedmont. The black polygon outlines compiled area of detailed geologic mapping. Dashed white rectangle outlines study area. c) Explanation of map units

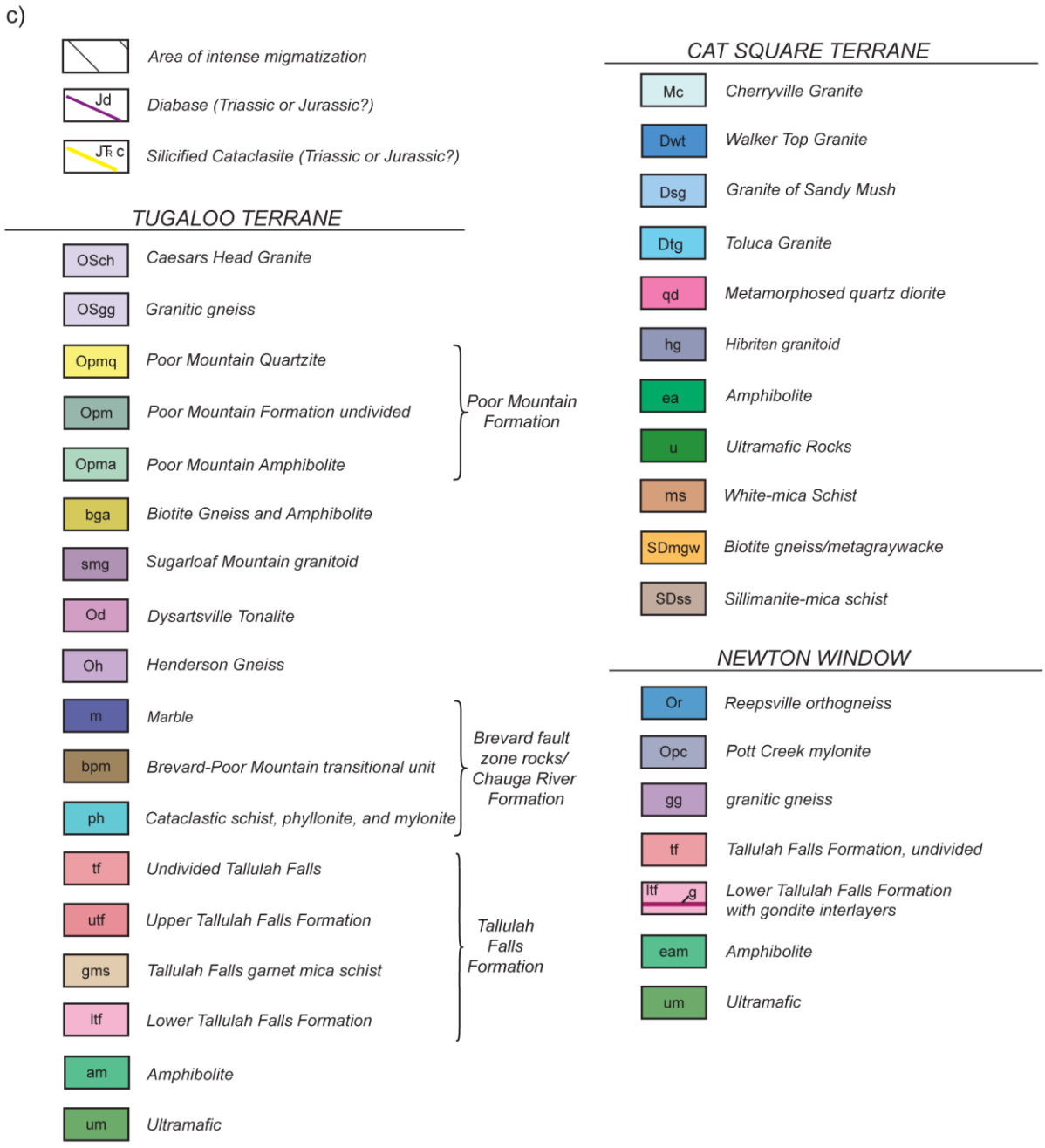

Figure 1-1. *continued*.

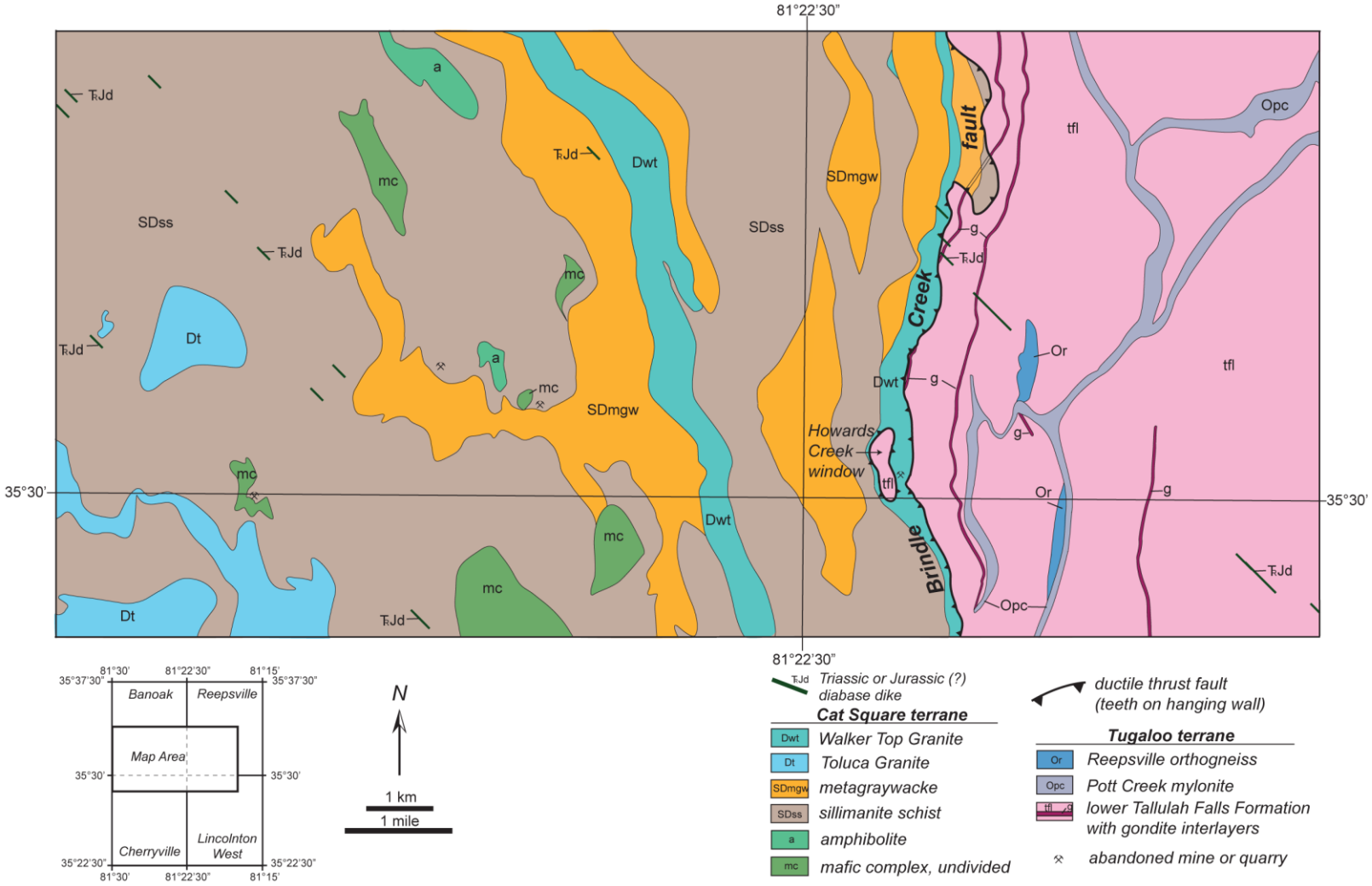

Figure 1-2. Simplified geologic map of portions of the Banoak, Reepsville, Lincolnton West, and Cherryville 7.5-minute quadrangles.

3.) Delimit the timing and conditions of emplacement of the Walker Top Granite and Vale charnockite xenoliths using zircon geochronology, whole-rock chemical analyses, isotopic analyses, and electron microprobe mineral chemical analyses in order to understand the occurrence of the Vale charnockite in the Inner Piedmont.

4.) Provide insight for the origin and evolution of outcrop and map-scale mafic complex and amphibolite bodies of the Cat Square terrane using whole-rock chemical analyses.

Location

The study area is located in west-central North Carolina, approximately 55 kilometers northwest of Charlotte via NC-27, 30 kilometers southeast of Morganton via NC-18, and 25 kilometers southwest of Hickory via NC-127 and U.S. Hwy. 10 (Fig 1-3). It covers ~140 km^2 in parts of Lincoln, Catawba, and Cleveland Counties in portions of the Banoak, Reepsville, Lincolnton West, and Cherryville 7.5-minute quadrangles. All outcrop and sample locations are identified by proximity to creeks and North Carolina State Roads in Lincoln County. The Banoak and Cherryville quadrangles share a border with the previously mapped Casar and Lawndale quadrangles, respectively. The region is dominated by low relief, with most outcrop exposures in and around creeks, on hillsides, and along roadsides.

Methodology

This study uses a combination of field and laboratory techniques. Detailed geologic mapping of 140 km^2 was conducted during two field seasons: January to August, 2007, and January to July, 2008. Mapping was done at 1:24,000-scale on standard U.S.G.S. 7.5-minute quadrangles. Traditional methods (field book, paper copy of maps) were used to record data during the first field season. The second season's data were recorded using an ArcPad form adopted from the North Carolina Geologic Survey on a hand-held Trimble GeoXT. Data from both seasons were compiled into databases in ArcGIS. The geologic map contacts were first digitized in Adobe Illustrator and then imported and attributed into ArcMap where the final map

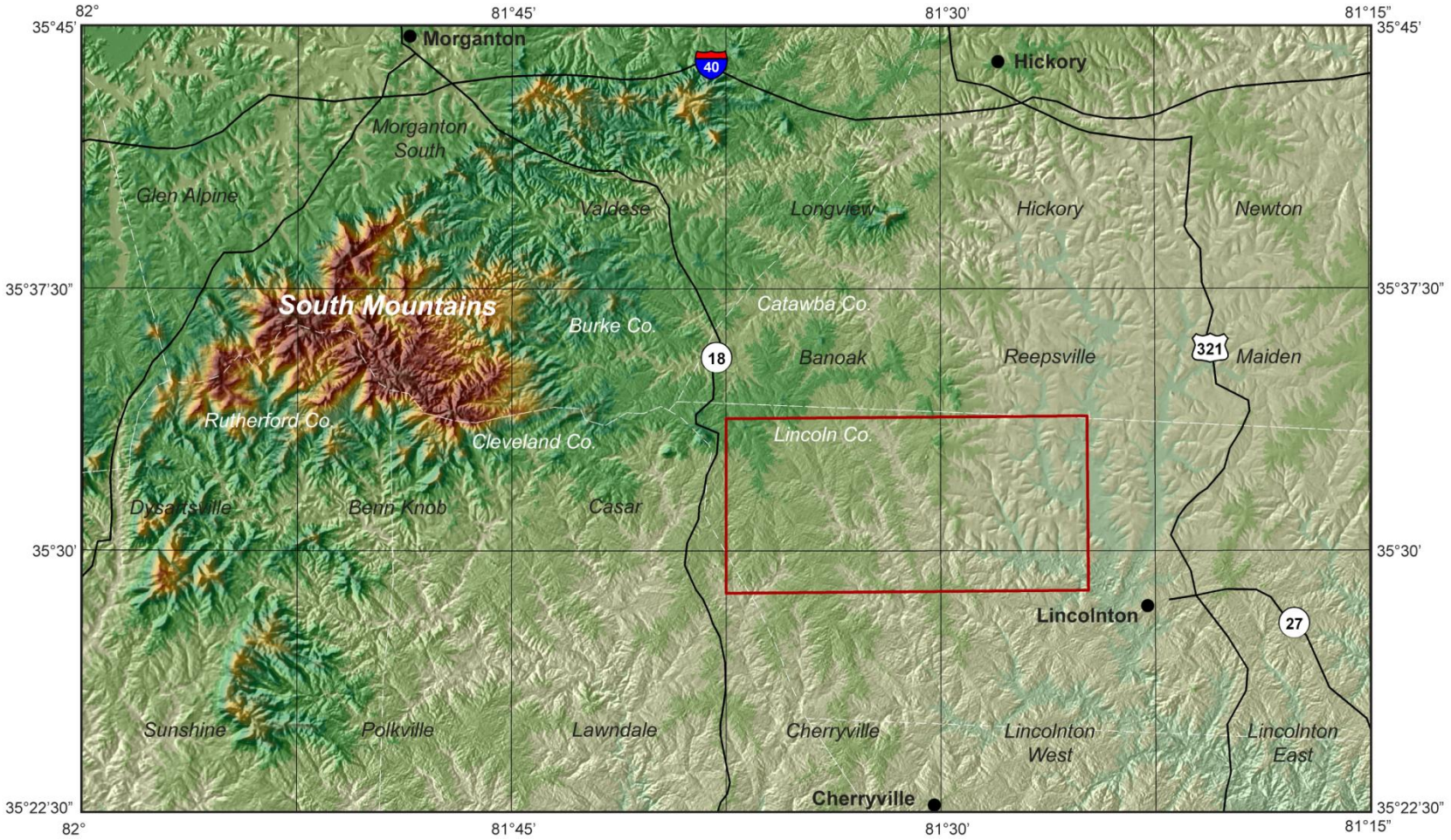

Figure 1-3. Hillshade map showing the location of study area relative to the South Mountains, quadrangle and county boundaries, main highways, and towns. Study area outlined by red box.

was completed (Plate 1). Structural data for foliations, lineations, folds, and joints were collected from >1,000 individual exposures within the field area (Plate 2; Appendix A). These data were plotted using standard lower-hemisphere equal-area projection stereonets on Stereonet v. 6.3.3 (Allmendinger, 2003).

Forty samples representative of the different rock types in the study area were collected for petrographic analysis. Standard sized (2.4 x 4.6 cm) and oversized (5.08 x 7.62 cm) thin sections were used for modal and fabric analyses. Modal analyses consisted of point counting using a stage and step sizes relevant for the grain size present in different rock types. Shear-sense data were obtained from oriented samples.

Eight fresh samples of granitic and mafic rocks were analyzed for major, minor, and trace-element abundances. The geochemistry was determined by inductively coupled plasma (ICP) emission spectrometry and instrumental neutron activation analysis (INAA) at Activation Laboratories (ActLabs) in Ancaster, Ontario. Tables in Chapters 5 and 6 indicate method used for each element analyzed. These data were plotted using IgPet05 software.

Electron microprobe mineral chemical analyses were collected from a fresh sample of the Vale charnockite. Analyses were collected on the Cameca SX 50 electron microprobe at the University of Tennessee. Crystallization temperatures were calculated using a two-pyroxene thermometer (QUILF; Anderson et al., 1993) and a graphical two-feldspar thermometer (Fuhrman and Lindsley, 1988).

Zircon analyses were collected on four samples within the study area using the Stanford University–U.S.G.S. sensitive high-resolution ion microprobe–reverse geometry (SHRIMP–RG). The SHRIMP–RG was used to collect $^{206}Pb/^{238}U$ and $^{207}Pb/^{206}Pb$ ages for detrital zircons and $^{206}Pb/^{238}U$ and $^{207}Pb/^{235}U$ ages for igneous zircons. Data were plotted using Isoplot v.3.0 (Ludwig, 2003). This technique was used due to the nature of the complex zircons in order to obtain more precise results to determine provenance, more recent magmatic ages, and metamorphic ages. Zircon separation and analysis were done using the methods described by Bream (2003).

Geologic Setting

The Inner Piedmont is the Neoacadian orogenic core of the southern Appalachians, exhibiting the widest area of high-grade metamorphic rocks in the mountain chain (Griffin, 1971; Hatcher, 2002). This polydeformed province is bound to the west by the Brevard fault zone and to the east by the Central Piedmont suture, extending ~700 km from North Carolina to Alabama (Hatcher, 2002) (Fig 1-4). The Brindle Creek fault defines a terrane boundary and separates the Tugaloo terrane of the western Inner Piedmont from the Cat Square terrane of the eastern Inner Piedmont.

The Brindle Creek fault was first mapped by reconnaissance as a lithologic contact by Goldsmith et al. (1988) in the Charlotte 1° x 2° quadrangle. Later detailed geologic mapping in the South Mountains of North Carolina interpreted this contact as a low-angle, eastward-dipping, Type F thrust fault that truncated map-scale synforms of Poor Mountain Formation rocks in the Mill Spring thrust sheet (Fig. 1-1) (Giorgis, 1999). Bream (2003) later proved that the Brindle Creek fault is a terrane boundary separating the eastern and western Inner Piedmont by using U-Pb SHRIMP detrital zircon geochronology. Detrital zircon populations revealed Laurentian (2.8, 1.8, 1.4, 1.1 Ga) and peri-Gondwanan affinities (600, 500 Ma) with an abundance of ~430 Ma ages. A minimum age for emplacement of the Brindle Creek thrust sheet is delimited by the 430 Ma youngest detrital zircons and the oldest igneous zircons of ~407 Ma (Walker Top Granite; Gatewood, 2007) in the Cat Square terrane.

The trace of the Brindle Creek fault extends ~400 km along strike from Winston-Salem, North Carolina, through the Brushy Mountains (Kalbas, 2003; Merschat, 2003; Wilson, 2006; Gatewood, 2007), South Mountains (Giorgis, 1999; Williams, 2000), South Carolina (Curl, 1998; Nelson et al., 1988), and Georgia (Merschat and Hatcher, 2007; Davis et al., 2009) (Fig. 1-4). The southern extent of the Brindle Creek fault is currently unknown, but is speculated to truncate against the Towaliga fault (Steltenpohl et al., in press; Hatcher and Steltenpohl, in preparation). The Brindle Creek fault has also been recognized east of the South Mountains where it frames western Inner Piedmont Tugaloo terrane rocks in the Newton window (Merschat et al., 2005a) (Fig. 1-1).

Figure 1-4. Tectonic map of the central and southern Appalachians. a) Inset map of the southeastern United States showing map area (shaded) in b. b) Simplified tectonic map of the central and southern Appalachians. Study area enclosed by white rectangle. BCF-Brindle Creek fault. BF-Burnsville fault. Cart. Terr.-Cartoogechaye terrane. CHMF-Chattahoochee-Holland Mountain fault. Cow. Terr.-Cowrock terrane. DGB-Dahlonega gold belt. FF-Forbrush fault. GLF-Gossan Lead fault. GMW-Grandfather Mountain window. NW-Newton window. SRA-Smith River allochthon, a possible outlier of the Carolina superterrane or Cat Square terrane rocks. SMW-Sauratown Mountains window. PMW-Pine Mountain window. Light gray-Probably western Tugaloo terrane rocks in Alabama and Georgia. A-Athens, GA. H-Hickory, NC. S-Statesville, NC. WS-Winston-Salem, NC. Figure modified from Merschat and Hatcher (2007).

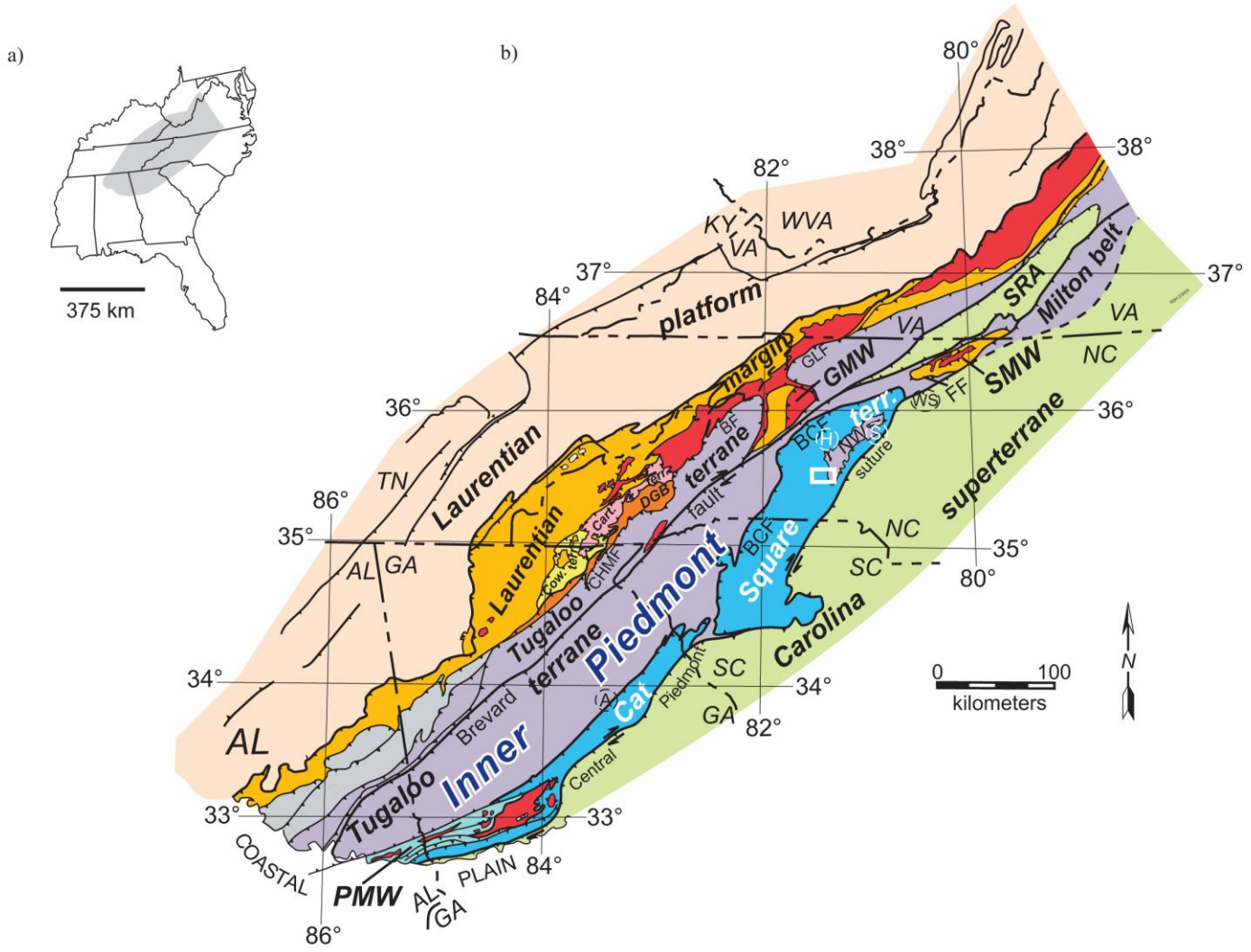
a)
375 km
b)
80°
38°
82°
KY
WVA
VA
37°
84°
platform
SRA
Milton belt
VA
NC
SMW
GMW
GLF
margin
36°
TN
Laurentian
terrane
BF
FF
WS
BCF
suture
superterrane
86°
35°
AL
GA
Laurentian
Cart.
DGB
fault
NC
SC
CHMF
Tugaloo
terrane
Piedmont
Square
Carolina
34°
Brevard
Piedmnt
Cat.
Central
Inner
Tugaloo
33°
COASTAL
PLAIN
PMW
0
100
kilometers
N

Rock Units

Western Inner Piedmont: Eastern Tugaloo Terrane

The western Inner Piedmont contains the eastern Tugaloo terrane with the Laurentian-affinity, Neoproterozoic-Cambrian Tallulah Falls–Ashe and Chauga River Formations unconformably overlain by the Poor Mountain Formation (Fig. 1-5; Hatcher, 2004). The three-part stratigraphy of the Tallulah Falls Formation makes up the majority of the Tugaloo terrane: lower graywacke-schist-amphibolite member, middle aluminous schist member, and upper graywacke-schist member (Hatcher, 2002). The western Inner Piedmont stratigraphically correlates across the Brevard fault zone with the Tugaloo terrane of the eastern Blue Ridge (Hatcher, 1987; Hopson and Hatcher, 1988; Merschat et al., 2005b). Dextral transpression along the Brevard fault zone has produced the repetition of the Tugaloo terrane units. Thrust sheets in the western Inner Piedmont were intruded by Ordovician-Silurian intermediate to felsic plutons during the Taconic orogeny. These plutons contain few to no inherited zircons compared to the Ordovician and Devonian plutons in the eastern Blue Ridge Tugaloo terrane (Mapes, 2002; Bream, 2003; Stahr et al., 2005; Hatcher et al., 2007). Detrital zircon populations from the Newton window suggest the Tallulah Falls Formation is the dominant exposed unit (Merschat et al., 2005a). Goldsmith et al. (1988) traced a single, folded gondite layer within the Tallulah Falls Formation near the western edge of the Newton window.

Eastern Inner Piedmont: Cat Square Terrane

The eastern Inner Piedmont consists of the mixed Laurentian and peri-Gondwanan affinity Siluro-Devonian aluminous schist overlain by biotite paragneiss of the Cat Square terrane. Map-scale bodies of amphibolites and ultramafic rocks, and undifferentiated mafic-ultramafic rocks occur throughout the Cat Square terrane. Small amphibolite and ultramafic bodies occur near the Brindle Creek fault in the Brushy and South Mountains (Giorgis, 1999; Merschat, 2003; Wilson, 2006), while larger mafic-ultramafic bodies occur in the eastern Cat Square terrane, near the Central Piedmont suture in North and South Carolina (Privett, 1984; Mittwede et al., 1987; Goldsmith et al., 1988). Wilson (2006) reported a mixed volcanic-arc and

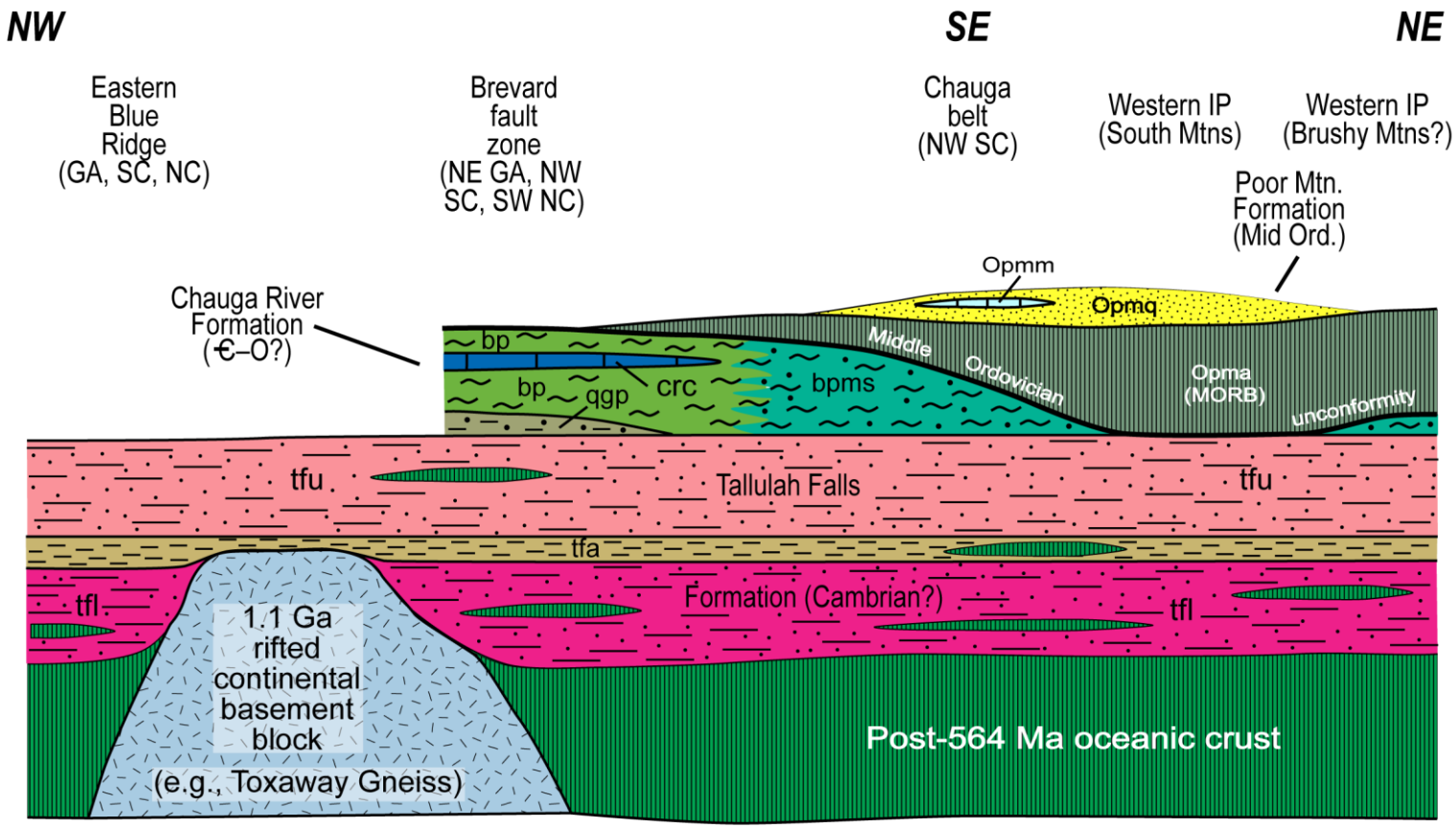

Figure 1-5. Stratigraphic relationships in the Tugaloo terrane. Vertical and horizontal scales are approximate: the northwest to southeast segment is expanded relative to the compressed southeast to northeast segment. Tallulah Falls members: tfl–lower graywacke-schist-amphibolite member; tfa–middle aluminous schist member; tfu–upper greywacke-schist member. Amphibolite, green vertical ruled lenses, occurs in all members of the Tallulah Falls, but is most common in the lower member. Chauga River Formation subdivisions: gqp–quartize and graphitic phyllonite; bp–Brevard Phyllite member; bpms–interlayered Brevard phyllite and metasiltstone; crc–Chauga River carbonate. Poor Mountain Formation members: Opma–Poor Mountain (Cedar Creek) amphibolite; Opmq–quartzite; Opmm–marble. Figure modified from Hatcher (2004).

enriched-type mid-ocean ridge basalt (E-MORB) signature for eastern Inner Piedmont amphibolites in the Brushy Mountains. The Hammet Grove mafic-ultramafic body in the South Carolina eastern Inner Piedmont was interpreted as a deformed ophiolite (Mittwede et al., 1987). Merschat and Hatcher (2007) proposed Cat Square terrane sediments were deposited in a Siluro-Devonian remnant ocean basin between Laurentia and the approaching peri-Gondwanan microcontinent Avalon (Carolina superterrane). Locally derived Devonian-Mississippian granitoid plutons intruded the Cat Square terrane during peak Neoacadian conditions after subduction and burial of the remnant ocean basin (Giorgis, 1999; Bier, 2001; Mapes, 2002; Mapes et al., 2002; Bream, 2003; Hatcher et al., 2007). These plutons contain little to no zircon inheritance similar to those of the western Inner Piedmont (Mapes, 2002; Gatewood, 2007; Byars et al., 2008a).

Previous Work

Reconnaissance mapping of the eastern Inner Piedmont was completed by Goldsmith et al. (1988) in the Charlotte 1° x 2° quadrangle. The Newton window was mapped as a northeast-southwest trending, doubly plunging antiform exposing biotite gneiss, biotite-hornblende gneiss, amphibolite, and ultramafic bodies (Fig. 1-6). These units were designated to be in lithologic contact with the surrounding aluminous schist, metagraywacke, and granites. The map pattern and unique assemblage exposed in the antiform raised interest for further study. Merschat et al. (2005a) sampled and obtained zircon age dates from three samples in the antiform (Fig. 1-6). Detrital zircons from two paragneisses (samples SP13 and SW6) revealed peaks at 1.0, 1.15, 1.2 Ga (Grenvillian) and 1.4 Ga (granite-rhyolite province?) implying a Laurentian provenance (Merschat et al., 2005a). A sample of biotite orthogneiss (sample R29) yielded a U-Pb age of 1050 ± 18 Ma with metamorphic rims of ~350 Ma, providing evidence that the biotite gneiss may be a fragment of Grenville crust. This age date was significant because it was only the second reported occurrence of continental basement rock found in the southern Appalachian Inner Piedmont, with the Forbush Gneiss of the Sauratown Mountains window being the first (McConnell, 1990; Horton and McConnell, 1991; Merschat and Hatcher, 2007) (Fig 1-4).

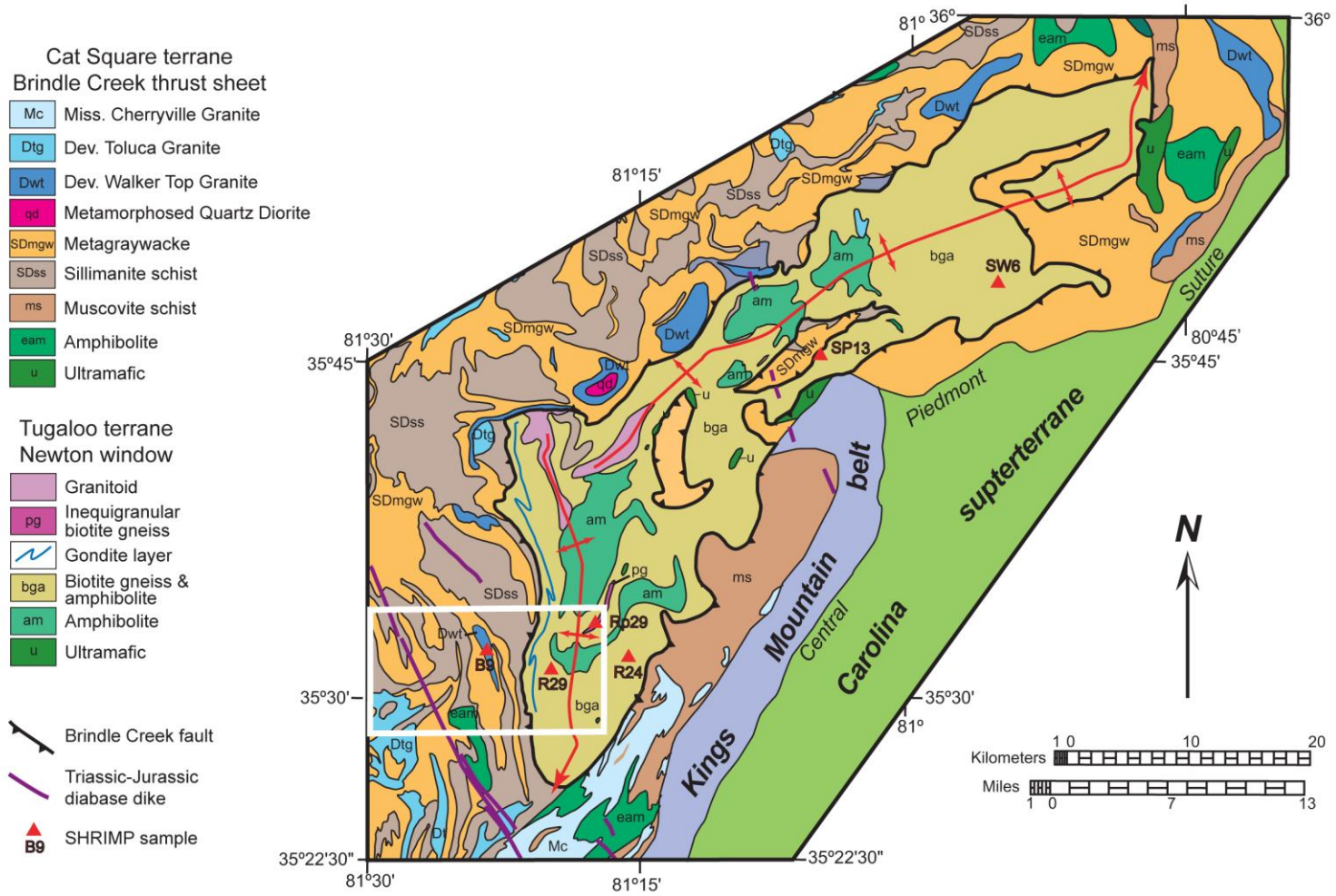

Figure 1-6. Geologic map of the Newton window slightly modified from Goldsmith et al. (1988), showing contacts and units mapped in reconnaissance (modified from Merschat et al., 2008). White rectangle outlines area mapped in detail in this study (see Fig. 1-2). SHRIMP samples SW6, SP13, and R29 are from Merschat et al. (2005a), R24 is from Merschat (2009) and this study, and B9 and Rp29 are from this study.

In addition to reconnaissance mapping, detailed geologic mapping has been completed over an area extending west of the Newton window in the South Mountains, to the Brevard fault zone in the Columbus Promontory (Overstreet et al., 1951, 1963; Butler, 1972; Lemmon and Dunn, 1973a, 1973b; Davis, 1993; Yanagihara, 1994; Bream, 1999; Giorgis, 1999; Hill, 1999; Williams, 2000; Bier, 2001) (Fig. 1-1, Plate 3). The geologic map completed for this study has been compiled with this area of previous detailed mapping providing evidence for the interpretation of regional structures from map patterns. These data and interpretations will be discussed in detail in the following chapters.

CHAPTER 2

ROCK UNITS

Introduction

Eleven distinct map units have been recognized from the two terranes within the study area: six in the Cat Square terrane, four in the Tugaloo terrane, and one common to both terranes (Fig. 2-1). Nine of these units were mapped in reconnaissance by Goldsmith et al. (1988), while two units were not recognized at that time (Fig. 1-6). Contacts of map units are correlated with those of detailed and reconnaissance geologic maps surrounding the study area (Plate 3; Fig. 1-1) (Overstreet et al., 1963; Goldsmith et al., 1988; Gilliam, in progress). Geometries of many of the contacts from reconnaissance mapping very closely reflect those mapped in detail during this study. Amphibolite bodies in the Newton window and the Cat Square terrane metagraywacke unit are not as extensive as previously mapped. Map units that are more extensive than Goldsmith et al. (1988) work include Triassic-Jurassic diabase dikes, the gondite layer, and inequigranular biotite gneiss (Pott Creek mylonite) in the Newton window, the Walker Top Granite, Toluca Granite, sillimanite schist, and amphibolite bodies in the Cat Square terrane (Figs. 1-6; 2-1). Previously unrecognized units include undifferentiated mafic complexes and the Reepsville orthogneiss.

Rock outcrops can be found along roadsides, in and along creek and river beds and cut banks, the sides of hills, and along some ridges within the study area. Saprolite is also very common in creek beds and cut banks. Extensive weathering in the Inner Piedmont makes the recognition of rock types in saprolite and soils an important part of detailed geologic mapping. Thus, saprolite and soil colors will be discussed and identified using slightly modified terminology of the Rock-Color Chart prepared by the Rock-Color Chart Committee (1948). Generally, rocks with more mafic minerals and higher iron content produce darker, reddish-brown soils, whereas more aluminous and silicate-rich rocks produce lighter, orange-red to light, tan-gray soils. Detailed field and petrologic descriptions of each rock unit of the Cat Square and Tugaloo terranes will also be discussed in this chapter. Location of samples used for petrologic,

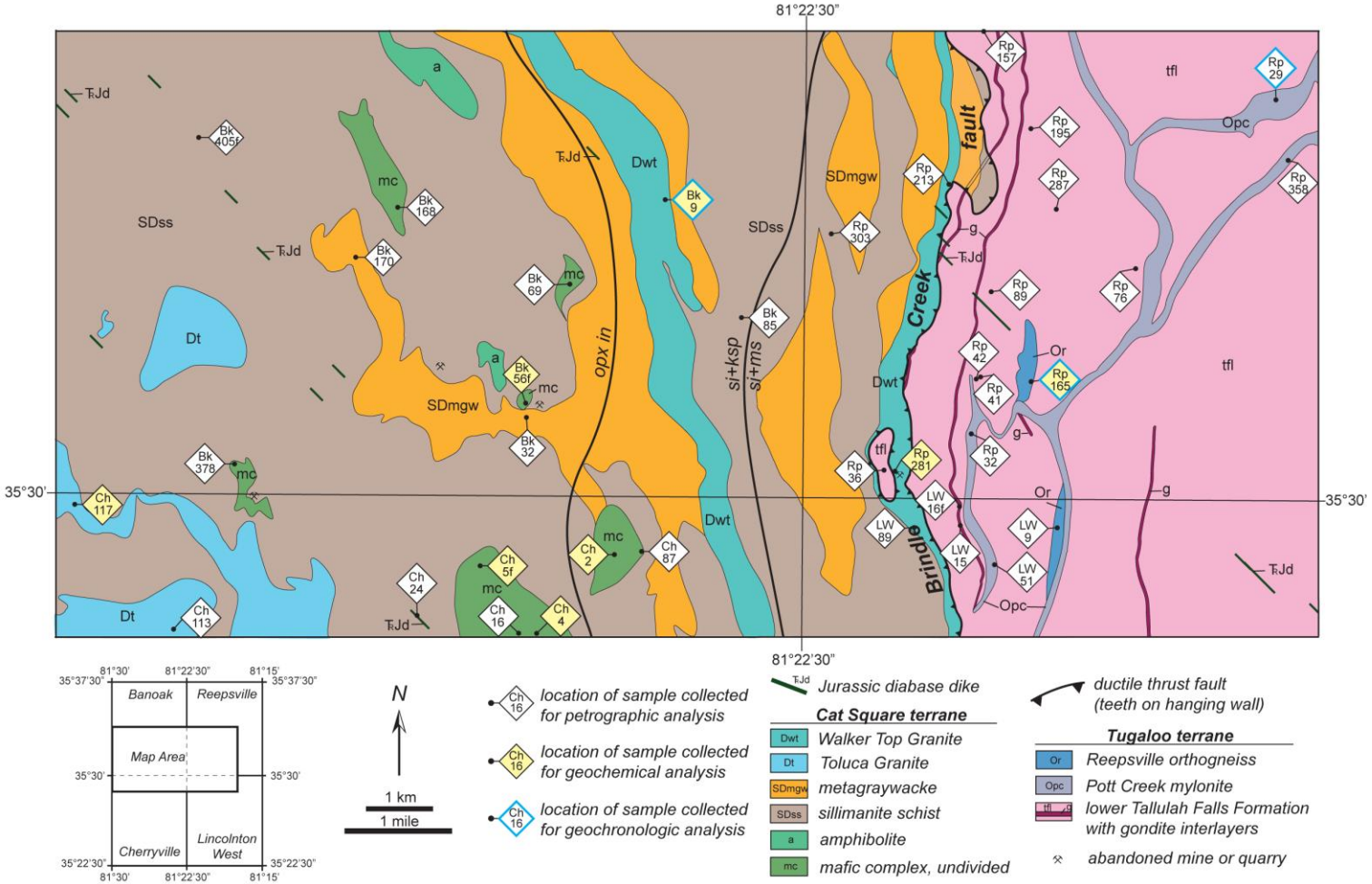

Figure 2-1. Simplified geologic map of portions of the Banoak, Reepsville, Lincolnton West, and Cherryville 7.5-minute quadrangles showing the locations of samples collected for petrologic, geochemical, and geochronologic analyses. Sample location Rp165 is the same location as R29 from Merschat et al. (2005a). Sample location Rp157 is the same location as R21 from Merschat (2009).

geochemical, and geochronologic analyses in this study are shown in Figure 2-1.

Newton Window/Western Inner Piedmont – Eastern Tugaloo terrane

Tallulah Falls-Ashe Formation

Rocks of the Newton window consist mainly of the Neoproterozoic-Cambrian(?) Tallulah Falls-Ashe Formation. The core of the doubly plunging Newton antiform was originally identified as a separate package of biotite gneiss, biotite-hornblende gneiss, amphibolite, and ultramafic rocks from the surrounding sillimanite schist–biotite gneiss-dominated assemblage (Goldsmith et al., 1988; Fig. 1-6). After recognition of the Newton antiform as a window through the Brindle Creek thrust sheet, Merschat et al. (2005a) correlated these rocks with those of the Tallulah Falls Formation in the Tugaloo terrane based on similar detrital zircon populations, rock units, and the presence of possible Grenville basement.

The upper and lower Tallulah Falls Formation, separated from by a middle aluminous schist member, are distinguished in the field by the greater concentration of amphibolite in the lower member than the upper member (Hatcher et al., 2005). Amphibolite and hornblende-biotite gneiss are abundant throughout the study area as interlayers and boudins. Minor amounts of pelitic schist were found in the Newton window, but there was not a mappable layer present. The absence of a middle aluminous schist, combined with the large concentration of amphibolite, permitted determination that only the lower Tallulah Falls Formation is present in the study area.

Detrital zircons were analyzed from a sample of migmatitic hornblende-biotite gneiss east of the study area in the Reepsville 7.5-minute quadrangle to verify the eastern extent of the Newton window as mapped by Goldsmith et al. (1988) (Plate 2; Fig. 1-6). The location of sample R24 is from an area mapped in reconnaissance as biotite gneiss, similar to rocks west of the Newton antiform that are now identified as Cat Square terrane metagraywacke. U-Pb SHRIMP analysis of the detrital zircons yielded ages ranging from 1.0-1.3 Ga with a single ~1.45 Ga age (Table 2-1; Fig. 2-2). These Grenville and possible granite-rhyolite province ages imply a Laurentian provenance, similar to other Newton window samples (Merschat et al., 2005a; Merschat, 2009).

Table 2-1. SHRIMP-RG U-Th-Pb analytical results for the lower Tallulah Falls Formation, Pott Creek mylonite and Reepsville orthogneiss.

				Total				Radiogenic Ratio						207-corrected		208-corrected		204-corrected ages (Ma)				
Analysis Number	Common ^{206}Pb (%)	U ppm	Th ppm	$^{232}Th/^{238}U$	$^{238}U/^{206}Pb$	error (%)	$^{207}Pb/^{206}Pb$	error (%)	$^{206}Pb/^{238}U$	error (%)	$^{207}Pb/^{206}Pb$	error (%)	$^{207}Pb/^{235}U$	error (%)	ρ	$^{206}Pb/^{238}U$	±1σ	$^{206}Pb/^{238}U$	±1σ	$^{206}Pb/^{238}U$	±1σ	$^{207}Pb/^{206}Pb$	±1σ	%Conc
lower Tallulah Falls Formation (R24)																								
R24-14.1	0.84	23	7	0.31	6.23	2.2	.0698	3.9	.1591	2.3	.0628	8.9	1.38	9.2	.246	960.6	20.5	956.0	20.5	951.6	19.9	703	189	135
R24-23.1	0.15	158	97	0.64	6.28	0.8	.0714	1.4	.1590	0.8	.0701	1.6	1.54	1.8	.443	952.0	7.5	952.3	8.0	951.3	7.2	932	34	102
R24-9.1	0.00	1514	36	0.02	7.38	0.3	.0704	0.6	.1356	0.3	.0704	0.6	1.32	0.6	.470	815.9	2.4	819.3	2.3	819.6	2.3	940	11	87
R24-2.1	0.00	41	14	0.35	5.68	1.5	.0718	3.7	.1761	1.5	.0718	3.7	1.74	4.0	.382	1048.7	16.0	1045.7	15.8	1045.8	14.9	979	76	107
R24-6.1	0.03	720	75	0.11	6.34	0.4	.0723	0.6	.1577	0.4	.0721	0.7	1.57	0.7	.487	942.2	3.3	945.8	3.3	944.0	3.2	989	13	95
R24-31.1	0.01	1701	240	0.15	6.14	0.2	.0724	0.4	.1629	0.2	.0723	0.4	1.62	0.5	.503	972.0	2.3	972.4	2.3	972.9	2.2	995	9	98
R24-32.1	0.00	1280	95	0.08	6.15	0.3	.0726	0.5	.1625	0.3	.0726	0.5	1.63	0.6	.500	969.3	2.7	969.1	2.6	970.5	2.6	1002	10	97
R24-15.1	0.00	174	140	0.83	6.22	0.9	.0727	1.5	.1609	0.9	.0727	1.5	1.61	1.7	.504	959.9	8.0	964.1	8.8	961.6	7.6	1006	30	96
R24-28.1	0.06	140	88	0.65	5.87	0.9	.0737	1.4	.1703	0.9	.0731	1.5	1.72	1.7	.503	1013.6	8.7	1010.1	9.2	1013.8	8.2	1018	31	100
R24-8.1	0.00	103	67	0.68	5.99	1.0	.0733	1.7	.1668	1.0	.0733	1.7	1.68	2.0	.511	993.6	9.8	994.4	10.4	994.6	9.3	1021	34	97
R24-21.1	0.01	889	436	0.51	6.28	0.4	.0736	0.9	.1591	0.4	.0735	0.9	1.61	1.0	.381	948.8	3.4	951.3	3.5	951.7	3.2	1027	18	93
R24-30.1	0.03	390	102	0.27	7.19	0.5	.0738	1.0	.1390	0.5	.0735	1.0	1.41	1.1	.471	832.8	4.4	838.2	4.4	839.0	4.2	1028	20	82
R24-10.1	0.00	585	90	0.16	6.03	0.4	.0737	0.7	.1659	0.4	.0737	0.7	1.69	0.8	.510	987.8	3.9	990.1	3.8	989.6	3.7	1034	14	96
R24-12.1	0.01	1010	219	0.22	5.84	0.3	.0739	0.5	.1712	0.3	.0738	0.6	1.74	0.6	.505	1018.0	3.2	1019.2	3.3	1018.8	3.1	1035	11	98
R24-27.1	0.00	141	81	0.59	5.73	0.8	.0740	1.4	.1746	0.8	.0740	1.4	1.78	1.6	.520	1037.4	8.5	1036.2	8.9	1037.5	8.1	1041	28	100
R24-35.1	0.00	2825	232	0.08	5.21	0.2	.0742	0.6	.1919	0.2	.0742	0.6	1.96	0.6	.308	1135.9	2.1	1131.3	1.9	1131.7	1.9	1046	11	108
R24-11.1R	0.00	23	6	0.27	6.20	2.3	.0742	3.9	.1614	2.3	.0742	3.9	1.65	4.5	.509	961.1	21.3	962.7	21.3	964.4	20.4	1047	78	92
R24-20.1	0.01	947	364	0.40	6.26	0.3	.0743	0.7	.1597	0.3	.0742	0.7	1.63	0.8	.432	951.3	3.3	950.1	3.6	954.9	3.1	1047	15	91
R24-7.1	0.01	1151	701	0.63	6.09	0.3	.0748	1.1	.1642	0.3	.0747	1.1	1.69	1.2	.254	976.9	2.9	978.9	3.0	980.2	2.7	1062	23	92
R24-17.1	0.00	88	44	0.52	6.73	1.3	.0748	2.3	.1486	1.3	.0748	2.3	1.53	2.7	.495	886.8	11.4	893.0	12.0	892.9	10.9	1063	46	84
R24-4.1	0.01	1486	279	0.19	6.16	0.2	.0751	0.9	.1624	0.2	.0750	0.9	1.68	0.9	.263	965.9	2.4	969.1	2.3	969.8	2.2	1068	18	91
R24-16.1	0.00	1013	666	0.68	6.28	0.4	.0750	0.6	.1593	0.4	.0750	0.6	1.65	0.7	.496	948.5	3.4	938.5	4.0	953.1	3.2	1069	13	89
R24-25.1	0.03	1379	242	0.18	6.67	0.3	.0754	0.7	.1499	0.3	.0751	0.7	1.55	0.8	.439	894.0	3.0	895.5	3.1	900.3	2.8	1072	14	84
R24-24.1	0.00	875	476	0.56	5.70	0.4	.0755	1.0	.1753	0.4	.0755	1.0	1.82	1.0	.342	1039.6	3.7	1035.9	4.6	1041.4	3.4	1081	20	96
R24-29.1	0.00	206	139	0.70	6.04	0.7	.0756	1.1	.1655	0.7	.0756	1.1	1.73	1.3	.522	983.1	6.6	981.4	7.1	987.1	6.3	1085	23	91
R24-1.1	0.00	186	122	0.68	5.50	0.7	.0763	1.1	.1818	0.7	.0763	1.1	1.91	1.3	.534	1075.3	7.2	1075.5	7.7	1076.6	6.9	1104	22	98
R24-22.1	0.00	166	88	0.55	5.50	0.8	.0765	1.6	.1818	0.8	.0765	1.6	1.92	1.8	.451	1075.2	8.3	1074.1	10.8	1076.7	7.8	1108	31	97
R24-26.1	0.00	1681	743	0.46	5.72	0.3	.0773	0.5	.1749	0.3	.0773	0.5	1.86	0.6	.531	1034.8	2.9	1036.1	3.0	1038.8	2.8	1129	9	92
R24-36.1	0.05	478	477	1.03	5.33	0.5	.0783	0.8	.1875	0.5	.0778	0.8	2.01	1.0	.521	1105.9	5.5	1104.6	6.2	1107.7	5.2	1143	17	97
R24-33.1	0.00	1176	80	0.07	5.68	0.3	.0780	0.5	.1760	0.3	.0780	0.5	1.89	0.6	.531	1040.5	3.1	1041.9	5.4	1045.1	3.0	1146	10	91
R24-3.1	0.01	1059	794	0.77	5.39	0.3	.0792	0.8	.1856	0.3	.0791	0.8	2.02	0.8	.355	1094.0	3.2	1094.9	3.4	1097.7	2.9	1174	15	94
R24-5.1	0.06	1761	1465	0.86	5.11	0.2	.0803	0.4	.1957	0.2	.0798	0.4	2.15	0.5	.513	1149.8	2.6	1150.3	3.1	1152.0	2.5	1193	8	97
R24-13.1	0.05	838	534	0.66	4.96	0.4	.0804	0.5	.2015	0.4	.0800	0.6	2.22	0.7	.520	1182.6	4.1	1181.7	4.3	1183.3	3.8	1196	11	99
R24-19.1	0.00	296	300	1.05	5.22	0.6	.0812	1.0	.1917	0.6	.0812	1.0	2.15	1.2	.543	1125.9	6.9	1131.6	7.8	1130.7	6.5	1225	19	92
R24-18.1	0.00	1157	732	0.65	5.58	0.3	.0812	0.6	.1793	0.3	.0812	0.6	2.01	0.7	.472	1055.5	3.4	1059.2	3.6	1063.2	3.2	1226	12	87
R24-34.1	0.04	992	470	0.49	6.87	0.4	.0876	5.9	.1456	0.4	.0872	6.0	1.75	6.0	.062	857.7	5.9	870.0	7.5	876.1	3.0	1365	115	64

Table 2-1. *continued*.

					Total				Radiogenic Ratio							207-corrected		208-corrected		204-corrected ages (Ma)				
Number	^{206}Pb (%)	U ppm	Th ppm	^{232}Th/	^{238}U/^{206}	(%)	^{207}Pb/^{206}	error (%)	^{206}Pb/^{238}	error	^{207}Pb/^{206}	error (%)	^{207}Pb/^{235}	error (%)	ρ	^{206}Pb/^{238}	±1σ	^{206}Pb/^{238}	±1σ	^{206}Pb/^{238}	±1σ	^{207}Pb/^{206}P	±1σ	%Conc
Pott Creek mylonite (Rp29)																								
WTR29-6F	0.00	320	26	0.08	20.26	0.9	.0533	3.3	.0494	0.9	.0533	3.3	0.36	3.5	.248	310.4	2.7	309.9	2.6	310.6	2.6	341	76	91
WTR29-11	0.00	364	25	0.07	20.12	0.7	.0546	1.9	.0497	0.7	.0546	1.9	0.37	2.1	.358	311.9	2.3	312.2	2.3	312.7	2.2	396	43	79
WTR29-4.	0.00	312	10	0.03	19.75	0.8	.0542	2.1	.0506	0.8	.0542	2.1	0.38	2.2	.353	317.8	2.5	318.1	2.5	318.4	2.5	380	47	84
WTR29-13	0.20	454	10	0.02	18.68	0.6	.0530	2.0	.0534	0.6	.0514	2.6	0.38	2.7	.238	336.2	2.1	335.8	2.1	335.5	2.1	260	60	129
WTR29-5F	0.55	132	1	0.01	15.96	1.1	.0524	3.0	.0623	1.2	.0480	5.6	0.41	5.7	.204	392.9	4.5	391.2	4.3	389.8	4.4	101	132	384
WTR29-9F	0.15	211	3	0.02	15.85	1.0	.0564	2.4	.0630	1.0	.0552	2.8	0.48	2.9	.330	393.5	3.8	394.6	3.7	393.8	3.7	421	62	94
WTR29-2(	0.08	331	25	0.08	14.11	0.7	.0576	1.7	.0708	0.7	.0569	1.8	0.56	1.9	.361	440.5	3.1	441.0	3.0	441.2	3.0	489	40	90
WTR29-10	0.13	231	3	0.02	13.93	0.9	.0579	2.1	.0717	0.9	.0568	2.4	0.56	2.6	.337	445.7	3.8	446.3	3.7	446.2	3.7	485	53	92
WTR29-8(	0.00	366	103	0.29	5.97	0.6	.0749	1.0	.1676	0.6	.0749	1.0	1.73	1.1	.519	996.0	5.7	997.8	5.8	998.8	5.4	1066	19	94
WTR29-1(	0.05	209	93	0.46	5.73	0.7	.0805	1.8	.1744	0.7	.0801	1.8	1.93	1.9	.380	1029.2	7.5	1036.1	7.6	1036.5	7.1	1200	36	86
WTR29-7(	0.00	252	104	0.43	5.75	0.8	.0758	1.8	.1740	0.8	.0758	1.8	1.82	2.0	.388	1031.5	7.8	1032.9	7.9	1034.0	7.4	1090	37	95
WTR29-9(	0.07	146	50	0.36	5.40	0.9	.0767	1.5	.1852	0.9	.0761	1.6	1.94	1.8	.503	1095.4	9.8	1092.9	9.8	1095.4	9.3	1097	32	100
WTR29-12	0.00	170	73	0.44	5.35	0.8	.0744	1.2	.1871	0.8	.0744	1.2	1.92	1.4	.540	1108.1	8.1	1105.9	8.2	1105.6	7.7	1052	24	105
WTR29-3(	0.07	291	134	0.47	4.71	0.6	.0850	0.9	.2123	0.6	.0845	0.9	2.47	1.1	.542	1237.2	7.2	1240.9	7.3	1240.9	6.8	1304	18	95
WTR29-6(	0.07	152	108	0.73	4.42	0.9	.0841	1.2	.2262	0.9	.0835	1.3	2.61	1.6	.555	1316.7	11.1	1316.2	11.9	1314.6	10.3	1282	25	103
WTR29-10	0.00	49	41	0.87	3.06	1.5	.1196	1.5	.3268	1.5	.1196	1.5	5.39	2.1	.701	1806.5	26.4	1815.3	26.6	1822.9	23.5	1950	27	93
WTR29-5.	0.11	140	1	0.01	19.32	1.1	.0538	2.7	.0517	1.1	.0526	3.1	0.37	3.3	.321	325.0	3.4	325.2	3.4	324.9	3.4	310	72	105
WTR29-1.	0.17	604	16	0.03	18.84	0.4	.0545	1.3	.0530	0.4	.0539	1.4	0.39	1.4	.307	332.8	1.5	333.4	1.4	333.2	1.4	369	31	90
WTR29-2.	-0.22	225	24	0.11	18.86	0.7	.0513	2.2	.0529	0.7	.0498	2.7	0.36	2.8	.259	333.7	2.4	333.0	2.4	332.4	2.4	185	64	180
WTR29-4.	0.32	297	33	0.12	13.92	0.6	.0584	1.5	.0717	0.6	.0565	2.2	0.56	2.3	.261	445.8	2.6	446.8	2.6	446.1	2.6	472	49	95
WTR29-3.	0.04	171	2	0.01	13.66	0.8	.0564	2.0	.0731	0.8	.0550	2.4	0.55	2.6	.296	455.2	3.4	455.2	3.3	454.6	3.3	410	55	111
Reepsville orthogneiss (R29/Rp165)																								
R29-6.1	0.60	172	37	0.22	18.47	1.2	.0561	2.5	.0538	1.2	.0513	4.7	0.38	4.8	.245	338.7	3.9	340.0	4.0	337.9	3.9	254	108	133
R29-28.2F	0.21	373	58	0.16	18.39	0.8	.0552	1.8	.0543	0.8	.0535	1.9	0.40	2.1	.399	340.5	2.8	341.2	2.8	340.6	2.7	349	43	98
R29-22.1F	1.60	189	56	0.31	18.21	1.1	.0628	2.3	.0540	1.3	.0500	10.2	0.37	10.3	.122	340.6	3.8	340.3	4.0	339.3	4.1	195	237	174
R29-27.1	0.60	285	17	0.06	18.21	0.9	.0589	1.9	.0546	0.9	.0541	3.2	0.41	3.3	.272	342.3	3.1	342.7	3.1	342.6	3.0	374	73	92
R29-12.1	0.00	302	108	0.37	18.27	0.9	.0551	2.0	.0547	0.9	.0551	2.0	0.42	2.2	.414	342.8	3.1	343.0	3.2	343.5	3.0	416	44	83
R29-2.1	0.07	678	210	0.32	17.77	0.6	.0562	1.3	.0563	0.6	.0556	1.5	0.43	1.6	.384	351.9	2.1	352.5	2.2	352.8	2.1	437	32	81
R29-1.1	0.17	196	16	0.09	16.14	1.1	.0570	2.3	.0618	1.1	.0556	2.7	0.47	2.9	.378	386.2	4.2	387.7	4.2	386.8	4.1	437	60	89
R29-7.1	0.00	512	41	0.08	14.71	0.7	.0567	1.3	.0680	0.7	.0567	1.3	0.53	1.5	.437	423.3	2.7	424.8	2.7	424.0	2.7	480	30	88
R29-13.1R	0.00	753	31	0.04	14.65	0.7	.0574	1.1	.0683	0.7	.0574	1.1	0.54	1.3	.513	424.6	2.8	425.5	2.8	425.7	2.7	508	25	84
R29-22.2)	0.00	79	3	0.03	14.70	1.6	.0535	3.4	.0680	1.6	.0535	3.4	0.50	3.7	.433	425.3	6.8	423.7	6.7	424.3	6.6	348	76	122
R29-14.2F	0.00	288	15	0.05	14.48	0.9	.0559	1.7	.0691	0.9	.0559	1.7	0.53	1.9	.442	430.4	3.7	430.5	3.6	430.6	3.6	448	39	96
R29-18.1R	0.13	340	7	0.02	13.45	0.8	.0571	1.5	.0743	0.8	.0560	1.6	0.57	1.8	.436	461.9	3.5	462.2	3.5	461.8	3.4	454	35	102
R29-26.1	0.01	2338	107	0.05	7.20	0.3	.0719	0.4	.1390	0.3	.0719	0.4	1.38	0.5	.550	834.2	2.1	839.6	2.0	838.9	2.0	982	8	85
R29-10.1	0.15	934	127	0.14	7.15	0.4	.0740	0.6	.1396	0.4	.0727	0.9	1.40	0.9	.417	837.0	3.3	844.0	3.2	842.4	3.1	1007	17	84
R29-20.1	0.03	755	180	0.25	7.12	0.4	.0741	0.7	.1404	0.4	.0738	0.7	1.43	0.9	.526	840.7	3.8	846.7	3.7	847.0	3.6	1035	15	82
R29-18.2C	0.25	1227	259	0.22	7.11	0.4	.0733	0.5	.1402	0.4	.0712	1.1	1.38	1.1	.325	842.1	3.0	845.8	3.0	845.9	2.9	964	22	88
R29-15.1	0.02	706	187	0.27	6.97	0.6	.0711	0.7	.1435	0.6	.0710	0.7	1.40	0.9	.615	861.5	4.7	863.7	4.8	864.5	4.6	956	15	90

Table 2-1. *continued*.

					Total				Radiogenic Ratio						207-corrected		208-corrected		204-corrected ages (Ma)				
Analysis Number	Common ^{206}Pb (%)	U ppm	Th ppm	$^{232}Th/^{238}U$	$^{238}U/^{206}Pb$	error (%)	$^{207}Pb/^{206}Pb$	error (%)	$^{206}Pb/^{238}U$	error (%)	$^{207}Pb/^{206}Pb$	error (%)	$^{207}Pb/^{235}U$	error (%)	ρ	$^{206}Pb/^{238}U$	±1σ	$^{206}Pb/^{238}U$	±1σ	$^{206}Pb/^{238}U$	±1σ	$^{207}Pb/^{206}Pb$	±1σ	%Conc
Reepsville orthogneiss (R29/Rp165) *continued*																							
R29-5.1	0.12	1348	286	0.22	6.77	0.3	.0732	0.5	.1476	0.3	.0721	0.6	1.47	0.7	.453	883.7	2.9	887.4	2.8	887.3	2.7	990	13	90
R29-19.1R	0.00	1148	79	0.07	6.71	0.3	.0712	0.5	.1489	0.3	.0712	0.5	1.46	0.6	.545	892.5	3.0	894.5	2.9	895.0	2.9	964	11	93
R29-25.1	0.07	662	113	0.18	6.66	0.5	.0727	0.7	.1500	0.5	.0721	0.9	1.49	1.0	.458	898.1	4.0	903.1	3.9	901.2	3.9	990	18	91
R29-29.1	0.34	99	49	0.51	6.62	1.2	.0759	1.8	.1506	1.2	.0731	2.9	1.52	3.2	.381	900.2	10.5	906.1	11.0	904.3	10.2	1016	59	89
R29-3.1	0.00	1022	556	0.56	6.61	0.4	.0725	0.6	.1513	0.4	.0725	0.6	1.51	0.7	.552	905.1	3.4	905.0	3.6	908.4	3.2	1001	12	91
R29-16.1	0.00	1189	398	0.35	6.59	0.4	.0724	0.6	.1517	0.4	.0724	0.6	1.51	0.7	.540	907.1	3.2	909.2	3.2	910.3	3.0	998	11	91
R29-8.1	0.04	694	82	0.12	6.47	0.5	.0745	0.9	.1545	0.5	.0742	0.9	1.58	1.0	.452	921.3	4.2	925.9	4.0	925.9	4.0	1047	18	88
R29-22.3C	0.10	466	255	0.57	6.44	0.6	.0737	0.8	.1552	0.6	.0729	0.9	1.56	1.1	.524	927.3	5.0	924.3	5.3	930.3	4.8	1010	18	92
R29-28.1	0.05	576	152	0.27	6.28	0.6	.0761	0.7	.1592	0.6	.0757	0.8	1.66	1.0	.618	946.9	5.6	952.0	5.6	952.2	5.3	1087	15	88
R29-13.2C	0.03	535	157	0.30	6.21	0.5	.0737	0.8	.1610	0.5	.0735	0.8	1.63	1.0	.551	959.7	4.9	961.7	4.9	962.2	4.7	1027	16	94
R29-9.1	0.00	666	227	0.35	6.16	0.5	.0745	0.7	.1623	0.5	.0745	0.7	1.67	0.8	.568	966.0	4.4	968.5	4.5	969.4	4.2	1056	14	92
R29-17.1	0.02	1081	269	0.26	6.12	0.4	.0728	0.5	.1635	0.4	.0726	0.6	1.64	0.7	.536	975.0	3.5	975.7	3.5	976.1	3.3	1004	12	97
R29-4.1	-0.03	364	117	0.33	6.11	0.6	.0733	1.1	.1638	0.6	.0735	1.1	1.66	1.3	.489	975.8	6.1	977.0	6.1	977.8	5.8	1027	23	95
R29-19.2C	0.06	362	138	0.39	6.06	0.7	.0726	0.9	.1649	0.7	.0721	1.0	1.64	1.2	.614	983.8	7.1	984.2	7.3	984.0	6.8	989	20	100
R29-22.4I	0.08	266	199	0.77	5.99	0.7	.0721	1.0	.1669	0.7	.0715	1.2	1.65	1.4	.526	996.0	7.0	992.0	7.6	995.1	6.6	972	24	102
R29-11.1	0.08	675	250	0.38	5.90	0.6	.0737	0.7	.1694	0.6	.0730	0.7	1.70	0.9	.631	1008.9	5.5	1008.7	5.6	1009.0	5.2	1013	14	100
R29-21.1	-0.03	531	171	0.33	5.88	0.5	.0748	0.7	.1700	0.5	.0750	0.8	1.76	0.9	.545	1009.7	5.0	1011.4	5.0	1012.1	4.8	1070	16	95
R29-23.1	0.00	367	165	0.47	5.83	0.6	.0761	0.9	.1715	0.6	.0761	0.9	1.80	1.1	.572	1016.8	6.1	1021.2	6.3	1020.2	5.8	1098	18	93
R29-12.2C	0.02	787	331	0.43	5.75	0.4	.0738	0.6	.1740	0.4	.0736	0.6	1.76	0.7	.572	1034.3	4.3	1032.8	4.4	1034.1	4.1	1029	12	100
R29-6.2C	0.02	680	186	0.28	5.73	0.5	.0741	0.6	.1746	0.5	.0739	0.7	1.78	0.8	.558	1037.2	4.6	1036.6	4.6	1037.3	4.4	1039	14	100
R29-24.1	0.00	104	62	0.62	5.65	1.1	.0730	1.6	.1769	1.1	.0730	1.6	1.78	2.0	.571	1051.7	11.5	1046.4	12.1	1050.2	10.9	1015	33	103
R29-14.1C	-0.02	680	381	0.58	5.48	0.4	.0760	0.6	.1825	0.4	.0761	0.6	1.92	0.8	.567	1079.9	4.6	1078.9	4.9	1080.7	4.4	1099	13	98

Note: Corrections for common Pb made using measured ^{204}Pb. See text for analytical details.

C = core; R = rim; X = xenocrystic core.

%Conc = 100 x [($^{206}Pb/^{238}U$ age) / ($^{207}Pb/^{206}Pb$ age)].

ρ = error correlation of Ludwig (1998).

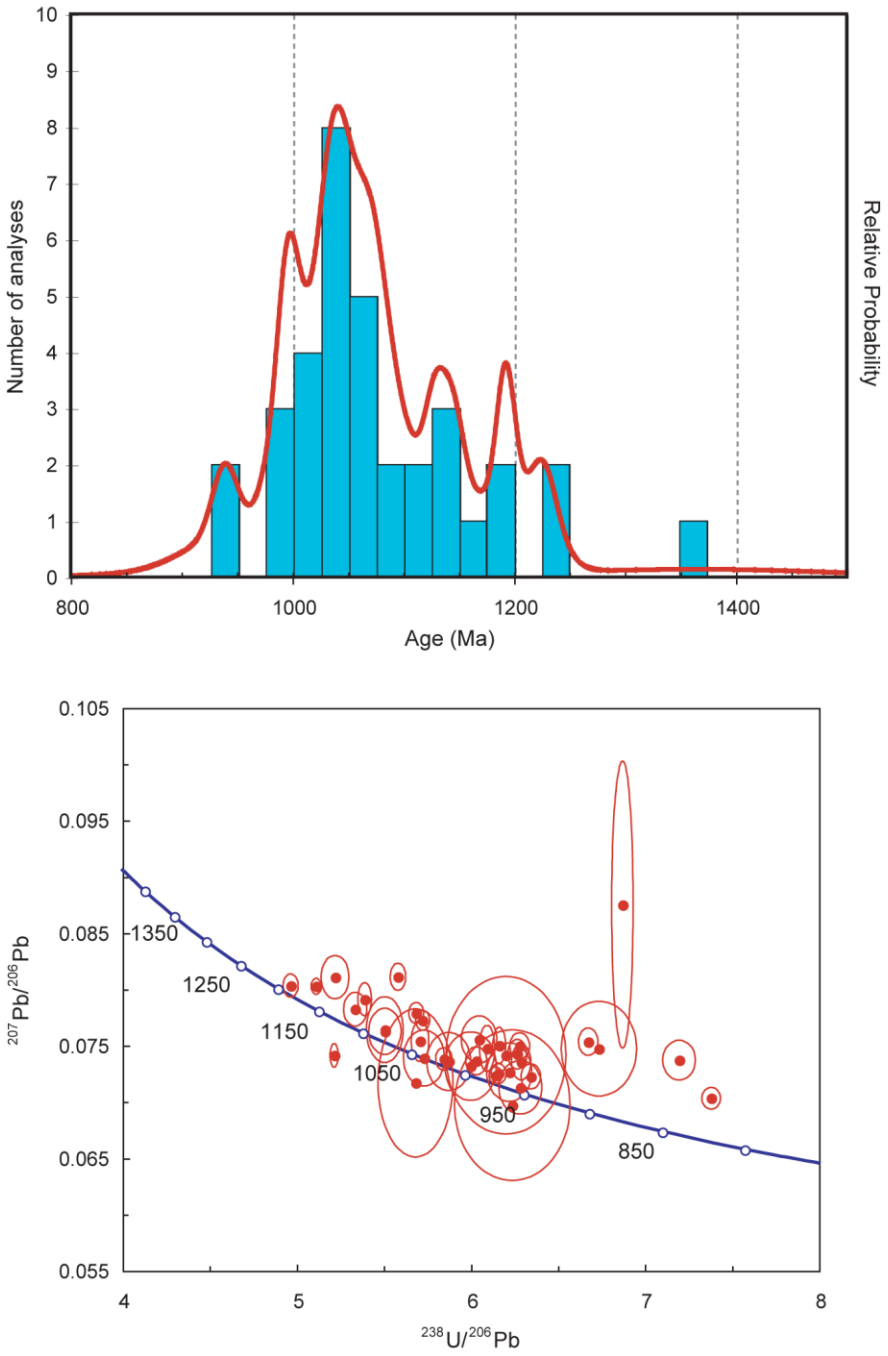

Figure 2-2. U-Pb SHRIMP-RG age results for lower Tallulah Falls Formation sample R24. a) Relative probability plot of all data. b) Tera-Wasserberg concordia diagram with all data plotted. Ages in Ma.

Typical mineral assemblages of the metagraywacke (biotite paragneiss) of the lower Tallulah Falls Formation consist of quartz, biotite, and plagioclase (An_{27-33}) ± garnet ± sillimanite ± muscovite with lesser amounts of opaques ± myrmekite, sphene, apatite, epidote, zircon, and retrograde sericite. Parallel alignment of micas ± sillimanite and quartzofeldspathic materials define foliation. Sheared plagioclase and quartz porphyroclasts are common within the lower Tallulah Falls Formation metagraywacke. Garnet porphyroblasts (1 to 10 mm) contain inclusions of biotite, quartz, muscovite, plagioclase, and fibrous sillimanite. Rare inclusion trails in garnets may indicate the presence of an earlier S_1 foliation (Fig. 2-3a). Evidence for retrograde metamorphism is observed in several samples. Some K-feldspar porphyroclasts have been fully replaced by myrmekite, although myrmekite typically occurs mostly along grain boundaries of quartz and plagioclase (Fig. 2-3b). Laths of muscovite ranging from subparallel to ~55° from foliation have overgrown myrmekitic porphyroclasts. Prismatic sillimanite grains are rimmed by fine-grained, retrograde muscovite (Fig. 2-3c).

Rock outcrops become decreasingly abundant, while the amount of saprolite outcrops increase, to the east of the Brindle Creek fault as the topography flattens closer to the South Fork of the Catawba River (Fig. 1-3). Saprolite color varies from light to moderate reddish-orange to dark brown, to light to medium gray depending on the rock type of interlayers present (Fig. 2-3d). Soils produced from the metagraywacke of the lower Tallulah Falls Formation are a moderate reddish-orange color.

Mappable interlayers of gondite occur in the lower Tallulah Falls Formation. The gondite unit is a fine- to medium-grained, equigranular, garnet quartzite composed of quartz and garnet with minor amounts of biotite, opaques, and alkali-feldspar (Fig. 2-4a). Goldsmith et al. (1988) traced out a single, folded layer of gondite extending north-south along the majority of the western side of the Newton antiform (Fig. 1-6). Three more layers were identified and traced out during my detailed mapping (Fig. 2-1). Layer thickness of the gondite ranges from 20 cm to 3.5 m (Fig. 2-4b). The gondite is readily recognizable and distinguished from surrounding metagraywacke and amphibolite by its blocky weathering and iridescent black-purple iron- and manganese-oxide staining (Fig. 2-4c). Soils produced are a very dark brownish red (Fig. 2-4c), much darker than the surrounding metagraywacke. Small folds, although rare, occur in the

Figure 2-3. Lower Tallulah Falls Formation metagraywacke. a) Photomicrograph of rare inclusion trails preserved in metagraywacke garnets in sample Rp42. Sample collected from outcrop in a tributary of Tanyard Creek, north of NC St. Rd. 1113 (Reepsville Road). b) Photomicrograph of sample Rp41 showing myrmekite replacement of a feldspar porphyroclast. Sample collected from outcrop downstream from station Rp42. c) Photomicrograph of prismatic sillimanite being replaced by fine grains of muscovite in a metapelitic interlayer from sample Rp42. d) Saprolite outcrop with metagraywacke and interlayers showing dependence of saprolite color on bedrock composition. Outcrop located in gully near the banks of the South Fork of the Catawba River, east of NC St. Rd. 1008 (Killian Road) (station Rp72). Mineral abbreviations: bt–biotite; gt–garnet; ms–muscovite; myr–myrmekite; op–opaque; pl–plagioclase; qtz–quartz; sil–sillimanite.

a)

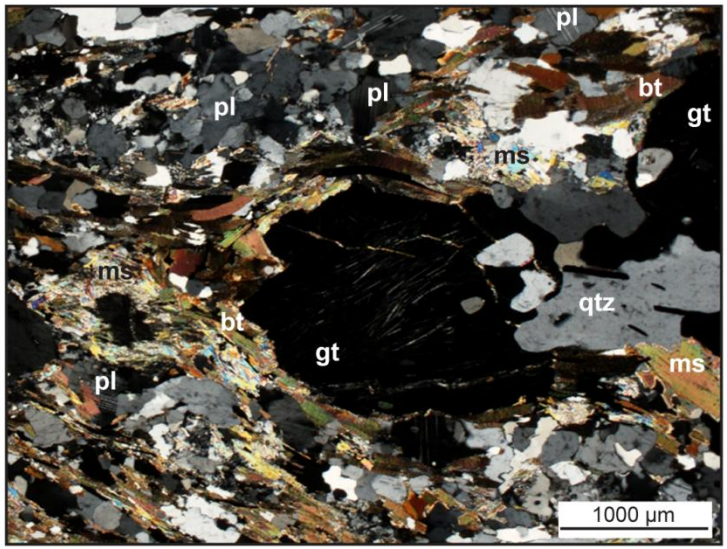
pl
pl
pl
bt
gt
ms
ms
qtz
bt
gt
pl
ms
1000 µm

b)

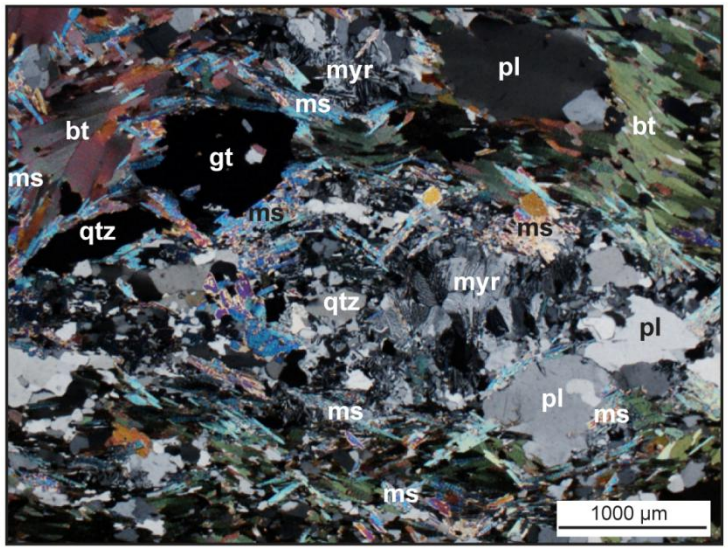
myr
pl
ms
bt
bt
gt
ms
ms
qtz
ms
myr
qtz
pl
pl
ms
ms
ms
1000 µm

c)

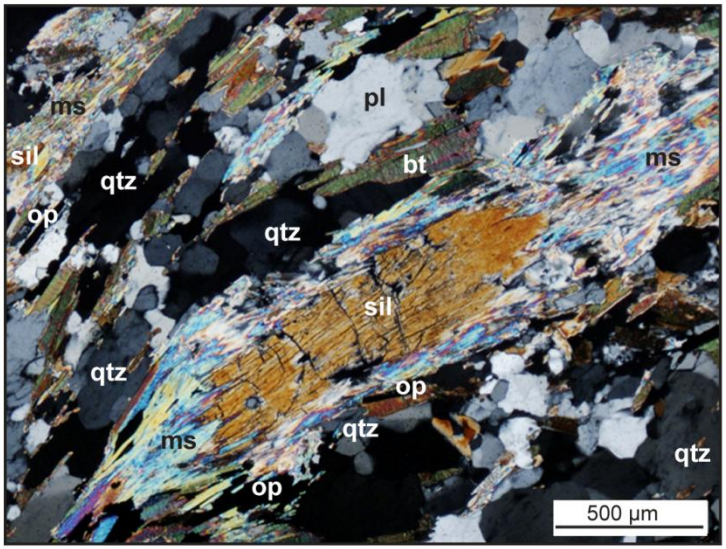
ms
pl
sil
bt
ms
qtz
op
qtz
sil
qtz
op
ms
qtz
qtz
op
500 µm

d)

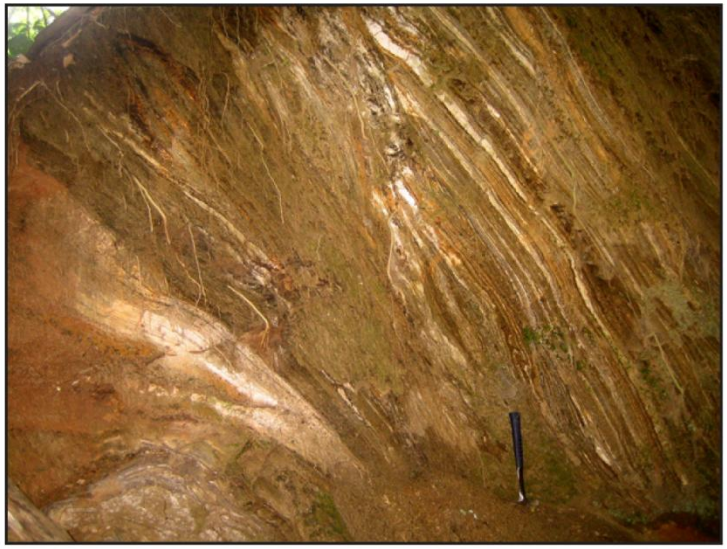

Figure 2-4. Gondite interlayer in the lower Tallulah Falls Formation. a) Photomicrograph of gondite showing typical texture and mineralogical assemblage in sample LW15. b) Outcrop showing typical thickness of the gondite, located in Howards Creek, west of NC St. Rd. 1200 (Alf Hoover Road) (station LW15). Rock hammer for scale. c) Outcrop of gondite showing blocky weathering habit and dark brownish-red color of the soils. Outcrop located on the south side of NC St. Rd. 1113 (Reepsville Road), east of the NC St. Rd. 1200 intersection (station Rp14). Rock hammer for scale. d) Fold in sample of gondite, collected on hillside north of station LW15. Dime for scale. Mineral abbreviations: bt–biotite; gt–garnet; kf–K-feldspar; ms–muscovite; qtz–quartz.

a)

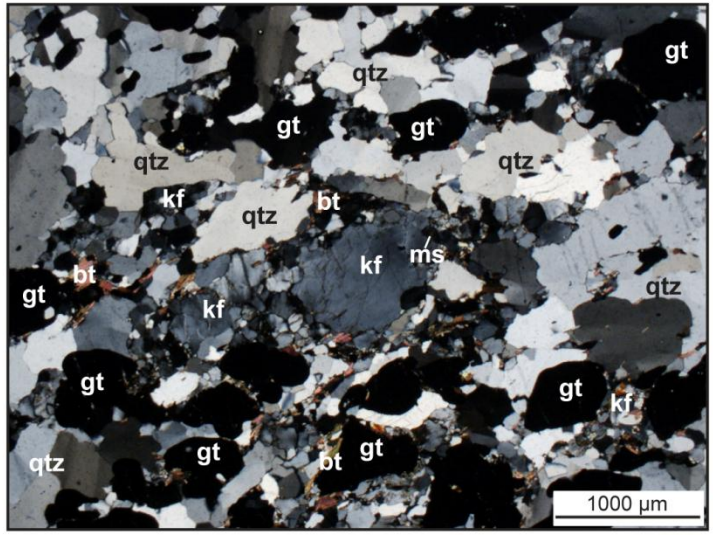
gt
qtz
gt
gt
qtz
qtz
kf
qtz
bt
kf
ms
bt
gt
qtz
kf
gt
gt
kf
qtz
gt
bt
gt
1000 µm

b)

c)

d)

gondite interlayer (Fig. 2-4d). The unit was likely deposited as an iron- and manganese-oxide rich silica layer of sediments or was influenced by Mn-rich fluids during a metamorphic event. The nature of the occurrence of the layers suggests the former hypothesis is more likely.

Bodies of biotite-hornblende gneiss and amphibolite occur as interlayers and discontinuous boudins in the lower Tallulah Falls Formation metagraywacke. Boudins range in size from 0.25 to 5 m in length (Figs. 2-5a, b). An earlier S_1 foliation is preserved in some boudins, while transposed to parallel the dominant S_2 foliation in others (Fig. 2-5a). Boudins and interlayers are locally migmatitic with coarse-grained hornblende (1 to 10 mm) and garnet (1 to 25 mm). The lack of amphibolite boudins in the Cat Square terrane metagraywacke separates the two units in the field.

Mineral assemblages of amphibolite bodies varies from dominantly equigranular, coarse-grained hornblende to inequigranular, fine- to medium-grained hornblende, plagioclase (An_{40-42}), epidote, and quartz ± garnet with lesser amounts of biotite, sphene, sericite, opaques, rutile, and apatite (Table 2-2). Foliation is defined by prismatic grains of pale to dark green pleochroic hornblende and biotite. Garnet, where present, contains inclusions of hornblende, biotite, quartz, and opaques. Inclusion trails are preserved in some garnets oblique to the S_2 foliation, likely reflecting an earlier S_1 foliation (Fig. 2-5c). Some samples contain symplectic overgrowths of epidote and plagioclase on hornblende grains in amphibolites from the Newton window, indicative of retrograde metamorphic processes (Fig. 2-5d). Amphibolite saprolite is black and white (moderately weathered) to pale orange (deeply weathered) in color while soils produced are moderate to dark, orange-brown.

Trace-element geochemistry of Newton window amphibolites, including one sample from the study area (noted as R21 in Merschat (2009) and Rp157 in Fig. 2-1) showed a range in tectonic environments between different discriminant diagrams. Nine samples from boudins, interlayers, and map-scale bodies of different localities in the Newton window plot mostly between MORB and island-arc tholeiite fields, with a few in the calc-alkaline fields (Merschat, 2009). Although there were some inconsistencies in the data, Merschat (2009) noted a MORB to island-arc setting is preferred for tectonic environment of the amphibolites.

Figure 2-5. Amphibolite boudins and interlayers in the lower Tallulah Falls Formation. a) Preserved S_1 foliation in a migmatitic boudin in Little Pott Creek, east of its intersection with NC St. Rd. (Cansler Road) (station Rp195). Brunton compass for scale. b) Large, migmatitic amphibolite boudin with transposed foliation in Tanyard Creek, west of NC St. Rd. 1438 (June Bug Road) (station Rp114). Rock hammer for scale. c) Photomicrograph of amphibolite composed entirely of hornblende in sample Rp76. Sample collected from tributary of Pott Creek, west of NC St. Rd. 1216 (Wyant Road). d) Photomicrograph showing unzoned and inclusion free garnet surrounded by symplectic intergrowths of epidote and plagioclase, hornblende, plagioclase, and quartz in sample Rp78. Sample collected from tributary of Pott Creek, west of NC St. Rd. 1216 (Wyant Road). Mineral abbreviations: bt–biotite; hbl–hornblende; pl–plagioclase; qtz–quartz; ser–sericite; sym–symplectite.

a)

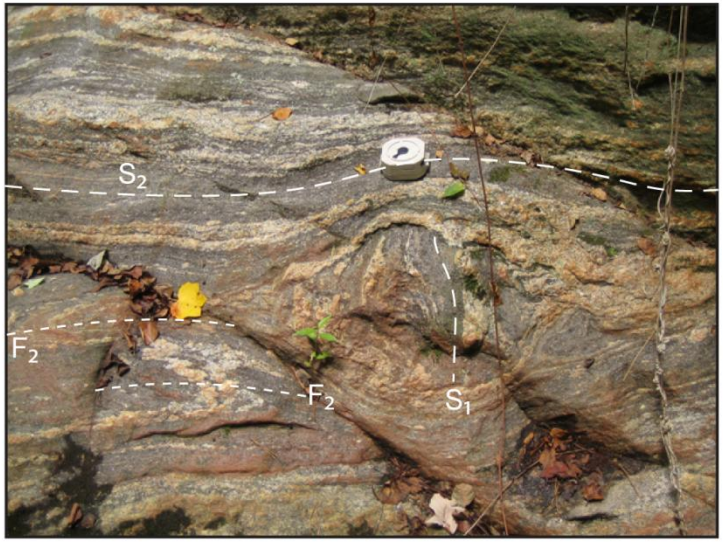
S_2
F_2
F_2
S_1

b)

c)

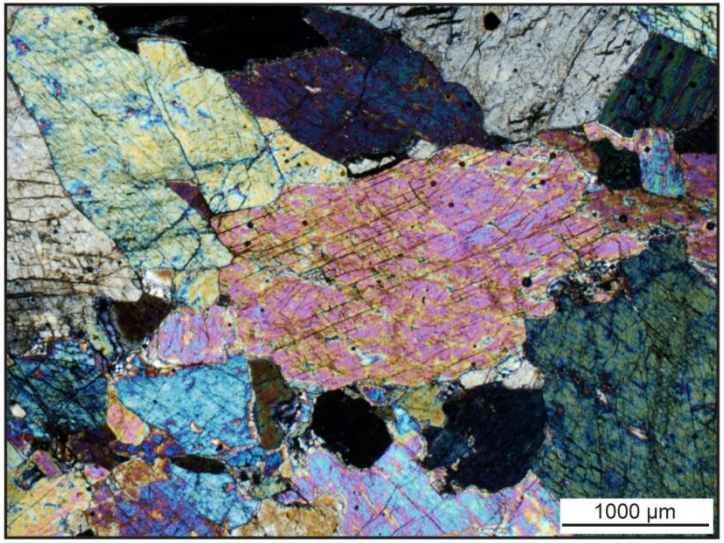
1000 µm

d)

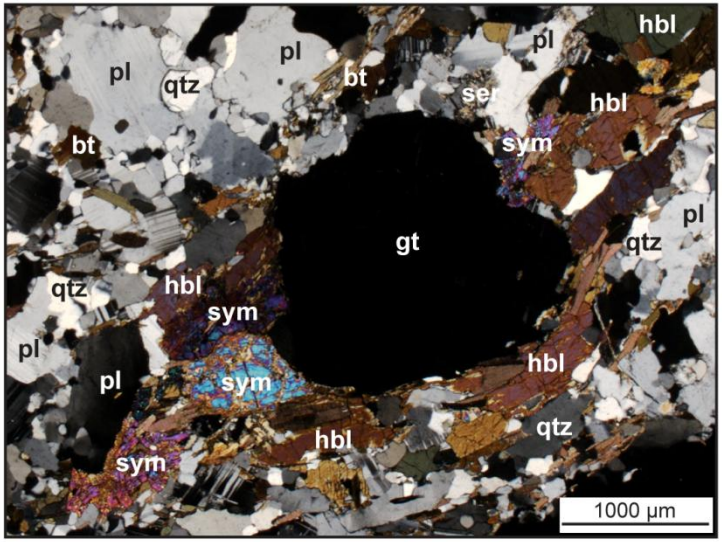
hbl
pl
pl
pl
qtz
bt
ser
hbl
bt
sym
pl
gt
qtz
qtz
hbl
sym
pl
hbl
pl
sym
qtz
hbl
sym
1000 µm

Table 2-2. Modal analyses of Tugaloo terrane amphibolites.

Sample	Rp78	Rp157
Rock Type	*amph*	*amph*
points counted	1089	1011
Plagioclase	54.7(An_{42})	20.6(An_{40})
Hornblende	13.0	56.1
Biotite	10.7	-
Quartz	15.1	0.8
Opaques	0.0	0.1
Epidote-clinozoisite	1.1	0.4
Symplectite	1.9	17.5
Apatite	0.3	tr
Zircon	tr	tr
Sericite	3.1	4.5
Total	100.0	100.0

(-) Indicates the mineral was not observed in thin section.

Trace (tr) minerals make up less than 0.1% of the thin section.

Plagioclase compositions were estimated using the Michel-Levy method (Nesse, 1991).

Pott Creek Mylonite

The Pott Creek mylonite, named in this study for exposures in and along Pott Creek and its tributaries in the Reepsville 7.5-minute quadrangle, is a porphyroclastic biotite gneiss. A less extensive body of this unit in the northeastern portion of this study area was mapped by Goldsmith et al. (1988) as inequigranular biotite gneiss (Fig. 1-6). Detailed mapping of this unit further into the Reepsville and Lincolnton West 7.5-minute quadrangles has revealed an anastomosing outcrop pattern (Fig. 2-1). The rock type is more resistant to weathering than the lower Tallulah Falls Formation, outcropping more on hillsides, making the unit easy to trace. Most outcrops have a rough texture from micas eroding out, leaving behind more resistant quartz grains. The Pott Creek mylonite saprolite is dominantly black with white feldspar clasts (partly weathered), reflecting similarities in color and texture of the bedrock. Soils produced are a moderate brownish red, only slightly redder than the lower Tallulah Falls Formation. Despite the abundance of outcrops of the Pott Creek mylonite, samples were not fresh enough for whole-rock chemical analysis.

Textural variations reflect the degree of mylonitization that ranges from protomylonite to mylonite. Feldspar porphyroclasts range in size from 1 to 60 mm, and are a white to off white and pale orange color from iron staining (Fig. 2-6a). Larger porphyroclasts are sometimes observed with 1 to 5 mm grains of muscovite in the center of the feldspars in hand sample and thin section. Fine- to medium-grained muscovite defines foliation with biotite in some samples (Fig. 2-6b). Sheared quartz and feldspar grains form a prominent lineation observed in most outcrops and trends ~350° with a shallow plunge ranging 5-24° (Fig. 2-6c).

Petrographic analysis of the mylonite yields an assemblage of biotite, plagioclase (An_{30}), quartz, garnet, alkali feldspar, and muscovite with lesser amounts of opaques, myrmekite, sphene, epidote, zircon, and retrograde sericite. Most garnets have inclusions of quartz ± biotite ± small fibrous sillimanite ± zircon. Evidence of recrystallization, such as recovery in grains and 120° grain boundaries, is observed in thin section (Fig. 2-6d).

One sample of the Pott Creek mylonite was collected for zircon geochronology (Rp29; Fig. 2-1). U-Pb ages did not produce a coherent concordia grouping to permit a distinct

Figure 2-6. Pott Creek mylonite in the Newton window. a) Outcrop of Pott Creek mylonite with variations in sizes of feldspar porphyroclasts. Outcrop located at the end of NC St. Rd. 1218 (Wilfong Road) (station Rp26). b) Photomicrograph of muscovite forming foliation with biotite and lath replacing K-feldspar porphyroclasts (bottom left-center) in sample Rp358. Sample collected from outcrop in the South Fork Catawba River, east of NC St. Rd. 1271 (Ritchie Road). c) View of foliation surface of the Pott Creek mylonite at station Rp26 with prominent lineation formed by sheared quartz and feldspar grains. Hammer for scale. Photograph by RDH. d) Photomicrograph of a partially recrystallized feldspar porphyroclast with muscovite replacing plagioclase grains in sample LW51. Sample collected from the side of a tributary to Howard's Creek, between NC St. Rd. 1200 (Alf Hoover Road) and the end of NC St. Rd. 1190 (Leonard Road). Mineral abbreviations: bt–biotite; gt–garnet; ks–K-feldspar; ms–muscovite; myr–myrmekite; op–opaque; pl–plagioclase; qtz–quartz.

a)

b)

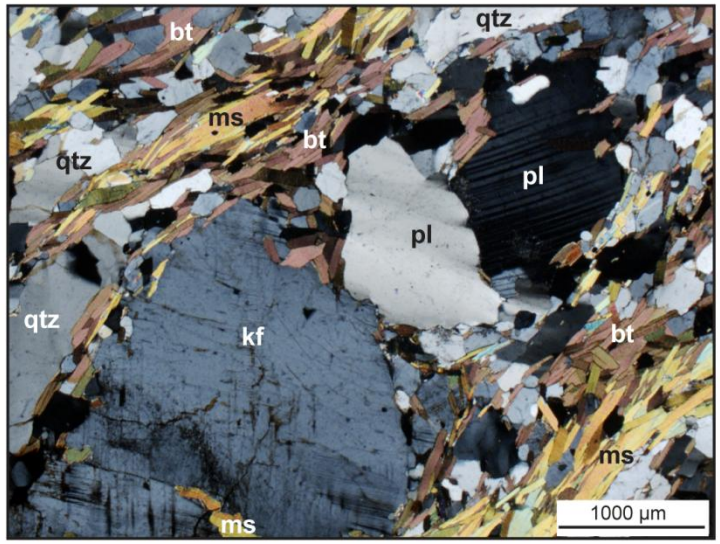
bt
qtz
ms
bt
qtz
pl
pl
qtz
kf
bt
ms
ms
1000 µm

c)


L2

d)

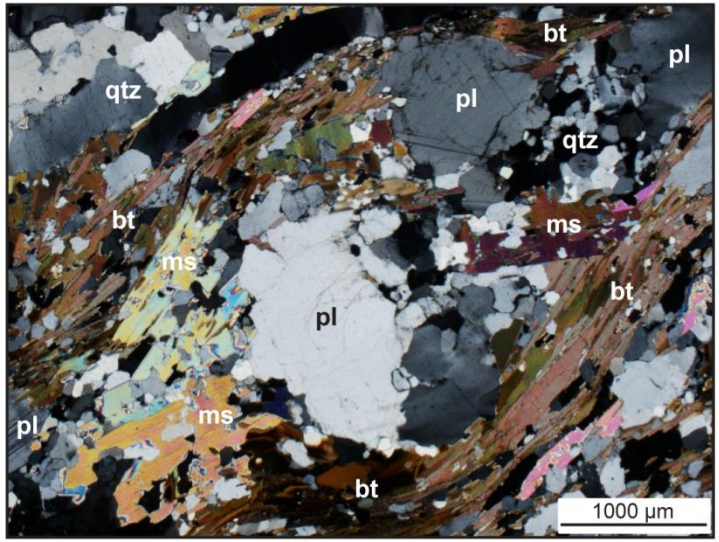
bt
pl
qtz
pl
qtz
bt
ms
ms
bt
pl
pl
ms
bt
1000 µm

formation age of this unit (Table 2-1). Instead, there are multiple peaks at 312, 334, 392, 445 Ma and 1.07, 1.1, 1.2, 1.3, and 1.95 Ga (Figs. 2-7a, b). Zircon shapes range from almost euhedral to anhedral and size ratios range from 1:1.5 to 1:3. Morphologies show xenocrystic cores outlined by oscillatory zoning, metamorphic rims, and dissolution of cores of some grains (Fig. 2-8a). Proterozoic ages from xenocrystic cores were flagged as discordant and having high Th/U ratios. Most cores have oscillatory or unzoned overgrowths. Analysis of zoned overgrowths yielded ~393 and ~445 Ma peaks. Ages of ~312 and ~334 Ma are from unzoned metamorphic rims, although a few analyses seem to be from zoned overgrowths. This apparent zoning may be a relict "ghost texture" from solid-state recrystallization during metamorphism (Corfu et al., 2003a).

Despite the presence of multiple zircon ages in this sample, an approximate age can be delimited based on zircon morphology and age distributions. A Proterozoic age of formation is not likely since most ages are from xenocrystic cores and do not yield a single, concordant Proterozoic age. A Late Ordovician age is possible, because these ages mostly came from oscillatory zoned overgrowths indicative of igneous crystallization. Assuming an Ordovician time of formation, a concordant age of 446 ± 3.1 Ma is produced from the zircon data (Fig. 2-7c). Devonian and Carboniferous ages are mostly from metamorphic rims and potentially relict zoned overgrowths. This would support a high-temperature metamorphic event corresponding with the Neoacadian and early Alleghanian orogenies (Fig. 2-7d).

The following hypothesis for the formation of the Pott Creek mylonite accounts for outcrop pattern, rock textures, composition, and zircon ages. The presence of large porphyroclasts of feldspar and ~446 Ma igneous overgrowths on zircons support interpretation of the Pott Creek mylonite having been a megacrystic, Ordovician granite, similar to that of the Henderson Gneiss, which was subsequently deformed during the Neoacadian and Alleghanian orogenies. The presence of inherited cores would separate it from other western Inner Piedmont plutons that do not have inheritance. Therefore, if the protolith of this mylonite is granite, it may have been a tabular intrusion as dikes or sills, rather than stocks or batholiths, in order to account for the amount of zircon inheritance. The outcrop pattern may be a result of the present-day erosional surface exposing the folded mylonite, or else the mylonite truly has an anastomosing

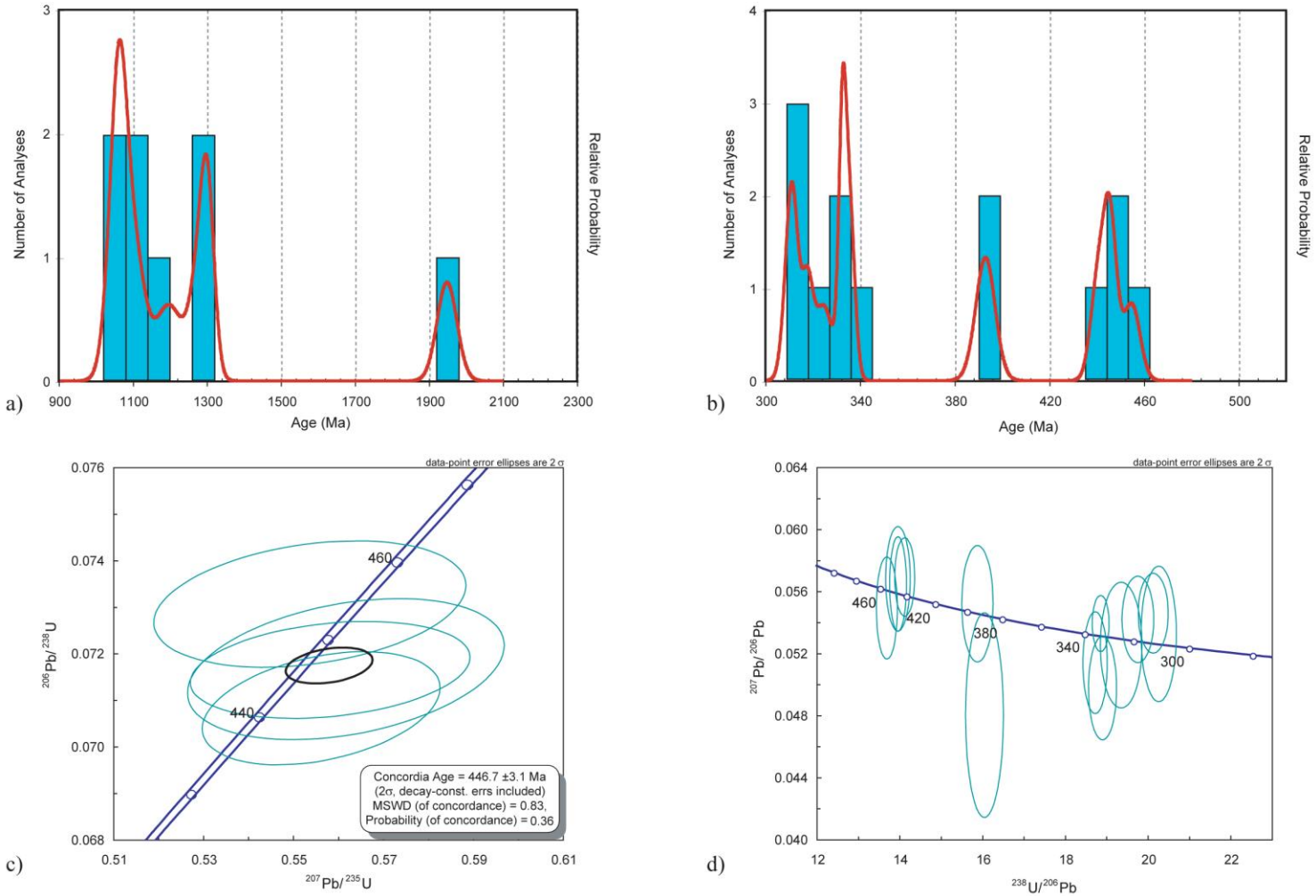

Figure 2-7. U-Pb SHRIMP-RG age results from the Pott Creek mylonite zircons. a) Relative probability plot showing multiple Proterozoic age peaks. b) Relative probability plot showing multiple Paleozoic age peaks. c) Concordia diagram of Ordovician ages thought to represent timing of formation of the Pott Creek mylonite protolith. Black circle is the calculated concordant age. d) Tera-Wasserberg plot of all Paleozoic ages.

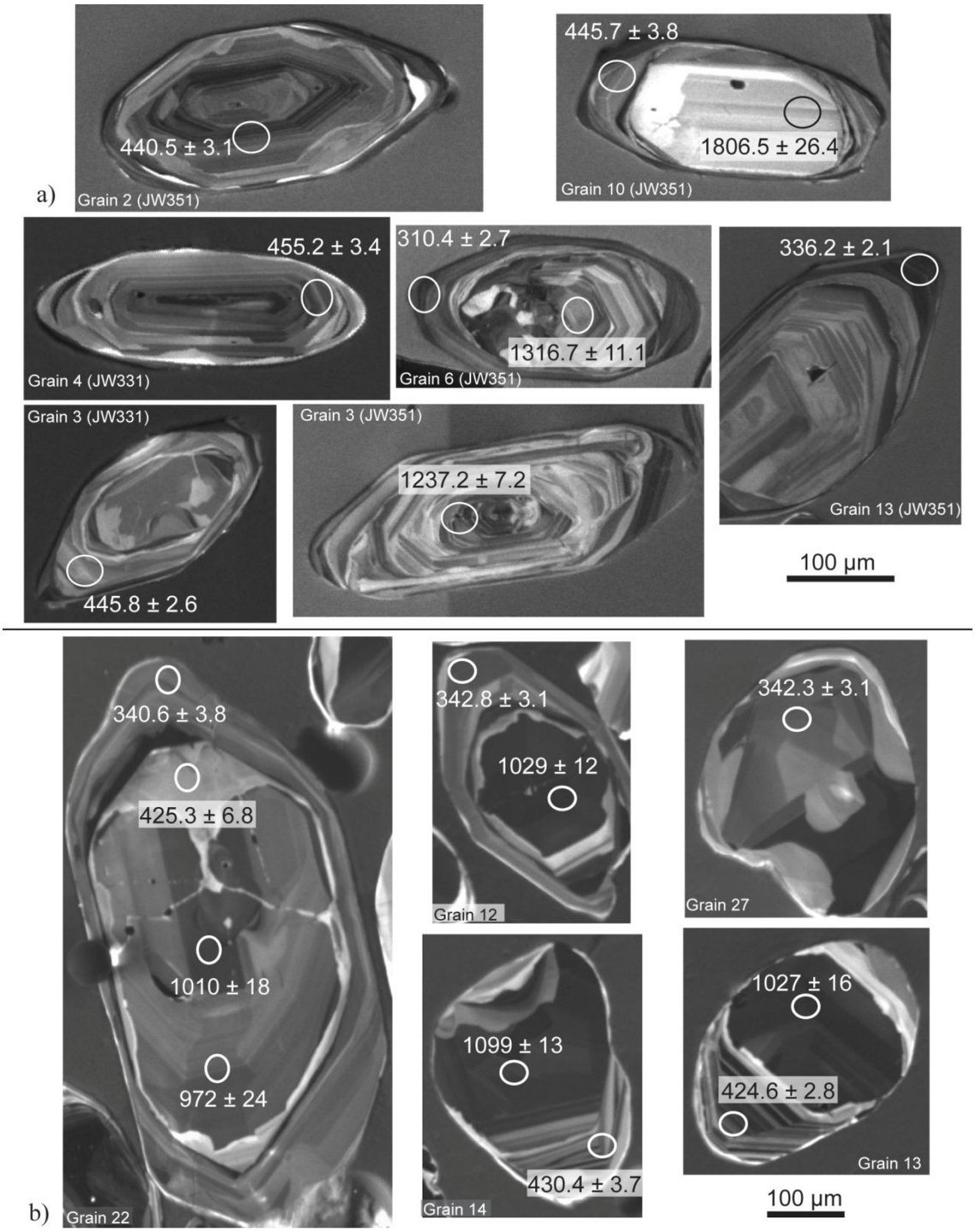

Figure 2-8. Cathodoluminescence images and ages representative of a) Pott Creek mylonite zircons and b) Reepsville orthogneiss zircons. Mount number, in parentheses, is indicated on Pott Creek mylonite zircons because zircons were analyzed two separate times, whereas Reepsville orthogneiss zircons are all on one mount. Size and location of spot analyses are indicated on each zircon. Ages in million years.

pattern from emplacement or post-emplacement deformation. All rocks observed in the Newton window are mylonitic from extensive shearing in the footwall of the Brindle Creek thrust sheet. This makes it difficult to argue the anastomosing pattern of the Pott Creek mylonite resulted from development of a fault and shear zone in Tugaloo terrane rocks.

Reepsville Orthogneiss

The Reepsville orthogneiss was one of the three samples initially dated to determine that the Newton antiform is a window through the Brindle Creek thrust sheet. This sample, identified by Merschat (2009) as R29 and as indicated in Figure 1-6, will herein be referred to as Rp165, the station number assigned during detailed geologic mapping (Fig. 2-1). Merschat et al. (2005a) and Merschat (2009) reported a U-Pb zircon age of crystallization at 1050 ± 18 Ma, with metamorphic rims of ~440 Ma and ~340 Ma leading to the interpretation of the orthogneiss as a possible fragment of Grenville crust. Based on this interpretation, and the limited exposure and occurrence of the Reepsville orthogneiss, it could be one of the easternmost occurrences of Grenville crust onto which Tugaloo terrane rocks were deposited. Metamorphic zircon rim ages would indicate these fragments were involved in both the Taconic and Neoacadian orogenies.

Further inspection of the Reepsville orthogneiss geochronologic data and comparison with data of the Pott Creek mylonite led to a second interpretation for the age of the orthogneiss. Multiple age peaks occur at 342, 352, 387, 425, and 463 Ma and 1.03 Ga (Table 2-1; Figs. 2-9a, b). Zircons from the Reepsville orthogneiss have euhedral to subhedral shapes and share similar morphologic characteristics as those in the Pott Creek mylonite: oscillatory zoning in xenocrystic cores, as well as overgrowths, metamorphic rims, resorbed grains, and relict textures (Fig. 2-8b). All Proterozoic ages are from xenocrystic cores of the zircons. The abundance of 1.0-1.1 Ga ages may be a result of a sampling bias or temperatures and zircon saturation in the melt during formation. Ordovician and Silurian ages were measured from oscillatory zoned overgrowths and a metamorphic embayment. Devonian and Carboniferous ages were measured in metamorphic rims and soccer ball zircons that formed during high-temperature metamorphism. Assuming zoned overgrowths producing Silurian ages are magmatic in origin, a concordant age of 426 ± 6.1 Ma is produced (Fig. 2-9c). The Reepsville orthogneiss may represent a pulse of magmatism

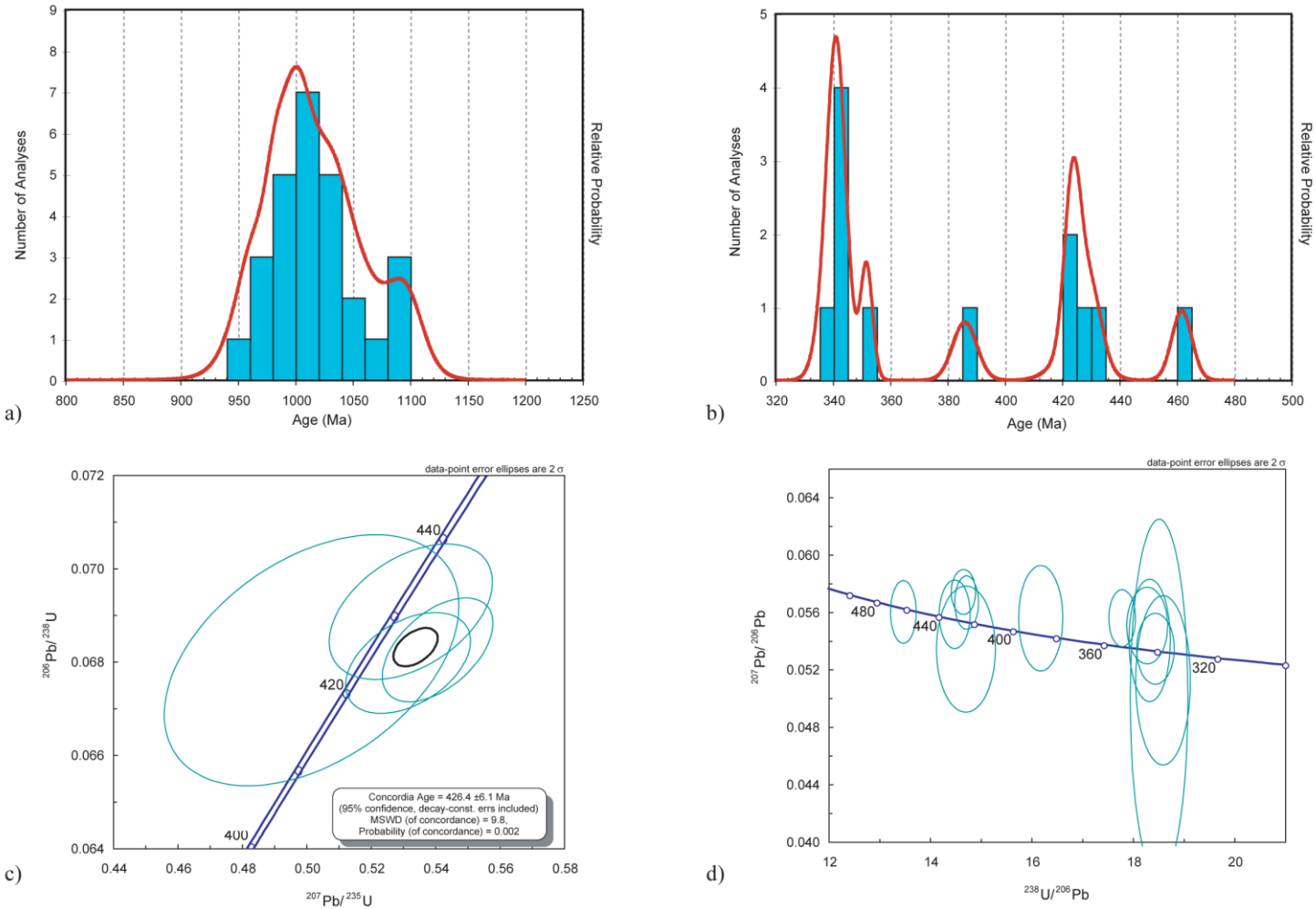

Figure 2-9. U-Pb SHRIMP-RG age results from the Reepsville orthogneiss zircons. a) Relative probability plot showing Proterozoic age peak from inherited cores at ~1025 Ma. b) Relative probability plot showing multiple Paleozoic age peaks. c) Concordia diagram of Silurian ages thought to represent timing of formation of the Reepsville orthogneiss. Black circle is the calculated concordant age. d) Tera-Wasserberg plot of all Paleozoic ages.

at the latest stages of the Taconic orogeny or during the beginning of the Acadian orogeny. Based on the proposed palinspastic location of the Tugaloo terrane of the western Inner Piedmont by Merschat and Hatcher (2007), rocks of the Newton window would have been near the Pennsylvania embayment, an appropriate location for participation in the Acadian orogeny. Other Paleozoic zircon ages in the sample support the participation of the orthogneiss in the Neoacadian and Alleghanian orogenies (Fig. 2-9d).

The Reepsville orthogneiss is an inequigranular, porphyroclastic biotite gneiss. Modal analyses of two orthogneiss samples from the two different map bodies reveal a granitic protolith using the IUGS classification scheme (Table 2-3, Fig. 2-10). Major constituents include quartz, plagioclase (An_{26-33}), alkali feldspar, and biotite (Fig. 2-11a). Minor amounts of garnet, opaques, myrmekite, muscovite and retrograde sericite are present with accessory minerals of epidote, zircon, and apatite. The thin sections analyzed have lesser amounts of biotite than observed in outcrop, based on the gneissic banding present in the rock.

Subtle differences between the Reepsville orthogneiss and Pott Creek mylonite help distinguish the two from each other and from the lower Tallulah Falls Formation. Overall, the Reepsville orthogneiss is more migmatitic (Fig. 2-11b) than the Pott Creek mylonite. Muscovite is rarely observed replacing feldspar porphyroclasts in the orthogneiss or lower Tallulah Falls Formation, but may be observed in the foliation with biotite in the orthogneiss. The presence of garnet porphyroblasts is minor to nonexistent in the Reepsville orthogneiss. Where present, they are <1.5 mm in size, compared to the Pott Creek mylonite where garnets are larger and more abundant. Both Reepsville orthogneiss and Pott Creek mylonite contain zircon and epidote, but apatite is observed only in the Reepsville orthogneiss, and sphene only in the Pott Creek mylonite. The lower Tallulah Falls formation typically consists of finer grained quartz-feldspar-biotite assemblages than the Reepsville orthogneiss and Pott Creek mylonite and has zircon, epidote, apatite, and sphene. Degree of mylonitization in all three rock types is variable and therefore not a good indicator for distinguishing one rock type from another.

Table 2-3. Modal analyses of the Reepsville orthogneiss.

Sample	Rp165*	LW9
points counted	1067	1014
Quartz	19.9	32.8
Plagioclase	23.9(An_{32})	22.9(An_{34})
K-feldspar	34.8	19.3
Biotite	12.5	8.3
Garnet	tr	1.0
Muscovite	0.9	tr
Opaques	0.2	0.5
Myrmekite	0.4	0.1
Epidote	0.1	tr
Sphene	tr	tr
Apatite	0.1	tr
Zircon	tr	tr
Hornblende	1.4	0.7
Sericite	5.9	14.4
Total	100.0	100.0

*Indicate sample collected for whole-rock geochemical analysis.
Trace (tr) minerals make up less than 0.1% of the thin section.
Plagioclase compositions were estimated using the Michel-Levy method (Nesse, 1991).

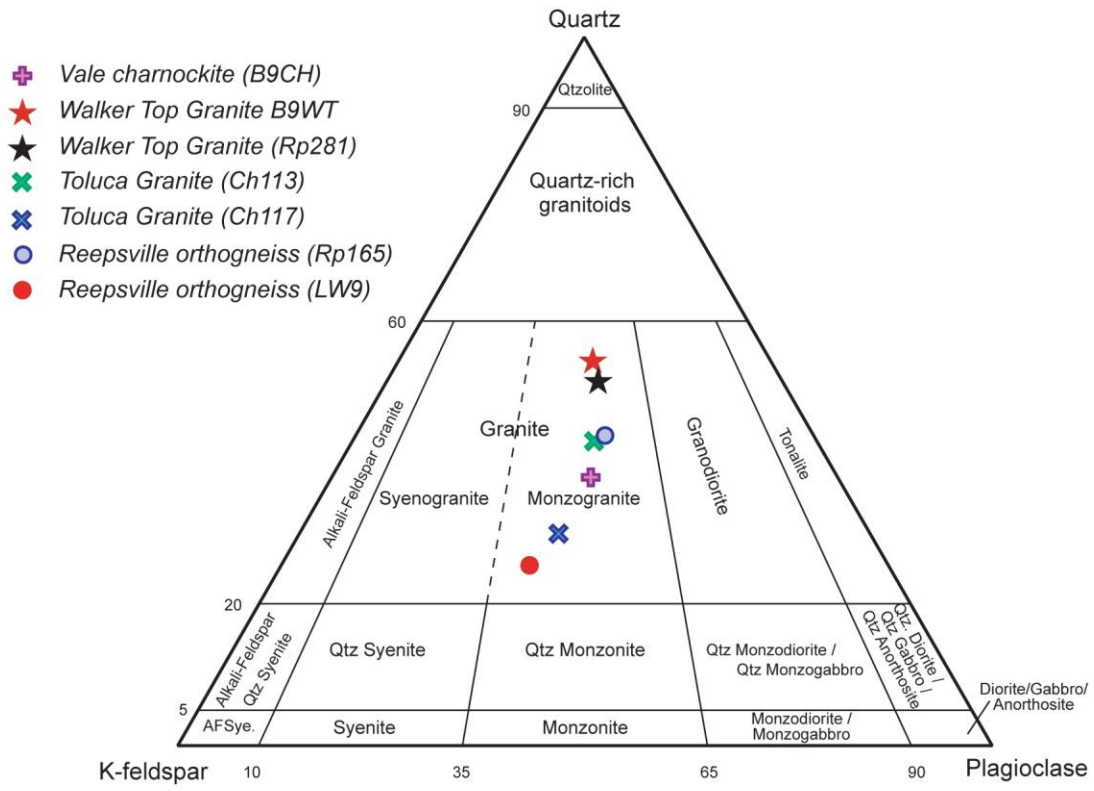

Figure 2-10. IUGS classification of the Tugaloo terrane Reepsville orthogneiss and Cat Square terrane granitoids in this study.

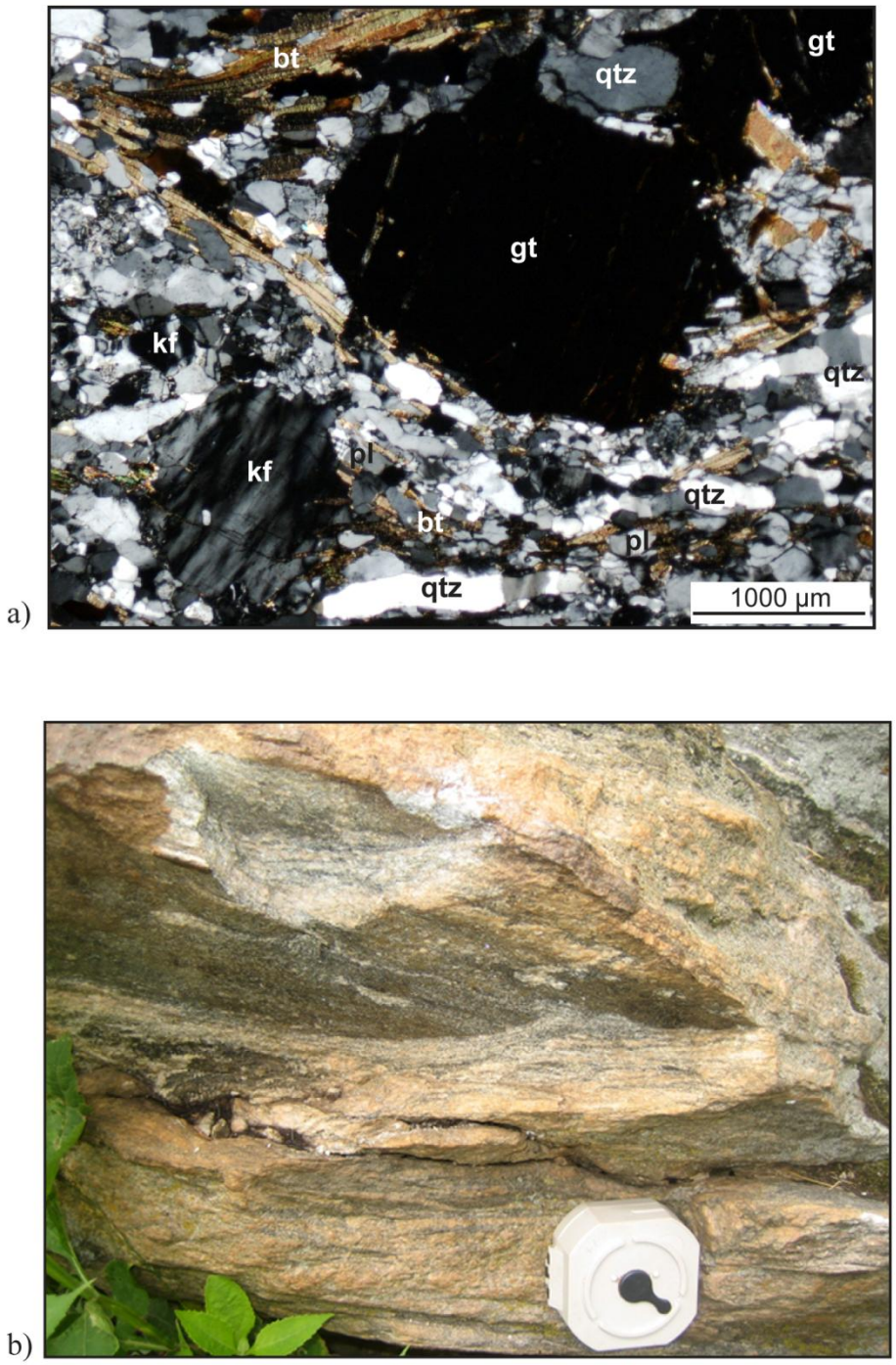

Figure 2-11. Reepsville orthogneiss in the Newton window. a) Photomicrograph of sample LW9 showing major constituents of rock unit. Sample collected from outcrop on northern bank of Howard's Creek, east of NC St. Rd. 1200 (Alf Hoover Road). Mineral abbreviations: bt–biotite; gt–garnet; kf–K-feldspar; pl–plagioclase; qtz–quartz. b) Outcrop of station Rp165 (R29 of Merschat et al. (2005a) and Merschat (2009)) from which samples were collected for geochronologic, geochemical, and petrographic analyses. Outcrop located in Tanyard Creek floodplain, north of NC St. Rd. 1113 (Reepsville Road). Brunton compass for scale.

Eastern Inner Piedmont - Cat Square terrane

The Cat Square terrane rocks, named after Cat Square, North Carolina, in the central portion of the study area, are the youngest sedimentary rocks in the crystalline core of the southern Appalachians with a maximum deposition age of ~430 Ma from detrital zircons (Bream, 2003). Prior to recognition of the Brindle Creek fault as a terrane boundary, rocks in the thrust sheet were identified as a repeated section of Tallulah Falls Formation of the Tugaloo terrane. A preliminary geochronologic study of the Inner Piedmont revealed the presence of a unique detrital zircon age suite for the Cat Square terrane (Bream, 2003). Ages would require sediment sourcing from both Laurentian and peri-Gondwanan sources.

Rocks of the Cat Square terrane were proposed by Merschat and Hatcher (2007) to represent the deformed equivalent of a remnant ocean basin. Palinspastic restoration of the terrane places the Cat Square basin near the Pennsylvania embayment, extending down to the Tennessee embayment (Merschat and Hatcher, 2007). Sediments shed from both Laurentia and the peri-Gondwanan terrane (Avalon) were deposited in the basin, resulting in detrital suites representing age populations having Laurentian and peri-Gondwanan affinities. The Cat Square basin was then zippered shut with the oblique, rotational collision between Laurentia and the approaching Carolina superterrane (Avalon). Subsequent deformation in the Neoacadian and Alleghanian orogenies transported the Inner Piedmont to its current location. The proposed stratigraphic section for this package of rocks consists of flysh facies sequence of interlayered pelitic and psammitic rocks overlying oceanic crust (Fig. 2-12). Mafic and ultramafic bodies are suggested to represent deformed and dismembered ophiolite components (Merschat and Hatcher, 2007).

Devonian to Mississippian plutons (325–407 Ma), such as the Walker Top Granite, Toluca Granite, Cherryville Granite, and Reedy River, Gray Court, and Sandy Mush plutons intruded the metasedimentary sequence of the Cat Square terrane (Fig. 2-13). Isotopic values for Cat Square terrane plutons have an evolved range of initial ε_{Nd} and $^{87}Sr/^{86}Sr$ values (-6.4 to -1.6 and 0.7054-0.77142; Mapes, 2002). These values closely resemble limited data for Cat Square terrane metasedimentary rocks (Mapes, 2002). Toluca and Cherryville granitoids of the

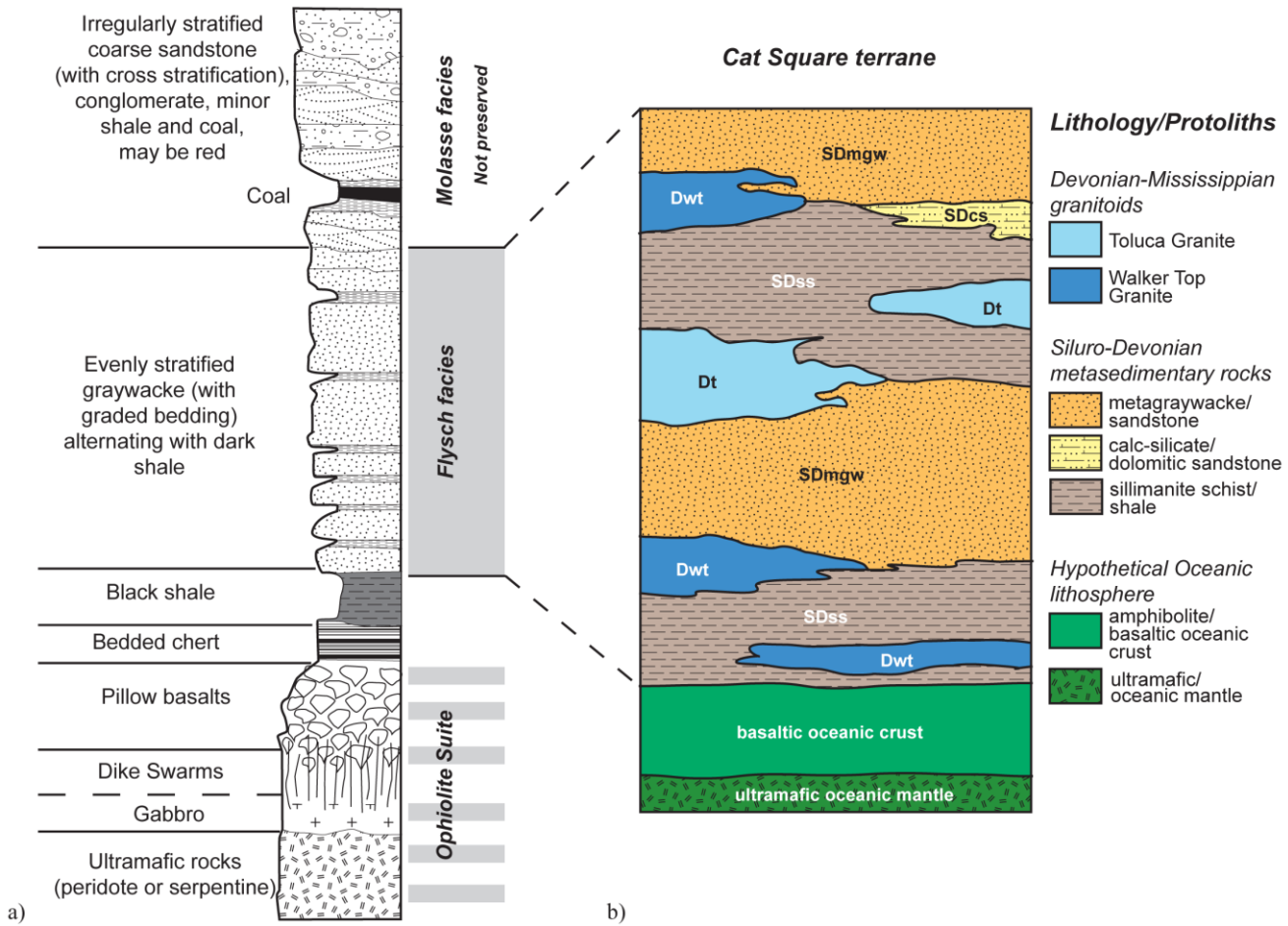

Figure 2-12. Proposed stratigraphic section for the Cat Square terrane. a.) Idealized stratigraphic column of a remnant ocean basin Gray shading indicates parts of the idealized stratigraphic section likely preserved in the Cat Square terrane. b.) Schematic stratigraphic column highlighting the similarities of the petrotectonic assemblage in the Cat Square terrane and the idealized stratigraphic column of a remnant ocean basin in part a (from Merschat and Hatcher, 2007). Dt–Toluca Granite; Dwt–Walker Top Granite; SDcs–calc-silicate; SDmgw–metapsammite; SDss–sillimanite schist. Figure from Merschat and Hatcher (2007).

Figure 2-13. Tectonic map of the southern Appalachians showing the distribution of Paleozoic plutons (modified from Hatcher et al., 2007). White box outlines study area. Arrows point to general location of sample collected for geochronology. See references herein for specific locations. Ordovician plutons dominate the Tugaloo terrane, with a suite of Devonian plutons in the western part of the terrane. Cat Square terrane plutons are dominantly Devonian-early Mississippian and younger. Sources of information: 1–Bream (2003); 2–Mapes (2002); 3–Miller et al. (2000) and Mapes et al. (2002); 4–Ranson et al. (1999); 5–A. K. Sinha (personal commun.); 6–Thomas (2001); 7–Stahr et al. (2005); 8–Vinson (1999); 9–Gatewood (2007); 10–Varnell et al. (2008); 11–this study. CPS–Central Piedmont suture; GMW–Grandfather Mountain window; GBMW–Great Balsam Mountains window; NW–Newton window; SMW–Sauratown Mountain window; SRA–Smith River allochthon; TR–Trimont Ridge massif; TFD–Tallulah Falls dome; TD–Toxaway dome; AA–Alto allochthon. Faults: AF–Allatoona; AnF–Anderson; BCF–Brindle Creek; BF–Burnsville fault; BFZ–Brevard; CF–Chattahoochee; GLF–Gossan Lead fault; HF–Hayesville; HLF–Hollins Line fault; HMF–Holland Mountain fault; PMF–Paris Mountain; RF–Ridgeway; SNF–Six Mile. Named Ordovician (purple) and Ordovician(?) (lighter purple) granitoids: an–Antreville; Och–Caesars Crossroads; Oh–Henderson; Opc–Persimmon Creek; Ot–Toccoa; Ow–Whiteside; st–Starr. Devonian and Devonian(?) plutons (light blue): Dlg–Looking Glass; Dpb–Pink Beds; Drf–Rocky Face; Dt–Toluca; Dwt–Walker Top; sm–Sandy Mush. Mississippian granitoids: Mc–Cherryville; Mgc–Gray Court; Mr–Rabun; Mrr–Reedy River; Mwc–Walnut Creek. Pennsylvanian granitoids: Pe–Elberton; Ppm–Pacolet Mills (Carolina superterrane). Towns: Av–Asheville; Gr–Greenville; Hk–Hickory; Sh–Shelby; W–Waynesville.

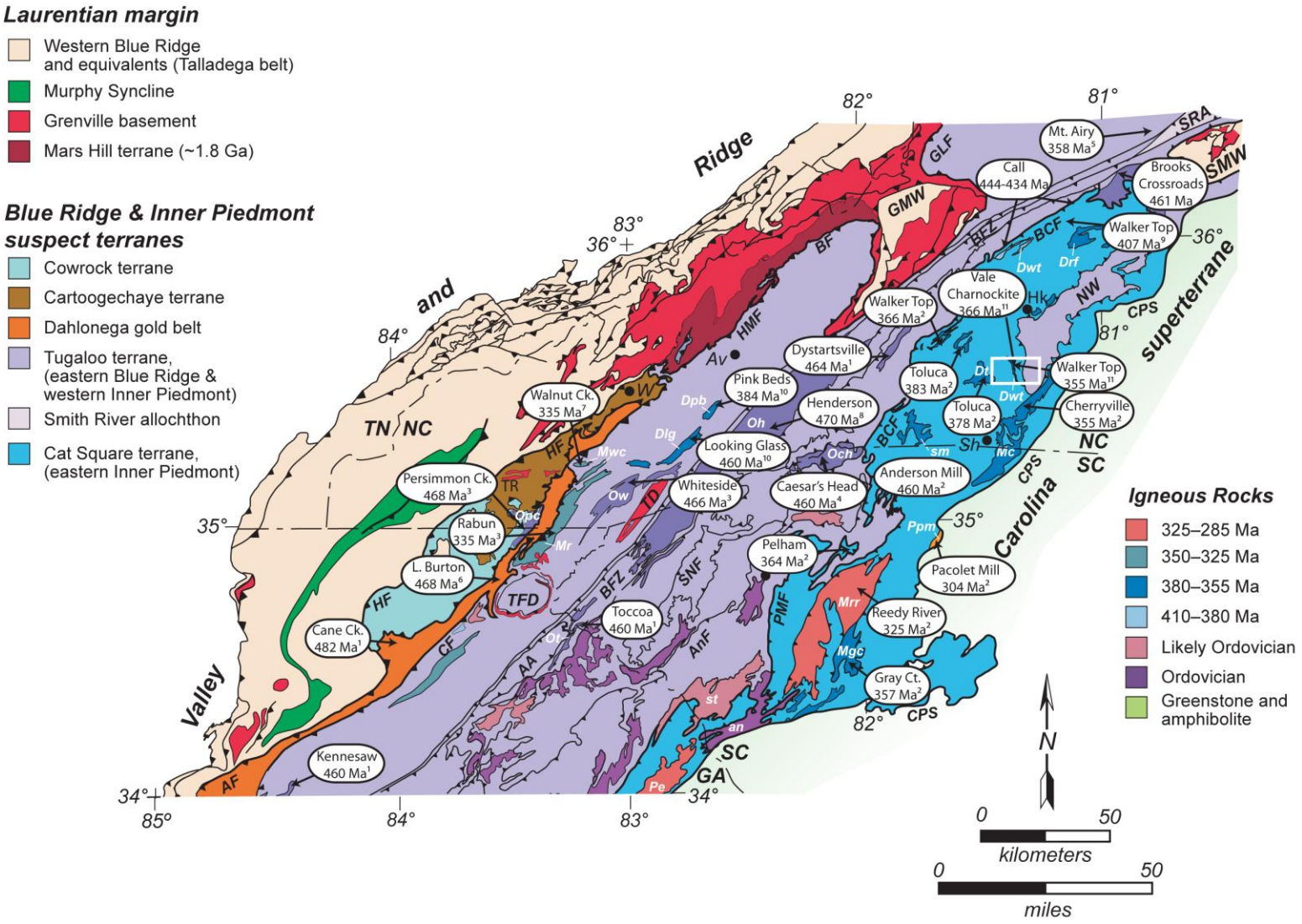
Laurentian margin
Western Blue Ridge and equivalents (Talladega belt)
Murphy Syncline
Grenville basement
Mars Hill terrane (~1.8 Ga)
Blue Ridge & Inner Piedmont suspect terranes
Cowrock terrane
Cartoogechaye terrane
Dahlonega gold belt
Tugaloo terrane, (eastern Blue Ridge & western Inner Piedmont)
Smith River allochthon
Cat Square terrane, (eastern Inner Piedmont)
Igneous Rocks
325–285 Ma
350–325 Ma
380–355 Ma
410–380 Ma
Likely Ordovician
Ordovician
Greenstone and amphibolite
Mt. Airy 358 Ma5
Call 444-434 Ma
Brooks Crossroads 461 Ma
Walker Top 407 Ma5
Vale Charnockite 366 Ma11
Walker Top 366 Ma2
Dystartsville 464 Ma1
Toluca 383 Ma2
Walker Top 355 Ma11
Toluca 378 Ma2
Cherryville 355 Ma2
Anderson Mill 460 Ma2
Pink Beds 384 Ma10
Henderson 470 Ma8
Looking Glass 460 Ma10
Caesar's Head 460 Ma4
Whiteside 466 Ma3
Walnut Ck. 335 Ma7
Persimmon Ck. 468 Ma3
Rabun 335 Ma3
L. Burton 468 Ma6
Cane Ck. 482 Ma1
Kennesaw 460 Ma1
Toccoa 460 Ma1
Pelham 364 Ma2
Pacolet Mill 304 Ma2
Reedy River 325 Ma2
Gray Ct. 357 Ma2
Ridge
and
Valley
Carolina superterrane
TN
NC
SC
GA
GLF
GMW
BF
HMF
BFZ
BCF
NW
CPS
SRA
SMW
HF
TFD
CF
AA
AF
SNF
AnF
PMF
TR
Av
W
Hk
Sh
sm
mc
Dpb
Oh
Dlg
Mwc
Ow
ID
Och
Ppm
Mrr
Mgc
Mr
Qpc
st
an
Pe
82°
81°
83°
84°
85°
36°
35°
34°
0
50
kilometers
miles
N

Cat Square terrane have $\delta^{18}O$ values above 10%, within the range of values for a continental source (9.5-11%) (Mapes, 2002). Mapes (2002) suggested these data reflect pluton generation from more evolved continental sources such as local metasedimentary or basement rocks.

Sillimanite Schist

The sillimanite schist (metapelite) unit is a major contributor to the geomorphology of the Inner Piedmont, forming topographically higher areas than the metagraywacke (Giorgis, 1999). Interlayers of metagraywacke, metasandstone, amphibolite, migmatite and deformed pegmatite are present in the sillimanite schist. Several outcrop-size, nonfoliated, quartz-muscovite pegmatites are also found in this unit. These pegmatites, located in the Shelby–Hickory pegmatite district, were mined for sheet mica prior to 1870 and scrap mica in the 1940s (Presnell, 1999; Fig. 2-1).

Modes of the fine- to coarse-grained, porphyroblastic schist include sillimanite, quartz, opaques ± biotite ± plagioclase ± garnet ± muscovite. Medium- to coarse-grained prismatic sillimanite defines the foliation in schist samples with grains ranging in size from 1 to 20 mm (Fig. 2-14a). Garnet porphyroblasts, typically 1-15 mm in size, but occasionally reach 50 mm, contain inclusions of quartz, but rarely in the form of inclusion trails. The presence and absence of muscovite in the schist in the central and western portions of the study area, respectively, may be indicative of the trace of the second sillimanite isograd present in the study area (Fig. 2-1; see Chapter 3). Layered migmatite parallels foliation, ranges from 1 cm to 1 m thick, and consists of quartz-feldspar ± garnet ± biotite ± muscovite ± sillimanite.

The sillimanite schist is easily identified based on weathering characteristics and sharp contrasts with surrounding lithologies. Colors of saprolite and soils vary slightly based on the interlayers present. Generally, saprolite and soils produced from sillimanite schist are purple- to tan-red and can contain flakes of muscovite, marble-size garnet cobbles, and friable pieces of sillimanite-rich rock (Fig. 2-14b).

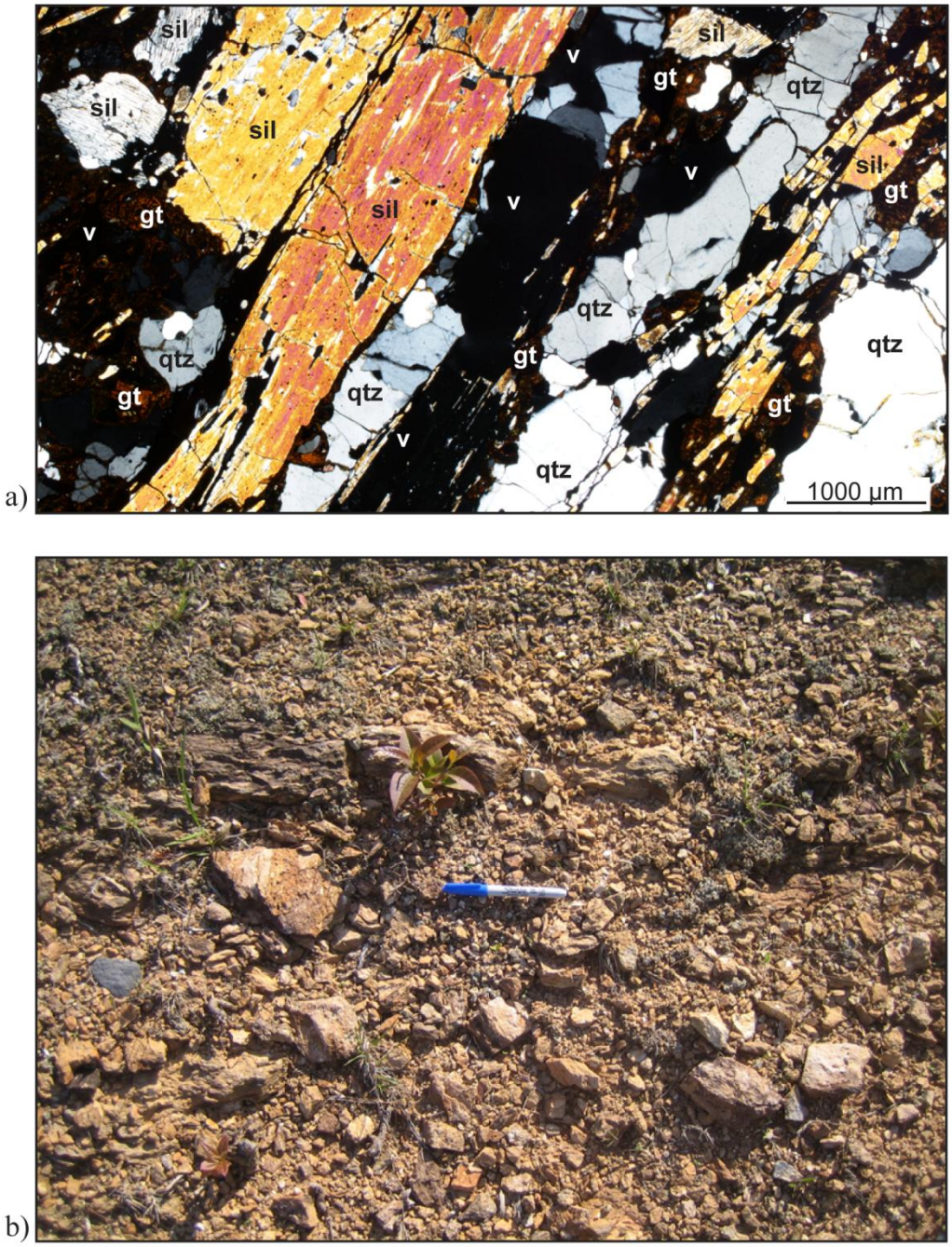

Figure 2-14. Cat Square terrane sillimanite schist. a) Photomicrograph showing prismatic grains of sillimanite forming foliation. Sample from hillside west of NC St. Rd. 1114 (Northbrook III School Road) between NC St. Rds. 1113 (Reeps Grove Church Road) and 1108 (Macedonia Church Road) (station Bk405). b) Small outcrop of sillimanite schist surrounded by purplish-red to tannish-red soils and float produced from weathering. Outcrop on hillside at the end of NC St. Rd. 1684 (Little Indian Creek Church Road) (station Ch73). Permanent marker for scale. Mineral abbreviations: gt–garnet; qtz–quartz; sil–sillimanite; v–void space in thin section.

Metagraywacke

The Cat Square metagraywacke (metapsammite) contains interlayers of metapelite, calc-silicate, metabasite, and migmatite. The lack of boudinaged bodies of amphibolite, compared with the lower Tallulah Falls Formation metagraywacke in the Newton window, assists in distinguishing between units in the field. Migmatitic layers parallel S_2 foliation and are composed of quartz, alkali-feldspar, plagioclase, biotite, and garnet (Fig. 2-15a). Petrographic analysis of metagraywacke samples reveals a mineral assemblage of quartz, plagioclase (An_{40}), biotite, alkali-feldspar, and muscovite with minor amounts of garnet, sillimanite, clinopyroxene, apatite, sphene, opaques, and zircon (Fig. 2-15b). Textural and mineralogical differences are attributed to compositional variations of the protolith and the presence of interlayers.

Metagraywacke weathering produces moderate, reddish-brown saprolite and soils, but may vary slightly based on present interlayers. Distinguishing between metagraywacke and Walker Top Granite soils is difficult because of similarities in soil color. However, metagraywacke soils lack feldspar clasts, and Walker Top Granite soils are a brighter red.

Mafic Complex and Amphibolite Bodies

Several map-scale mafic complexes and amphibolite bodies occur in the sillimanite schist unit of the Cat Square terrane (Fig 2-1). Mafic complexes are undifferentiated interlayers of metadiorite, amphibolite, and metagabbro. Nine samples representing different textures and mineralogies found in the mafic complex and amphibolite bodies were collected for petrographic analysis (Fig. 2-1). Of these, four samples were analyzed for major oxide and trace elements. Whole-rock geochemistry and the tectonic setting of these rocks will be further discussed in Chapter 6.

Modal analysis reveals varying mineral assemblages between metabasites containing plagioclase (An_{45-65}) ± hornblende ± biotite ± clinopyroxene ± orthopyroxene ± quartz ± garnet ± olivine with minor amounts of opaques (Table 2-4). Accessory minerals include epidote, apatite, sphene, and zircon. Alteration products of sericite and chlorite are occasionally observed. The abundance of orthopyroxene in several of the mafic complex samples suggests the appearance of

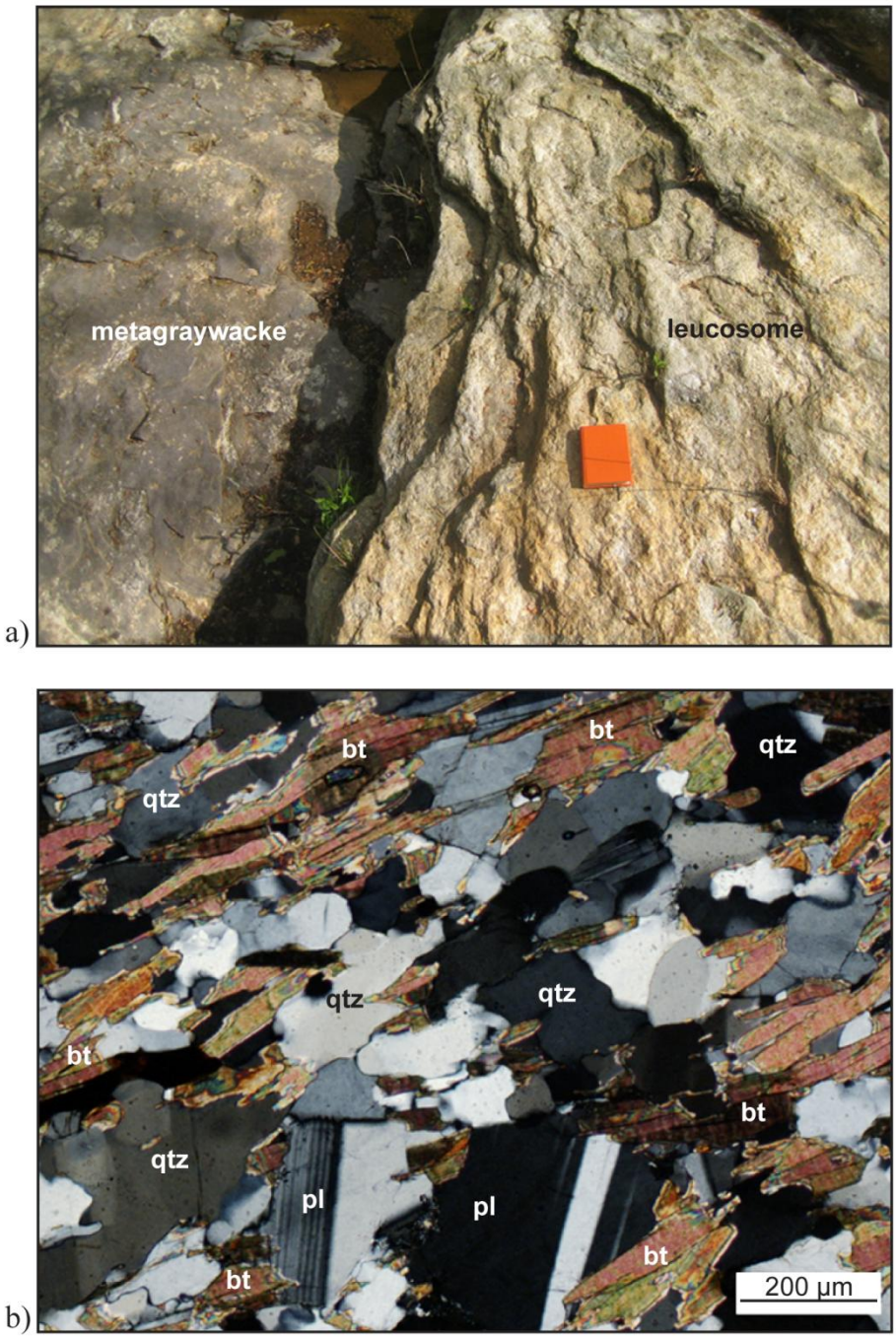

Figure 2-15. Cat Square terrane metagraywacke in Little Indian Creek, east of the intersection of NC St. Rds. 1128 (John Beam Road) and 1129 (Beam Lumber Road) (station Bk32). a.) Outcrop of migmatitic metagraywacke. Reflectivity of the sun on the rocks makes the metagraywacke look like Walker Top Granite and the leucosome like schist. Field book for scale. b.) Photomicrograph of the metagraywacke. Mineral abbreviations: bt–biotite; pl–plagioclase; qtz–quartz.

Table 2-4. Modal analyses of Cat Square terrane mafic complexes and amphibolite bodies.

Sample	Ch 2*	Ch 4*	Ch5f*	Ch16	Ch87	Bk378	Bk69	Bk168	Bk56f*
Rock Type	*amph*	*mg*	*mg*	*md*	*amph*	*md*	*md*	*md*	*md*
points counted	1042	1107	1027	1019	1104	1101	1096	1060	1107
Plagioclase	44.3(An_{45})	47.7(An_{58})	53.8(An_{63})	58.3(An_{52})	36.6(An_{62})	38.3(An_{51})	53.5(An_{55})	56.6(An_{50})	40.8(An_{45})
Hornblende	20.1	18.7	7.1	0.2	37.4	-	6.6	0.6	11.2
Biotite	25.5	15.4	6.7	17.7	-	28.7	14.2	20.5	15.4
Quartz	9.5	1.4	-	16.3	3.3	23.2	4.2	13.7	8.3
Clinopyroxene	-	11.5	9.6	1.8	19.5	9.2	18.3	5.1	19.4
Orthopyroxene	-	1.2	17.7	5.7	0.2	-	1.6	3.3	4.1
Olivine	-	-	0.2	-	-	-	-	-	-
Opaques	-	2.1	4.2	0.1	3.0	0.1	1.0	tr	0.6
Epidote-Clinozoisite	tr	0.7	-	tr	tr	tr	tr	tr	tr
Apatite	0.3	0.4	0.1	tr	0.1	0.5	-	0.3	tr
Sphene	-	-	-	-	tr	-	-	-	tr
Zircon	tr	tr	-	tr	tr	tr	0.1	tr	-
Sericite	0.3	0.9	0.5	-	-	0.1	0.5	-	0.2
Chlorite	-	-	-	-	-	-	-	tr	-
Total	100.0	100.0	100.0	100.0	100.0	100.0	100.0	100.0	100.0

mg - metagabbro; amph - amphibolite; md - metadiorite.

(-) Indicates the mineral was not observed in thin section.

*Indicate samples collected for whole-rock geochemical analysis.

Trace (tr) minerals make up less than 0.1% of the thin section.

Plagioclase compositions were estimated using the Michel-Levy method (Nesse, 1991).

the orthopyroxene isograd in the study area indicating granulite facies metamorphic conditions. Pyroxenes, where present, are breaking down to hornblende and biotite as a result of hydration and retrogression. Migmatitic layers containing quartz, plagioclase ± garnet, are locally present within the mafic complex and amphibolite bodies. Typical soils are dark to very dark brownish red.

Samples from mafic complexes were separated into different rock types including metagabbro, amphibolite, and metadiorite based on color, texture, and silicate mineral content (Table 2-4). Two metagabbro samples have a dark, greenish-black color with a medium- to coarse-grained, granoblastic texture (Figs. 2-16a, b). A minor amount (< 2%) to absence of quartz in thin sections of these samples suggests a more mafic protolith than other mafic complex samples. Sample Ch5f appears to have relict igneous texture and transitions from a medium-fine to medium-coarse grain size (Fig. 2-16a). Some pyroxenes in sample Ch5f have exsolution lamellae, a feature rarely seen in other samples from mafic complexes (Fig. 2-16c). Preserved textures indicate these rocks were dry when metamorphosed under possible granulite facies conditions.

Amphibolite samples are dominantly black from high amounts of hornblende and biotite ± clinopyroxene, with varying amounts of plagioclase (Figs. 2-17a, b). Amphibolite bodies and interlayers are granoblastic, medium-grained, and locally contain garnet. Petrographic analyses of amphibolite samples Ch2 and Ch87 reveal variant mineralogies, although they are similar in outward appearance. Ch2 is composed mainly of plagioclase, hornblende, biotite and quartz; Ch87 lacks biotite and instead consists of two pyroxenes and opaques (Figs. 2-17c, d).

Metadiorite samples have a higher color index than metagabbros and amphibolites, and most contain higher amounts of quartz (Fig. 2-18a). Textures range from medium-grained granoblastic to coarse-grained schistose with a weak to moderate foliation defined by alignment of biotite, hornblende, and quartzofeldspathic material (Figs. 2-18b). Myrmekite is commonly observed in metadiorite samples. Some samples have fine exsolution lamellae of orthopyroxene in clinopyroxene grains, while others contain clinopyroxene which appears optically zoned with hornblende retrograde replacement in the core, although these features are not frequently observed (Fig. 2-18c, d).

Figure 2-16. Metagabbro from undifferentiated Cat Square terrane mafic complexes. a) Rock from which sample Ch5f was collected. Dark colored area is fresh surface; lighter colored green is weathered surface. Relict igneous textures, though not visible in this photograph, are observed in this sample from medium-coarse grains (top) to medium-fine (bottom). Sample is float located east of NC St. Rd. 1127 (Houser Farm Road) (near station Ch5). Field book for scale. b) Granoblastic texture in sample Ch4. Color index in photograph higher than in hand sample. Sample collected from outcrop in Little Creek, east of NC St. Rd. 1146 (Fairview School Road) (station Ch4). Nickel for scale. c) Photomicrograph of texture and mineralogy of sample Ch5f. d) Photomicrograph of granoblastic texture in sample Ch4. Mineral abbreviations: bt–biotite; cpx–clinopyroxene; hbl–hornblende; op–opaque; opx–orthopyroxene; pl–plagioclase; qtz–quartz; ser–sericite.

a)

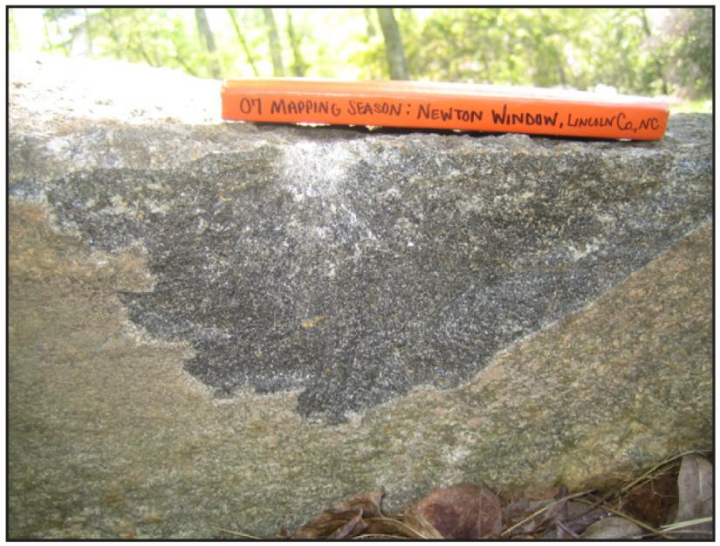
07 MAPPING SEASON: NEWTON WINDOW, LINCOLN Co., NC

b)

c)

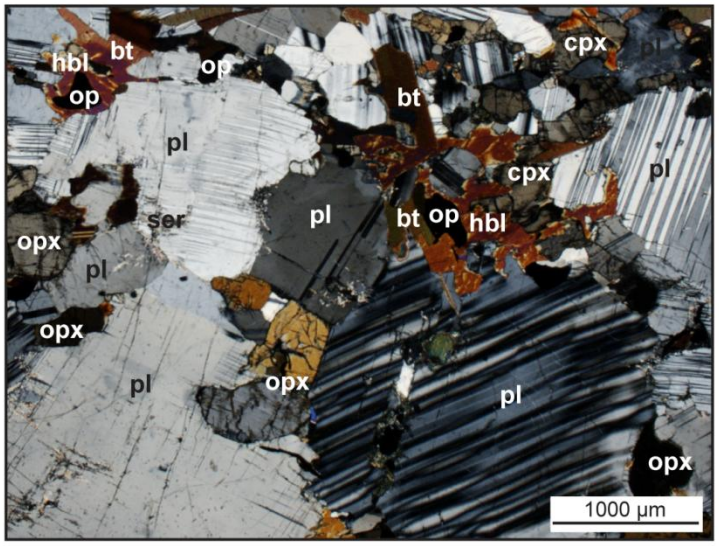
hbl
bt
op
op
bt
cpx
pl
pl
cpx
pl
ser
pl
bt op hbl
opx
pl
opx
pl
opx
pl
pl
opx
1000 µm

d)

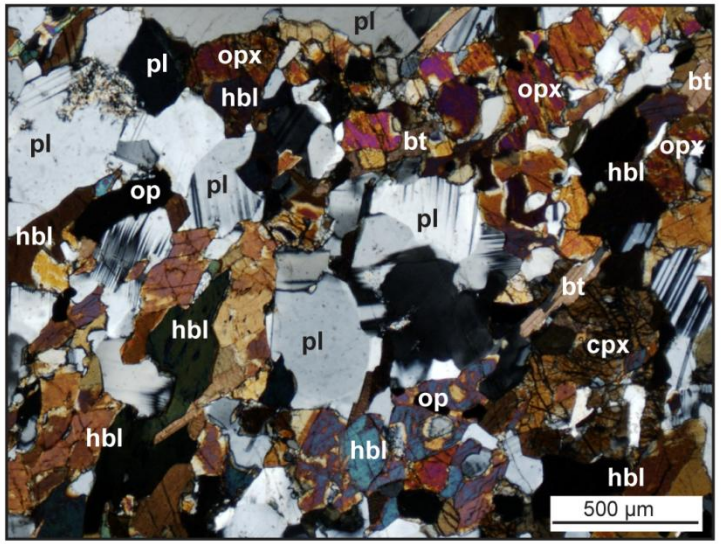
pl
pl
opx
hbl
opx
bt
pl
bt
opx
hbl
op
pl
hbl
pl
bt
hbl
pl
cpx
op
hbl
hbl
hbl
500 µm

Figure 2-17. Amphibolite from Cat Square amphibolite bodies and undifferentiated mafic complexes. a) Migmatitic amphibolite outcrop from which sample Ch2 was collected, located on NC Hwy 27, west of its intersection with NC St. Rd. 1147 (Tower Rd.) (station Ch2). b) Amphibolite sample Ch87, northeast of station Ch2, on the hillside of Indian Creek (station Ch87). Nickel for scale. c) Photomicrograph of sample Ch2. d) Photomicrograph of sample Ch87. Note differences in mineralogy from sample Ch2 (e.g., lack of biotite). Mineral abbreviations: bt–biotite; cpx–clinopyroxene; cz–clinozoisite; hbl–hornblende; myr–myrmekite; op–opaque; pl–plagioclase; qtz–quartz.

a)

b)

c)

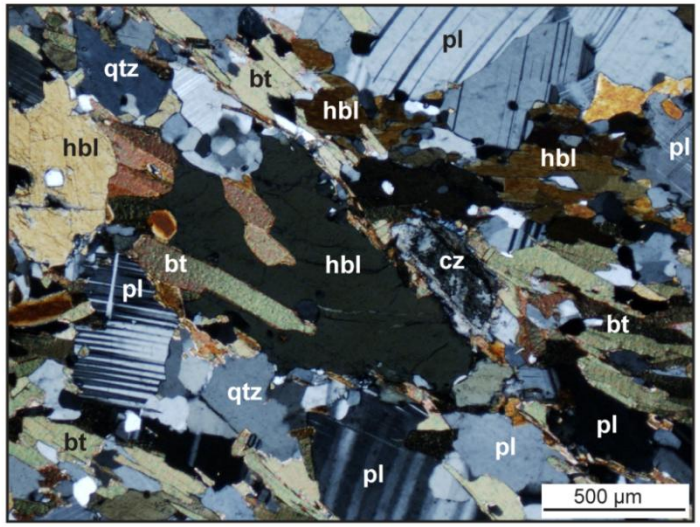
qtz
bt
pl
hbl
hbl
pl
hbl
bt
hbl
cz
pl
bt
qtz
bt
pl
pl
pl
500 µm

d)

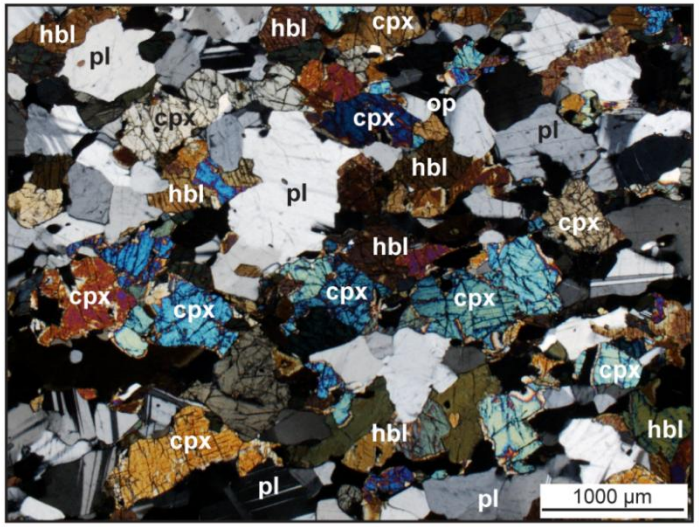
hbl
hbl
cpx
pl
cpx
cpx
op
pl
hbl
hbl
pl
cpx
hbl
cpx
cpx
cpx
cpx
cpx
cpx
hbl
hbl
pl
pl
1000 µm

Figure 2-18. Metadiorite from undifferentiated Cat Square terrane mafic complexes. a) Representative sample of metadiorite at sample location Ch16, located on hillside, south of Little Creek and west of NC St. Rd. 1146 (Fairview School Road). Rock hammer for scale. b) Medium-coarse grained schistose texture of sample Bk378, located on the bank of Glenn Creek, north of NC St. Rd. 1135 (Ed Willis Road). c) Photomicrograph of fine orthopyroxene exsolution lamellae in clinopyroxene grains in sample Bk168. Sample collected from a Little Indian Creek feeder stream, south of NC St. Rd. 1113 (Reeps Grove Church Road). d) Photomicrograph of optically zone clinopyroxene in sample Bk69. Hornblende occurs as an intergrowth in the core of the grain and on the rims of the grain as a primary mineral or ~~is~~ results from the breakdown of clinopyroxene. Apparent optical zoning may reflect compositional changes or different crystallographic orientations of the clinopyroxene. Sample collected from hillside of Indian Creek past the end of NC St. Rd. 1739 (Wells Road). Mineral abbreviations: bt–biotite; cpx–clinopyroxene; hbl–hornblende; op–opaque; opx–orthopyroxene; pl–plagioclase; qtz–quartz; v–void from hole in thin section.

a)

b)


Estwing

c)

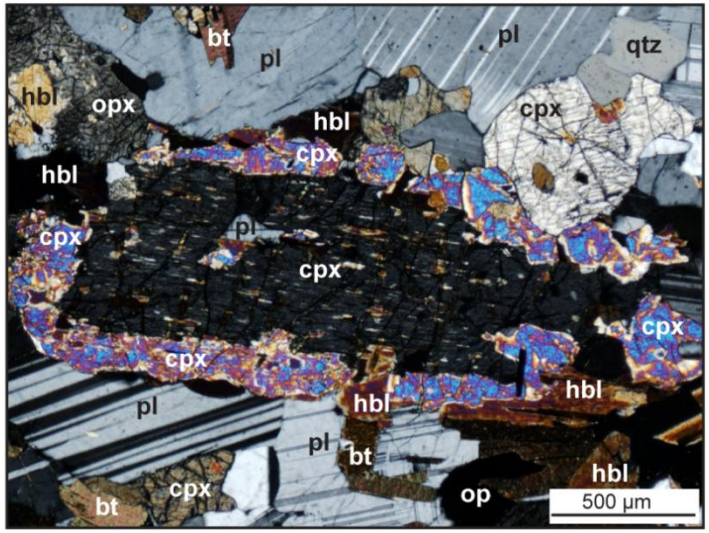
bt
pl
pl
qtz
hbl
opx
hbl
cpx
cpx
hbl
cpx
pl
cpx
cpx
cpx
cpx
hbl
hbl
pl
pl
bt
hbl
bt
cpx
op
500 µm

d)

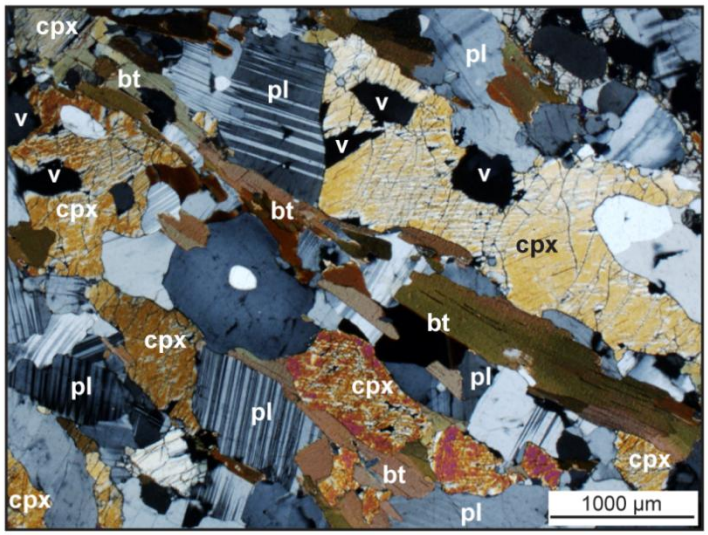
cpx
pl
bt
pl
v
v
v
v
v
cpx
bt
cpx
bt
cpx
pl
cpx
pl
pl
bt
cpx
cpx
bt
pl
1000 µm

Walker Top Granite

The Walker Top Granite was originally mapped in reconnaissance as a more shallow, less deformed version of the western Inner Piedmont Henderson Gneiss (Goldsmith et al., 1988). A detailed study by Giorgis (1999) confirmed the textural, mineralogical, and geochemical similarities of the two plutons. Geochronologic data indicated crystallization ages of ~407 Ma (Gatewood, 2007), ~366 Ma (Mapes, 2002), and ~355 Ma (this study; Chapter 5), prohibiting correlation of the Walker Top Granite and ~470 Ma (Mapes, 2002) Henderson Gneiss. Instead, similarities between the plutons are attributed to comparable igneous processes based on both rock types plotting in the volcanic-arc field on tectonic discriminant diagrams (Giorgis et al., 2002). The Walker Top Granite, however, is suggested to be anatectic and may exhibit a volcanic-arc signature retained from material from which it was derived (Mapes, 2002). The occurrence of Henderson Gneiss is constrained to the Tugaloo terrane in the western Inner Piedmont and the Walker Top Granite to the Cat Square terrane.

Two elongate bodies of Walker Top Granite occur within the study area—one truncates against the Brindle Creek fault, and the other trends NNW-S in the central portion of the study area (Fig. 2-1). The location of these bodies on the flanks of a map-scale sheath fold indicates the original geometry of the Walker Top Granite in the study area was a tabular pluton. Gatewood (2007) also noted the Walker Top Granite occurring in the Brindle Creek fault zone in the Brushy Mountains and concluded a sill-like body of the granite occupies the lowermost portion of the thrust sheet.

The Walker Top Granite is a medium to dark gray with textures ranging from megacrystic granite to protomylonite to ultramylonite. Ultramylonites are observed only along the Brindle Creek fault. Modal analysis of two samples analyzed for whole-rock geochemistry confirm a granitic composition on the IUGS pluton classification scheme (Table 2-5; Fig. 2-10; Streckeisen, 1976). The matrix consists of fine- to medium-grained alkali feldspar, biotite, plagioclase (An_{36-43}), quartz and opaques. Subhedral to anhedral, sheared alkali feldspar megacrysts (1-6 cm) contain ubiquitous mantled (myrmekitic) rims, and are aligned subparallel to the foliation (Figs. 19a, b). Garnet porphyroblasts range in size from 1 to 11 mm and are

Table 2-5. Modal analyses of Cat Square terrane plutons.

Sample	B9-CH^*	B9-WT*	Rp281*	Ch113	Ch117*
Rock Unit	Vale Charn	Walker Top	Walker Top	Toluca	Toluca
points counted	1019	1184	1035	1023	1065
Quartz	32.1	39.9	37.0	34.6	27.0
Plagioclase	26.9(An_{36})	17.4(An_{43})	18.6(An_{44})	23.8(An_{21})	28.7(An_{27})
K-feldspar	25.9	16.2	16.4	22.2	34.9
Hornblende	0.5	-	-	-	-
Biotite	5.7	18.6	20.2	5.6	3.6
Muscovite	-	0.3	0.6	2.1	1.8
Chlorite	-	0.2	0.0	-	-
Sericite	tr	1.1	3.0	8.0	0.7
Myrmekite	2.6	2.2	0.8	1.0	0.8
Epidote	0.2	-	-	-	-
Garnet	-	2.3	2.1	2.8	2.5
Opx	3.9	-	-	-	-
Cpx	1.0	-	-	-	-
Opaques	1.0	1.8	1.4	0.0	-
Apatite	tr	0.1	0.0	-	-
Zircon	0.3	tr	0.0	0.0	0.0
Pyrite	tr	-	-	-	-
Sphene	tr	tr	0.0	-	-
Total	100.0	100.0	100.0	100.0	100.0

(-) Indicates the mineral was not observed in thin section.

^ Indicates sample collected for electron microprobe analysis.

*Indicate samples collected for whole-rock geochemical analysis.

Trace (tr) minerals make up less than 0.1% of the thin section.

Plagioclase compositions were estimated using the Michel-Levy method (Nesse, 1991).

Figure 2-19. Late Devonian-early Mississippian Walker Top Granite. a) Sample showing variation in feldspar phenocrysts from an abandoned quarry near the Brindle Creek fault on the north bank of Howards Creek, east of NC St. Rd. 1193 (Wise Road) (near station Rp280). Eraser (12.5cm) for scale. b) Photomicrograph showing typical texture and assemblage. c) Photomicrograph of sample LW89 showing prismatic sillimanite aligned with foliation from sample on NC St. Rd. 1192 (Jim Wise Road), close to the Brindle Creek fault. d) Outcrop with metagraywacke xenoliths in drainage to Howard's Creek, northeast of the intersection of NC St. Rd. 1002 (Cat Square Road) and NC St. Rd. 1125 (Houser Road) (station Rp270). Rock hammer for scale. Mineral abbreviations: bt–biotite; gt–garnet; kf–alkali-feldspar; myr–myrmekite; pl–plagioclase; qtz–quartz; sil–sillimanite.

a)

b)

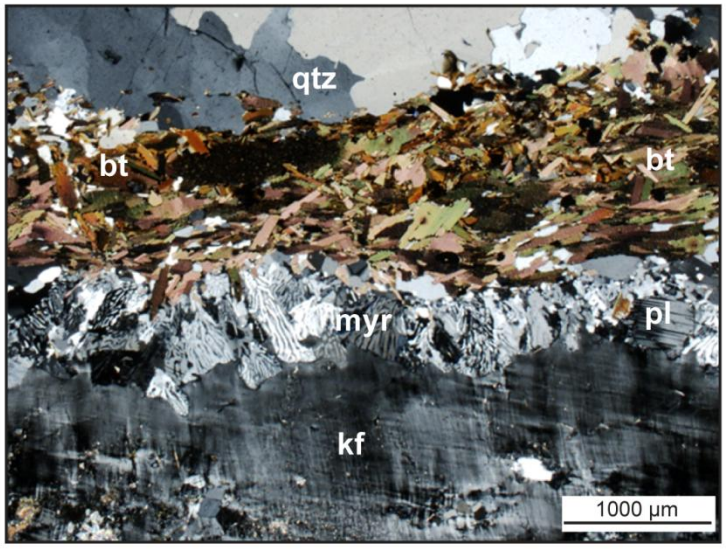

c)

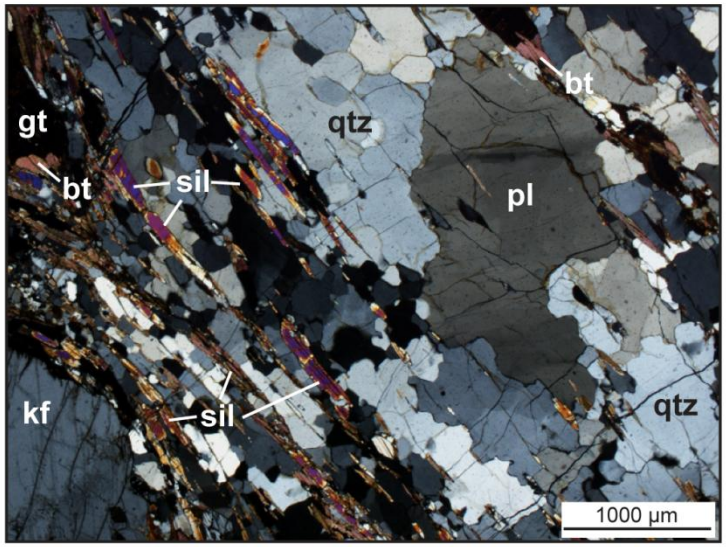

d)

locally abundant. Prismatic sillimanite is present in one sample of Walker Top Granite (Fig. 2-19c). Its presence can be attributed to significant input and melting of the adjacent sillimanite schist during pluton emplacement. Accessory minerals include apatite, sphene, and zircon, with alteration minerals of chlorite, sericite, and muscovite. Moderately weathered Walker Top Granite saprolite exposures are a gray-color with residual white clasts of feldspar, closely resembling color and texture of bedrock. Soil colors produced from the granite weathering are a moderate reddish brown and commonly have popcorn-sized and shaped pieces of feldspar megacrysts.

Xenoliths of amphibolite, metagabbro, migmatitic metagraywacke, quartzite and aluminous schist have been recognized in the Walker Top Granite in previous studies of the Brushy and South Mountains. Only limited amounts of metagraywacke and charnockite xenoliths were observed in the study area (Figs. 2-19d, 2-20a). Charnockite xenoliths were recognized during reconnaissance mapping by Goldsmith et al. (1988) in the Walker Top Granite at Vale, North Carolina. Details of its occurrence will be discussed in the following section and in Chapter 5.

Vale charnockite

The occurrence of the Vale charnockite, located in a roadcut outcrop near the Vale Post Office, was noted by Goldsmith et al. (1988) in reconnaissance mapping as a xenolith within the Walker Top Granite. Kish (1997) named this hypersthene-bearing granite the Cat Square charnockite for the Cat Square crossroads 1 km west of Vale. Modal analysis performed in this study verifies the xenoliths are charnockite based on the IUGS classification as a granite and the presence of orthopyroxene in the sample (Fig. 2-10; Table 2-5). Because of its location in Vale, it will herein be referred to as the Vale charnockite. Geochronologic and geochemical data collected on the Vale charnockite are presented and discussed in detail in Chapter 5 with proposed formation and emplacement hypotheses. No saprolite or soils were observed for the Vale charnockite because of its limited extent to a single outcrop of fresh to slightly weathered rock.

At first glance, the Vale charnockite and Walker Top Granite can be difficult to

Figure 2-20. Devonian Vale Charnockite. a) Walker Top Granite (WT) and Vale charnockite (VC) at the Vale, North Carolina, outcrop on NC St. Rd. 1113 (Reepsville Road). Weathered surfaces obscure the contact between the two granites. b) Gradational contact between the Vale charnockite and Walker Top Granite with concordant foliation, grain size, and grain shape. c) Fresh surface of the Vale charnockite. d) Photomicrograph of the Vale charnockite showing typical texture and mineralogical assemblage. Mineral abbreviations: bt–biotite; cpx–clinopyroxene; kf–k-feldspar; hbl–hornblende; myr–myrmekite; op–opaque; opx–orthopyroxene; pl–plagioclase; qtz–quartz; zr–zircon.

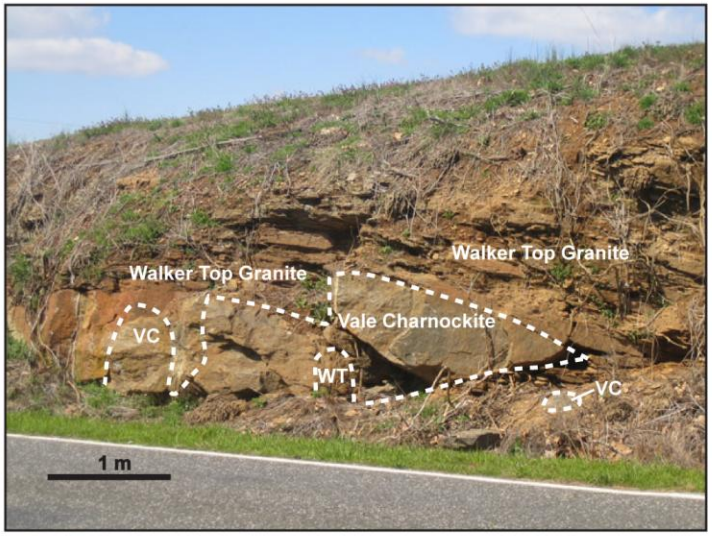
Walker Top Granite
Walker Top Granite
Vale Charnockite
VC
WT
VC
1 m

a)

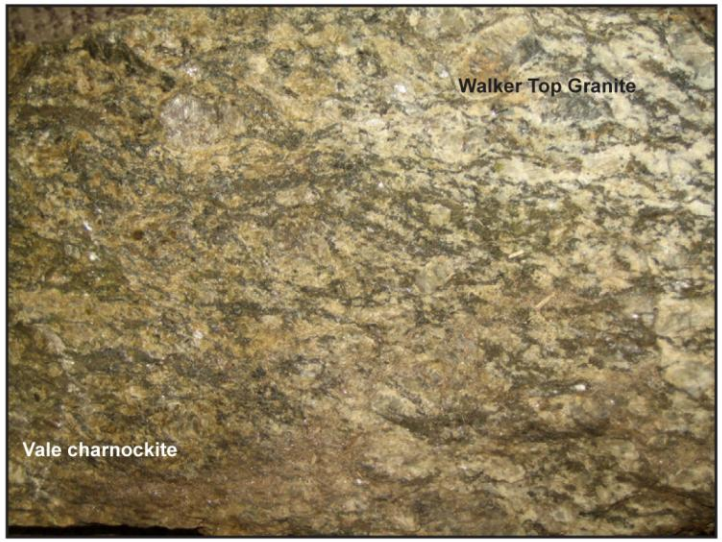
Walker Top Granite
Vale charnockite

b)

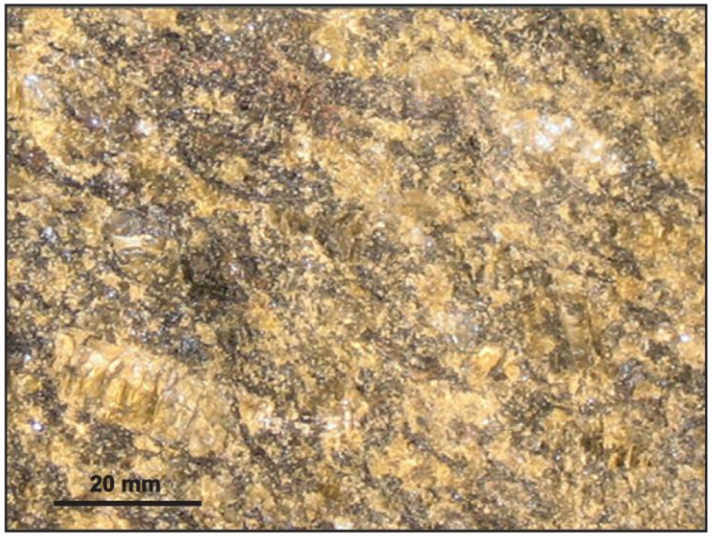
20 mm

c)

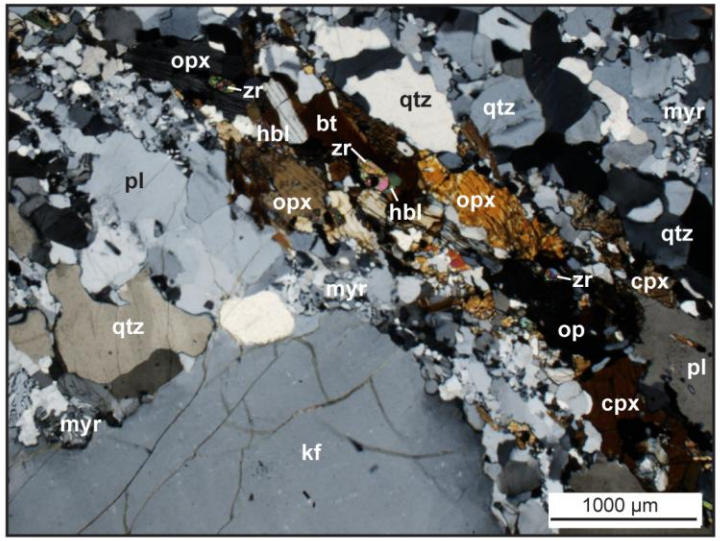
opx
zr
qtz
qtz
myr
hbl
bt
zr
pl
opx
hbl
opx
qtz
zr
cpx
myr
qtz
op
pl
cpx
myr
kf
1000 µm

d)

distinguish in outcrop due to the foliation concordance, textural similarities (moderately foliated, megacrystic, inequigranular gneiss), and appearance of weathered surfaces (Figs. 2-20a, b). On closer inspection of fresh surfaces of the two granites, however, color and compositional differences become very apparent. The Vale charnockite is a dark, brown-green color with semi-translucent, brownish-olive green alkali-feldspar megacrysts mantled by thin myrmekite rims (Fig. 2-20c). Fine-grained, subhedral to anhedral phenocrysts of orthopyroxene form foliation with lesser amounts of biotite compared to the biotite-rich, pyroxene-absent Walker Top Granite.

Petrographic analysis of the anhydrous charnockite reveals alkali-feldspar megacrysts surrounded by a matrix of plagioclase (An_{44}) and quartz. Mafic bands are composed mainly of biotite and orthopyroxene with minor amounts of fine-grained clinopyroxene, hornblende, ilmenite and garnet (Fig. 2-20d). Accessory minerals include epidote, apatite, pyrite, sphene, and zircon. Orthopyroxenes are observed breaking down to biotite and hornblende, indicative of small amounts of water present in the melt or post-crystallization hydration during retrograde metamorphism.

Toluca Granite

The Toluca Granite, previously named the Whiteside Granite (Keith and Sterrett, 1931) and Toluca Quartz Monzonite (Griffitts and Overstreet, 1952), occurs as bodies of variable size and thickness (Goldsmith et al., 1988). The type locality is located in the town of Toluca, North Carolina, in the Lawndale 7.5-minute quadrangle, southwest of the study area (Plate 3). U-Pb SHRIMP zircon ages from a sample of Toluca Granite from the Casar 7.5-minute quadrangle, west of the study area, yielded a crystallization age of 378 ± 4 Ma with two inherited cores of 1036 ± 178 Ma and 1236 ± 144 Ma (Mapes, 2002; Fig. 2-13). Monazite ages from the same locality produced an age of 368 ± 2 Ma (Mapes, 2002). Zircons from a second Toluca Granite in the South Mountains contain two possible cores at 406 ± 10 Ma and 433 ± 4 Ma with a crystallization age of 383 ± 2 Ma (Mapes, 2002). The Toluca Granite is the only pluton in the Cat Square terrane with inherited cores.

Several whole-rock geochemical studies have been conducted on samples of Toluca Granite (Bier, 2001; Mapes, 2002; Wilson, 2006), including one sample from this study. These

data are presented in Chapter 5. The Toluca Granite spans the fields of volcanic-arc and syn-collisional granite on tectonic discriminant diagrams. Mapes (2002) noted that although data support Inner Piedmont plutons are anatectic melts of variable composition crust, the rocks do exhibit some characteristics of subduction related magmas, such as relative high field strength element (HFSE) depletion, that do suggest derivation from a subduction related material.

The well-foliated Toluca Granite is a light gray and white, medium-grained granite composed of plagioclase (An_{21-27}), alkali feldspar, quartz, muscovite, biotite, and garnet with minor amounts of myrmekite, opaques, and zircon (Figs. 2-21a, b; Table 2-5). Subhedral to anhedral grains of feldspar (<7 mm) and garnet (<2 mm) occur as phenocrysts in the Toluca Granite. Large muscovite grains occur parallel to foliation and within feldspar grains as a result of deuteric alteration (Fig. 2-21c). Sericite also occurs as a later hydrothermal alteration product. Four map-scale bodies of Toluca Granite were mapped in the western and southwestern portions of the study area (Fig. 2-1). The sizes of these bodies are variable within the study area, as well as throughout the Cat Square terrane, as noted by Griffitts and Overstreet (1952), Goldsmith et al. (1988), and Bier (2001). The Toluca Granite is only in contact with sillimanite schist in the study area, but it has also been mapped in contact with metagraywacke (Plate 3; Fig 1-1). No xenoliths were observed in this study, although they have been noted in the Toluca Granite-equivalent(?) Rocky Face pluton in the Brushy Mountains (Wilson, 2006). Outcrops of Toluca Granite form exfoliation surfaces on creeks and hillsides, and in creeks (Fig. 2-21d). Saprolite and soils produced from the Toluca Granite are distinctly different and easily distinguished from surrounding rock units by their medium tan-gray color. Pea- to sand-size grains of garnet and quartzofeldspathic material, produced by weathering of the granite, are sometimes present in the soils.

Mesozoic Features

Diabase Dike

Triassic-Jurassic diabase dikes are observed in creek beds and on hillsides as nearly vertical spheroidally weathered boulders with an ~N45°W orientation (Fig. 2-22a). The olivine-

Figure 2-21. Devonian Toluca Granite. a) Typical texture of the Toluca Granite with sand-sized grains of garnet and quartzofeldspathic material in saprolite produced from weathering of the granite. Outcrop located on the bank of Glenn Creek, east of NC St. Rd. 1141 (Norman Parker Road) (station Ch110). Quarter for scale. b) Photomicrograph of the Toluca Granite showing typical texture and mineralogical assemblage. c) Photomicrograph of muscovite replacing feldspar grains as a product of retrograde metamorphism. d) Outcrop of Toluca Granite showing exfoliation surfaces in Buffalo Creek, west of NC St. Rd. 1117 (Rockdale Road) (station Ch117). Mineral abbreviations: bt–biotite; gt–garnet; kf–alkali-feldspar; ms–muscovite; myr–myrmekite; pl–plagioclase; qtz–quartz.

a)

b)

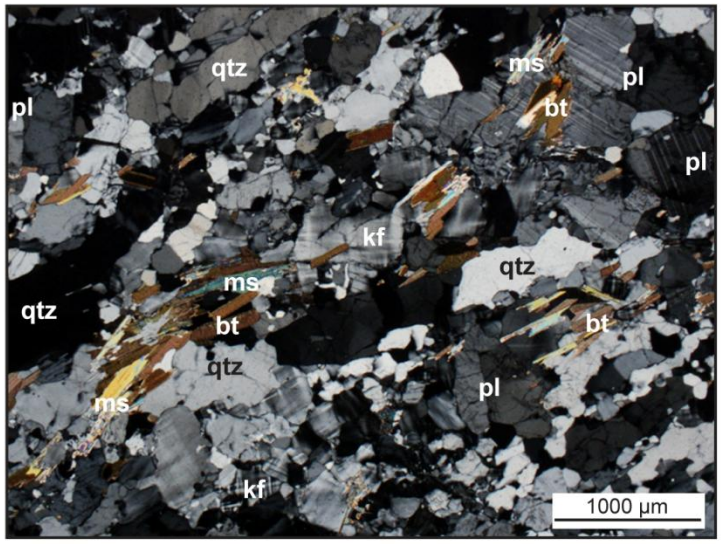
qtz
ms
pl
pl
bt
pl
kf
qtz
ms
qtz
bt
bt
qtz
pl
ms
kf
1000 µm

c)

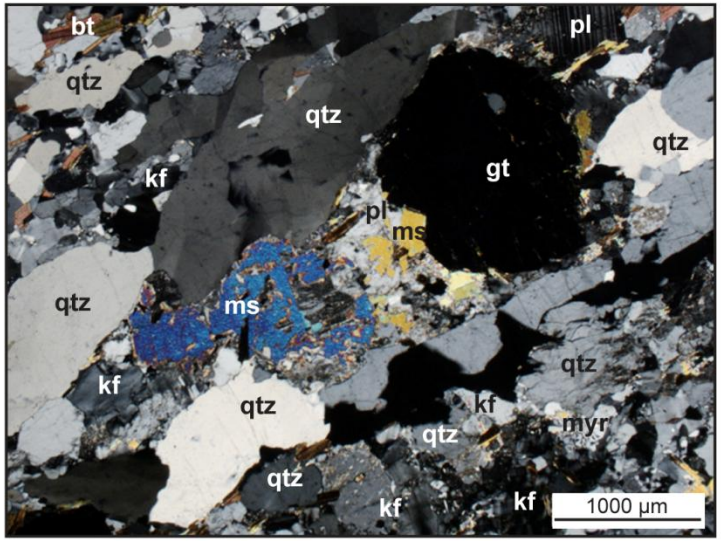
bt
pl
qtz
qtz
qtz
kf
gt
pl
ms
qtz
ms
qtz
kf
qtz
kf
myr
qtz
qtz
kf
kf
1000 µm

d)

normative diabase has an aphanitic, ophitic texture with olivine and pyroxene phenocrysts surrounded by randomly oriented, bladed crystals of plagioclase (Fig. 2-22b). No contacts or contact aureoles were observed in exposures of diabase dike. Emplacement of the diabase dikes in a consistent orientation throughout the Carolina superterrane and Inner Piedmont is attributed to the development of tension fractures (May, 1971) and rapid magma emplacement in these fractures (Hatcher, 2006) during the break-up of Pangea at ~199 Ma (Hames et al., 2000).

a)

b)

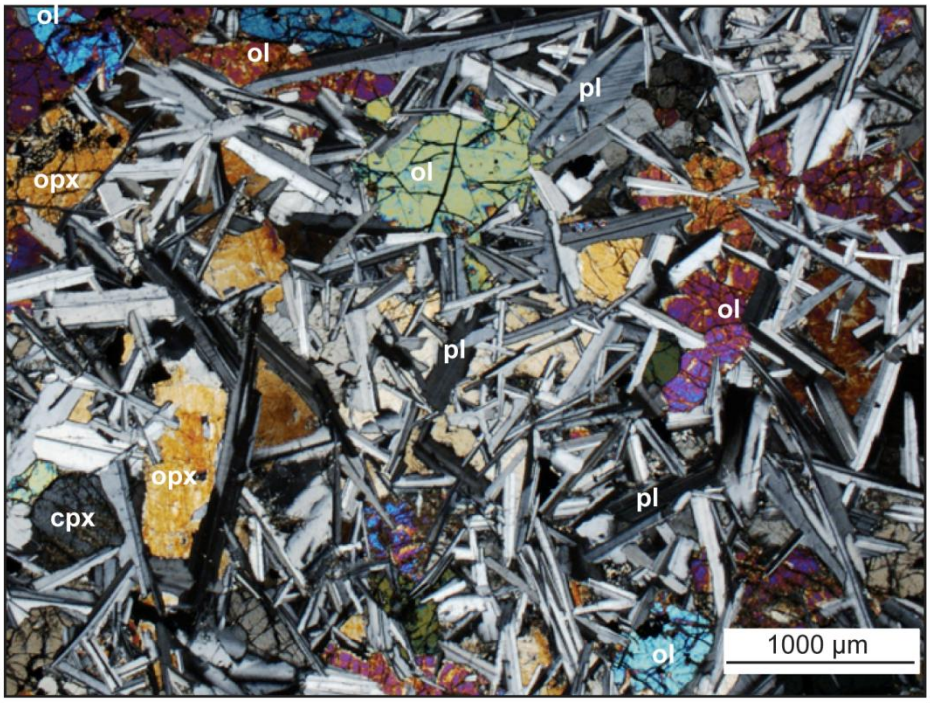

Figure 2-22. Mesozoic diabase dike. a) Typical spheroidal and elongate boulders of diabase in a tributary to Little Creek, between NC St. Rd. 1127 (Houser Farm Road) and NC Hwy 274 (station Ch24). Rock hammer for scale. b) Photomicrograph of sample Ch24 showing ophitic texture of the diabase dike. Mineral abbreviations: cpx–clinopyroxene; pl–plagioclase; ol–olivine; opx–orthopyroxene.

CHAPTER 3

METAMORPHIC RELATIONSHIPS IN THE NEWTON WINDOW, EASTERN INNER PIEDMONT

The core of the southern Appalachians is composed of high-grade metamorphic rocks accreted during multiple orogenic events. Deformational and thermal overprinting make it difficult to separate metamorphic assemblages from each orogenic event. Determining metamorphic relationships through the compilation of metamorphic isograds and metamorphic ages with granite crystallization ages and cross-cutting relationships of structural features in the southern Appalachians permits delineation of metamorphic domains directly associated with shared tectonothermal events (Fig. 3-1). Of the three main events recognized for this region, the Taconic, Neoacadian, and Alleghanian orogenies, metamorphic domains suggest the Inner Piedmont was involved in the latter two: high-temperature metamorphism during the prograde Neoacadian orogeny (360-345 Ma) (Davis, 1993; Bier, 2001; Merschat and Kalbas, 2002; Merschat et al., 2005a, b; Fig. 3-2) and moderate temperature metamorphism during the Alleghanian orogeny (330-300 Ma) (Dennis and Wright, 1997a).

The metamorphic grade of the Inner Piedmont increases from the Brevard fault zone eastward across the core of the Inner Piedmont from garnet-staurolite (in South Carolina) and staurolite-kyanite (in North Carolina) to sillimanite I (sillimanite + muscovite) (Butler, 1991; Hatcher and Goldberg, 1991) and sillimanite II (sillimanite + K-feldspar) grades (Mirante and Patiño-Douce, 2000; Bier, 2001; Merschat, 2003; Wilson, 2006; Gatewood, 2007; Fig. 3-3). Retrograde assemblages occur along the Brevard fault zone from brittle reactivation during the Alleghanian orogeny (Hatcher, 1993). Metamorphic isograds are concordant with regional structures across the whole of the Inner Piedmont, indicating pre- or syn-metamorphic regional deformation and emplacement of Inner Piedmont thrust sheets. Bream (2003) suggested these thrust sheets were emplaced at minimum pressure and temperature (P-T) estimates for peak metamorphism of the Inner Piedmont. Peak P-T estimates from eastern and western Inner Piedmont rocks range from 500–800 °C and 3–8 kbar indicating a Barrovian metamorphic P-T

Figure 3-1. Metamorphic domains depicting components of the southern Appalachian Blue Ridge and Inner Piedmont with shared tectonothermal events. Extent of the domains was defined from areas with similar zircon rim ages, continuation of metamorphic isograds, and structural features. The Alleghanian event is more extensive than depicted in this diagram, but has been recorded throughout the Inner Piedmont (see Fig. 3-3). Black box outlines study area. Index mineral abbreviations: u–unmetamorphosed. sc–sub-chlorite. c–chlorite. b–biotite. g–garnet. st–staurolite. k-st–kyanite+stauralite. k–kyanite. si–sillimanite. si II–sillimanite II. gr–granulite. BC–Brindle Creek fault. BFZ–Brevard fault zone. BF–Burnsville fault. CHM–Chattahoochee-Holland Mountain fault. GL–Gossan Lead fault. SMW–Sauratown Mountain window. Figure modified from Merschat (2009).

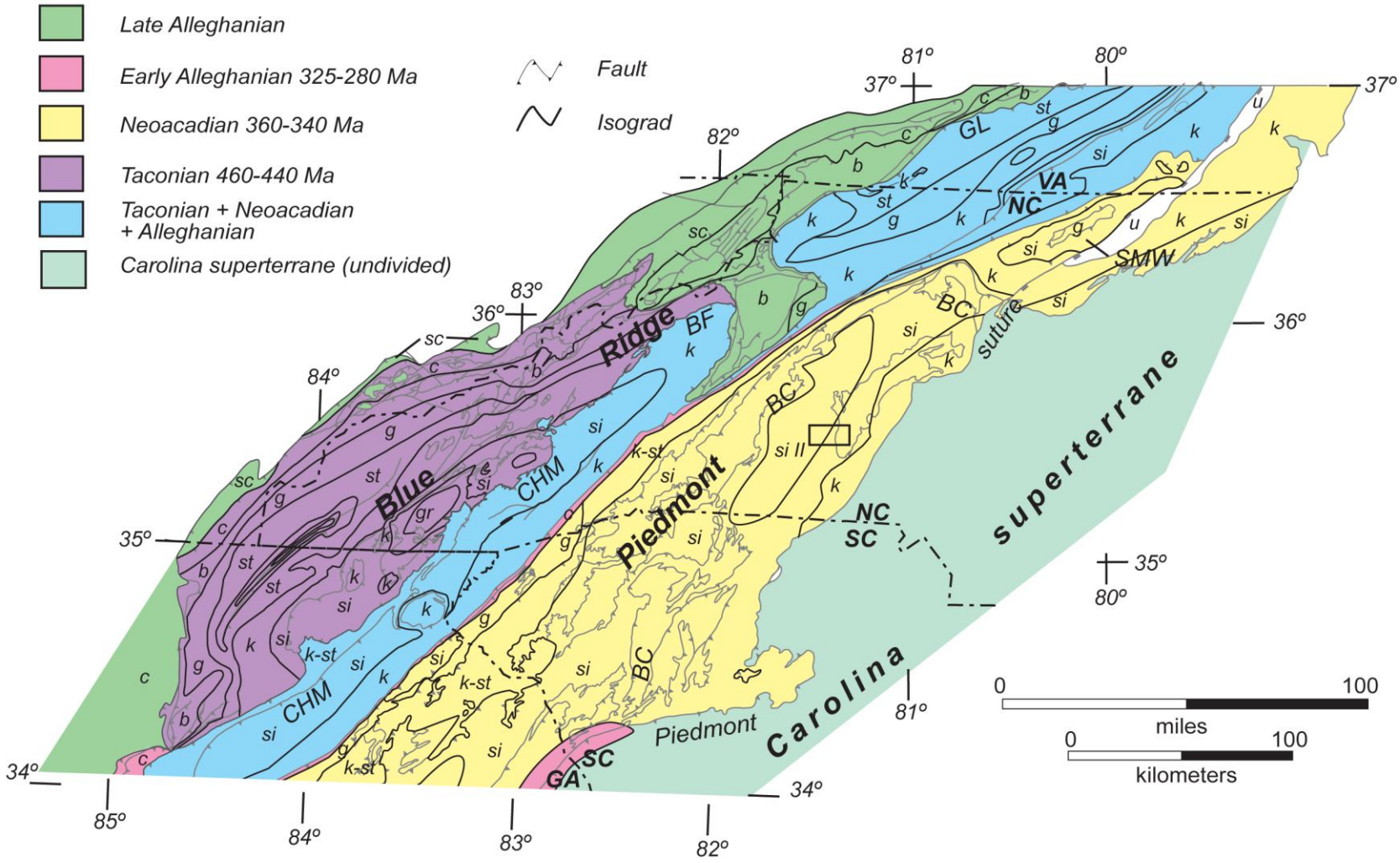
Late Alleghanian
Early Alleghanian 325-280 Ma
Neoacadian 360-340 Ma
Taconian 460-440 Ma
Taconian + Neoacadian + Alleghanian
Carolina superterrane (undivided)
Fault
Isograd
Blue Ridge
BF
Piedmont
Carolina superterrane
Piedmont
CHM
BC
suture
GL
VA
NC
SMW
SC
GA
si II
0
100
miles
kilometers
81°
80°
37°
82°
83°
36°
84°
35°
34°
85°

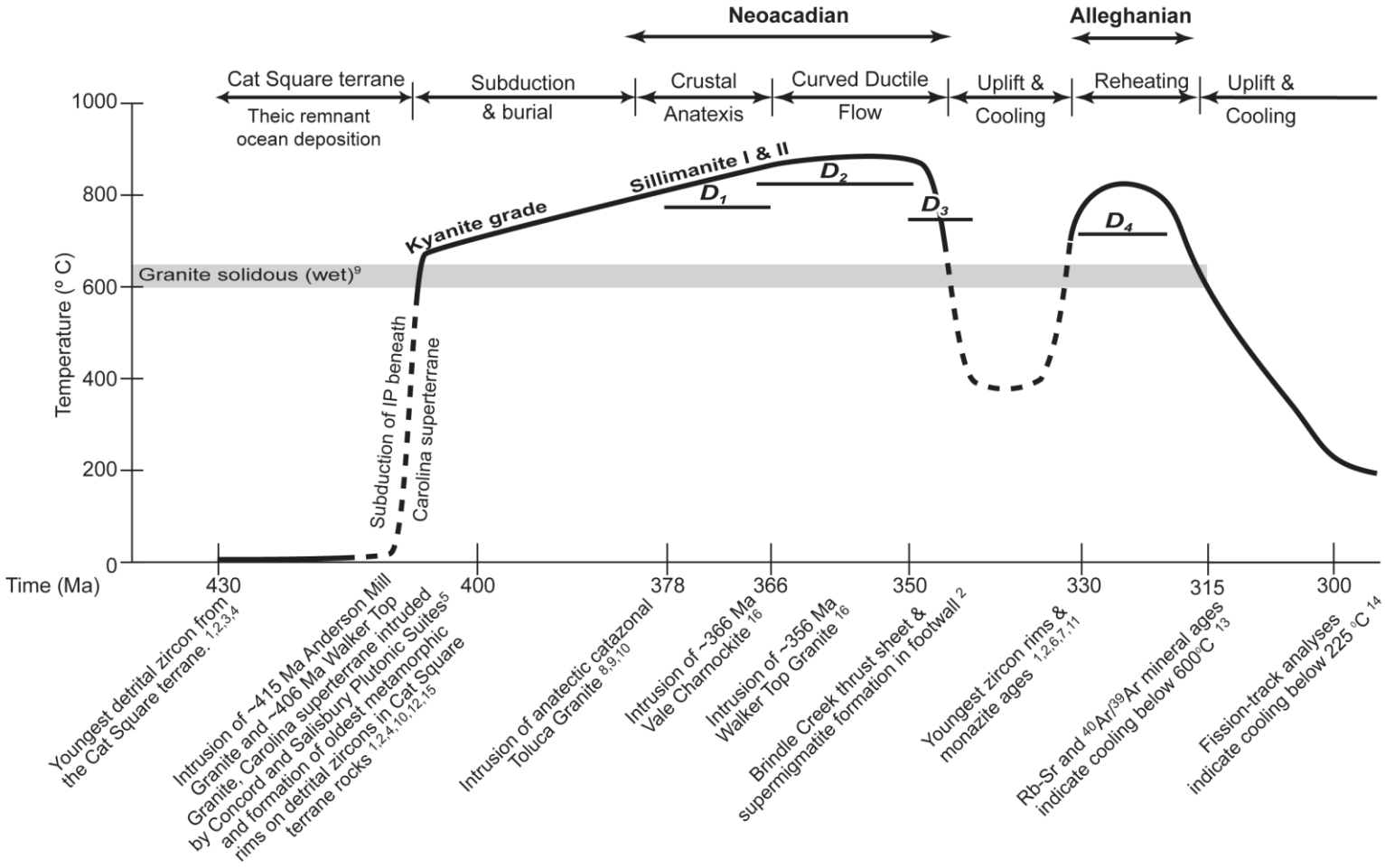

Figure 3-2. Tectonothermal history of the Cat Square terrane. Sources of data are: 1–Bream (2002); 2–Bream (2003); 3–Bream et al. (2001) 4–Bream et al. (2004); 5–McSween et al. (1984); 6–Carrigan et al. (2001); 7–Dennis and Wright (1997a, b); 8–Giorgis et al. (2002); 9–Luth et al. (1964); 10–Mapes (2002); 11–Mapes et al. (2001); 12–Gatewood (2007); 13–van Breemen and Dallmeyer (1984); 14–Naeser et al. (2001); 15–Butler and Fullagar (1978); 16–Byars et al. (2008a). Figure modified from Hatcher and Merschat (2006) and Gatewood (2007).

Figure 3-3. Metamorphic isograd map of the southern Appalachian Blue Ridge and Inner Piedmont compiled from various studies (Hadley and Goldsmith, 1963; Carpenter, 1970; Hadley and Nelson, 1971; Rankin et al., 1972; Espenshade et al., 1975; Goldsmith et al., 1988; Merschat and Wiener, 1988; Eckert et al., 1989; Hopson et al., 1989; Butler, 1991; Hatcher and Goldberg, 1991; Quinn, 1991; Nelson et al., 1998; Settles, 2002; Higgins et al., 2003; Merschat, 2003; Tull and Holm, 2005; Hatcher and Merschat, 2006; Hatcher et al., 2007; Tull, 2007). Sources of zircon rim and monazite data are Dennis and Wright (1997a,b)[1]; Carrigan et al. (2003)[2]; Hibbard et al. (2003)[3]; Moecher et al., (2004)[4]; Ownby et al. (2004)[5]; Berquist et al. (2005)[6]; Moecher et al. (2005)[7]; B. Miller et al., (2006)[8]; Corrie and Kohn (2007)[9]; Dennis (2007)[10]; Gatewood (2007)[11]; Byars et al. (2008a)[12]; this study[13]. Unlabeled ages are data presented in Merschat (2009). Ar/Ar, Sm/Nd, and Rb/Sr mineral ages are from Dallmeyer et al. (1986); Dallmeyer (1988); Connelly and Dallmeyer (1993); Goldberg and Dallmeyer (1997). White box outlines study area. Figure modified from Merschat (2009).

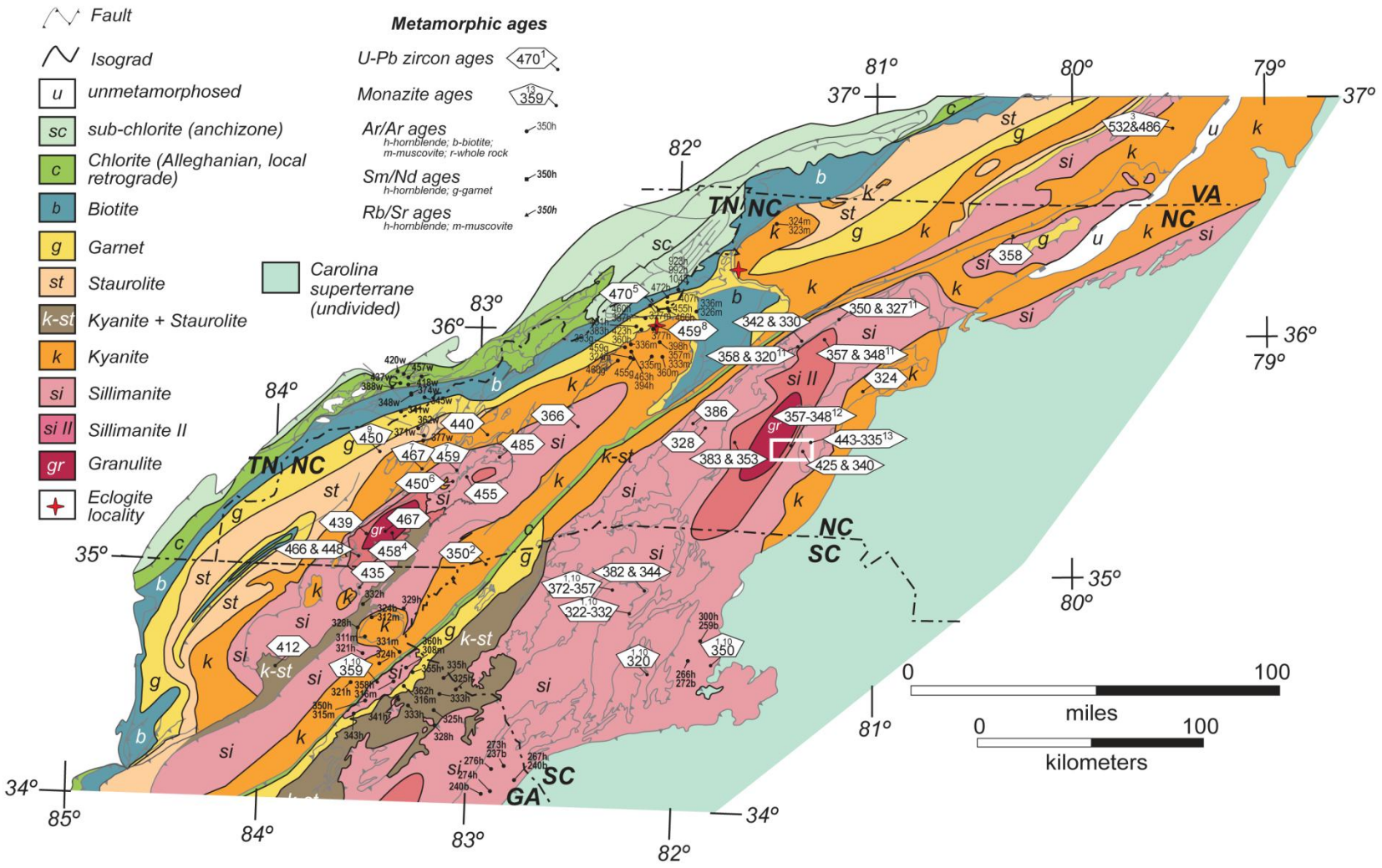
Fault
Isograd
u unmetamorphosed
sc sub-chlorite (anchizone)
c Chlorite (Alleghanian, local retrograde)
b Biotite
g Garnet
st Staurolite
k-st Kyanite + Staurolite
k Kyanite
si Sillimanite
si II Sillimanite II
gr Granulite
Eclogite locality
Metamorphic ages
U-Pb zircon ages
Monazite ages
Ar/Ar ages
h-hornblende; b-biotite; m-muscovite; r-whole rock
Sm/Nd ages
h-hornblende; g-garnet
Rb/Sr ages
h-hornblende; m-muscovite
Carolina superterrane (undivided)
TN
NC
SC
GA
VA
81°
80°
79°
37°
82°
83°
36°
84°
35°
34°
85°
0
100
miles
kilometers

path (Davis, 1993; Yanagihara, 1994; Hill, 1999; Mirante and Patino-Douce, 2000; Bier et al., 2002; Mapes, 2002; Merschat and Kalbas, 2002; Gatewood, 2007; Fig. 3-4). The Barrovian P-T path recorded in Inner Piedmont rocks is typical of a path encountered during crustal thickening during collision at convergent boundaries, followed by erosion and thermal relaxation (Spear, 1993).

Field and Petrographic Observations

Mineral assemblages found in the study area confirm the Cat Square and Tugaloo terranes underwent a high-grade metamorphic event. Sillimanite is abundant in metapelites and some metapelitic interlayers in metagraywackes. Ortho- and clinopyroxene are present in mafic complex and amphibolite interlayers and bodies, while clinopyroxene is found in some Cat Square terrane metagraywacke samples. Garnet is ubiquitous throughout the study area. Migmatites and deformed pegmatites in both terranes parallel the dominant S_2 foliation indicative of their emplacement prior to or during the development of the S_2 foliation in peak metamorphic conditions. Hydration and breakdown of pyroxenes to biotite and hornblende, and the seritization and replacement of feldspars by muscovite, are indicative of retrograde metamorphism. Nonfoliated, quartz-muscovite pegmatites, likely late-stage features, occur in bodies of sillimanite schist.

Evidence for first and second sillimanite grade, as well as granulite facies conditions, is observed in thin sections of samples throughout the majority of the field area in both Cat Square and Tugaloo terranes. Sillimanite ranges from small to large, prismatic grains. In the central and eastern portions of the field area, sillimanite occurs in a metapelitic layer in the lower Tallulah Falls Formation (Fig. 3-5a) and a body of Walker Top Granite near the Brindle Creek fault (Fig. 3-5b). Although muscovite can be found in migmatite in the sillimanite schist, it does not coexist with sillimanite in the western portion of the study area. Instead, feldspar, quartz, and garnet grains are observed in the schist (Fig. 3-5c). The absence of muscovite and presence of feldspar in sillimanite schist likely indicates the second sillimanite isograd reaction:

$$\text{Muscovite} + \text{Quartz} = \text{K-feldspar} + \text{Sillimanite} + \text{Water} \qquad (3\text{-}1)$$

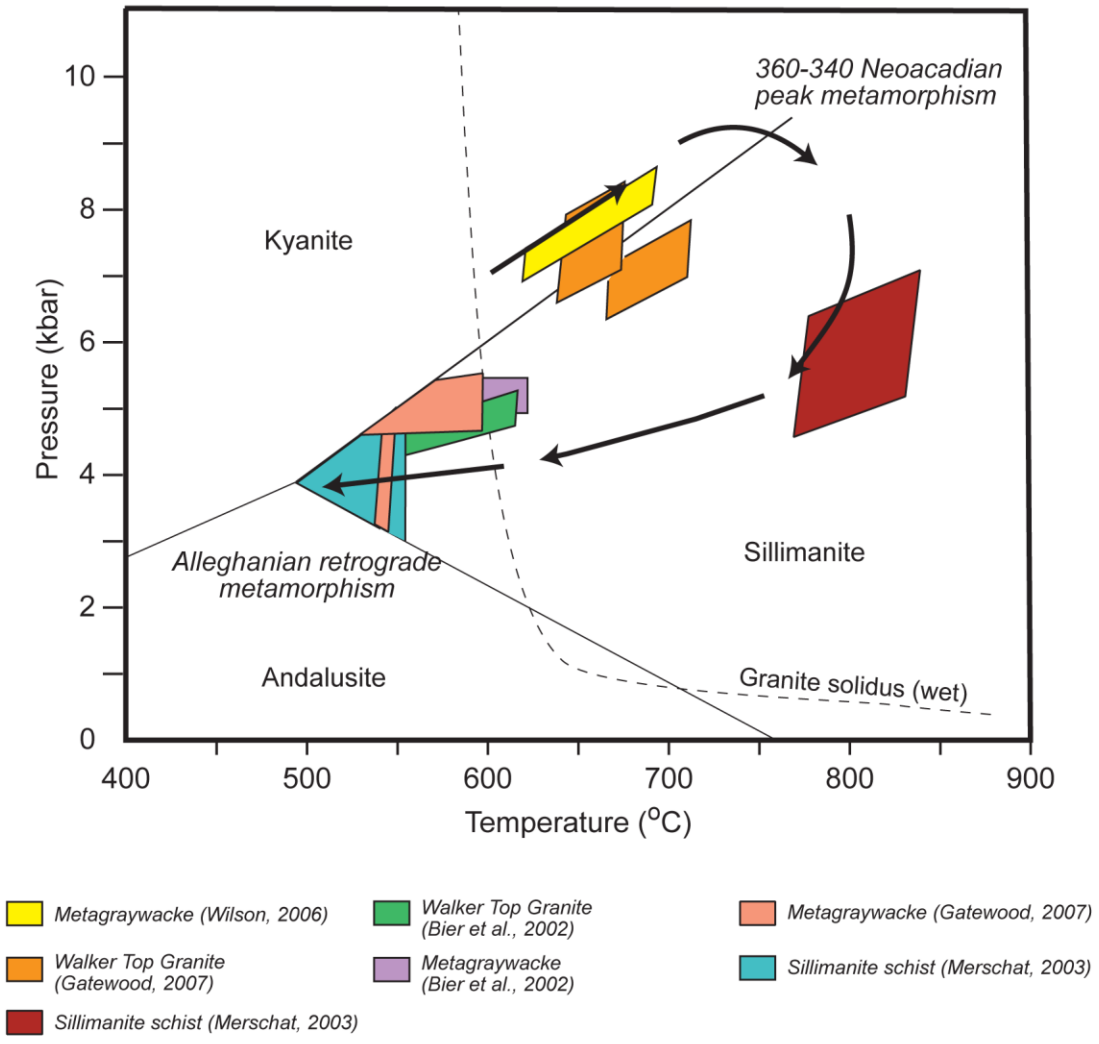

Figure 3-4. Projected pressure-temperature-time path of the Cat Square terrane (modified from Gatewood, 2007).

Figure 3-5. Photomicrographs showing mineral relationships from Cat Square terrane aluminous schist. a) Prismatic sillimanite grains being replaced by muscovite in sample Rp42. Sample collected from outcrop in a tributary of Tanyard Creek, north of NC St. Rd. 1113 (Reepsville Road). b) Small grains of prismatic sillimanite with garnet, quartz, feldspar, and biotite in Walker Top Granite (sample LW89). Sample collected from outcrop on NC St. Rd. 1192 (Jim Wise Road), located near the southern exposure of the Brindle Creek fault in the south-central portion of the study area. c) Large grains of prismatic sillimanite with garnet, quartz, and feldspar in sample Bk405f from the northwestern corner of the study area. Sample from hillside west of NC St. Rd. 1114 (Northbrook III School Road) between NC St. Rds. 1113 (Reeps Grove Church Road) and 1108 (Macedonia Church Road). Mineral abbreviations: bt–biotite, gt–garnet, kf–K-feldspar, ms–muscovite; op–opaque; pl–plagioclase; qtz–quartz, sil–sillimanite.

a)

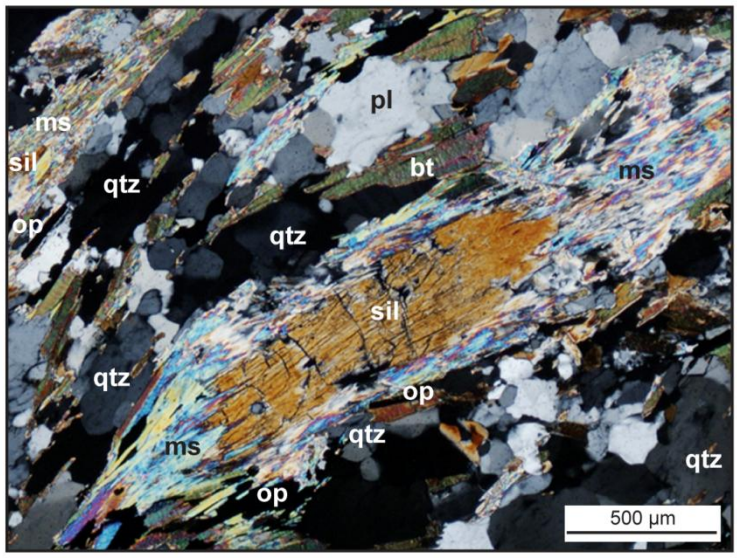
ms
sil
qtz
op
pl
bt
ms
qtz
sil
qtz
op
qtz
ms
op
qtz
qtz
500 µm

b)

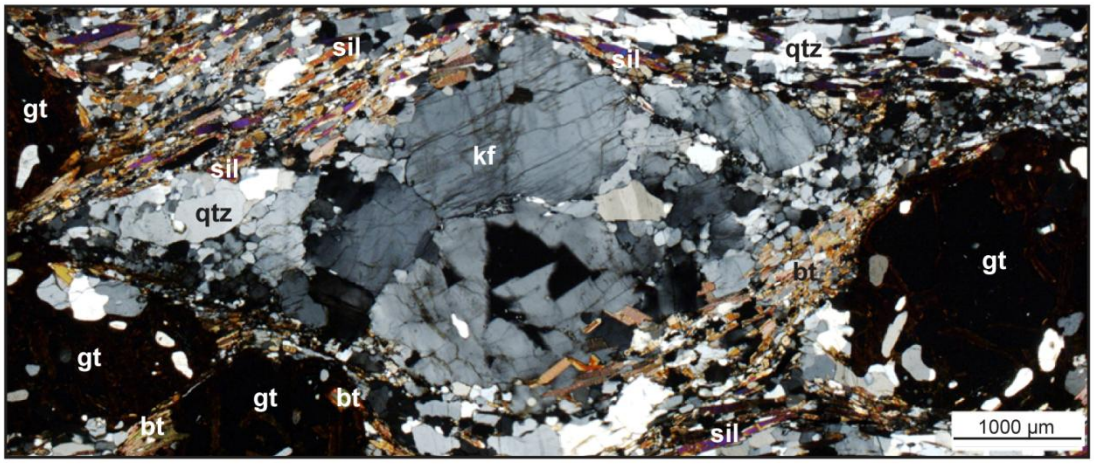
sil
sil
qtz
gt
kf
sil
qtz
gt
bt
gt
gt
bt
bt
sil
1000 µm

c)

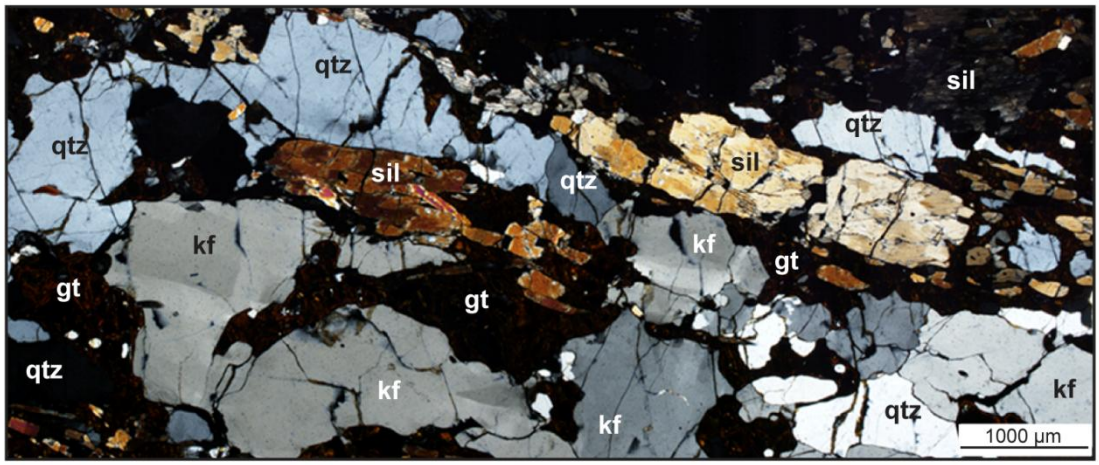
qtz
sil
qtz
qtz
sil
qtz
sil
kf
kf
gt
gt
gt
qtz
kf
kf
qtz
kf
1000 µm

Orthopyroxene has been observed in several mafic complex and amphibolite bodies, as well as metabasite interlayers in the metagraywacke, in the Cat Square terrane, indicating the presence of the orthopyroxene isograd. The appearance of orthopyroxene records the transition from amphibolite to granulite facies metamorphism. The general reaction for this transition is

$$\text{Hornblende} + \text{Quartz} = \text{Orthopyroxene} + \text{Clinopyroxene} + \text{Plagioclase} + H_2O \qquad (3\text{-}2)$$

The trace of the orthopyroxene isograd was based on modal analyses of metabasite samples (Table 2-4) and field observations (Fig 3-6).

Garnet cores in rocks of both the Cat Square and Tugaloo terranes preserve inclusion trails of an earlier foliation (Fig. 3-7). For rocks of the Cat Square terrane, earlier foliation could have been developed during initial metamorphism during the Neoacadian orogeny, or the garnets developed during peak conditions while the dominant S_2 foliation formed. Tugaloo terrane rocks may have had a similar formation history, but inclusion trails oblique to the S_2 foliation may also be an earlier Taconic S_1 foliation in the garnets.

Retrograde metamorphism affected rocks in the study area and appears to have been more pervasive in the eastern portion of the study area based on the abundance of sericite and muscovite. Muscovite laths replace feldspar grains in multiple samples and may pseudomorph sillimanite in a few samples (Figs. 3-8a, b). Pyroxene grains in some mafic complex and amphibolite bodies in the Cat Square terrane have broken down to hornblende, biotite, and opaque grains (Fig. 3-8c). Amphibolite bodies in the Newton window commonly have symplectic intergrowths of plagioclase and epidote on the edges of hornblende grains (Fig. 3-8d). In some samples, this intergrowth is pervasive, having completely replaced the hornblende grains.

Timing of Inner Piedmont Metamorphism

Rocks of the eastern and western Inner Piedmont have recorded metamorphic ages indicative of shared Neoacadian and Alleghanian metamorphic events. U-Pb zircon rim and Ar/Ar ages plotted versus distance from the Brevard fault zone (Fig. 3-9) show that there is no significant

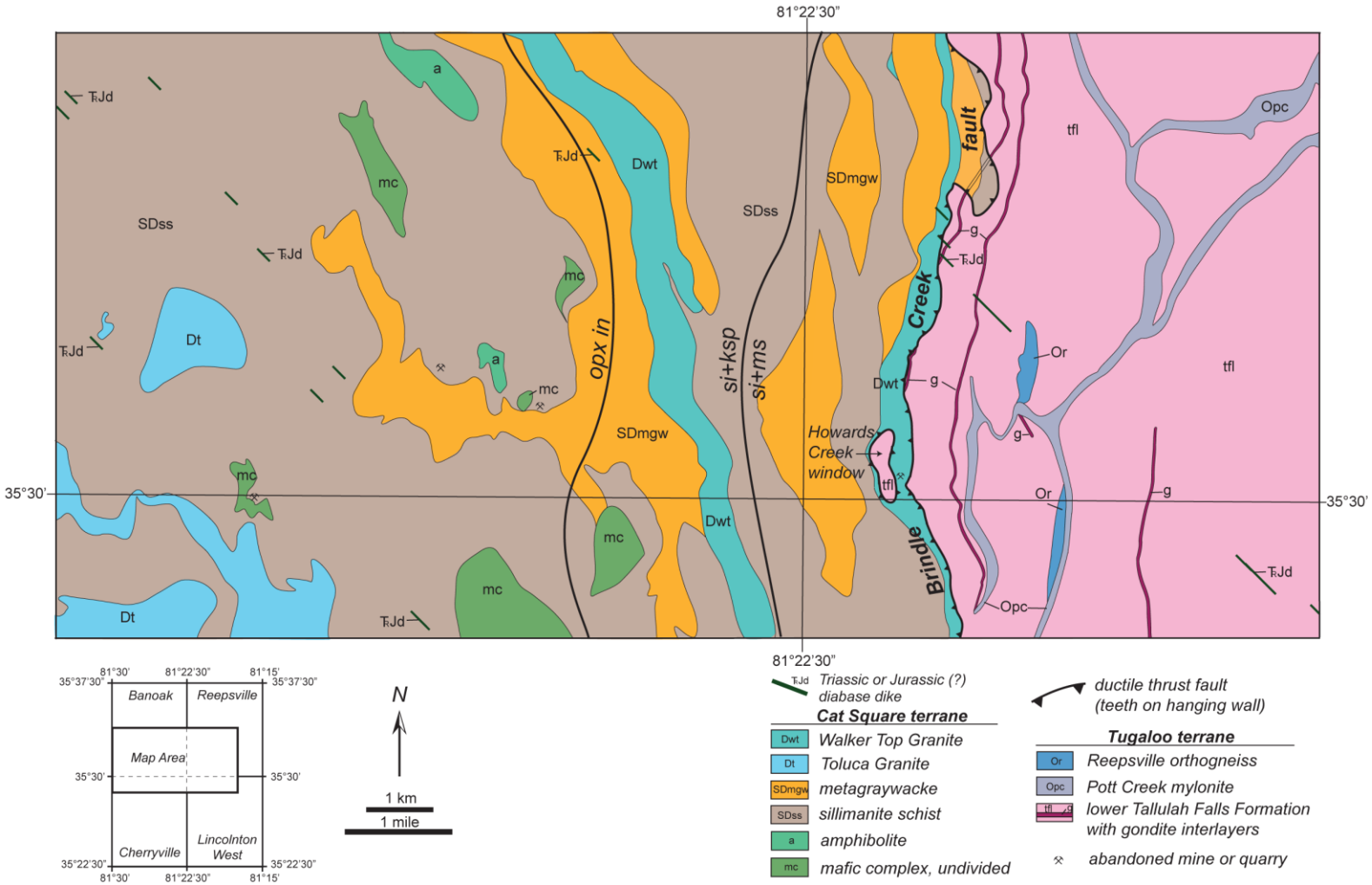

Figure 3-6. Simplified geologic map of portions of the Banoak, Reepsville, Lincolnton West, and Cherryville 7.5-minute quadrangles showing the approximate location of the second sillimanite (si+ksp) and orthopyroxene isograds. Mineral abbreviations: ksp–K-feldspar; ms–muscovite; opx–orthopyroxene; si–sillimanite.

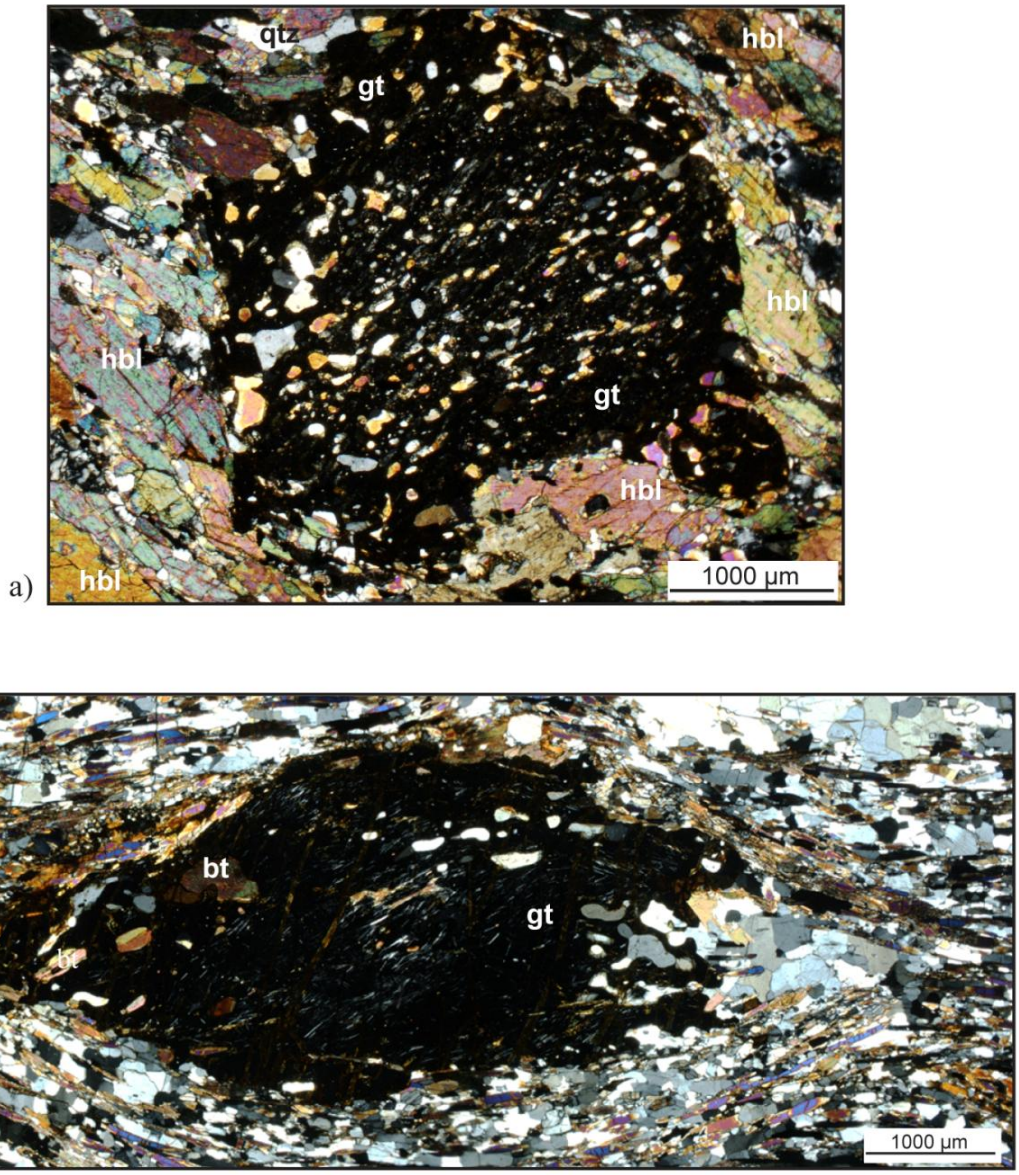

Figure 3-7. Photomicrographs showing garnets with inclusion trails from Cat Square and Tugaloo terrane rock units. a) Photomicrograph of hornblende forming S_1 perpendicular to S_2 foliation in Newton window amphibolite sample Rp-TFA. b) Photomicrograph of Walker Top Granite from sample location LW89, near the Brindle Creek fault. Outcrop located at the end of NC St. Rd. 1192 (Jim Wise Road). Preserved inclusion trails may reflect earlier S_2 foliation prior to garnet growth and deformation associated with the Brindle Creek fault. Mineral abbreviations: bt–biotite; gt–garnet; hbl–hornblende; qtz–quartz.

Figure 3-8. Evidence of retrograde metamorphism in thin sections from samples in the Cat Square and Tugaloo terranes. a) Muscovite lath replacing plagioclase grain in sample LW51. b) Muscovite after prismatic sillimanite grains in sample Rp303. Sample from small creek located between NC St. Rds. 1206 (Ward Road) and 1207 (Perry Jonas Road). c) Hydration of pyroxenes to hornblende and biotite in sample Bk168. Sample collected from a Little Indian Creek feeder stream, south of NC St. Rd. 1113 (Reeps Grove Church Road). d) Symplectic intergrowth of plagioclase and epidote in sample Rp157. Sample collected from Rhodes Mill Creek, east of NC St. Rd. 1214 (Johnson Road). Mineral abbreviations: ap–apatite; bt–biotite; cpx–clinopyroxene; hbl–hornblende; ms–muscovite; op–opaque; pl–plagioclase; qtz–quartz; ser–sericite; sym–symplectite; v–void.

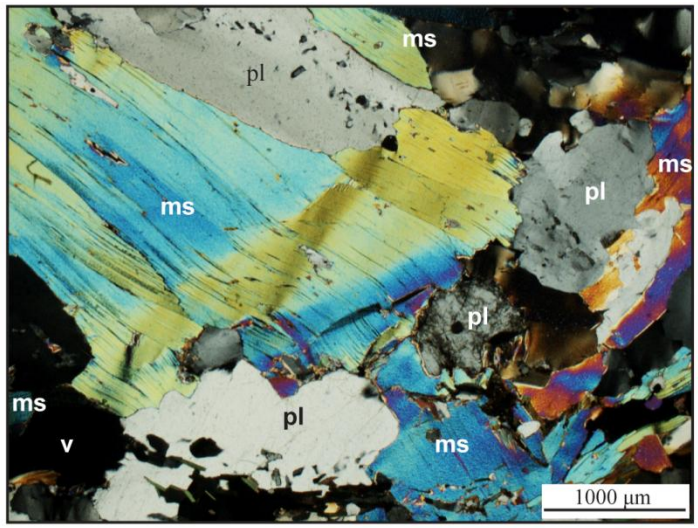
ms
pl
ms
ms
pl
pl
ms
pl
v
ms
1000 µm

a)

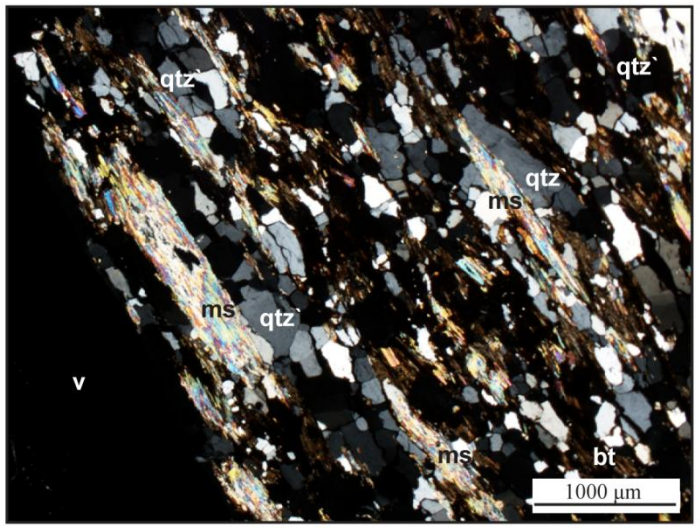
qtz
qtz
qtz
ms
ms
qtz
v
ms
bt
1000 µm

b)

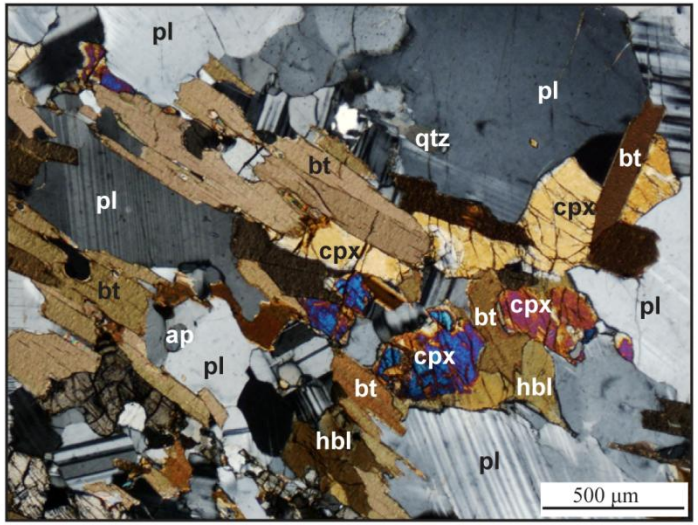
pl
pl
qtz
bt
bt
pl
cpx
cpx
bt
cpx
pl
ap
pl
cpx
bt
hbl
hbl
pl
500 µm

c)

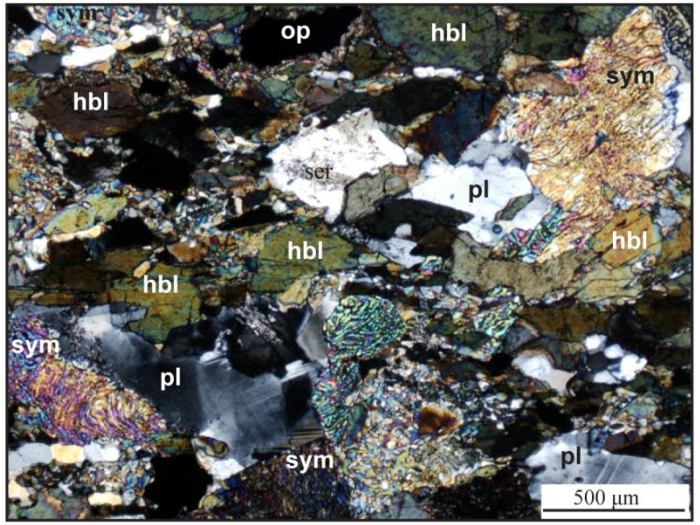
sym
op
hbl
hbl
sym
set
pl
hbl
hbl
hbl
sym
pl
sym
pl
500 µm

d)

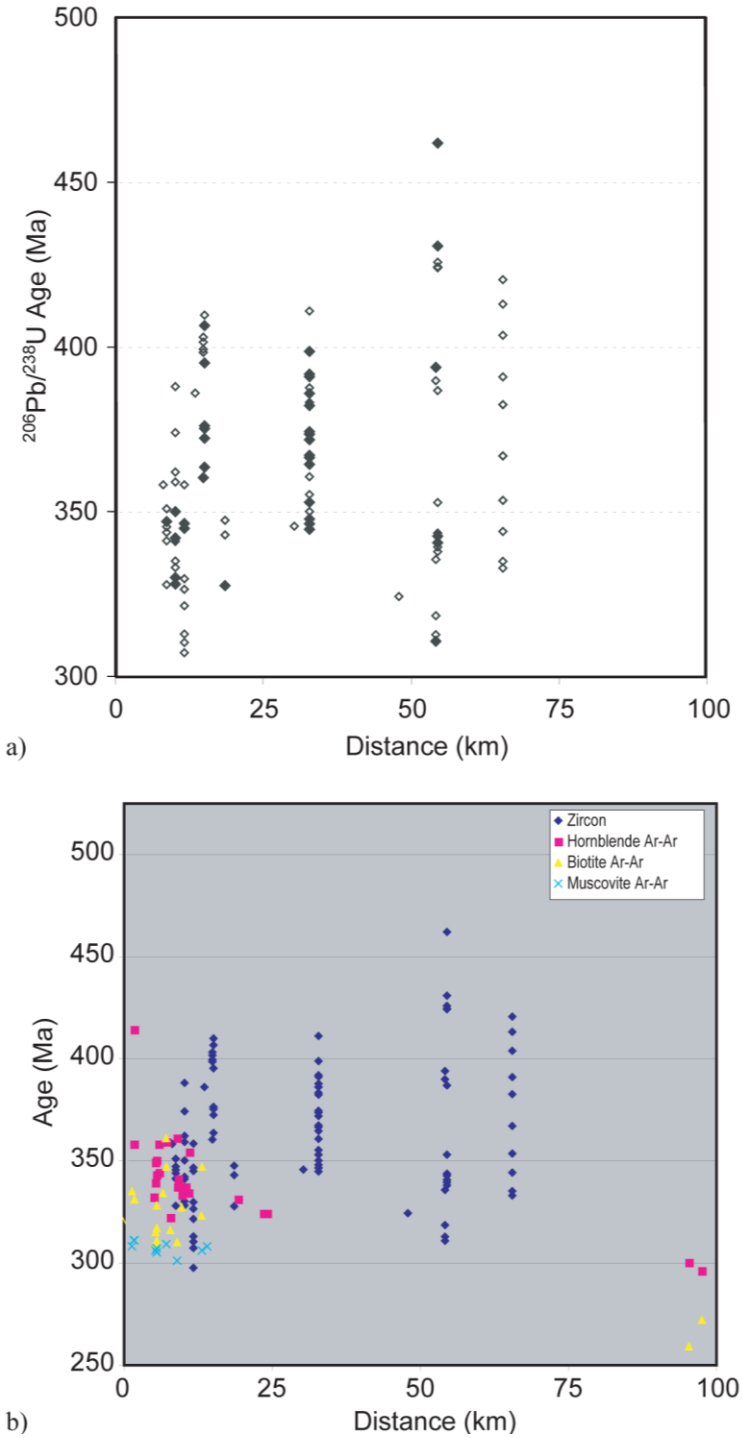

Figure 3-9. Plots of thermochronometer age versus distance from the Brevard fault zone (distance = 0) measured normal to strike of the Brevard fault zone. a) $^{206}Pb/^{238}U$ zircon rim ages from Bream (2003), Merschat et al. (2005a), Gatewood (2007), and Byars et al. (2008a). Solid diamonds indicate ±10% discordance and open diamonds indicate greater ±10% discordance. b) Published Ar-Ar ages from Dallmeyer et al. (1986) and Dallmeyer (1988), and $^{206}Pb/^{238}U$ zircon rim ages. Figure from Merschat (2009).

change in metamorphic ages with increasing distance from fault zone. The majority of metamorphic ages range from 300 to 400 Ma with a few ages between 400 and 450 Ma. The lack of significant amounts of Ordovician ages in the Inner Piedmont greatly contrasts with the eastern Blue Ridge, where a large portion of metamorphic ages are Ordovician (Fig. 3-3). In addition to metamorphic ages, timing of the Neoacadian and Alleghanian orogenies in the Inner Piedmont is further constrained by the development of anatectic melts in the Cat Square terrane (Fig. 2-13).

The western Inner Piedmont and Newton window consist of Tugaloo terrane rocks, similar to those of the eastern Blue Ridge. Although there are no direct lines of evidence for the Taconic orogeny (480-450 Ma) in the western Inner Piedmont as in the eastern Blue Ridge, three samples from the Newton window yielded zircon rim ages corresponding to late Taconic magmatism and metamorphism (Merschat, 2009; this study; Fig. 3-3). Mineralogic evidence for this earlier event is rarely found in Tugaloo terrane rocks in the Inner Piedmont due to overprinting and transposition during peak Neoacadian conditions. Presence of Ordovician-age granites in the western Inner Piedmont, similar to the eastern Blue Ridge, would suggest the occurrence of an earlier event (Ranson et al., 1999; Vinson, 1999; Miller et al., 2000; Mapes, 2002; Bream, 2003; Gatewood, 2007; Fig. 2-13). Neoacadian metamorphism is recorded in zircon rims, monazites, and Ar/Ar ages of the western Inner Piedmont. The gap in timing of metamorphism and pluton emplacement between the Taconic and Neoacadian orogenies may represent post-collisional uplift and cooling of the Tugaloo terrane (Bream, 2003).

Three metamorphic age peaks, ~360, ~345, and 330-325 Ma, delimited from zircon rim, monazite, and Ar/Ar ages, are commonly reported and discussed for the Inner Piedmont (Fig. 3-10). Based on the compilation of U-Pb metamorphic rim ages, there are two older peaks at ~375 Ma and 394 Ma. The three oldest peaks coincide with emplacement ages of anatectic granitoids in the Cat Square terrane (Fig. 2-13). The ~360 Ma peak (Dallmeyer et al., 1986; Dallmeyer, 1989; Dennis and Wright, 1997a, b; Carrigan et al., 2001; Kohn, 2001; Kalbas et al., 2002; Bream, 2003; Merschat et al., 2005a; Gatewood, 2007; Byars et al., 2008a), is the first metamorphic event the Tugaloo, Cat Square, and Carolina terranes have in common, indicating the accretion of the Cat Square and Carolina terranes during the Neoacadian orogeny (Merschat

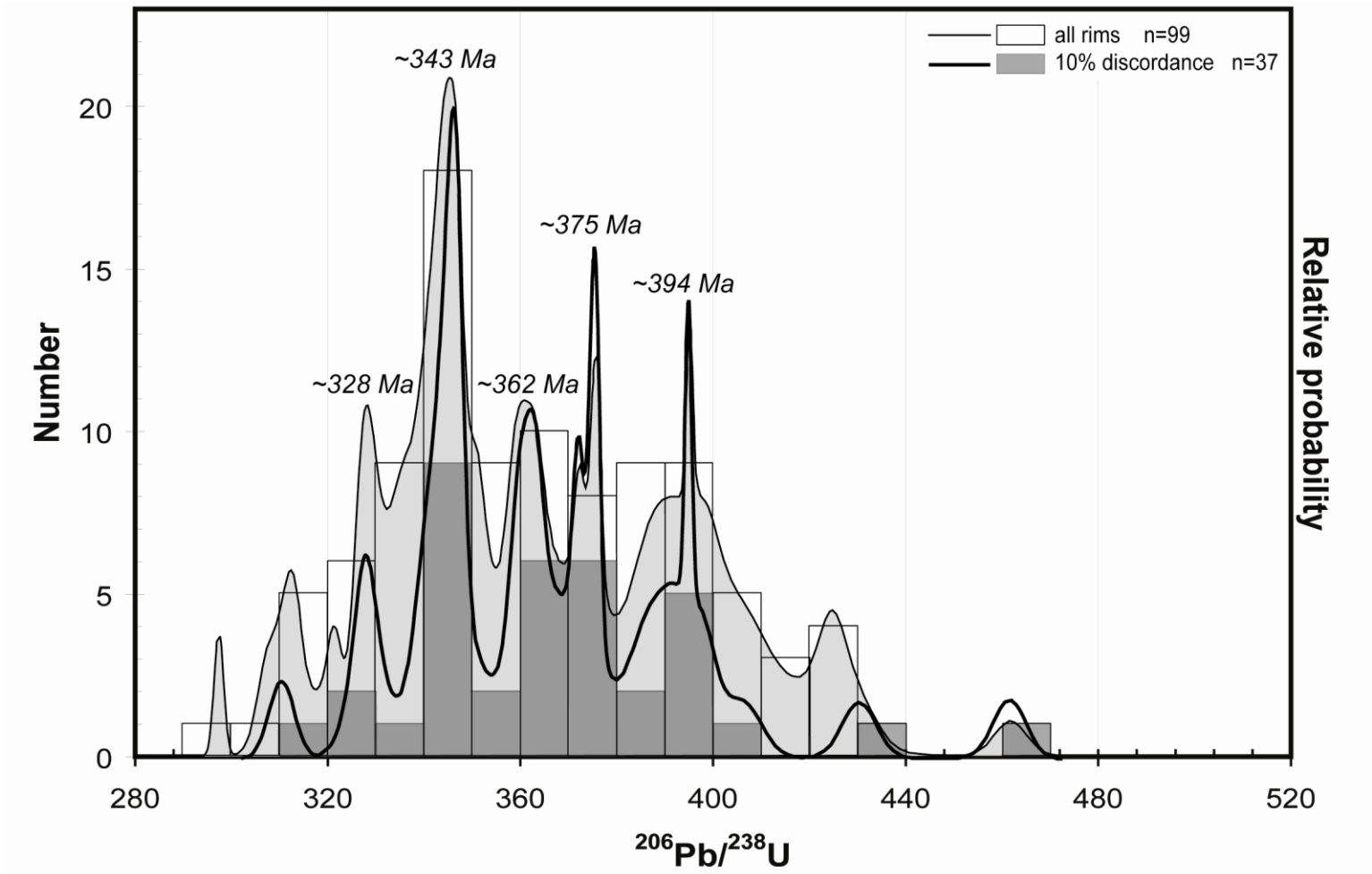

Figure 3-10. Relative probability plot and histogram of ^{204}Pb-corrected ^{206}Pb/^{238}U SHRIMP zircon rim ages. Thicker line and darker histogram bins represent only zircon rim ages that ±10% discordant. Sources of data include Bream (2003), Merschat et al. (2005a), Gatewood (2007), and Byars et al. (2008a). Plots created using Isoplot v. 3.0 (Ludwig, 2003). Figure from Merschat (2009).

and Hatcher, 2007). This timing is speculated to be associated with the initial northwest-directed channel flow of Inner Piedmont and eastern Blue Ridge rocks from movement on the Neoacadian Brevard fault zone and the emplacement of hot, ductile thrust sheets at the beginning of peak Neoacadian metamorphic conditions (Merschat et al., 2005b). After the emplacement of the thrust sheets, the Inner Piedmont remained hot until ~345 Ma (Kish, 1997; Bream 2003; Kalbas, 2003; Merschat et al., 2005b; Byars et al., 2008a), when the terrane began to cool (Bream, 2003). The youngest metamorphic peak, 330-325 Ma, records the youngest thermal event in the southern Appalachians when rocks of the Inner Piedmont were reheated with the initial deformation during the early Alleghanian orogeny (Dennis and Wright 1997a, 1997b; Mirante and Patiño-Douce, 2000; Bream, 2003; Kalbas, 2003; Hatcher and Merschat, 2006). Ductile reactivation occurred along the Brevard fault zone and Central Piedmont suture during this time (Merschat et al., 2005b). The extent of pervasive features formed in the Alleghanian is not as prominent as those associated with the Neoacadian orogeny.

Migmatization

Extensive migmatization has been observed in Inner Piedmont rocks by several studies in the past 40 plus years (Griffin, 1967, 1974; Goldsmith et al., 1988; Hatcher, 1993). More recently, a concentrated zone of super migmatization has been defined within a ~7 km-wide zone west of the Brindle Creek fault in the western Inner Piedmont of North and South Carolina (Giorgis, 1999; Williams, 2000; Bier et al., 2002; Hatcher and Merschat, 2006; Plate 3; Fig. 1-1). A similar occurrence of excessive melting from thrust sheet emplacement is observed beneath the Six Mile thrust sheet in northwestern South Carolina (Griffin, 1969; Hatcher and Merschat, 2006). These “super migmatites” demonstrate that these areas were at or near minimum melt conditions, or conditions were above the wet granite solidus, consistent with high temperature estimates obtained for the Inner Piedmont (Luth et al., 1964; Bream, 2003; Hatcher and Merschat, 2006). The spatial association of super migmatite with large, ductile thrust sheets, specifically the Brindle Creek thrust sheet, is attributed to the emplacement of the thrust sheet while hot, causing crustal thickening and jointly producing intense footwall migmatization (Hatcher, 2002; Merschat and Kalbas, 2002). The migmatitic nature of Cat Square terrane rocks

in the South and Brushy Mountains has been noted by past studies of Goldsmith et al. (1988), Giorgis (1999), Williams (2000), Bier (2001), Kalbas (2003), Merschat (2003), Wilson (2006), and Gatewood (2007).

Constraints for the formation of migmatites have been obtained in the western Inner Piedmont migmatites of North Carolina and Georgia. In the Brushy Mountains, Kalbas (2003) calculated migmatites have a P-T range of 600-700 °C and 3.0-7.7 kbar. Zircon rims in these migmatites record metamorphic peaks at 342 ± 5 and 330 ± 3 Ma may reflect timing of localized melting (Kalbas, 2003). Formation conditions of migmatites in northeast Georgia have been estimated to have occurred at 330 ± 10 Ma during peak thermal granulite facies conditions of 790 ± 50 °C and 8.3 ± 0.5 kbar (Mirante and Patiño-Douce, 2000). Compositions of migmatites show similar alkali contents with melting experiments of 1-4 percent added water from Patiño-Douce and Beard (1995) and Patiño-Douce (1996). Mirante and De La Rosa (2001) concluded from this that high water activities played an important role during melting of the Inner Piedmont core during the Neoacadian, although it may have not been a free phase.

Pressure and Temperature Estimates

Western Inner Piedmont

Previous geothermobarometry studies of the North Carolina western Inner Piedmont have yielded P-T estimates of 3.5-6.5 kbar and 530-690 °C (Davis,1993; Yanagihara, 1994; Hill, 1999; Fig. 3-11a). Hill (1999) documented a prograde sequence of sillimanite after kyanite, indicative of specific conditions of formation: pressure ranging from 5 to 7 kbar where kyanite is produced but sillimanite stability is reached at the temperature at which muscovite is breaking down. Hill (1999) and other studies documented first sillimanite grade assemblages for the western Inner Piedmont. In the northeast Georgia Inner Piedmont, metamorphic conditions have been observed in Tallulah Falls Formation equivalent rocks in the Tugaloo terrane at 640-790 °C and 6-8 kbar (Mirante and Patiño-Douce, 2000; Fig. 3-11a). Mirante and Patiño-Douce (2000) suggested, based on limited samples, that the western Inner Piedmont underwent rapid

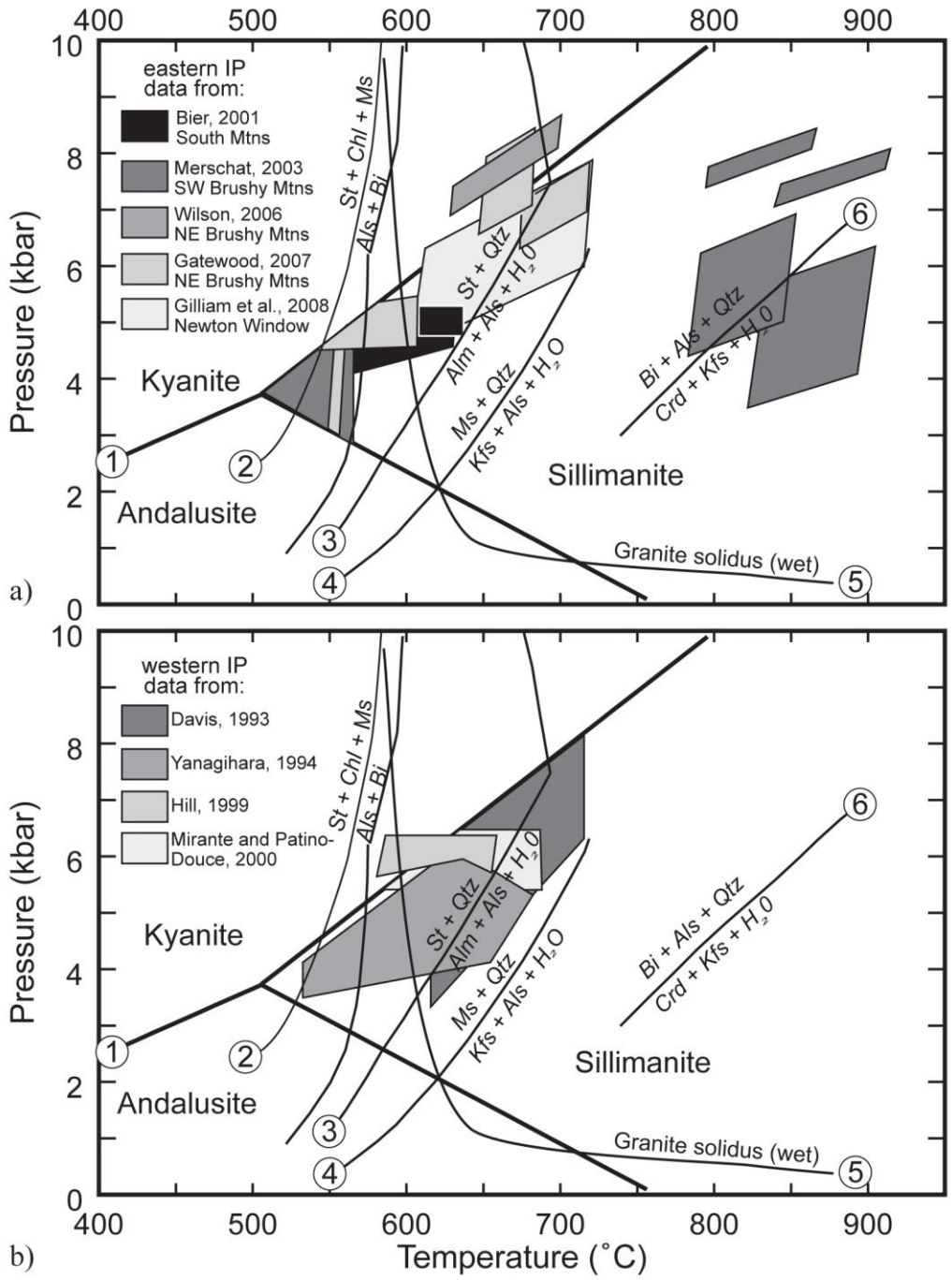

Figure 3-11. Metamorphic P-T estimates plotted for recent Inner Piedmont studies. a) P-T estimates for western Inner Piedmont. b) P-T estimates for eastern Inner Piedmont. Univariant curves are from: (1) Holdaway (1971); (2) Albee (1965); (3) Pigage and Greenwood (1982); Chatterjee and Johannes (1974); (5) Luth et al. (1964); and (6) Holdaway and Lee (1977). Mineral abbreviations: St–staurolite, Chl–chlorite, Ms–muscovite, Als–aluminum silicate, Bi–biotite, Qtz–quartz, Alm–almandine, Kfs–potassium feldspar, Crd–cordierite. Figure modified from Gatewood (2007).

exhumation under very dry conditions, based on the lack of any retrograde metamorphic assemblages and minimum P-T estimates from Georgia. This is not likely the case in North Carolina, because retrograde assemblages are present.

Eastern Inner Piedmont

Metamorphic conditions reported in the eastern Inner Piedmont are similar to or higher than those of the western Inner Piedmont, with second sillimanite grade and locally granulite facies conditions documented in the Cat Square terrane in the South and Brushy Mountains (Giorgis, 1999; Bier, 2001; Merschat, 2003). P-T estimates range from 3-8.7 kbar and 500-840 °C (Bier, 2001; Bier et al., 2002; Merschat, 2003; Wilson, 2006; Gatewood, 2007; Fig. 3-11b). Zircon saturation temperatures for Inner Piedmont plutons of 730-910 °C record anatectic magma generation at the climax of the Neoacadian orogeny (Mapes, 2002; Miller et al., 2003). Gilliam et al. (2008) reported metamorphic conditions from Tallulah Falls Formation in the Newton window at 610-725 °C and 6-7.5 kbar, recording burial and exhumation conditions.

Summary

The southern Appalachian Inner Piedmont records a single, protracted, Barrovian-style prograde metamorphic path during the Neoacadian and Alleghanian orogenies. Evidence for Taconic deformation and metamorphism in the Tugaloo terrane, if present prior to the Neoacadian, was mostly obliterated. The core of the Inner Piedmont reached first sillimanite grade conditions with a zone of second sillimanite and locally granulite facies conditions occurring mostly in the Cat Square terrane. Recorded occurrences of second sillimanite conditions are in the southeastern Brushy Mountains, the south central South Mountains, and west of the Newton window in the Banoak 7.5-minute quadrangle in North Carolina and granulite facies conditions in northeast Georgia, the South Mountains, and west of the Newton window. Elevated pressures and temperatures from crustal thickening and the emplacement of hot thrust sheets produced “super” migmatites in the Tugaloo terrane and extensive migmatization in the Cat Square. The metamorphic conditions observed in the Inner Piedmont

required burial depths of 15-20 km during the Neoacadian orogeny (Merschat and Hatcher, 2007).

CHAPTER 4

STRUCTURES OF THE WESTERN NEWTON WINDOW AND EASTERN CAT SQUARE TERRANE: THEIR ROLE IN INTERPRETATION OF INNER PIEDMONT STRUCTURES

Introduction

Geologic structures are an integral part of mountain chains that allow geologists to interpret their complex orogenic histories. The Appalachian Mountains are a perfect example of this, having formed from the amalgamation of multiple terranes over several hundred million years. Structural and radioactive elements, such as reactivated faults, superposed folds, and zircon rims, act as recorders over time, preserving polyphase deformation from multiple orogenic events. Interpretation of these structures through detailed geologic mapping of 7.5-minute quadrangles and individual outcrops, where multiple generations of folds can be observed, provides a greater understanding of the orogenic history of regions.

At least six distinct deformation events, related to the three mid-Paleozoic orogenies, have been identified throughout the Blue Ridge and Inner Piedmont of the southern Appalachians (Table 4-1) (Hatcher and Butler, 1979; Hopson and Hatcher, 1988; Davis, 1993; Hopson, 1994; Yanagihara, 1994; Bream, 1999). Four of the six events, referred to as D_1-D_4, formed under moderate- to high-temperature ductile conditions. The last two preserved events, D_5 and D_6, formed under moderate- to low-temperature conditions during periods of brittle extension. The structural elements of this study will be discussed within the framework of these six deformation events.

The Inner Piedmont is a migmatitic, polydeformed composite terrane consisting of a gently dipping stack of southwest-directed ductile Type-F thrust sheets (Fig. 1-1) (Griffin, 1969, 1971, 1974; Merschat et al., 2005b; Merschat and Hatcher, 2007). The Brindle Creek thrust sheet, emplaced by the Brindle Creek fault, is the uppermost thrust sheet in the Inner Piedmont containing the plutons and deep-water metasedimentary rocks of the Cat Square terrane. The Brindle Creek fault is a low-angle, east-dipping, southwest-directed thrust in the South and

Table 4-1.Summary and relative timing of deformation events in the northern Inner Piedmont, North Carolina.*

DEFORMATION EVENTS			STRUCTURES			METAMORPHIC CONDITIONS	REGIONAL EVENTS	OROGENY & TIMING
			FABRICS	FOLDS	FAULTS			
	D_1	D_{1wIP}	S_1 local foliation preserved in boudins	F_{1wIP}: intrafolial, rootless folds; folds preserved in boudins; map-scale folds in TCFZ footwall	TCFZ emplacement	moderate pressure and temperature	arc accretion to Laurentian margin and deposition of western IP Ordovician bimodal volcanics	Taconian orogeny 480-450 Ma
		D_{1eIP}	S_1 regional axial planar foliation foliation	F_{1eIP}: intrafolial and rootless folds; folds preserved in boudins; refolded recumbent, and isoclinal folds	initial development of the CPS	high pressure, upper amphibolite, kyanite-grade; above minimum melt conditions	initial subduction of Cat Square terrane sediments beneath Carolina terrane	Acadian orogeny intrusion of ~407 Ma Walker Top Gneiss in eIP
	D_2		S_2: penetrative foliation; L_2: mineral lineation	F_2: reclined, tight to isoclinal, and recumbent folds; meso- and macroscale SW-vergent passive flow sheath folds	emplacement of ductile IP thrust sheets of BCFZ, TCFZ, MSFZ; early movement and deflection along Neoacadian BFZ	high temperature, upper amphibolite (granulite?) facies; sillimanite I and II grade; first shared thermal event between eIP and wIP	transpressional accretion of eastern IP and Carolina terrane; SW-directed ductile extrusion and crustal flow of IP	Neoacadian orogeny 360-340 Ma
	D_3		S_3: rare mesoscopic foliation, subparallel to S_2	F_3: folding of BCFZ; reclined, open to tight, NW-vergent folds	continued movement along ductile fault zones; further SW-deflection of IP thrust sheets	high temperature, lower pressure conditions; sillimanite I grade	continued emplacement of eastern IP and Carolina terrane; uplift, unroofing, and cooling of IP	Late Neoacadian orogeny
	D_4		dextral S-C and shear-related fabrics in MSFZ, TCFZ, BCFZ, BFZ, and CPS	F_4: Inclined to upright, tight to closed, NW-SE trending, SW-vergent folds	ductile reactivation of BFZ; dextral oblique-slip motion on MSFZ and BCFZ in northeastern IP	moderate to low pressure and temperature brittle conditions	emplacement of composite Blue Ridge-Piedmont type C thrust sheet; regional dextral strike-slip motion along large faults	Alleghanian orogeny 330-300 Ma
	D_5		Joints	F_5: regional open, broad, trend NE & NW, formation of Newton antiform	brittle reactivation and dextral strike-slip motion along BFZ	low pressure and temperature brittle conditions	regional uplift, unroofing, and cooling followed by rifting	late Alleghanian uplift; Mesozoic extension
	D_6		Joints	F_6: regional broad, open folds, trend NE	Meso- and macroscale normal faults	low pressure and temperature brittle conditions	continued rifting and uplift	Cenozoic uplift

*Modified from Davis, 1993; Yanagihara, 1994; Bream, 1999; Giorgis, 1999; Hill, 1999; Williams, 2000; Bier, 2001; Kalbas, 2003; Merschat, 2003; Merschat et al., 2005a; and Gatewood, 2007. BCFZ=Brindle Creek fault zone; BFZ=Brevard fault zone; CPS=Central Piedmont suture; MSFZ=Mill Spring fault zone; TCFZ=Tumblebug Creek fault zone.

Brushy Mountains and moderate to steeply west-dipping, north-to-northwest-directed thrust framing the Newton window in North Carolina. The western trace of the Brindle Creek fault extends further southwest across South Carolina, and into Georgia, and possibly into Alabama where it becomes a steeply dipping dextral strike-slip fault (Merschat et al., 2008; Davis, 2009; Fig. 1-4). The Brindle Creek fault contains ~1 km of mylonite in the Brushy Mountains (Gatewood, 2007); it is recognized by the truncation of Cat Square terrane metasedimentary units and Walker Top Granite against Tugaloo terrane rocks in the western Inner Piedmont and Newton window. The Newton window, located in the eastern Cat Square terrane, was originally mapped as a broad northeast-southwest trending, doubly plunging antiform by Goldsmith et al. (1988). Rocks in the window dip moderately to steeply west beneath Cat Square terrane rocks along the west-central boundary (Plate 1); and along the east-central boundary, dip to the east toward the Kings Mountain belt and Central Piedmont suture.

Deformation Events

D_1 Deformation

D_1 features are mainly limited to Blue Ridge terranes deformed during the Taconic orogeny (480 to 450 Ma) (Merschat et al., 2005b). Evidence for a D_1 event in the western Inner Piedmont is not as abundant due to the transposition of earlier fabrics during the Neoacadian orogeny. Previous foliations may be locally preserved in amphibolite boudins and as inclusion trails in garnets. Occurrence of Ordovician plutons in the western Inner Piedmont, such as the Henderson Gneiss, Caesar's Head Granite, and Dysartsville Tonalite (Fig. 2-13), is also indicative of its participation in the Taconic orogeny.

Tugaloo terrane rocks in the Newton window have several features that record Taconic deformation. Amphibolite boudins and garnet inclusion trails with an S_1 foliation occur in the study area (Figs. 2-5a, 3-7). Ordovician-age overgrowths of Pott Creek mylonite and Reepsville orthogneiss zircons provide evidence that these rocks were affected by the Taconian thermal event. The Pott Creek mylonite has an anastomosing outcrop pattern, likely from post-emplacement deformation, with a concordant U-Pb SHRIMP age of 446.7 ± 3.1 Ma. The

Reepsville orthogneiss has a U-Pb SHRIMP age of 426.4 ± 6.1 Ma and occurs as two isolated bodies adjacent to the Pott Creek mylonite, near the Brindle Creek fault (Plate 1; Fig. 4-1).

D_2 Deformation

The most penetrative and pervasive fabrics in the southern Appalachians were produced during the D_2 event of the Neoacadian orogeny (360-340 Ma) (Table 4-1; Davis, 1993; Giorgis, 1999; Merschat et al., 2005b). Dominant structural elements, S_2 foliation, L_2 mineral lineation, and F_2 folds formed as a result of the collision and subduction of the Inner Piedmont beneath the Carolina superterrane, and the initial movement of the Brevard fault zone and other Inner Piedmont faults (Merschat et al., 2005b). These structural elements, as well as shear sense indicators, form an arcuate pattern across the Inner Piedmont, changing orientation from north-south in the eastern Inner Piedmont, to east-west in the central Inner Piedmont, to southwest-northeast in the western Inner Piedmont as rocks were buttressed and deflected along the Brevard fault zone (Goldsmith, 1981; Merschat et al., 2005b; Hatcher and Merschat, 2006). Merschat et al. (2005b) and Hatcher and Merschat (2006) proposed this pattern represents an exhumed, tectonically forced orogenic channel with southwest-directed flow buttressed against the Brevard fault zone (see below).

Foliation

Over 1,000 measurements of S_2 foliation were collected in portions of the Banoak, Reepsville, Lincolnton West, and Cherryville 7.5-minute quadrangles (Plates 1, 2; Appendix 1). Foliation is formed by the planar alignment of high-temperature minerals including sillimanite, biotite, hornblende, feldspars, and pyroxenes. S_2 foliations in the study area are dominantly north-south (eastern half) to northwest-southeast (western half) striking and moderate to gently dipping to the west with a mean foliation orientation of 172°, 22° W. Compositional and migmatitic layering parallel S_2 foliation, indicative of extensive transposition during the Neoacadian orogeny. The presence of S_2 in the ~378 Ma Toluca Granite (Mapes, 2002), ~366 Ma Vale charnockite, and ~356 Ma Walker Top Granite suggests formation of S_2 syn- to post-emplacement of granites.

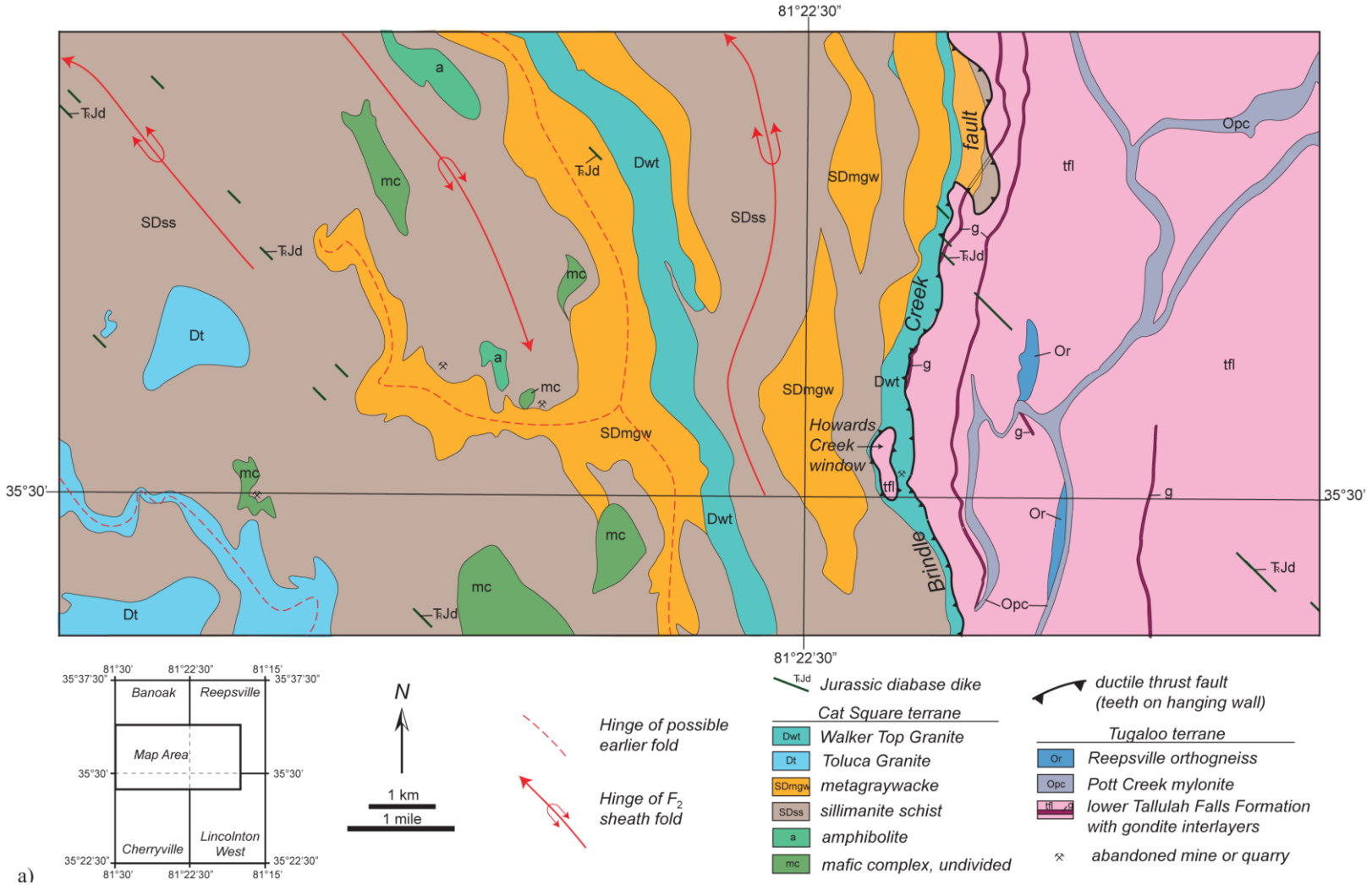

a)

Figure 4-1. Simplified geologic map of the study area in portions of the Banoak, Reepsville, Lincolnton West, and Cherryville 7.5-minute quadrangles illustrating major rocks units, faults, and map-scale sheath folds.

Form lines extracted from S_2 foliations show the study area consists of three domains (Fig. 4-2). Domain I consists of dominantly northwest-southeast striking foliation (mean S_2 is 152°, 17° W) (Fig. 4-3). The north-south striking S_2 in domain II, in the east-central portion of the study area, shows no significant change in orientation across the Brindle Creek fault (mean S_2 is 182°, 32° W). Domain III data is not as consistently homogeneous as the previous two, but has a general northeast-southwest trend (mean S_2 is 195°, 26° W). Domains I, II, and all domains combined (I-III) show the study area is folded with a β-axis non- to subhorizontally plunging to the south-southeast (Fig. 4-3). Domain III shows the opposite with a shallowly north-plunging fold. The north-plunging fold of Newton window data may be the result of the doubly plunging Newton antiform.

Lineation

L_2 mineral lineation is defined by quartz and feldspar(s), micas, sillimanite, and hornblende grains in the plane of S_2 foliation (Fig. 2-6c). L_2 dominantly trends N to N24°W and plunges 5-30° with a mean orientation of 51°, 325°, although some lineations are oppositely trending to the south-southeast (Fig. 4-4). The parallel alignment of L_2 with F_2 fold axial orientations (Fig. 4-4), S-C fabrics, sheared porphyroclasts and porphyroblasts, and map-scale sheath fold axes suggest synchronous deformation. The preferred mineral orientation of L_2 has been interpreted as a mineral stretching lineation based on their alignment with shear-sense indicators (Davis, 1993; Giorgis, 1999; Merschat et al., 2005b; Hatcher and Merschat, 2006).

Folds

F_2 folding related to Neoacadian deformation is represented by recumbent to reclined, tight-to-isoclinal and recumbent folds (Fig. 4-5a). F_2 fold axial orientations are parallel to L_2 mineral lineations (Fig. 4-4). S_2 parallel to subparallel to fold axes of F_2 suggests they are coeval. As with mineral lineations, fold axial orientations trend both north and south; most in Domain I trend south and to the north in Domain II (Fig. 4-4). No fold axes were measured in Domain III because of limited observation.

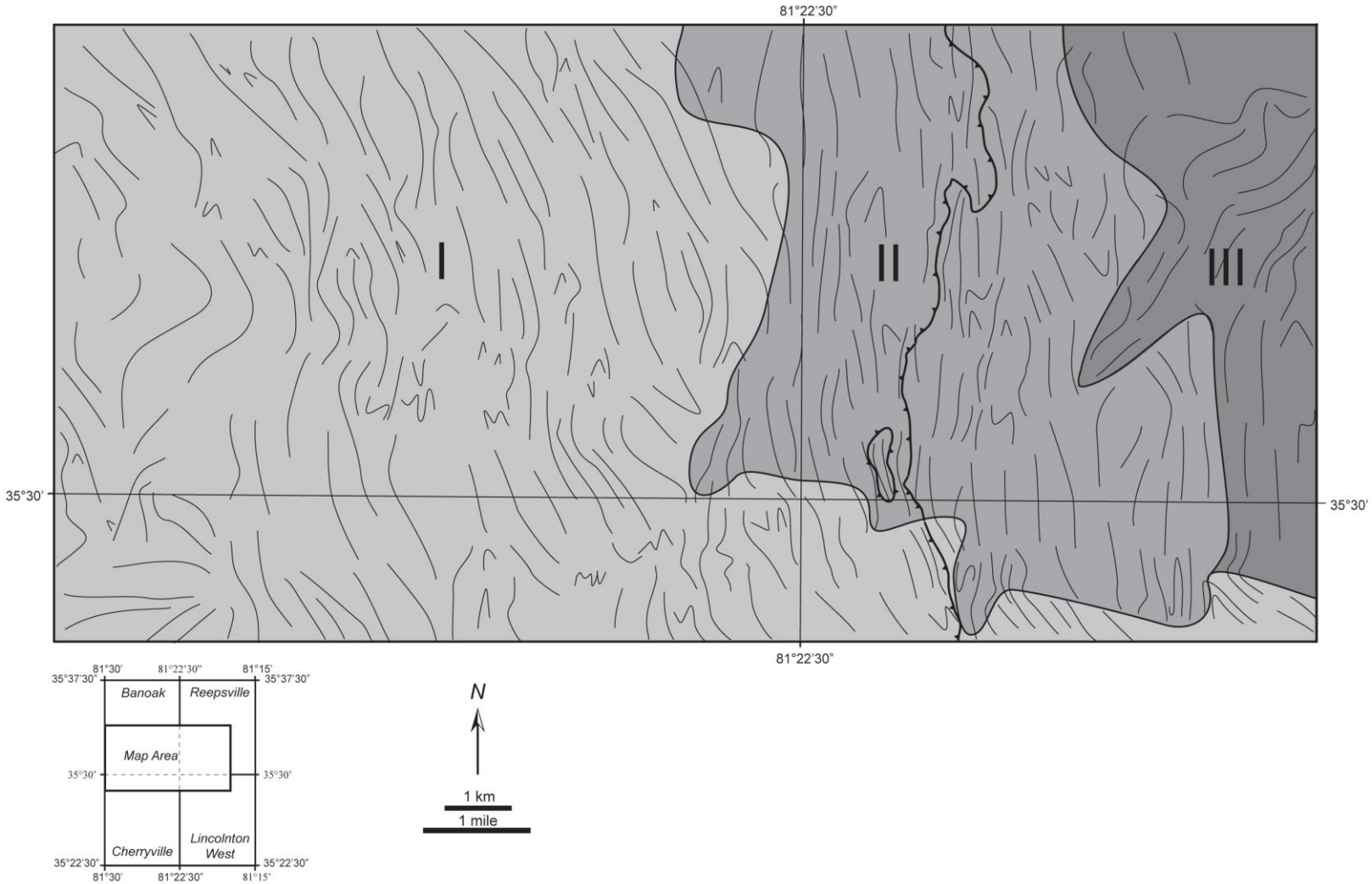

Figure 4-2. S_2 foliation form-line and domain map of the study area in portions of the Banoak, Reepsville, Lincolnton West, and Cherryville 7.5-minute quadrangles.

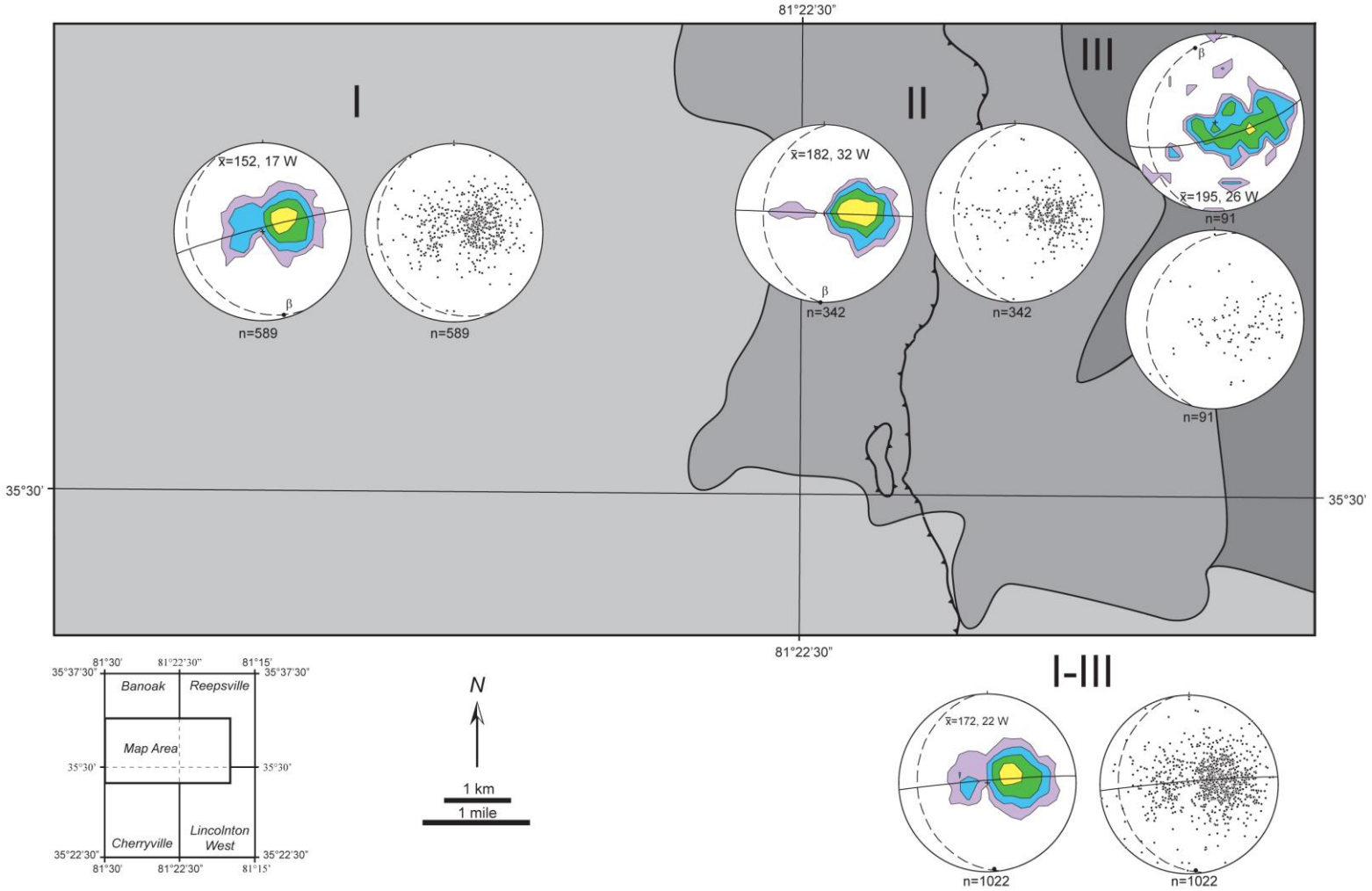

Figure 4-3. Scatter plots and equal-area, lower hemisphere contoured diagrams of poles to S_2 foliation in portions of the Banoak, Reepsville, Lincolnton West, and Cherryville 7.5-minute quadrangles. Mean orientations of foliation (dashed line), beta axis, and fold axial surfaces (solid line) are shown for each domain and all domains combined.

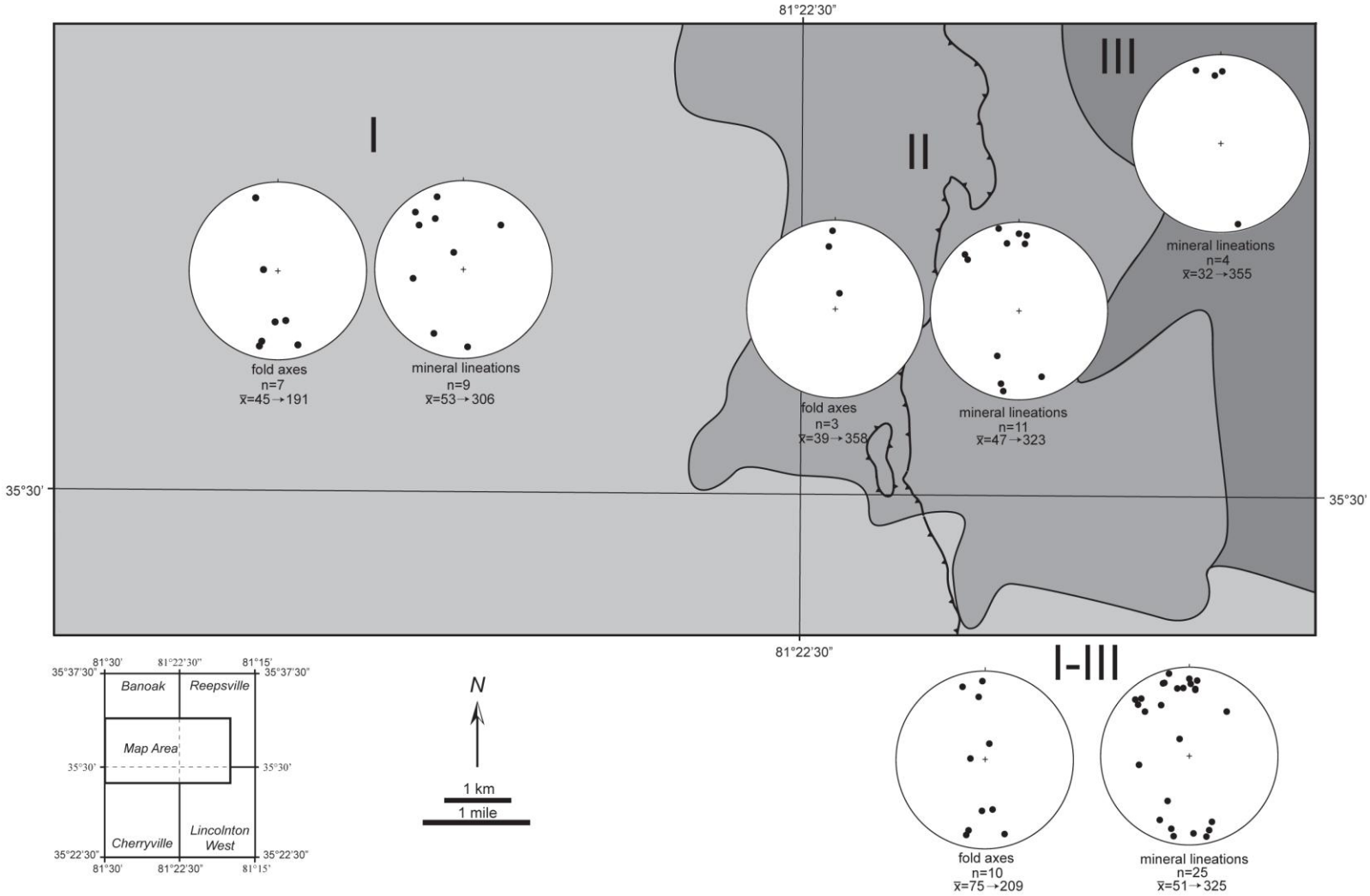

Figure 4-4. Scatter plots of poles to L_2 mineral lineation and F_2 fold axial orientations in portions of the Banoak, Reepsville, Lincolnton West, and Cherryville 7.5-minute quadrangles. Mean vector indicated for each below the respective diagram.

a)

b)

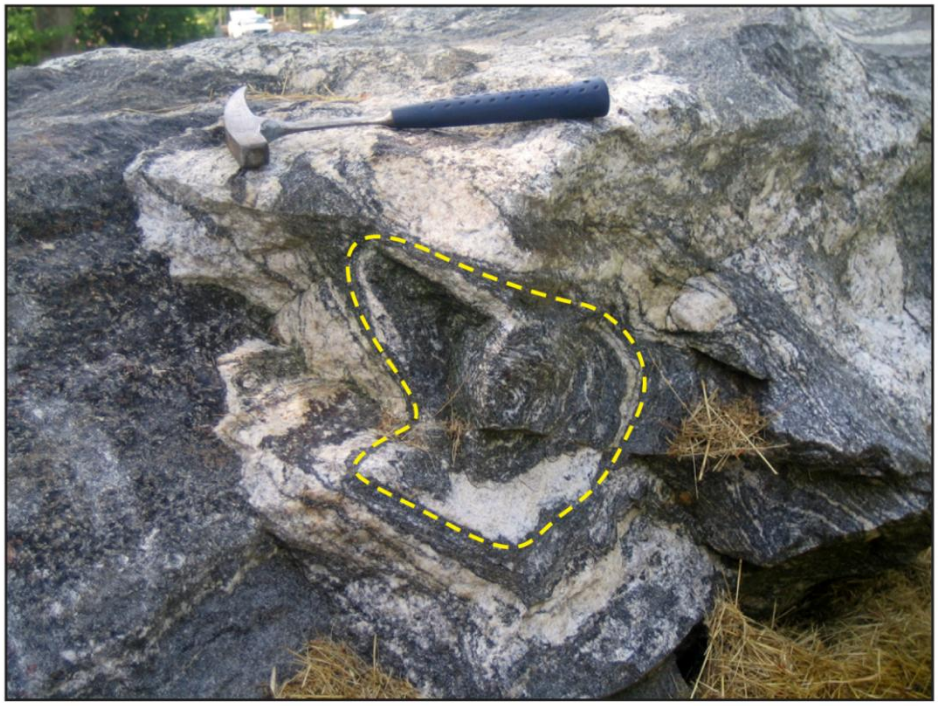

Figure 4-5. F_2 folds. a) Recumbent fold in lower Tallulah Falls Formation metagraywacke. Outcrop located in a tributary of Tanyard Creek, north of NC St. Rd. 1113 (Reepsville Road) (station Rp40). Hammer for scale. b) Possible sheath fold in migmatitic amphibolite boulder from Cat Square terrane mafic complex. Boulder located on the south side of NC Hwy 27 from station Ch2, west of NC St. Rd. 1147 (Tower Road). Hammer for scale.

Meso-scale sheath folds were not recognized at outcrop scale, except for one potential fold in an out-of-place boulder of Cat Square terrane migmatitic amphibolite (Fig. 4-5b). Other Inner Piedmont workers have identified meso-scale sheath and noncylindrical folds (Davis, 1993; Bream, 1999; Hill, 1999; Wilson, 2006). Map patterns in the study area support the existence of map-scale sheath folds when compiled with surrounding geologic maps (see below). There is also possible evidence for an earlier folding prior to the development of the map-scale sheat folds based on map patterns (Fig. 4-1).

Faults

Ductile Neoacadian faulting during the D_2 event emplaced multiple thrust sheets, including the Tumblebug Creek, Walhalla, Six Mile-Sugarloaf Mountain, Mill Spring, and Marion thrust sheets in the western Inner Piedmont, and the Brindle Creek thrust sheet of the eastern Inner Piedmont. The western exposure of the Brindle Creek fault truncates footwall synclines preserving Middle Ordovician Poor Mountain rocks (Plate 3) (Giorgis, 1999; Bier, 2001; Merschat et al., 2005b). The eastern exposure of the Brindle Creek fault, outlining the Newton window, traces north-south through the Reepsville and Lincolnton West 7.5-minute quadrangles (Plate 1; Fig. 4-1). Consistent foliation orientations on both sides of the Brindle Creek fault indicate the thrust sheet was emplaced syn- to late-dominant S_2 foliation formation and peak metamorphic conditions. Outcrops of the Brindle Creek fault contain strongly mylonitic Walker Top Granite, where feldspar megacrysts are sheared out to small porphyroclasts or into quartz ribbons (Fig. 4-6a). Shear-sense indicators near the Brindle Creek fault, such as rotated porphyroclasts and S-C fabrics, indicate a top-to-the-north transport for the Cat Square terrane in the study area (Fig. 4-6b).

D_3 and D_4 Deformation

Ductile D_3 and D_4 events occurred post-peak Neoacadian metamorphism with high- to moderate-temperatures transitioning from late-stage Neoacadian to the Alleghanian orogeny (330 to 300 Ma) (Table 4-1). D_3 records continued movement on and folding of Inner Piedmont faults. Local, mesoscale thrust faults observed in the study area, with minor amounts of

a)

b)

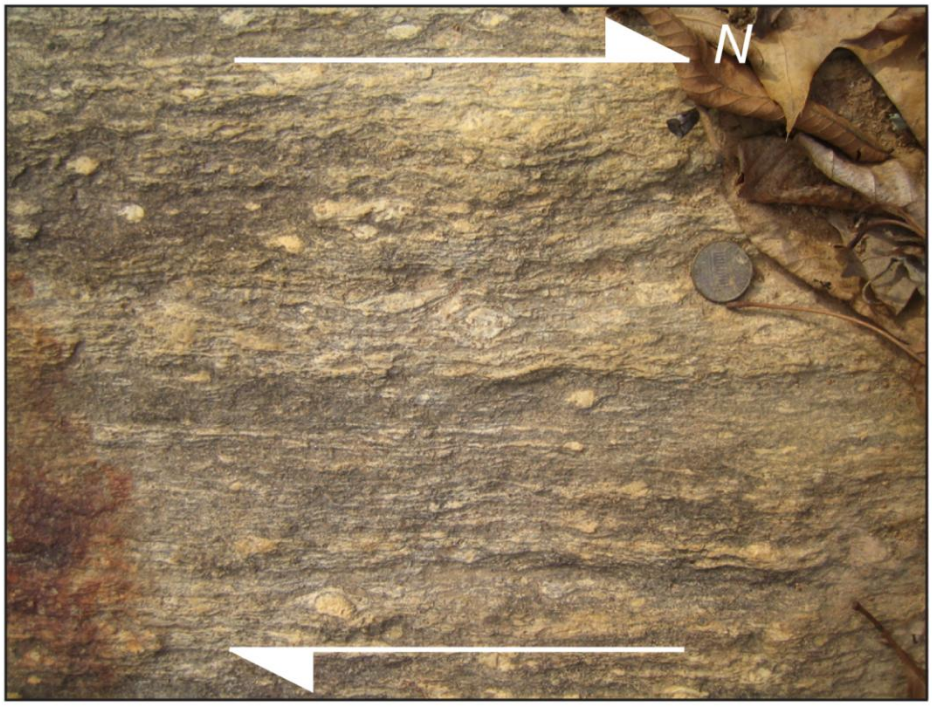

Figure 4-6. Brindle Creek fault shear zone exposure in Howards Creek where the Brindle Creek fault frames a smaller window to the east of the main exposure of the fault, west of NC St. Rd. 1193 (Wise Road). a) Mylonitic Walker Top Granite float showing bands of feldspar and quartz from intense shearing. Quarter for scale. b) Outcrop of mylonitic Walker Top Granite with feldspar porphyroclasts indicating top-to-the-north shear sense at station Rp243. Penny for scale.

displacement of S_2 compositional layering, are attributed to D_3 (Fig. 4-7a). The outcrop pattern of the Brindle Creek fault framing the Newton window, and the occurrence of the smaller Howards Creek window west of the main fault exposure, suggest the fault underwent F_3 reclined, open-to-tight folding (Fig. 4-1). Folding and doming of the Brindle Creek fault has also been noted in the Brushy Mountains (Wilson, 2006) and South Mountains (Giorgis, 1999). Few meso-scale F_3 folds were observed in outcrop in the study area (Fig. 4-7b, c). A rare S_3 foliation, mostly observed as a weak axial planar foliation, is parallel to subparallel to S_2 foliation (Merschat et al., 2005b). In the Brushy Mountains, S_3 is well developed along the strongly mylonitic Brindle Creek fault (Merschat et al., 2005b).

Reactivation of the Brevard fault zone and segments of the central Piedmont suture occurred during D_4. Few inclined to upright, tight to closed F_4 folds were observed in the study area (Fig. 4-8). Gatewood (2007) indicated dextral oblique-slip motion occurred on the Brindle Creek fault during D_4, leading to the development of dextral S-C and shear-related fabrics.

D_5 and D_6 Deformation

D_5 and D_6 brittle deformation events are related to Mesozoic extension associated with the breakup of the supercontinent Pangea and continued Cenozoic uplift, respectively (Table 4-1; Merschat et al., 2005b). Common D_5 and D_6 features seen in the Inner Piedmont are brittle movements on faults associated with the Brevard fault zone, macro- and meso-scale normal faults, regional open folds, Triassic-Jurassic diabase dikes, siliceous cataclasite, and joints. Alleghanian faults, such as the reactivation of the Brevard fault zone with dextral strike-slip motion (i.e., Rosman fault), record late, brittle deformation. Macro-scale normal faults, activated by Mesozoic extension, produced Triassic-Jurassic basins in the Appalachians. Meso-scale normal faults, cutting the dominant S_2 foliation, occur in the study area and are mostly observed in saprolite outcrops of Tugaloo terrane rocks in the Newton window (Fig. 4-9). The normal faults in this outcrop are filled with a gray material that appears to be characteristic of pseudotachylyte. A possible reservoir, or area where the friction melt collected, occurs near the

Figure 4-7. D_3 structural features in the study area. a) Mesoscale thrust faults with minor amounts of displacement in a metabasite. Arrows indicate direction of displacement. Outcrop located in Glenn Creek, north of NC St. Rd. 1135 (Ed Willis Road) at station Ch144. Hammer for scale. b) Saprolite outcrop with reclined, tight F_3 fold in lower Tallulah Falls Formation metagraywacke. Outcrop located at station Rp72, on the banks of the South Fork of the Catawba River, east of NC St. Rd. (Killian Road). Hammer for scale. c) Reclined, tight to open F_3 folds in a schistose metabasite interlayer in the Cat Square terrane metagraywacke. Outcrop located in Little Indian Creek, east of the intersection of NC St. Rds. 1128 (John Beam Road) and 1129 (Beam Lumber Road) (station Bk38). Field book for scale.

a)

b)

Figure 4-8. F_4 folds. a) Upright, open fold of Cat Square terrane metagraywacke saprolite. Outcrop located in tributary to Little Indian Creek, south of NC St. Rd. 1122 (Lingerfelt Road). Hammer for scale. b) Inclined, closed fold of Cat Square terrane metagraywacke saprolite. Outcrop located in tributary to Howards Creek, east of NC St. Rd. 1194 (Howards Creek Mill Road). Outcrop approximately 3 meters high.

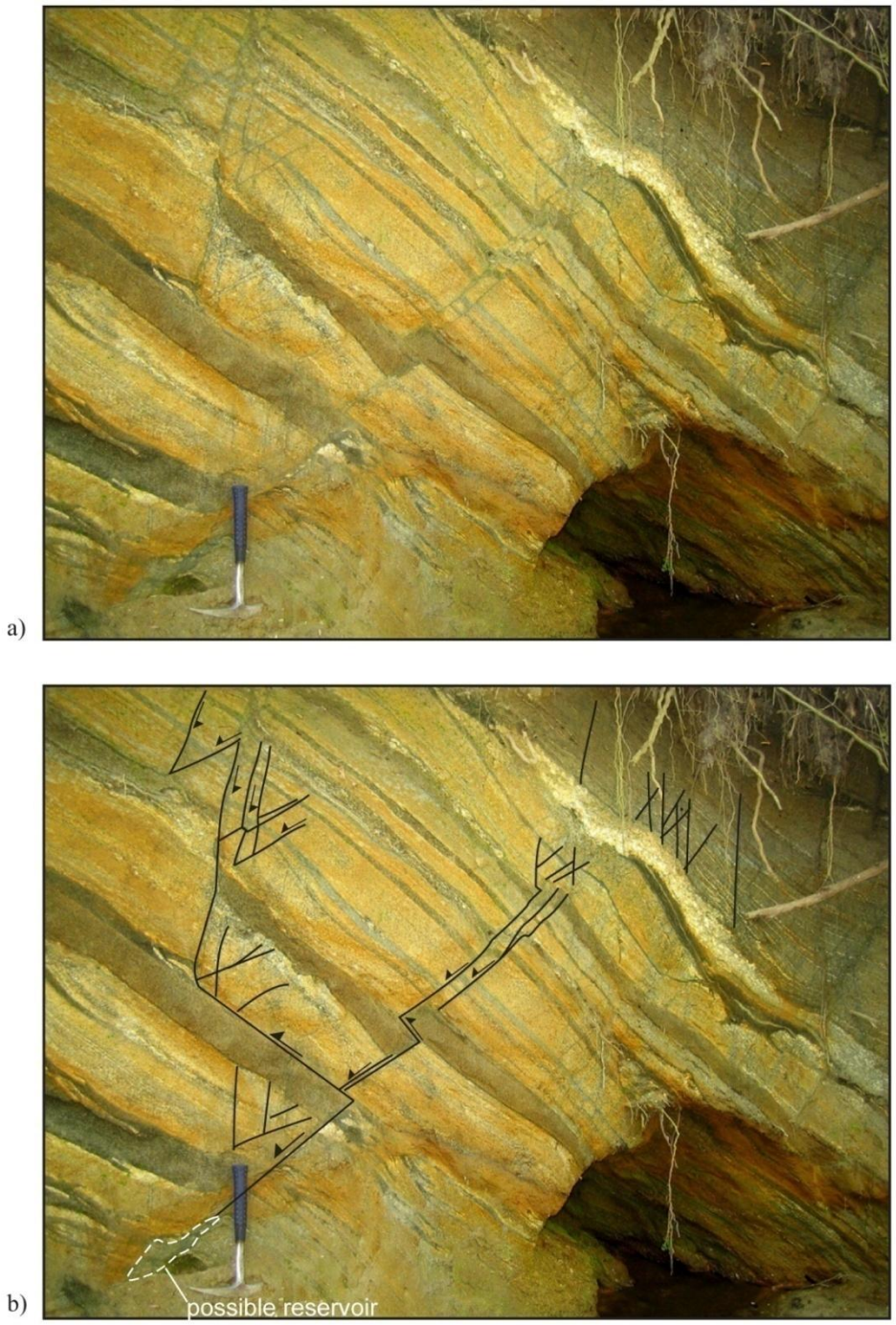

Figure 4-9. Saprolite outcrop of the lower Tallulah Falls Formation metagraywacke overlain by an amphibolite interlayer separated by migmatite. These units have been normal faulted during regional uplift associated with the D_5 event. Outcrop located in tributary to Howards Creek, east of NC St. Rd. 1203 (Owl's Den Road). a) Saprolite outcrop. b) Saprolite outcrop (a) annotated to outline faults and potential pseudotachylyte reservoir. Arrows show directions of displacement. Faults were not drawn across migmatite because it is uncertain if they cut the migmatite or if the migmatite was emplaced post-normal faulting.

bottom of the outcrop. Faults splay from an S_2 parallel fault and crosscut S_2 foliations and each other (Fig. 4-9). It is difficult to tell if the faults crosscut the migmatite between the metagraywacke and amphibolite. Understanding this relationship, and knowing if this is indeed pseudotachylyte, could have important implications related to the strain rate and uplift history of these rocks by recording the amount of slip and magnitude of paleoearthquakes. However, this is mostly speculation, because the potential pseudotachylyte is only observed in saprolite at this one outcrop.

Regional open folding of the Inner Piedmont, F_5, produced domes (i.e., Brushy Mountains; Wilson, 2006; Gatewood, 2007), antiforms (Newton antiform; Goldsmith et al., 1988) and synforms (i.e., the Cat Square terrane in North Carolina; Hatcher and Merschat, 2006). Meso-scale, open F_5 folds were observed along several series of outcrops in creeks in the study area.

Two dominant sets of diabase dikes, emplaced at ~199 Ma (Hames et al., 2000) during Mesozoic extension related to D_5, are observed in the southern Appalachians: a north-south set that converges near Charleston and Georgetown, South Carolina, and diverges northward into Virginia; and a northwest-trending set in Georgia, South Carolina, and North Carolina (Ragland et al., 1983). Several outcrops of the northwest-trending diabase dikes occur in the study area (Fig. 4-1). Siliceous cataclasite does not occur in the study area, but has been mapped ~8 km to the north (Gilliam, in progress). Three principal, unfilled joint sets occur in the study area. The dominant set is oriented northwest-southeast at ~95° and ~275° with two other sets at ~70°/250° and ~350° (Fig. 4-10). These joint sets dominantly cause blocky weathering in the gondite unit and both Cat Square and Tugaloo terrane metagraywacke units. Most joints have a moderate to steep dip (50-90°).

Local and Regional Map Patterns

Compilation of detailed geologic mapping of the west-central boundary of the Newton window with surrounding detailed and reconnaissance geologic maps, as well as domain data,

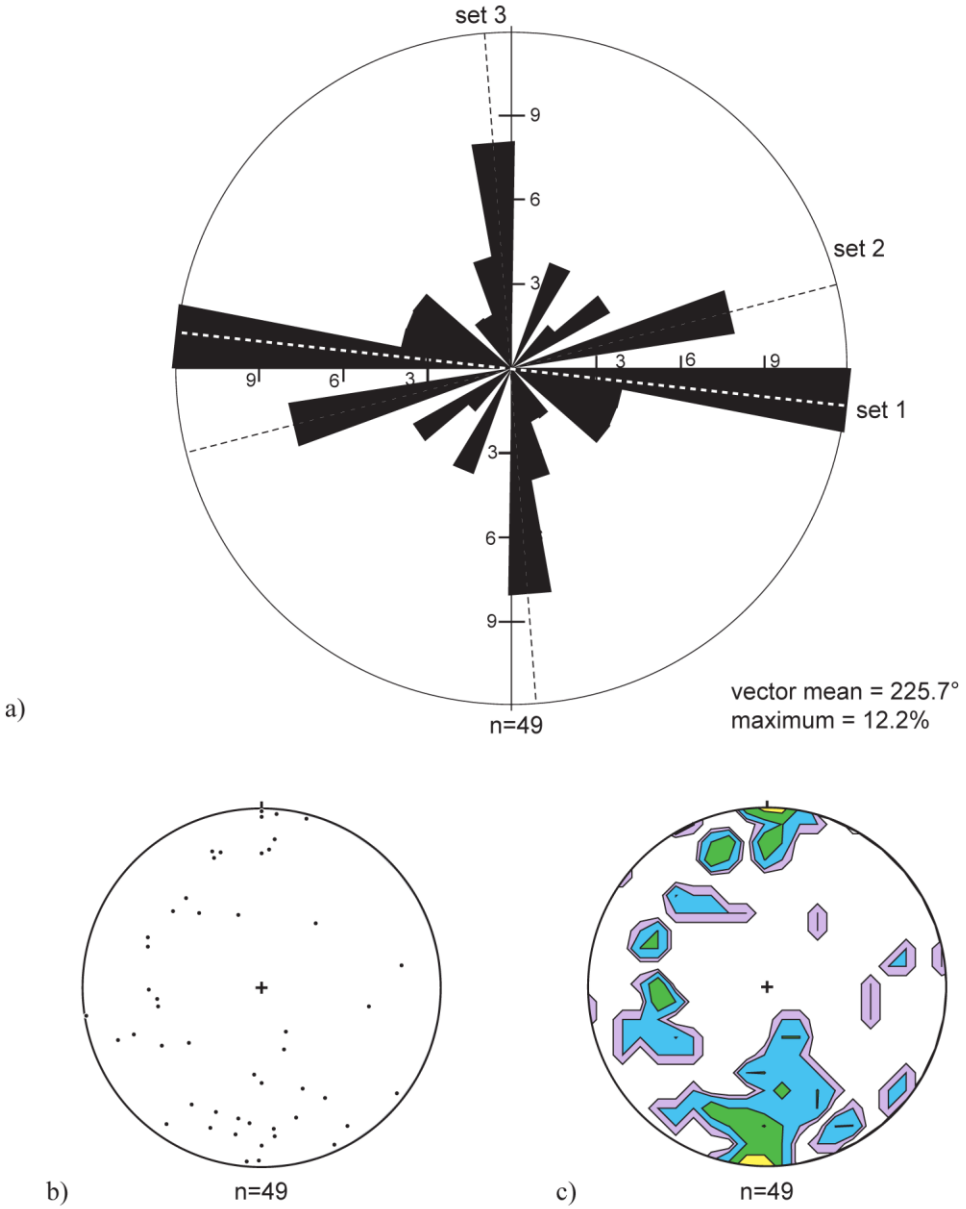

Figure 4-10. Distribution of joint orientations in study area. a) Rose diagram showing the orientation of strike planes of joint sets. The circle diameter represents 12 percent of the data. b) Lower hemisphere equal-area scatter plot of 49 poles to joint surfaces. c) Contoured lower hemisphere equal-area fabric plot of 49 points to joint surfaces. Contours are at 1, 2, 4, 8 percent per one percent area.

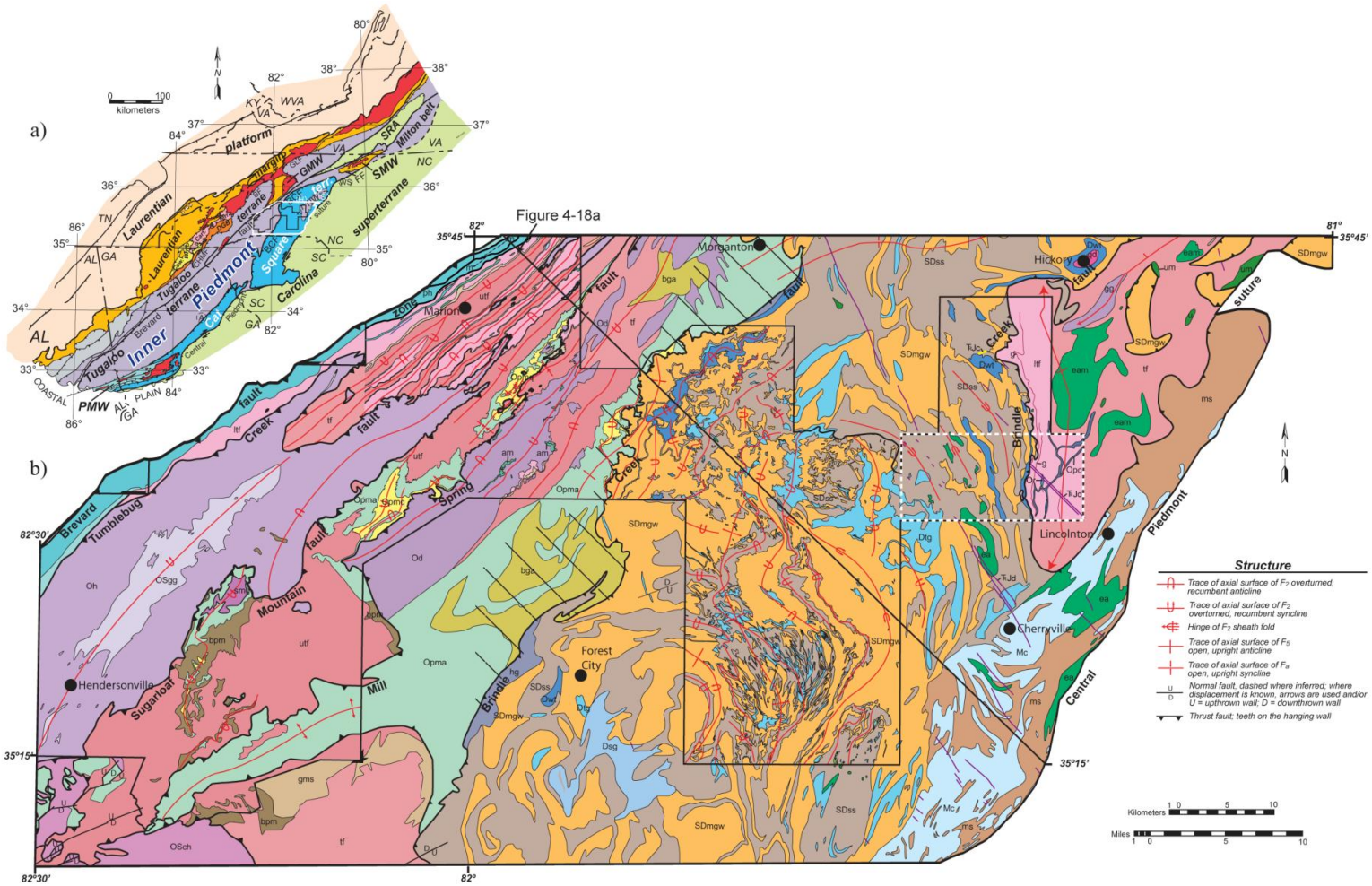

Figure 4-11. a) Simplified tectonic map showing location of map area in part b White polygon outlines map area in part b. Black polygon outlines compiled area of detailed geologic mapping. Figure modified from Merschat and Hatcher (2007). See Fig 4-1 caption for explanation of abbreviations. b) Simplified geologic map of the Columbus Promontory, South Mountains, Hickory-Cherryville area in the North Carolina Inner Piedmont. The black polygon outlines compiled area of detailed geologic mapping. Dashed white rectangle outlines study area. c) Explanation of map units.

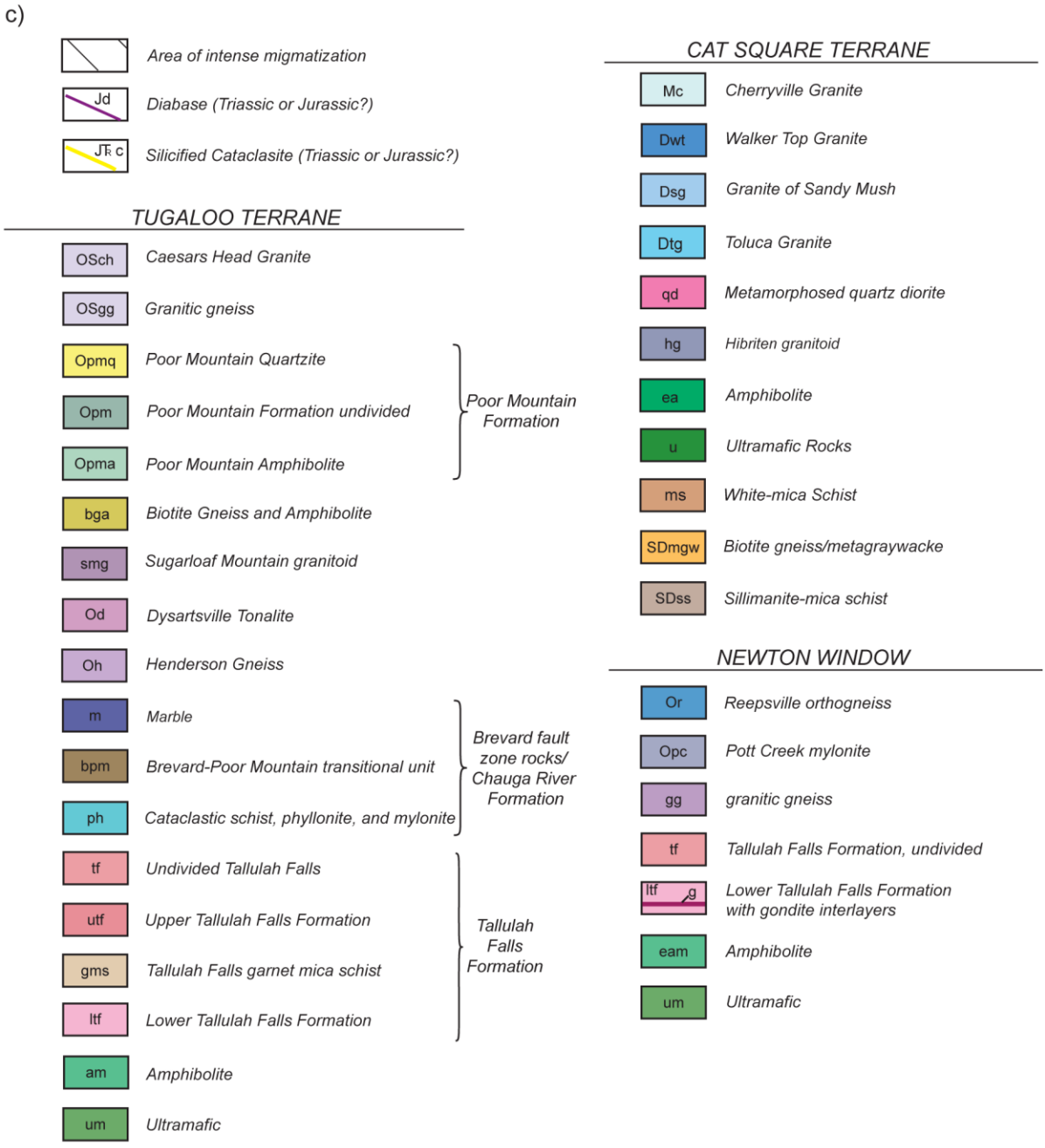

Figure 4-11. *continued.*

provides significant insight to local and regional structures based on map patterns (Figs. 4-11,12).

Map patterns in the southern Appalachian Inner Piedmont are those typical of patterns reported for sheath folds such as tubular- or tongue-shaped map patterns, disconnected bodies of a rock unit surrounding the hinge of the fold, and opposite verging folds on opposing limbs of the fold (Merschat et al., 2005b). Detailed geologic mapping in the Brushy Mountains led to identification of the map-scale, northeast-plunging Big Warrior and Poplar Springs sheath folds, and west- to southwest-plunging Ellendale and Gilreath sheath folds in the western Cat Square terrane (Kalbas, 2003; Merschat, 2003; Wilson, 2006; Gatewood, 2007). These sheath folds are outlined by Devonian plutons such as the Walker Top Granite, Toluca Granite, and Rocky Face pluton (Toluca Granite equivalent?). In the South Mountains, a southeast-plunging map-scale sheath fold, cored by Cat Square terrane metagraywacke, was identified based on map patterns, mineral lineation orientations, and domain data (domains III-VII in Fig. 4-12; Bier, 2001; Bier et al. 2002). A series of large, northeast-plunging flattened tubular sheath folds are cored by the megacrystic Henderson Gneiss in the western Inner Piedmont (Merschat et al., 2005b). The original geometry of the granitoid bodies (i.e., stocks or batholiths versus tabular plutons) and amount of heterogeneous simple shear during deformation control the location of granitoids in sheath folds (Merschat et al., 2005b).

Map-scale sheath folds in the study area are not fully evident until put into regional context with surrounding detailed and reconnaissance maps (Fig. 4-13). Tongue-shaped map patterns show that portions of three sheath folds dominantly cored by sillimanite schist and outlined by metagraywacke and Walker Top Granite occur within the study area: two north-northwest plunging separated by a southeast-plunging sheath fold (Fig. 4-14a). Strain may have been taken up mostly by the weaker sillimanite schist in the sheath folds, although mylonitization is pervasive in the study area. Near the exposure of the Brindle Creek fault, extension occurred in the eastern limb of the easternmost sheath fold with north-northwest-directed transport of the Cat Square terrane (top-to-the-north shear-sense indicators at fault outcrops), causing the separation of once continuous bodies of metagraywacke and Walker Top Granite (Figs. 4-14). Isolated mafic complexes and amphibolite bodies, five of which are located

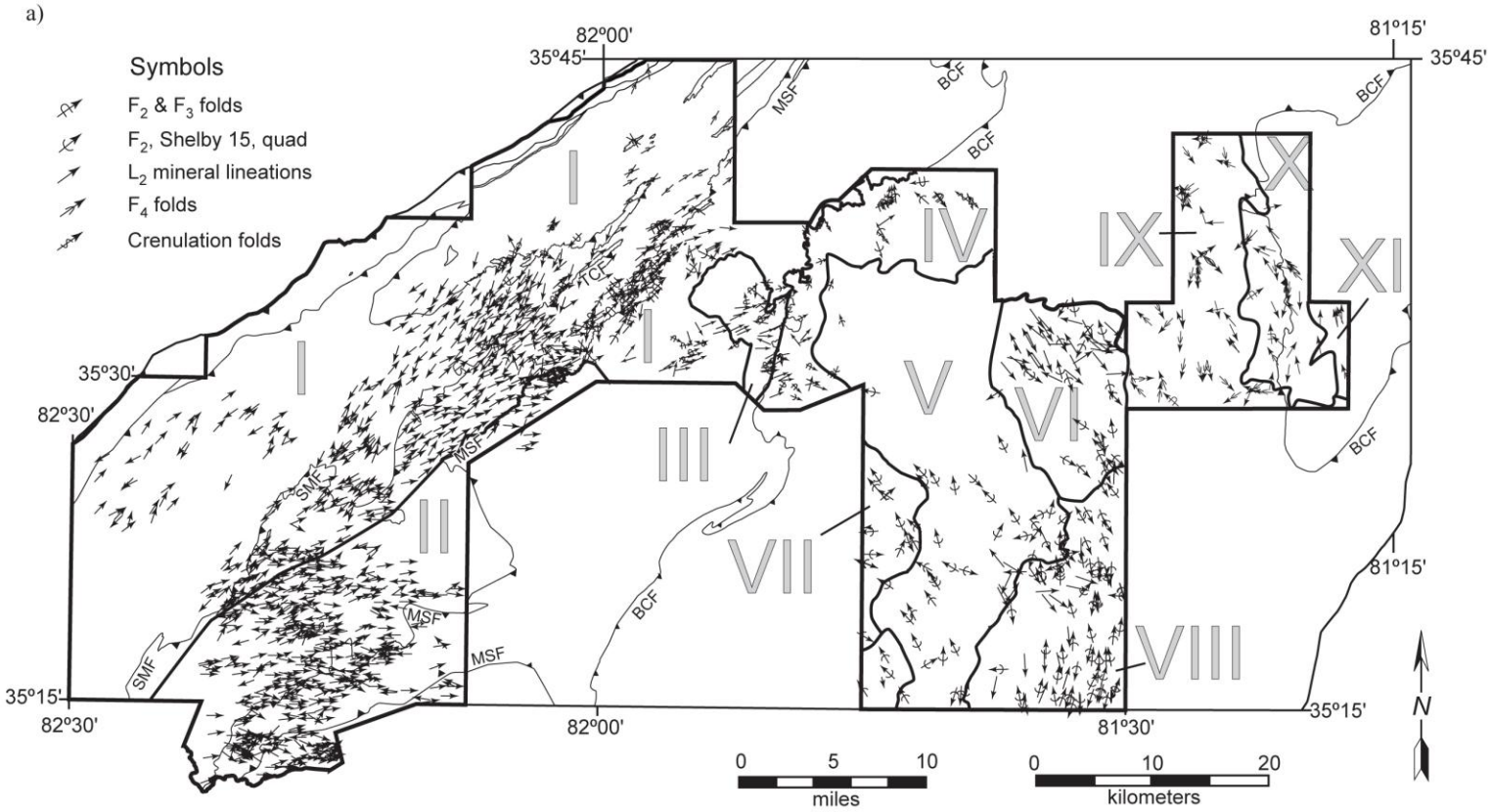

Figure 4-12. a) Compiled domains of the Columbus Promontory, South Mountains, and Hickory-Cherryville areas (modified from Merschat et al., 2005b). Mineral lineations and fold axes are shown to illustrate curved lineation pattern in the north-central Inner Piedmont. Data in domain II from Davis (1993). Domains IV-VIII were compiled by Bier (2001) and Bier et al. (2002). Folds compiled from that area in the southeast part of the map were assumed to be F_2. Domains IX-X north of this study area from Gilliam (in progress). BCF–Brindle Creek fault; MSF–Mill Spring fault; SMF–Sugarloaf Mountain fault; TCF–Tumblebug Creek fault. b) Contoured lower-hemisphere, equal-area plots of poles to foliation, and trends of fold axes and mineral lineations for the South Mountains and Columbus Promontory domains (I-VIII) defined in (a). Plots from Merschat et al. (2005b). c) Contoured lower-hemisphere, equal-area plots of poles to foliation, and trends of fold axes and mineral lineations for Newton window domains IX-XI. Data compiled from this study and Gilliam (in progress). Folds plotted in (b) and (c) include only passive and flexural flow F_2 and F_3 folds. Contours are at 1, 2, 4, 8, 16, and 20 percent per one percent area. Axial surfaces were not measured in all folds and were not available in domains IV-VIII.

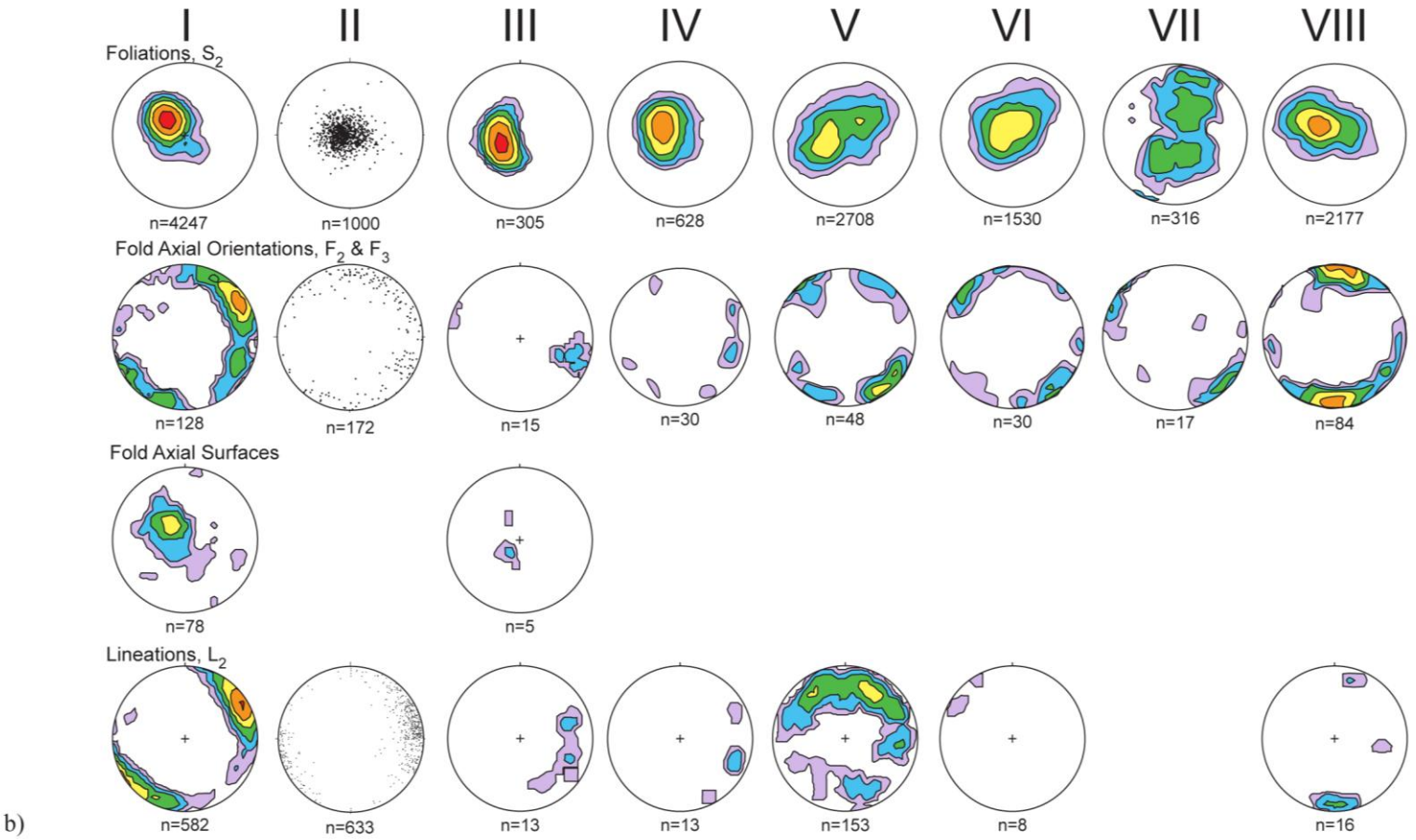

b)

Figure 4-12. *continued.*

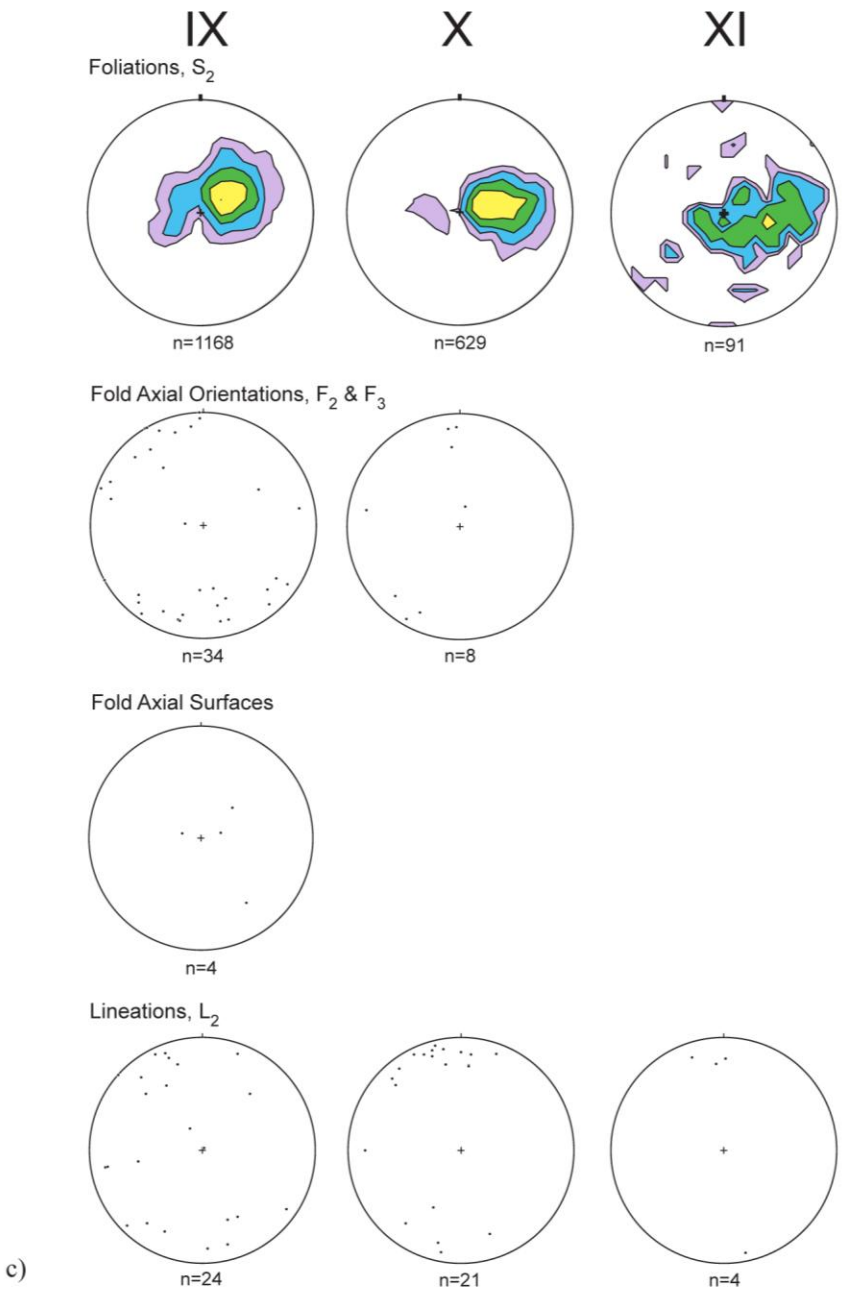

Figure 4-12. *continued.*

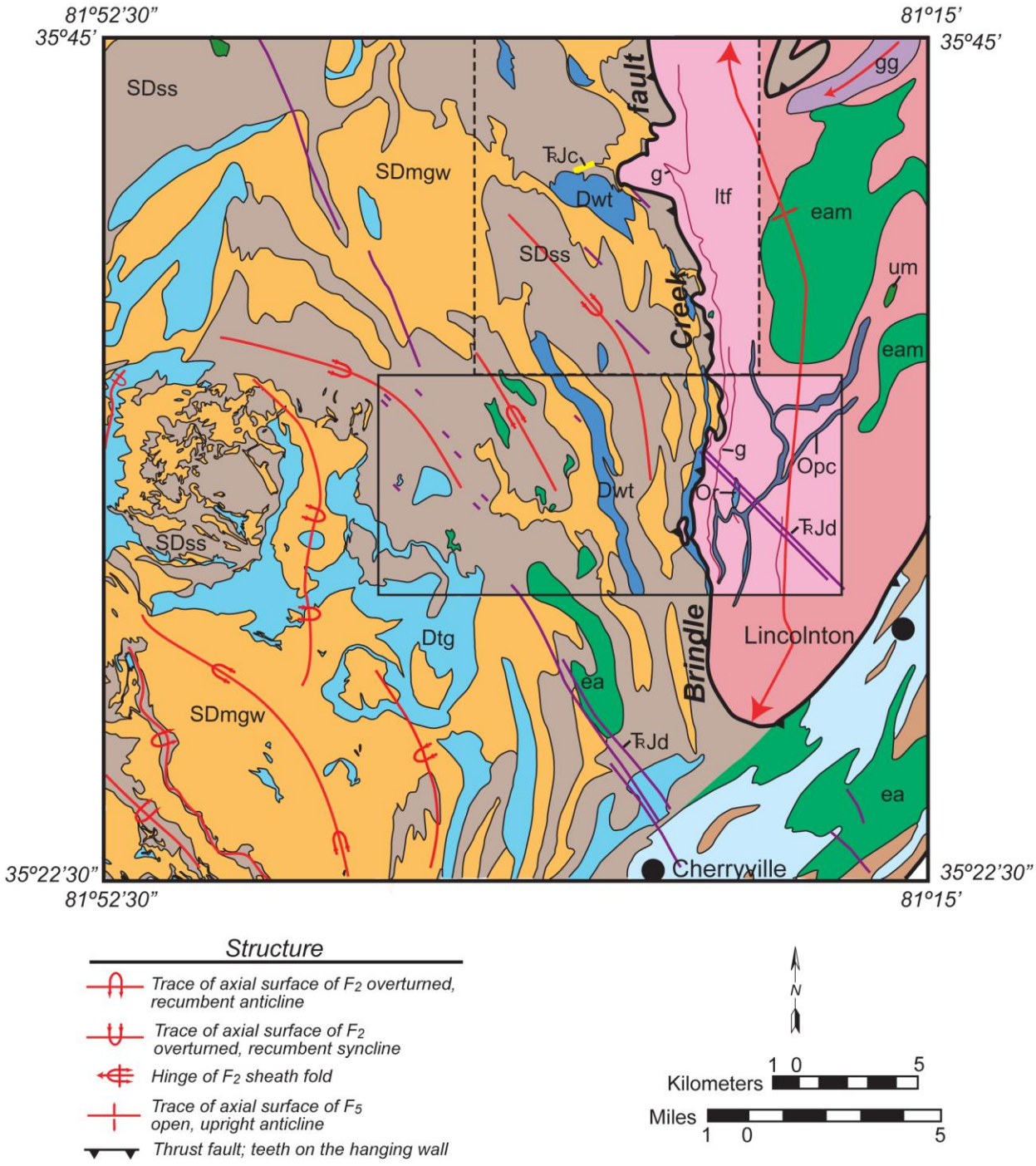

Figure 4-13. Simplified geologic map of the western border of the Newton window showing map-scale sheath folds in the study area in a regional context. Figure enlarged from compiled Columbus Promontory, South Mountains, Hickory-Cherryville map in Fig. 4-12. Study area outlined in black box. Area outlined by dashed box north of study area from detailed geologic mapping of Gilliam (in progress). Map units same as in Fig. 4-11.

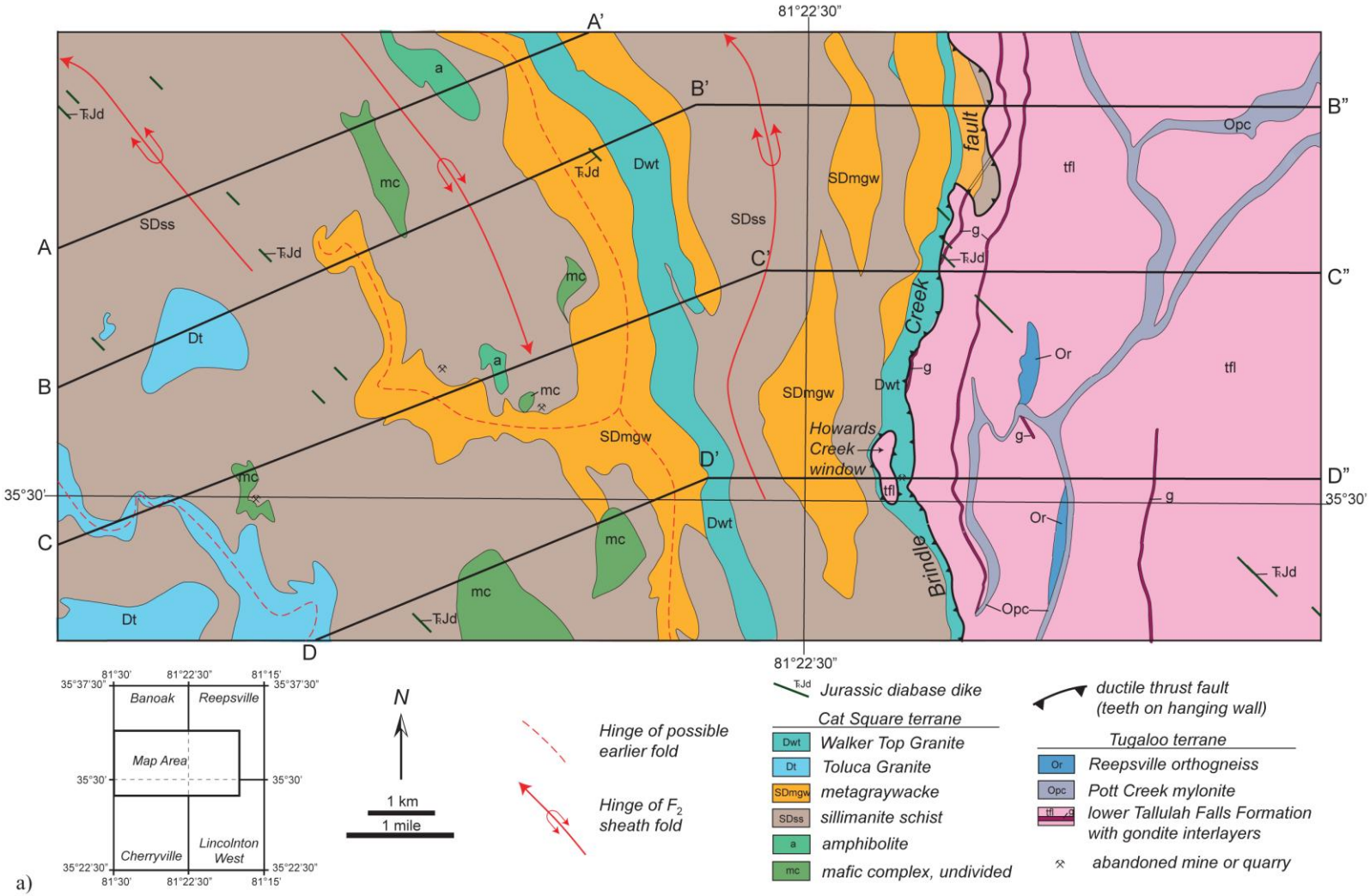

a)

Figure 4-14. a) Simplified geologic map of the study area in portions of the Banoak, Reepsville, Lincolnton West, and Cherryville 7.5-minute quadrangles showing the locations of cross sections. b) Cross sections through the study area. Abbreviations for rock units same as in legend of part a.

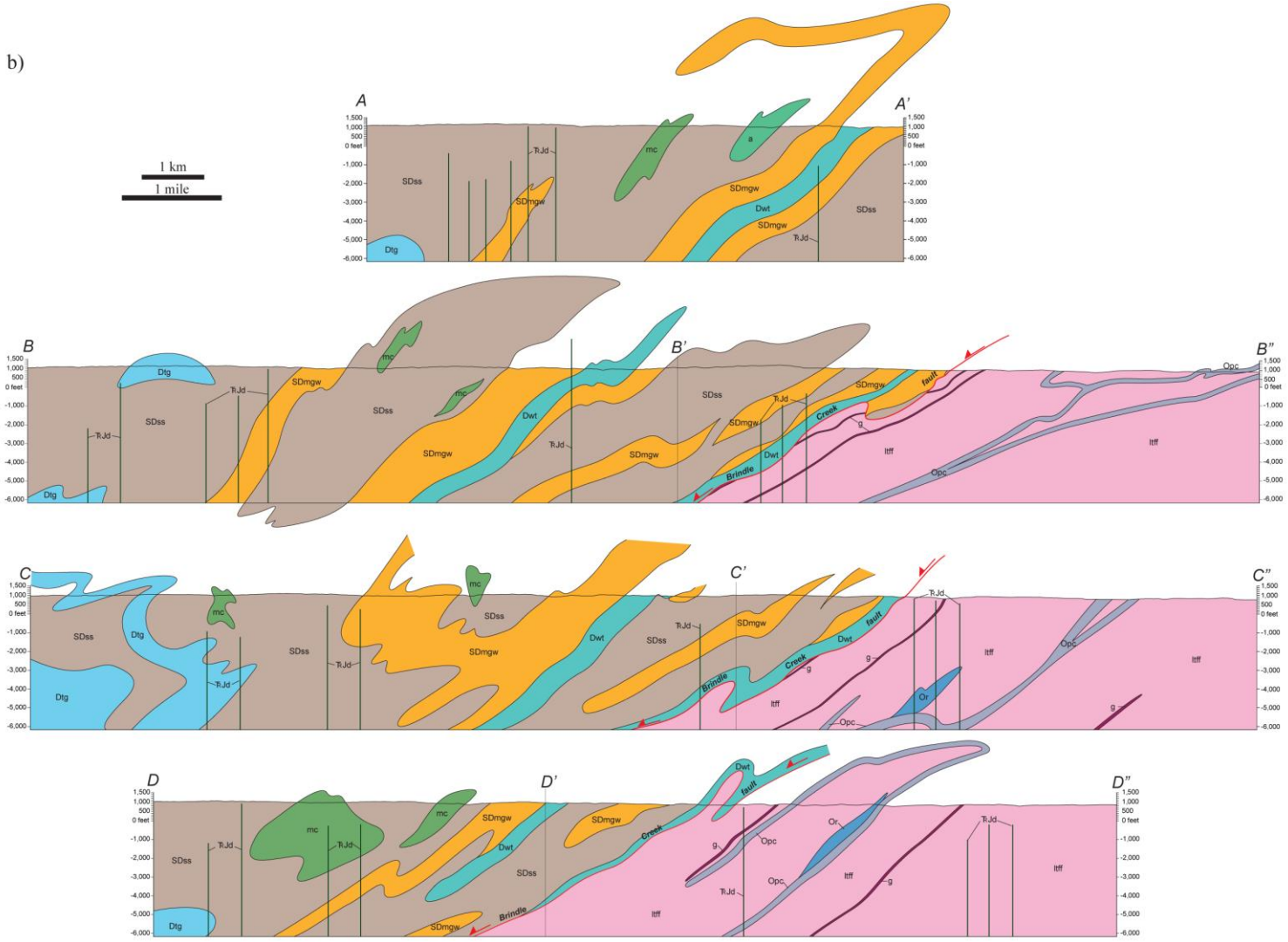

Figure 4-14. *continued.*

in the core of the southeast-plunging sheath fold, may have once been continuous prior to the formation of the sheath folds. Outcrops of western Walker Top Granite body sometimes had top-to-the-south or southeast shear sense. Pervasive mylonitization, opposite verging lineations, fold axes, and shear sense indicators are attributed to the formation of F_2 map-scale sheath folds and later deformation.

Sheath fold formation in the Inner Piedmont is likely synchronous with emplacement of the Brindle Creek fault and formation of the dominant structural grain at mid-crustal depths, near peak Neoacadian metamorphic conditions. Timing of this deformation is constrained to post-emplacement of Devonian to Mississippian (407-355 Ma) granitoids that occur on the limbs of sheath folds in the Cat Square terrane. Truncation of the Walker Top Granite and some of these sheath folds against the Brindle Creek fault in the Brushy Mountains (Merschat, 2003; Wilson, 2006; Gatewood, 2007) and Newton window indicates final movement of the fault occurred after formation of the sheath folds. Sheath folds developed as a product of noncoaxial ductile flow (Bier et al., 2002; Merschat and Kalbas, 2002; Merschat et al., 2005b).

Cross–Section Interpretation

Four cross sections were drawn through the study area to illustrate different parts of sheath folds, discontinuous bodies of metagraywacke and mafic complexes, the folded Brindle Creek fault and the nature of the Pott Creek mylonite (Plate 1; Fig. 4-14). Three of the four sections (B-B", C-C", D-D") bend along their length to stay perpendicular to the dominant foliation.

Based on the map pattern geometry and cross section analysis, sheath folds have a tubular shape (sections A-A', B-B", C-C"; Plate 1; Fig. 4-14). The three sheath folds are cored by sillimanite schist and outlined by metagraywacke and Walker Top Granite. The eastern and central sheath folds are illustrated in the cross sections, but the magnitude of the westernmost sheath fold does not permit depiction in these cross sections. The map pattern and geometry of the Toluca Granite in section C-C' may indicate it outlines another sheath fold with an anvil shape, cored by sillimanite schist, similar to the Ellendale sheath fold in the Brushy Mountains (Merschat, 2003). This anvil shape is not reflected in the section, because the profile line trends

parallel to oblique to the foliation in this portion of the study area. It would be better reflected along a different orientation of a cross section.

As previously discussed, discontinuous bodies of metagraywacke, mafic complexes, and amphibolite are attributed to extension related to the north-directed flow and formation of F_2 sheath folds. Sections B-B", C-C", and D-D" (Plate 1; Fig 4-14b) depict the subsurface geometries of these bodies. In section D-D", geometries suggest later F_3 folding may also contribute to the separation of two mafic complexes.

F_3 to F_5 folding is reflected in the Brindle Creek fault trace and several Cat Square terrane units in cross section. Reclined, tight F_3 folding of the Brindle Creek fault (sections B-B", C-C", D-D") resulted in the formation of the small Howards Creek window, while upright, open to closed F_4-F_5 folds produced further truncation of the gondite layer in the Newton window. F_3 to F_5 folds are found in all Cat Square terrane units, but are mostly observed in the Toluca Granite and metagraywacke units. Regional late, open F_5 folding is responsible for formation of the Newton antiform and overall synformal shape of the Cat Square terrane. This is reflected by Z-shaped folding in the cross sections.

The anastomosing pattern of the Pott Creek mylonite has been interpreted as a product of post-plutonic emplacement deformation. Section B'-B" trends parallel to foliation of the unit in the northern portion of the study area, and thus is reflected as having an apparent horizontal orientation in cross section, although the true dip of the unit is to the north. The strike of the mylonite becomes oblique to perpendicular to the section line shown by a westward dip in cross section. Section C'-C" show the convergence of two portions of mylonite. Section D'-D" depicts the Pott Creek mylonite as being a tight to isoclinal fold. The repetition of the gondite layer on both sides of the mylonite in this section may be a result of this folding.

Inner Piedmont Structural Grain and Tectonic Model

Structural components of the Inner Piedmont, including the dominant S_2 foliation, L_2 mineral lineation, F_2 fold hinges, and shear-sense indicators, define an arcuate pattern (Figs. 4-12 and 4-15). This pattern was first recognized by Goldsmith (1981) as defined by L_2 mineral lineations and F_2 fold hinges. Flow paths derived from mineral lineations and fold axes suggest

Figure 4-15. Pattern of dominant S_2 foliation and lineation in the northern Inner Piedmont. Figure from Merschat et al. (2005b). a) Histogram of 4,587 dip-strike measurements of dominant foliation. b) Form-line map of S_2 foliation. Form lines are parallel to strike; teeth on trend lines indicate dip direction. Density of form lines indicates density of data coverage used in map compilation. New data collected after this map was compiled reinforce the broad patterns depicted on this map. c) Histogram of 764 mostly mineral lineations. Note the dominance of gentle plunge. d) Distribution of measure lineation (filtered to create spacing). Arrowhead indicates direction of plunge; arrowhead on both ends of line indicates horizontal lineation. Line on each measurement indicates trend. Additional measurement added to this data set since the original compilation was made (see Fig. 4-13 and Merschat et al., 2005b, their Fig. 7) reinforce the curved pattern illustrated by the data. Sources of foliation and lineation data are listed in Hatcher (2001, 2002) and Merschat et al. (2005b). Location of study area outlined by black rectangle.

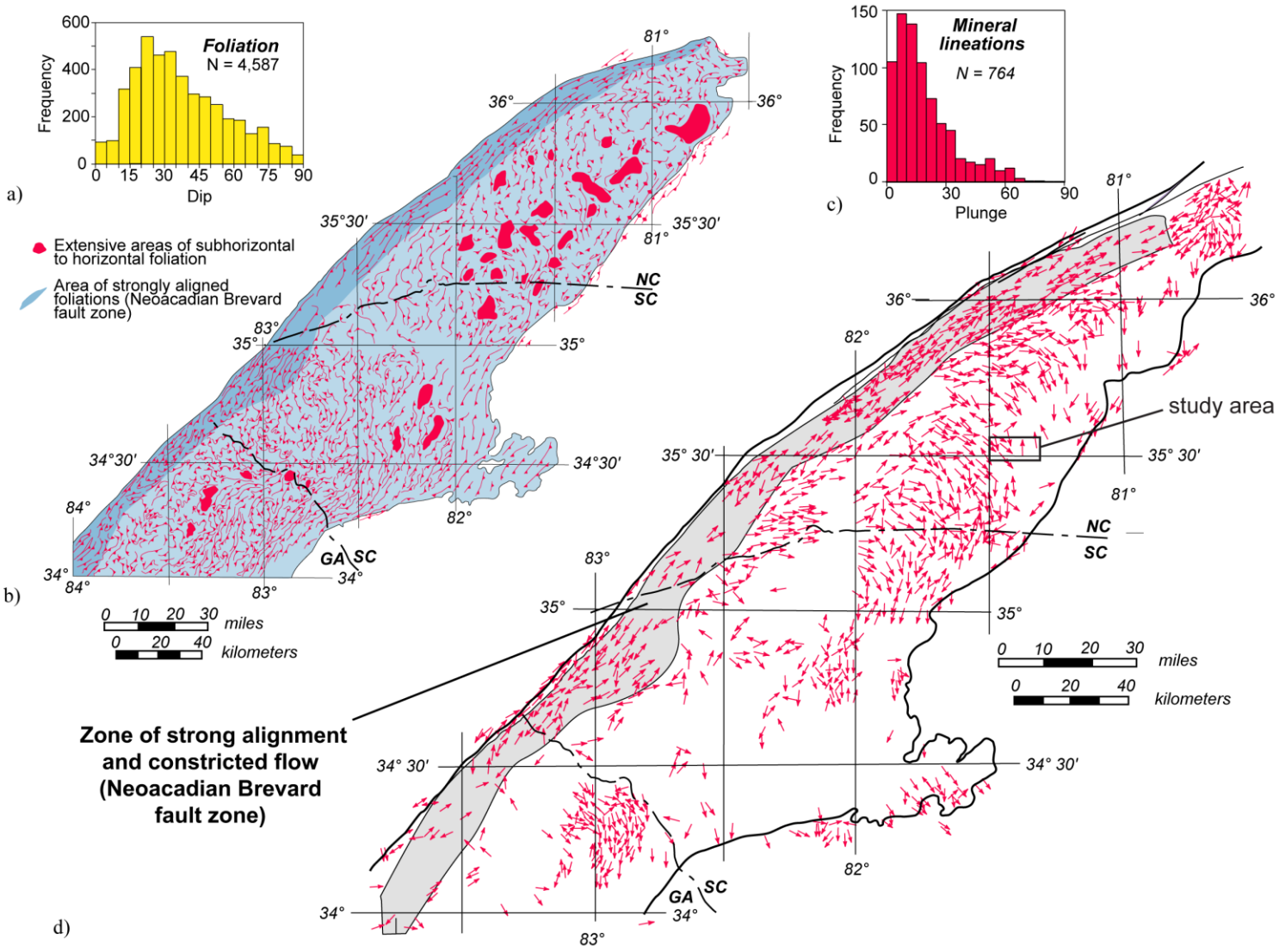
a)
Foliation
N = 4,587
Frequency
Dip
b)
Extensive areas of subhorizontal to horizontal foliation
Area of strongly aligned foliations (Neoacadian Brevard fault zone)
NC
SC
GA
miles
kilometers
c)
Mineral lineations
N = 764
Plunge
study area
d)
Zone of strong alignment and constricted flow (Neoacadian Brevard fault zone)

anticlockwise flow across the Inner Piedmont. Noncoaxial, ductile flow was initially directed toward the north-northwest along the Central Piedmont suture, then deflected west in the central Inner Piedmont, and southwest along the Brevard fault zone buttress, as indicated by a zone of strongly aligned structural elements (Fig. 4-16; Hatcher, 2001; Merschat et al., 2005b). Based on the aforementioned data, the southern Appalachian Inner Piedmont is proposed to be the result of a tectonically forced, orogenic strike-parallel channel (Hatcher and Merschat, 2006). The channel is a product of oblique north to south collision between the Carolina superterrane and Laurentia during the Neoacadian orogeny. Channel flow was confined by the Central Piedmont suture (upper boundary) and the Brevard fault zone (lower boundary), producing a series of southwest-directed Type F imbricate faults. The lack of confinement to the southwest during the collision allowed mid-crustal extrusion to the southwest (Hatcher and Merschat, 2006). Hatcher and Merschat (2006) suggested the structural configuration of the Inner Piedmont compares favorably with the Beaumont et al. (2004) 2D model HT-HET (Fig. 4-17). This model introduced initial anisotropies and produced a series of Type F imbricates over20 million years of deformation, similar to the long thermal history of the Neoacadian orogeny.

The 3D kinematic and channel flow model developed by Merschat et al. (2005b) and Hatcher and Merschat (2006) shows the Inner Piedmont deformed as a ductile flowing mass as evidenced by migmatite, anatectic melts, and the plastic rheology of involved lithologic assemblages. Other evidence for the mid-Paleozoic channel is also seen in the structural domains defined through detailed geologic mapping in North Carolina (Fig. 4-12, Merschat et al., 2005b), Georgia (Higgins et al., 2003); and Alabama (Bentley and Neathery, 1970; Neilson, 1988); west- to southwest-vergent thrust sheets (Merschat et al., 2005b); curved and southwest-directed map- and meso-scale sheath folds (Merschat, 2003; Wilson, 2006; Gatewood, 2007; this study); and curved magnetic anomalies in aeromagnetic data (Hatcher et al., 2007; Davis et al., 2009). Foliation, lineation, and fold axis data collected during detailed geologic mapping and interpretation of map patterns of the west-central boundary of the Newton window support the channel flow model for the eastern edge of the Inner Piedmont. Mineral lineations, F_2 sheath fold axes, and shear-sense indicators along the Brindle Creek fault indicate a north-northwest-

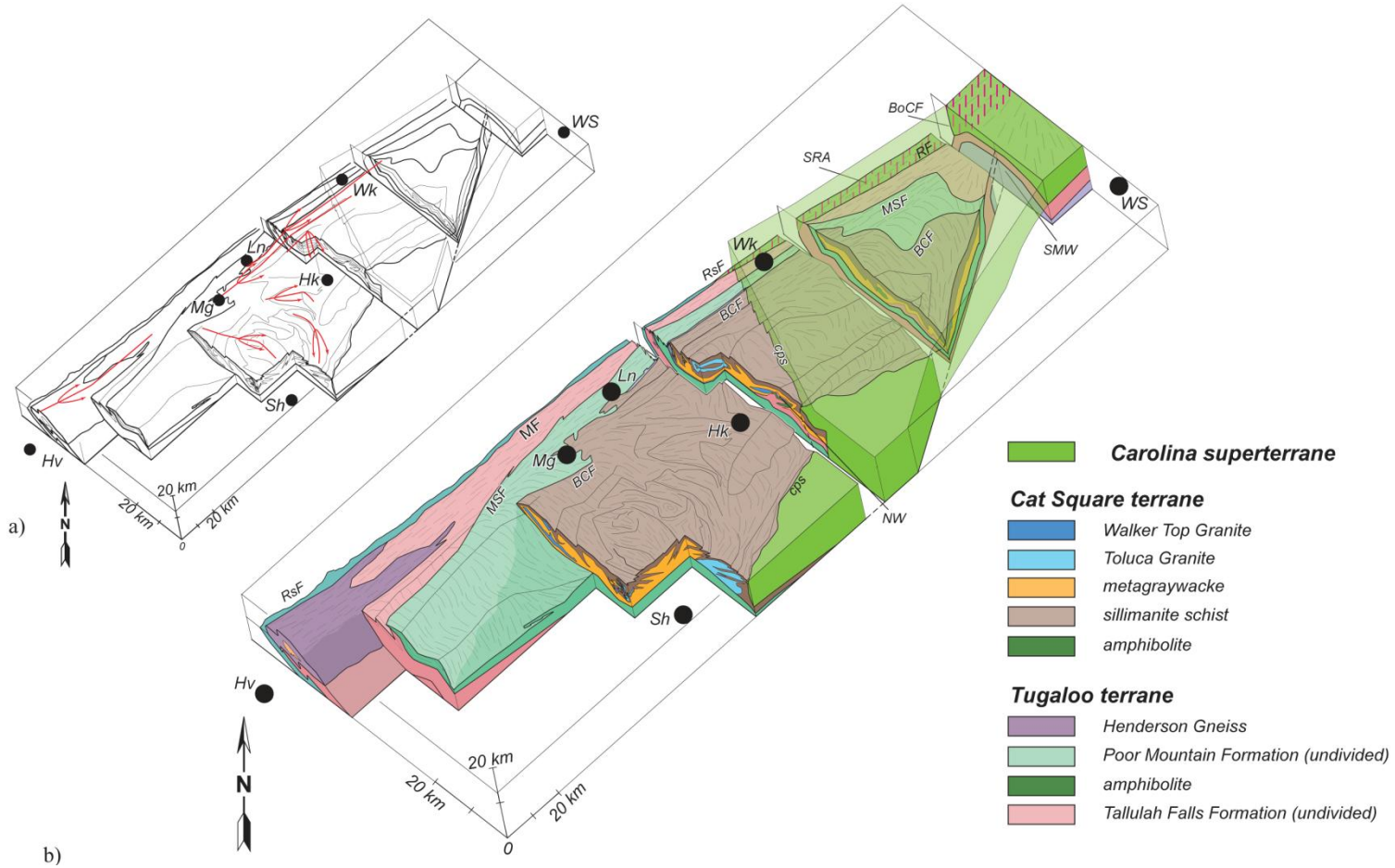

Figure 4-16. 3D block diagram of the Inner Piedmont in North Carolina, from near Hendersonville to Winston-Salem. Trend lines on the surface of the block were drawn from mineral lineations. Vertical exaggeration is 1.3:1:1 (X:Y:Z). Figure from Merschat et al. (2005). a) Outline of 3D block diagram showing location of map-scale sheath folds. b) More detailed 3D block diagram in part a showing major tectonic units. BCF–Brindle Creek fault; BoCF–Bowens Creek fault; cps–Central Piedmont suture; MSF–Mill Spring fault; MF–Marion fault; NW–Newton window; RF–Ridgeway fault; RsF–Rosman fault; SMW–Sauratown Mountains window; SRA–Smith River allochthon. Towns: Hk–Hickory; Hv–Hendersonville; Ln–Lenoir; Mg–Morganton; Sh–Shelby; Wk–Wilkesboro; WS–Winston-Salem.

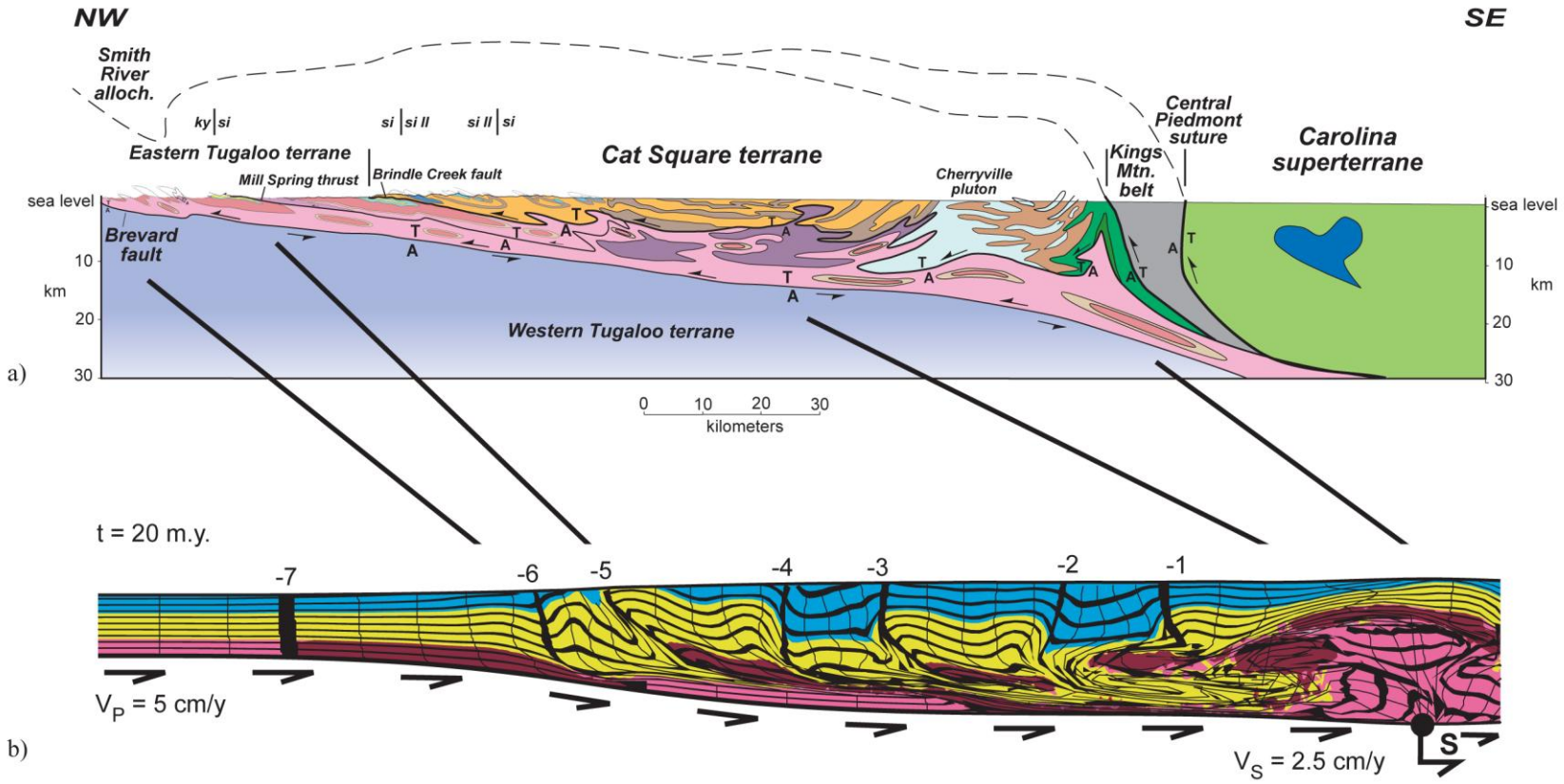

Figure 4-17. Comparison of a cross section (a) through the Inner Piedmont in North Carolina with Beaumont et al. (2004) channel flow model HT-HET (b). Figure from Hatcher and Merschat (2006). a) Configurations of Inner Piedmont structures and mid-Paleozoic Brevard fault zone were extrapolated from surface geologic maps of Goldsmith et al. (1988) and Bier et al. (2002) (Fig. 4-13b). Cross-section line shown in Fig. 4-13b. Rock unit colors at surface for eastern Tugaloo terrane and Cat Square terrane same as in Fig. 4-13c. Other unlabeled colors: purple below Cat Square terrane–Ordovician pluton; dark blue in Carolina superterrane–Devonian pluton. Abbreviations: A–away; ky–kyanite; si–sillimanite; si II – sillimanite II; T–toward. b) Colors represent materials of higher (blue, yellow) and lower (pink, red) viscosity.

directed transport before curving east-west and southwest-northeast in areas of adjacent detailed geologic mapping in the South Mountains and Columbus Promontory.

CHAPTER 5

TIMING AND IMPLICATIONS FOR EMPLACEMENT OF THE PALEOZOIC-AGE VALE CHARNOCKITE AND WALKER TOP GRANITE

Introduction

Since the documentation of the existence and first age determination of the Vale Charnockite xenolith (Goldsmith et al., 1988; Kish, 1997), little attention has been give to the details of its occurrence. Noticing similarities of the Vale charnockite with the charnockitic Cunningham granite of the Pine Mountain window in central Georgia, Kish (1997) dated zircons from the charnockite in hopes of revealing Precambrian basement in the Inner Piedmont. These U-Pb ages, however, indicate a middle Paleozoic crystallization of 348-357 Ma ($^{206}Pb/^{238}U$) and 360-380 Ma ($^{207}Pb/^{206}Pb$), similar to other Inner Piedmont plutons. Charnockite has been recognized only in this outcrop after much detailed mapping in the North Carolina Cat Square terrane. The rarity of Paleozoic age charnockites in the southern Appalachians, and the world, makes the Vale charnockite a very unique rock.

Charnockitic rocks of both igneous and metamorphic origin have been documented worldwide in a variety of tectonic settings. The common characteristic of all charnockites is the relatively dehydrated condition of the rock with an orthopyroxene or fayalite-bearing assemblage. The mechanisms for formation of charnockites has been an intensively studied and debated topic since the introduction of the name "charnockite" was proposed to describe the hypersthene-bearing granitic rocks in Madras, India, by Holland (1900). Documented charnockites exhibit a wide range of ages (Table 5-1), geochemical characteristics, tectonic environments, petrologic processes, pressures, and temperatures. In the Appalachians, charnockites have assisted in interpreting crustal evolution in the Long Range Mountains of Newfoundland, Adirondacks in upstate New York, Wilmington Complex in Delaware, the Blue Ridge of northern and central Virginia, and the Pine Mountain window of Georgia and Alabama. Timing of emplacement for these charnockitic bodies ranges from 425-485 Ma and 1.0 -1.5 Ga (Table 5-1). In the Adirondacks and Virginia, these bodies are associated with anorthosite-

Table 5-1. Locations and ages of igneous charnockite bodies around the world. References: 1–Hansen & Stuk (1989); 2–Barnes et al. (2006); 3–Kish (1997); 4–Weiss & Troll (1989); 5–Irwin et al. (1987); 6–Kagami et al. (1990); 7–Bucher & Frost (2006); 8–Raith et al. (1988); 9–Miller et al. (1996); 10–Duchesne & Wilmart (1997); 11–Young & Black (1991); 12– Aftalion et al. (1988); 13–Paul et al. (1990); 14–Heaman et al. (2002); 15–Zhao et al. (1997); 16–Pettinghill et al. (1984); 17–Mora & Valley (1985); 18–Kish & Odom (1999); 19–Tollo (2001); 20–Sheraton et al. (1992); 21–Hamilton et al. (2004); 22–Zhou et al. (1995); 23–Post (2000); 24–Nijland & Senior (1991); 25–Pattison (1991); 26–Hubbard & Whitley (1979); 27–Welin & Gorbatschev (1978); 28–Frost et al. (1999); 29–Bridgwater et al. (1974); 30–Corfu et al. (2003b); 31–Aftalion et al. (1991); 32–Ormaasen (1977); 33–Malm & Ormaasen (1978); 34–Jordt-Evangelista (1997); 35–Battacharya & Sen (2000); 36–Peucat et al. (1989); 37–Taylor et al. (1988); 38–Grew & Manton (1984); 39–Buhl et al. (1983); 40–Van Reenen et al. (1988); 41–Stern et al. (1994); 42–Percival et al. (2003); 43–Christoffel et al. (1999); 44–McGregor & Friend (1992); 45–Frost et al. (2000).

Location	Charnockite Body	Age	References
Mesozoic			
Big Sur, Central California		81 Ma	1
Klamath Mountains, California	Ironside	170 Ma	2
Paleozoic			
Vale, North Carolina	Vale Charnockite	348-370 Ma	3
Western Scottish Highlands	Ballachulish	412 Ma	4
Sri Lanka, SW Highlands		420-490 Ma	5,6
Queen Maud Land, Antarctica	Thor Range	500 Ma	7
Proterozoic			
S Kerala, S India		550 Ma	8
Madurai Block, southern India	Cardamom Hill charnockite massif	588 ± 6 Ma	9
Southern Norway	Bjerkreim	930 Ma	10
Mawson Coast, Antarctica	Mawson Charnockite	959 ± 58 Ma	11
Orissa, E India		970 Ma	12, 13
Long Range Mountains, Newfoundland	Potato Hill Charnockite	999 ± 4 Ma	14
Prince Charles Mountains, Antarctica	Prince Charles Mountains charnockites	1000 Ma	15
central VA BR, Virginia	Pedlar River Charnockite	1021 ± 36 Ma	16
Oaxacan Complex, Mexico		1080 Ma	17
Pine Mountain basement massifs	Woodland Gneiss	1080 Ma	18
VA BR; Thornton Gap to Wolftown		1146 ± 6 Ma	19
Bunger Hills, Antarctica	Charnockite Peninsula pluton	1151 ± 4 Ma	20
Adirondacks, New York	Gore Mountain Charnockite	1154 ± 17 Ma	21
Southwest Norway	Hidderskog	1160 Ma	22
Windmill Islands, Antarctica	Ardery Charnockite Intrusions (ACI)	1163 ± 7 Ma	23
Adirondacks, New York	Diana Complex	1164 ± 11 Ma	21
Pine Mountain basement massifs	Cunningham granite	1165 Ma	18
Adirondacks, New York	Snowy Mountain Charnockite	1174 ± 25 Ma	21
Adirondacks, New York	Minerva Charnockite	1176 ± 9 Ma	21
Bamble, S Norway		1.31 Ga	24
W Ontario, Grenville Province		1.31 Ga	25
Southwest Sweden	Varberg	1400 Ma	26
Varberg, SW Sweden		1.42 Ga	27
Laramie Range, Wyoming	Sherman granite	1435 Ma	28
Long Range Mountains, Newfoundland	Western Brook Pond Charnockite	1466 ± 10 Ma	14
central VA BR, Virginia	Pedlar River Charnockite	1489 ± 118 Ma	16
Ketilidian, S Greenland		1.78 Ga	29
Lofoten Islands, Northern Norway		1792 Ma	30
S Lake Baikal, Siberia		1.87 - 1.89 Ga	31
Lofoten Islands, Northern Norway	Hopen charnockite	1950 Ma	32, 33
Sao Francisco Craton-Costeiro Mobile Belt Transition zone, Brazil	Pedra Dourada Charnockite	Paleoproterozoic	34
Archean			
Mysore, South India	Kabbaldurga charnockite	Late Archean	35
N Tamil Nadu, S India		2.40 - 2.57 Ga	36
S Karnataka, S India		2.52 - 2.58 Ga	37, 38, 39
N Transvaal, Limpopo Belt, S. Africa		2.67 Ga	40
Archaean Minto block, northeastern Superior Province, Canada	Minto	2688, 2725 Ma	41
	Desliens	2723 Ma	42
	Utsalik	2725 Ma	43
Bjornesund, SW Greenland		2.80 Ga	44
Wind River Range	Louis Lake	2630 Ma	45

mangerite-charnockite-granite (AMCG) massifs.

This study includes petrologic, geochemical, geochronologic, and isotopic analyses of the Vale charnockite and enclosing Walker Top Granite in an effort to resolve the petrologic and tectonic evolution of the charnockite. Due to the limited extent and occurrence of the Vale charnockite, these results will be compared to other charnockites to delimit a working hypothesis for the formation and emplacement mechanisms.

Sample Description

The Vale charnockite occurs as several xenoliths within the Walker Top Granite of the Cat Square terrane (Fig. 5-1). The main occurrence of the Vale charnockite, located in the western portion of the outcrop, is a large, lenticular xenolith that is 3.7 m long and has a variable thickness ranging from 0.7 m to 1.1 m. Along the length of the outcrop, several other smaller pods up to 1 m in length can be found with contact relationships similar to the main, larger xenolith. The contact relationship between the Vale charnockite and Walker Top Granite varies from sharp to gradational at the boundaries of the xenoliths (Fig. 5-1). The sharp contact may be an apparent contact because the quality of weathered surfaces makes it difficult to determine whether the contact is sharp or gradational. At the gradational contact, foliation, grain size, and grain shape are concordant across a color change from white-gray to translucent brown-green feldspars. Compositionally, there is a transition from orthopyroxene-clinopyroxene-hornblende-biotite-bearing mafic bands in the charnockite to dominantly biotite in mafic bands of the Walker Top Granite. More detailed field and petrologic descriptions (Figs. 2-19, 2-20), and modal analyses (Table 2-5) for the Vale charnockite and Walker Top Granite at the Vale exposure are provided in Chapter 2.

Granitoid Geochemistry

Methodology

Fresh samples of both the Vale charnockite and Walker Top Granite were collected at the Vale outcrop ~100 m west of the Vale Post Office along NC St. Rd. 1113 (Reepsville Road) in

Figure 5-1. Contact relationships between the Walker Top Granite and Vale charnockite in the Vale, North Carolina, south-facing outcrop along NC St. Rd. 1113 (Reepsville Road). The larger body of the Vale charnockite occurs on the western portion of the outcrop. Smaller occurrences of charnockite, outlined in white in the upper, panoramic photograph, are observed toward the central portion of the outcrop. The solid white lines represent a solid contact; the dashed white lines represent a gradational contact. Abbreviations: WT-Walker Top Granite; VC-Vale charnockite.

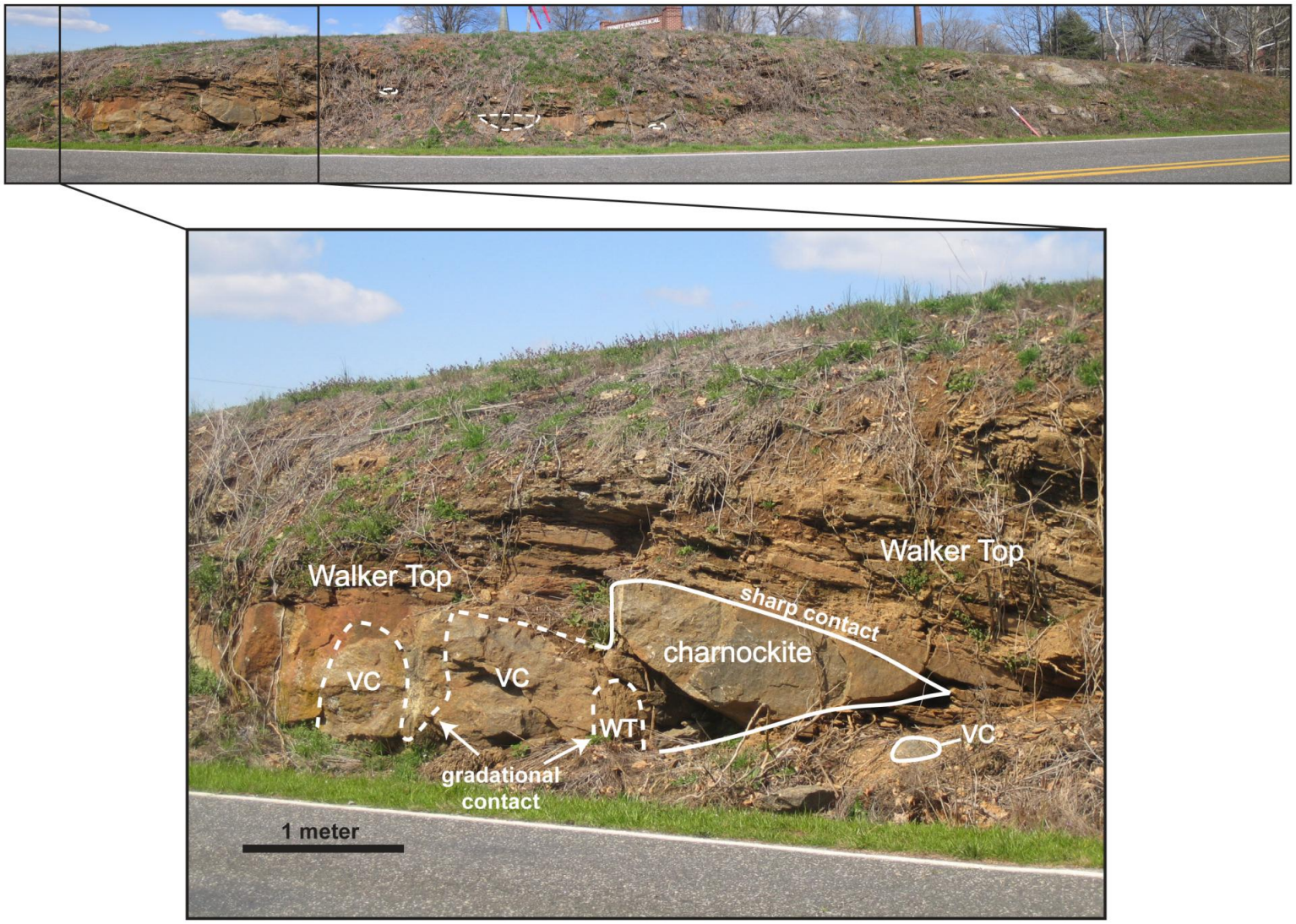
Walker Top
Walker Top
sharp contact
charnockite
VC
VC
WT
VC
gradational
contact
1 meter

the Banoak 7.5-minute quadrangle (Fig. 5-2). In addition, geochemical analyses are presented here of one sample of Toluca Granite and a second sample of Walker Top Granite from the Cherryville and Reepsville 7.5-minute quadrangles, respectively (Fig. 5-2). Each sample was cut into three or more thin (5.0 cm x 3.0 cm x 1.0 cm) representative slabs on a diamond bit trim saw, rinsed with isopropyl alcohol and dried. Slabs were broken into 1.0 cm x 0.5 cm or smaller fragments. Approximately 30 grams of each sample were crushed into a fine powder using an alumina ceramic mill and Shatterbox™. Powders were sent to Activation Laboratories in Ancaster, Ontario, for whole-rock geochemical analysis. Major elements, and Ba, Be, Sr, V, and Y were determined using inductively coupled plasma (ICP) emission spectroscopy employing lithium metaborate/tetraborate fusion (FUS-ICP). Total digestion (TD-ICP) methods were used to determine Ag, Cd, Cu, Ni, Pb, S, and Zn. Trace and rare earth elements (REE) were determined by fusion methods (FUS-MS) and instrumental neutron activation analysis (INAA) (Table 5-2). Data plots were constructed using Igpet05 and CIPW norms were calculated using the CIPW application.

Major Element Compositions

Normative mineralogy was calculated using major elements obtained in whole-rock analyses (Table 5-3). FeO/Fe_2O_3(total) was assumed to equal 0.89 (Rollinson, 1993), because only total iron was measured during analysis. Walker Top and Toluca samples meet the 10 percent normative quartz requirement to be classified on the Barker (1979) modified normative feldspar (Ab-An-Or) diagram (Fig. 5-3). The Vale charnockite was also plotted although its normative quartz is 9.36. All samples cluster in the granite field close to the granite-granodiorite boundary. This observation is consistent with modal mineralogy (Table 2-5; Fig. 2-10). The Vale charnockite produces a variable normative mineralogic composition compared to the Walker Top and Toluca Granites (Table 5-3). The presence of normative hypersthene and diopside, from elevated concentrations of Fe_2O_3(total), MnO, and CaO, is also consistent with ortho- and clinopyroxene present in modal mineralogy (Table 2-5).

Differences in major element compositions can be more readily distinguished by looking at variation diagrams (Fig. 5-4). The Vale charnockite is an outlier with respect to its SiO_2

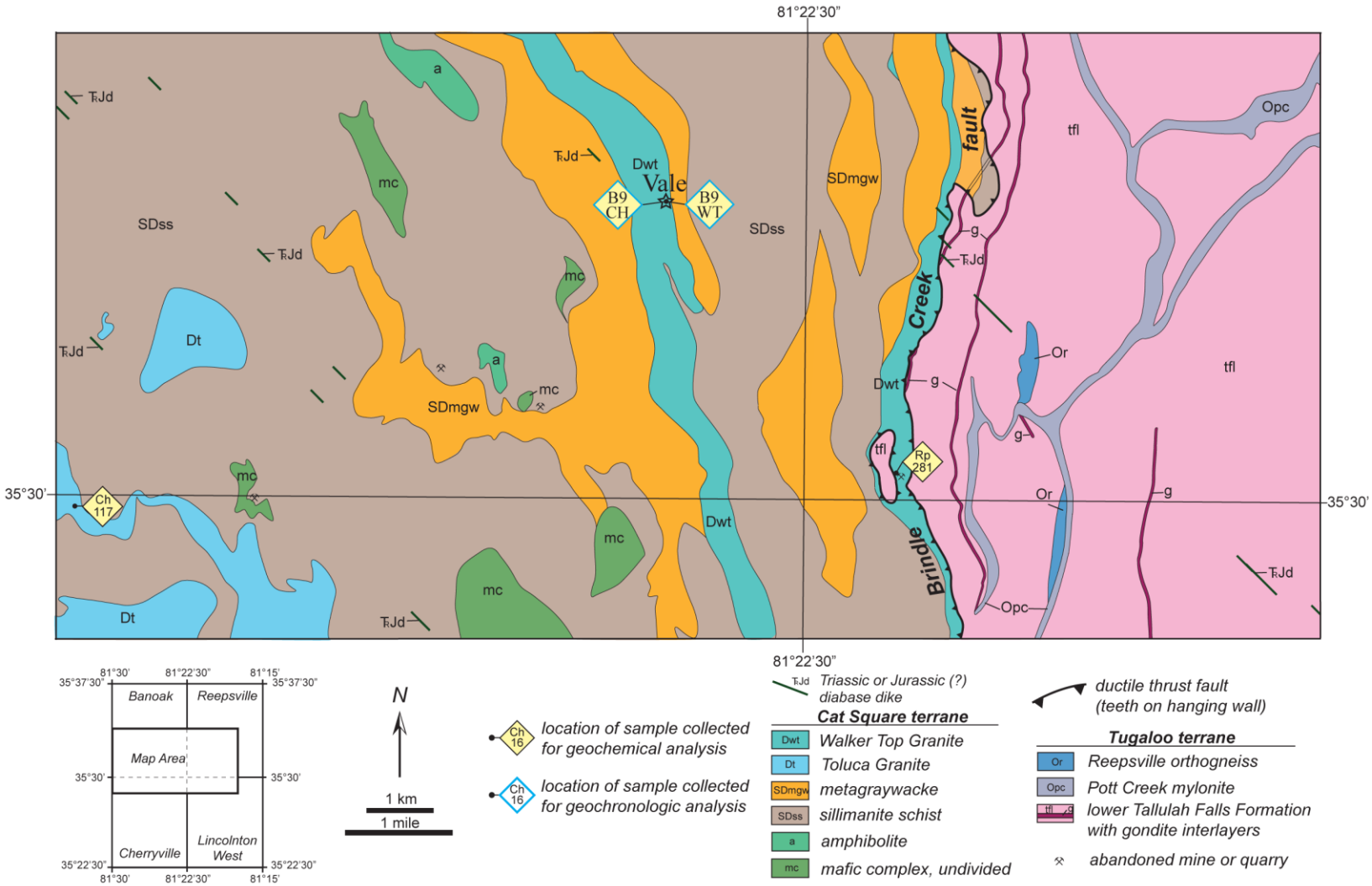

Figure 5-2. Simplified geologic map of the study area showing the location of granite samples collected for whole-rock geochemical analysis and geochronology.

Table 5-2. Whole-rock oxide weight percents and trace element (ppm and ppb) concentrations for the Walker Top Granite and Vale charnockite.

	Sample ID	B9-WT	B9-CH	Rp281	Ch117
	Rock Unit	Walker Top Granite	Vale Charnockite	Walker Top Granite	Toluca Granite
Analysis Type	Detection Limit				
FUS-ICP					
SiO_2	0.01%	64.67	59.35	64.81	71.65
Al_2O_3	0.01%	15.01	16.22	15.35	14.85
Fe_2O_3(total)	0.01%	7.21	8.81	5.9	3.01
MnO	0.001%	0.124	0.127	0.088	0.1
MgO	0.01%	1.84	1.68	1.41	0.47
CaO	0.01%	3.22	4.12	3.11	2.19
Na_2O	0.01%	2.56	3.26	2.5	3.16
K_2O	0.01%	3.47	4.26	4	3.73
TiO_2	0.001%	0.99	1.335	0.95	0.189
P_2O_5	0.01%	0.33	0.44	0.3	0.06
LOI		0.23	-0.26	0.72	0.31
	TOTAL %	99.67	99.35	99.13	99.72
Ba	1 ppm	679	1051	869	477
Be	1 ppm	2	2	1	3
Sr	2 ppm	184	221	217	204
V	5 ppm	78	76	75	13
Y	1 ppm	71	33	44	30
INAA					
Au	1 ppb	< 1	< 1	< 1	< 1
As	1 ppm	< 1	< 1	< 1	< 1
Br	0.5 ppm	< 0.5	< 0.5	< 0.5	1
Co	0.1 ppm	14.1	13.7	11	3
Cr	0.5 ppm	33.1	27.9	31	8
Hg	1 ppm	< 1	< 1	< 1	< 1
Ir	1 ppb	< 1	< 1	< 1	< 1
Sb	0.1 ppm	< 0.1	0.2	0.1	0.1
Sc	0.01 ppm	17.1	16.6	13.2	9.5
Se	0.5 ppm	< 0.5	< 0.5	< 0.5	< 0.5
W	1 ppm	< 1	< 1	< 1	< 1

Table 5-2. *continued.*

Sample ID	Detection Limit	B9-WT	B9-CH	Rp281	Ch117
Rock Unit		Walker Top Granite	Vale Charnockite	Walker Top Granite	Toluca Granite
Analysis Type					
FUS-MS					
Bi	0.1 ppm	< 0.1	< 0.1	< 0.1	< 0.1
Cs	0.1 ppm	1.1	0.9	0.7	0.9
Ga	1 ppm	26	26	20	15
Ge	0.5 ppm	1.3	1.3	1.6	1.9
Hf	0.1 ppm	9.6	22.8	11.1	5.7
In	0.1 ppm	< 0.1	< 0.1	< 0.1	< 0.1
Mo	2 ppm	< 2	< 2	< 2	< 2
Nb	0.2 ppm	25.7	39.9	13.4	5.6
Rb	2 ppm	150	99	120	113
Sn	1 ppm	< 1	< 1	< 1	< 1
Ta	0.1 ppm	1	1.5	0.5	0.2
Th	0.05 ppm	29.9	6.57	30.4	18.5
U	0.05 ppm	1.72	1.63	1.06	2.93
Zr	1 ppm	388	978	484	190
La	0.05 ppm	74.8	65.1	91.7	42.8
Ce	0.1 ppm	159	138	183	88.7
Pr	0.02 ppm	17.8	15.9	24.8	10.9
Nd	0.05 ppm	63.1	58.5	81.7	37.3
Sm	0.01 ppm	12.7	11.8	14.8	7.77
Eu	0.005 ppm	1.61	2.42	2.26	1.46
Gd	0.02 ppm	10.4	9.43	11.2	6.57
Tb	0.01 ppm	1.7	1.23	1.71	1.03
Dy	0.02 ppm	11	6.52	9.06	5.98
Ho	0.01 ppm	2.52	1.22	1.69	1.1
Er	0.01 ppm	8.21	3.51	4.76	3
Tl	0.05 ppm	0.98	0.65	0.76	0.85
Tm	0.005 ppm	1.23	0.503	0.675	0.42
Yb	0.01 ppm	7.31	3.19	3.99	2.61
Lu	0.002 ppm	1.03	0.489	0.55	0.362
TD-ICP					
Ag	0.5 ppm	< 0.5	< 0.5	< 0.5	< 0.5
Cd	0.5 ppm	0.5	< 0.5	< 0.5	< 0.5
Cu	1 ppm	13	8	20	37
Ni	1 ppm	15	12	16	< 1
Pb	5 ppm	27	24	27	39
S	0.001%	0.058	0.043	0.056	0.007
Zn	1 ppm	110	139	77	40

Table 5-3. CIPW Normative mineralogy of analyzed granitoid samples.

	Sample ID	B9-WT	B9-CH	Rp281	Ch117
	Rock Unit	Walker Top Granite	Vale Charnockite	Walker Top Granite	Toluca Granite
Normative mineralogy					
Quartz		24.2	9.9	24.2	32.1
Corundum		2.0	—	2.0	1.8
Orthoclase		20.5	25.2	23.6	22.0
Albite		21.7	27.6	21.2	26.7
Anorthite		13.8	17.1	13.5	10.5
Diopside		—	0.4	—	—
	wollastonite	—	0.2	—	—
	enstatite	—	0.1	—	—
	ferrosilite	—	0.2	—	—
Hypersthene		12.4	13.3	9.7	4.9
	enstatite	4.6	4.1	3.5	1.2
	ferrosilite	7.8	9.2	6.1	3.7
Magnetite		1.6	1.9	1.3	0.7
Ilmenite		1.9	2.5	1.8	0.4
Apatite		0.8	1.0	0.7	0.1

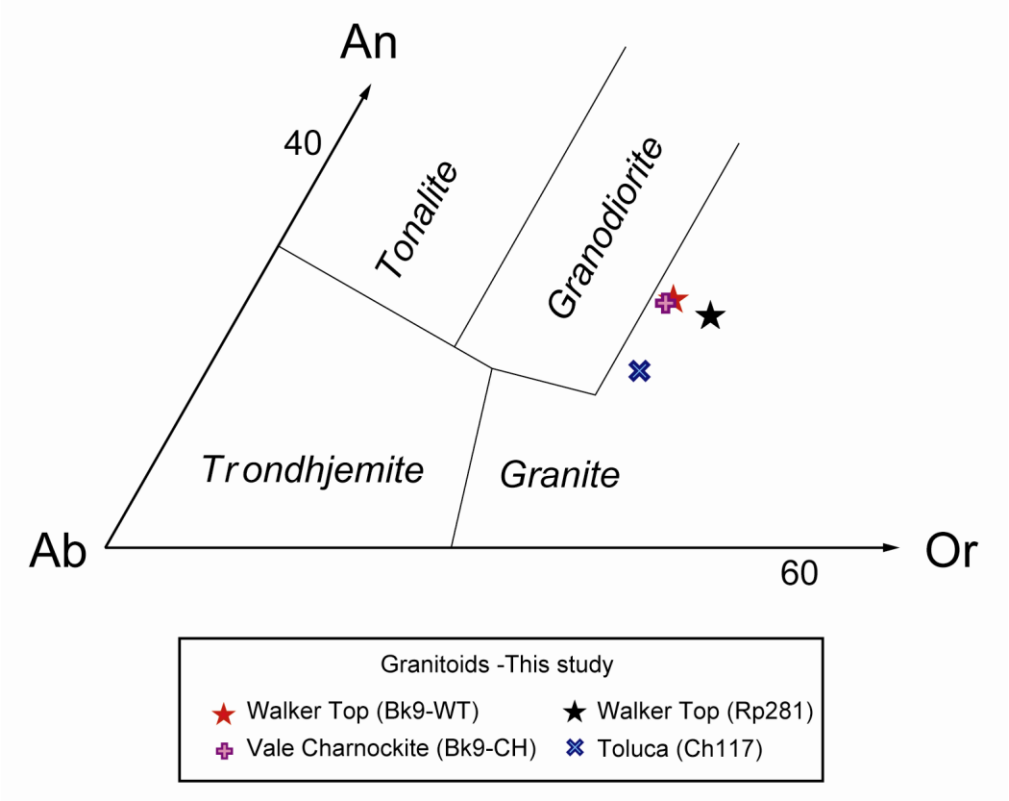

Figure 5-3. Ab-An-Or diagram (Barker, 1979) showing the composition of rocks based on normative values.

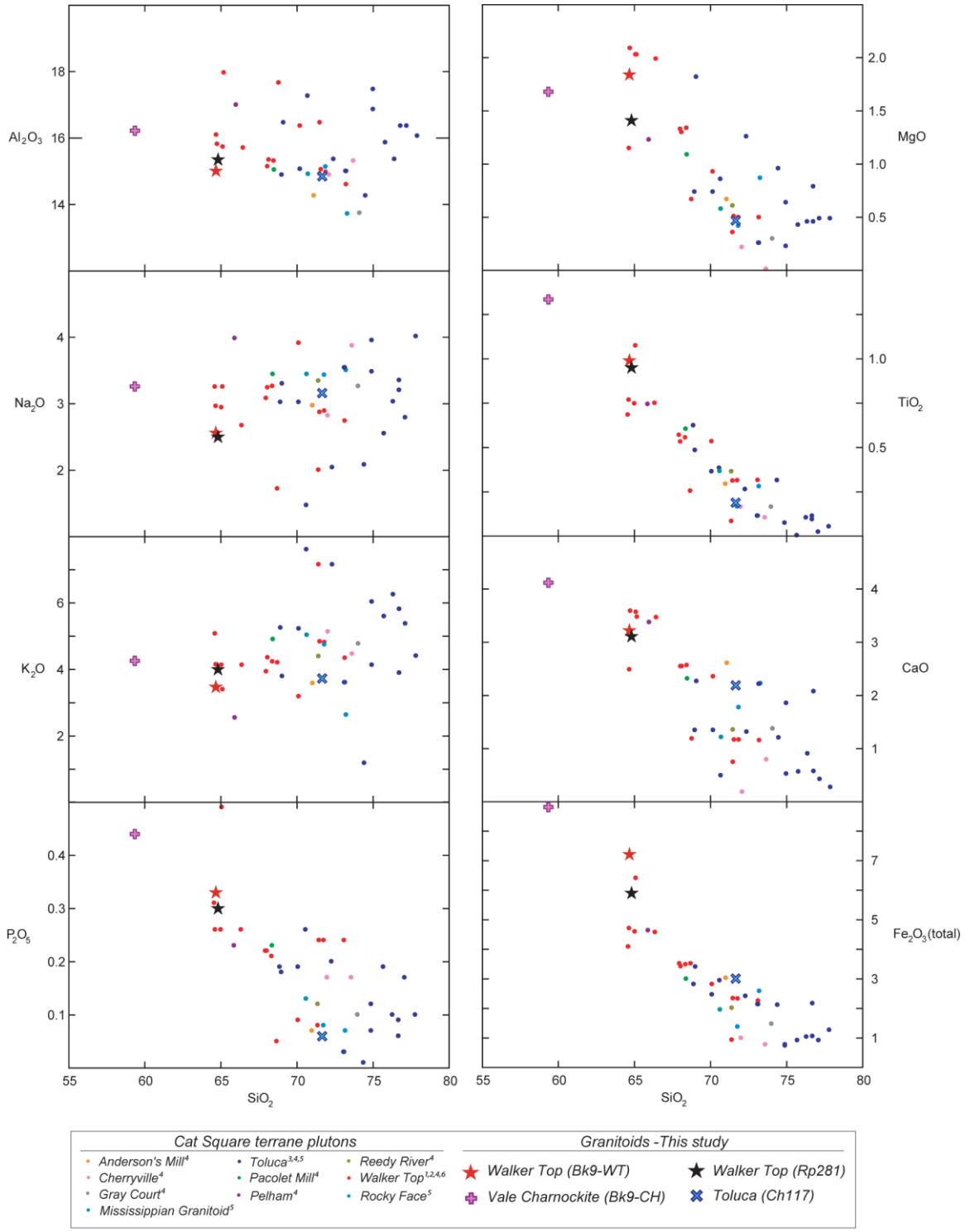

Figure 5-4. Harker variation diagrams showing variation of major-element oxides with silica in Cat Square terrane plutons. Sources: 1–Giorgis, 1999; 2–Vinson, 1999; 3–Bier, 2001; 4–Mapes, 2002; 5–Wilson, 2006; 6–Gatewood, 2007.

weight percent (59%) when compared to this and previous studies of Cat Square terrane plutonic rocks. Walker Top Granite samples from across the Cat Square terrane, including the two samples in this study, have the second lowest amounts of SiO_2 (65-70%) compared to other granitoids in the terrane (66-78%). Overall, the Vale charnockite and Walker Top Granite from the Vale outcrop distinguish themselves with higher amounts of Fe_2O_3(total), CaO, P_2O_5, TiO_2, MgO, while having similar amounts of K_2O, Na_2O, and Al_2O_3 as other granitoids (Fig. 5-4). Chemical composition variations are reflected in the modes of the samples as described in Chapter 2 (Table 2-5). Using the Alkali Saturation Index (ASI) and Modified Alkali-Lime Index (MALI), the Walker Top Granite is metaluminous calc-alkalic while the Vale charnockite is metaluminous alkali-calcic (Figs. 5-5a, b).

Frost et al. (2001) proposed a classification of granitic rocks based on Fe number (Fe #) [FeO/(FeO+MgO)] with larger Fe# values being ferroan and lower values magnesian. Both samples from the Vale outcrop have larger Fe # values classifying them as ferroan (Fig. 5-5c). Other Cat Square terrane granitoids span the transition between ferroan and magnesian in composition (Fig. 5-5c). Frost and Frost (2008) noted that most magnesian plutons tend to be calcic or calc-alkalic whereas ferroan ones tend to be alkali or alkali-calcic. The majority of charnockites, including the Vale charnockite, remain metaluminous and are ferroan alkali to alkali-calcic.

Rare Earth Element Compositions

Rare earth element (REE) diagrams were used in order to see if there were significant disparities in source chemistry during magmatic evolution (i.e., fractionation). The Vale charnockite and Walker Top Granite have very similar REE concentrations with a well-defined negative Eu anomaly and steep negative slope when normalized to condrite (Fig. 5-6a). The granites have the same light REE concentrations (~200 x condrite), but the Walker Top Granite has a more negative Eu anomaly and elevated levels of heavy REEs (~40 x vs. ~20 x condrite). This difference can be accounted for by the larger amount of garnet in the Walker Top Granite (Table 2-5). The second Walker Top Granite sample (Rp281) and Toluca Granite (Ch117) parallel the trend of the Vale charnockite. When normalized to upper continental crust, samples

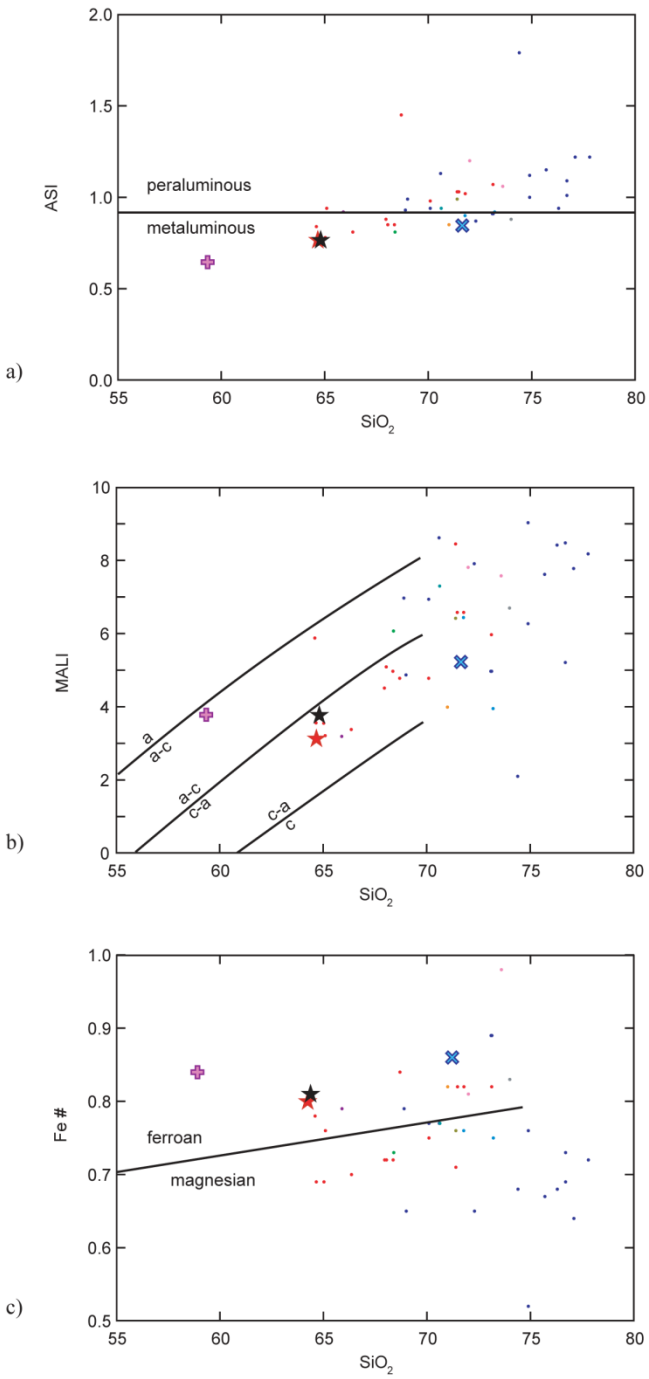

Figure 5-5. Classification of Cat Square terrane plutons. a) Variation of the aluminum saturation index (ASI) with silica. ASI = Al/(K + Na + 2Ca) where cation values are in parts per million. b) Variation of the modified alkali lime index (MALI) with silica. MALI = $(Na_2O + K_2O) – CaO$ where oxide values are in weight percent. Abbreviations: a - alkalic, a-c = alkali-calcic, c-a = calc-alkalic, c = calcic. Boundaries after Frost et al. (2001a). c) Iron and magnesium variation plotted as Fe# (Frost et al., 2001). Fe# = $Fe_2O_3(T)/(Fe_2O_3(T)+MgO)$ where oxide values are in weight percent and $Fe_2O_3(T)$ represents total iron measured during analysis. Boundary after Frost et al. (2001). Symbols same as in Fig. 5-4.

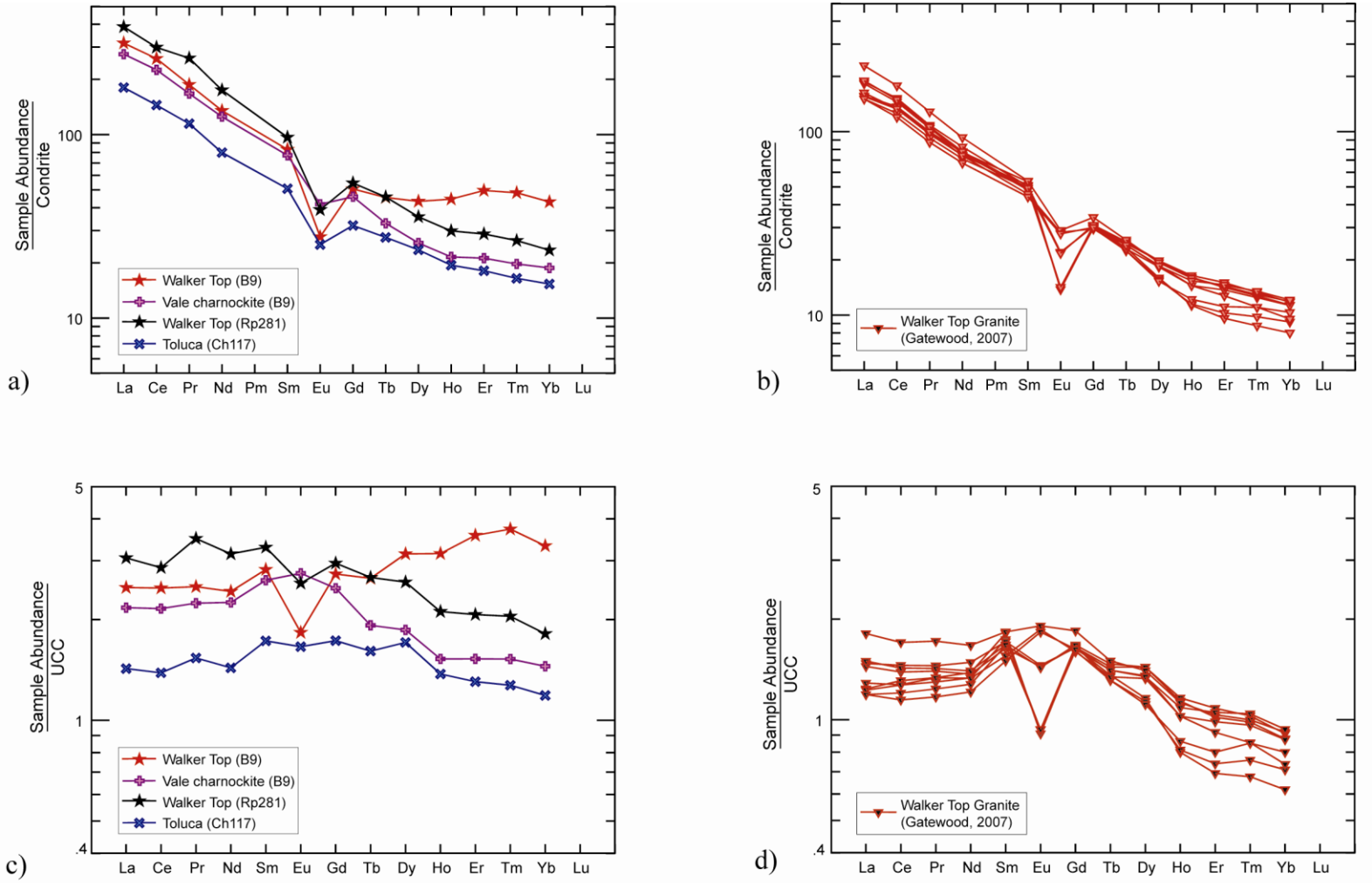

Figure 5-6. Condrite-normalized REE plots (Sun and McDonough, 1989) of a) granites from this study and b) other Walker Top Granite samples (Gatewood, 2007). Upper Continental Crust normalized plots (Taylor and McLennan, 1985) of c) granites from this study and d) other Walker Top Granite samples (Gatewood, 2007).

have comparable trends that are relatively flat and only slightly enriched (Fig. 5-6b). These patterns and abundances of REEs resemble those of other Walker Top Granites sampled in the Cat Square terrane (Gatewood, 2007) (Figs. 5-6c, d).

Trace Element Compositions

Another way to delimit changes in overall chemistry of source and crystal-melt processes is observation of the trace element character of the granites. Again, the Vale charnockite and Walker Top Granite have very similar values and trends (Figs. 5-7, 5-8a). Variation diagrams of select trace elements plotted against silica reflect these similarities (Fig. 5-7). Overall, the Vale charnockite has elevated values of Ba, V, Cr, Nb, Zr, Ni, and Sc relative to other Cat Square terreane granites and similar amounts of Rb, Th, and Sr. On a primordial mantle normalized spider diagram, all granites have an enrichment of large ion lithophile (LIL) and high field strength (HFS) elements. Marked differences between the Vale granites occur as lower concentrations of Th and higher concentrations of Hf and Zr in the Vale charnockite. An added zircon with the right concentration of these HFS elements in the Vale charnockite powder analyzed could explain these variations. Other minor variations seen in concentrations of Nb and Ta could be due to abundance or lack of minerals such as sphene, ilmenite, and rutile (Fig. 5-8a). Cat Square terrane plutons have similar trace element trends between bodies (Fig. 5-8b).

Tectonic Discriminant Diagrams

Several discriminant diagrams were utilized in order to approximate tectonic environments for formation of the granites, understanding that these plots are subjective to mineral assemblage, and a range of other factors. The Walker Top Granite and Vale charnockite plot in both the volcanic-arc and within-plate granite fields on bivariate diagrams constructed by Pearce et al. (1984; Fig. 5-9). Pearce et al. (1984) suggested the accumulation of ferromagnesian minerals and minor phases may shift a point from the volcanic-arc to within-plate granite field on Nb-Y and Rb-(Y+Nb) plots. When further subdivided using Hf-Rb/30-Ta*3 and Hf-Rb/10-Ta*3 plots, all Walker Top Granite samples and the Vale Charnockite plot in the volcanic-arc

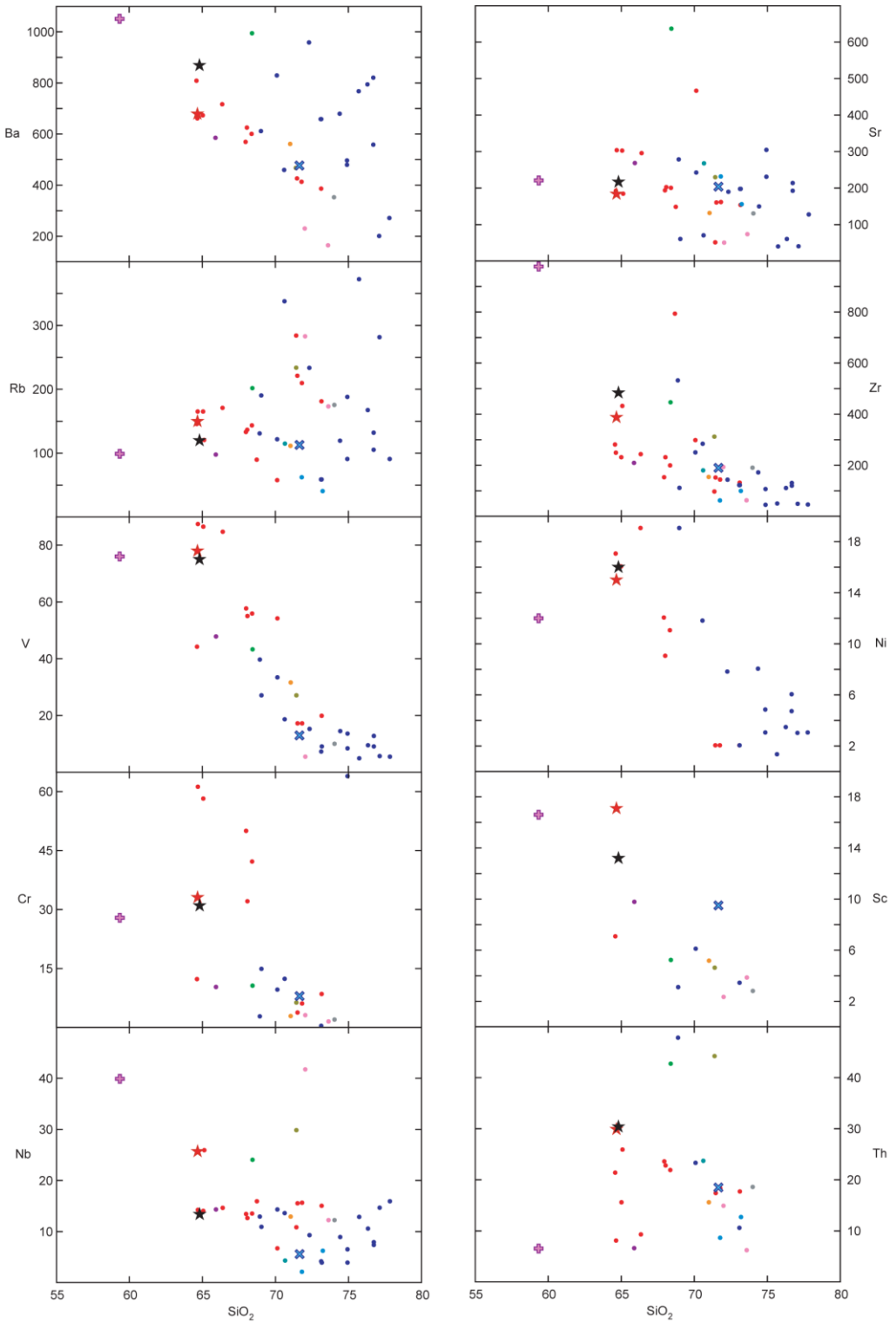

Figure 5-7. Harker variation diagrams showing variation of select trace elements with silica in Cat Square terrane plutons. Symbols same as in Fig. 5-4.

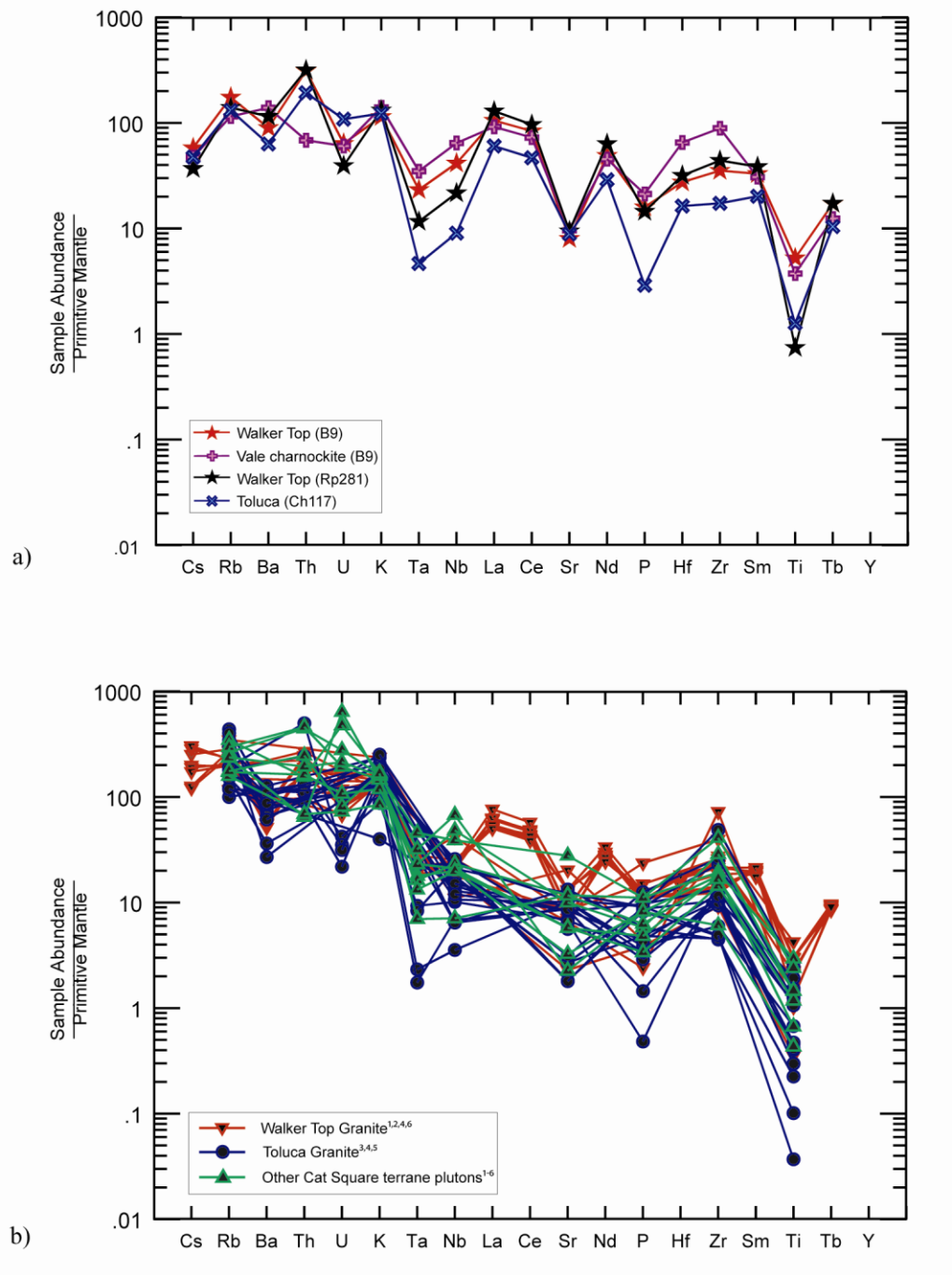

Figure 5-8. Primitive mantle-normalized trace elements (Wood et al., 1979) from a) granites in this study and b) other Cat Square terrane plutons. Sources: 1–Giorgis, 1999; 2–Vinson, 1999; 3–Bier, 2001; 4–Mapes, 2002; 5–Wilson, 2006; 6–Gatewood, 2007.

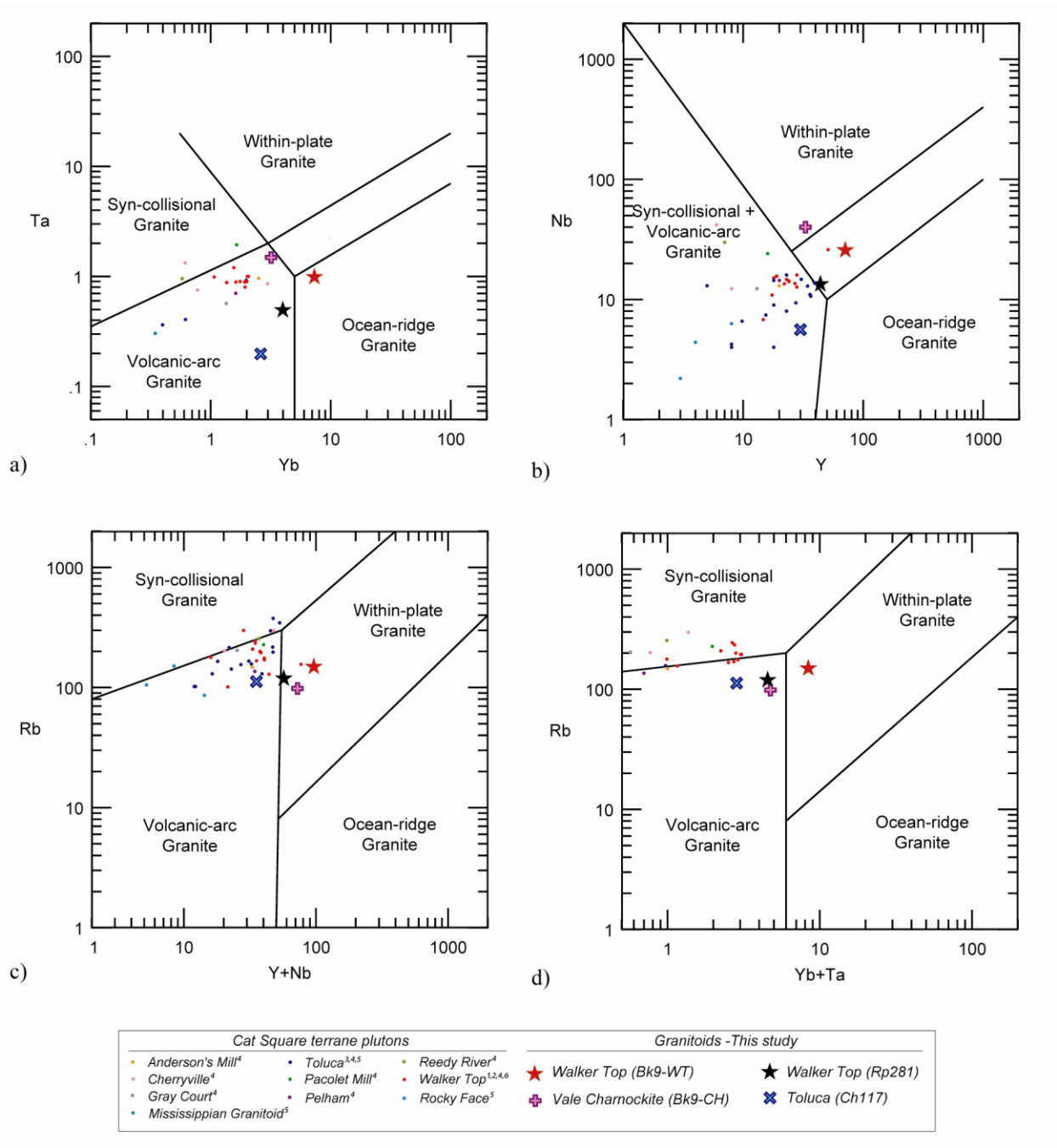

Figure 5-9. Tectonic discriminant diagrams (Pearce et al., 1984). Sources: 1–Giorgis, 1999; 2–Vinson, 1999; 3–Bier, 2001; 4–Mapes, 2002; 5–Wilson, 2006; 6–Gatewood, 2007.

field (Figs. 5-10a, b). Assuming a volcanic-arc affinity for the granites, Rb/Zr-Nb and Rb/Zr-Y plots (Brown et al., 1984) indicate these granites are normal to mature continental arc granites, illustrating a positive correlation with an increase in values with increasing arc maturity (Figs. 5-10c, d). Zr-10^4Ga/Al and Nb-10^4Ga/Al plots show that the Vale Charnockite and Walker Top Granite samples are A-type granites, while the Toluca Granite falls in the I- and S-type granites field (Figs. 5-10e, f). The Zr-10^4Ga/Al diagram may not be the best indication of granite types because the amount of Zr is adversely affected based on the number of zircon grains in the analyzed powder.

Zircon Saturation Thermometry

Whole-rock Zr concentration (ppm) values were used in zircon saturation thermometry calculations to obtain temperature estimates for comparison to those of Mapes (2002) and Miller et al. (2003). The equation used for these calculations is from Harrison and Watson (1983). Zircons in the Walker Top Granite and Vale charnockite lack xenocrystic cores and have minimal metamorphic rim overgrowths (see next section), indicating the melts were Zr undersaturated. Miller and Meschter (2001) and Miller et al. (2003) suggested estimates for inheritance–poor rocks approximate minimum magmatic temperatures. Previous estimates for zircon saturation temperatures (T_{Zr}) for Inner Piedmont plutons ranged from 810 to 950° C and averaged ~837° C (Mapes, 2002; Miller et al., 2003).

The Vale charnockite has a considerably higher amount of Zr (978 ppm) compared with the Walker Top Granite (388 ppm) at the Vale outcrop and other Inner Piedmont plutons (200-800 ppm; Miller et al., 2003) (Fig. 5-7). This difference does not have much effect in T_{Zr} differences for the granites. The Vale charnockite has a T_{Zr} of 839° C, while the Walker Top Granite has a T_{Zr} of 802° C. The other Walker Top (484 ppm) and Toluca Granite (190 ppm) samples presented here produce T_{Zr} of 824° C and 768° C, respectively. These results are consistent with those previously mentioned and are minimum temperature estimates. It is important to note that these temperatures are below typical dry melting conditions and within the range of normal hydrous melts. Hydrous magmatic mineral assemblages of Inner Piedmont

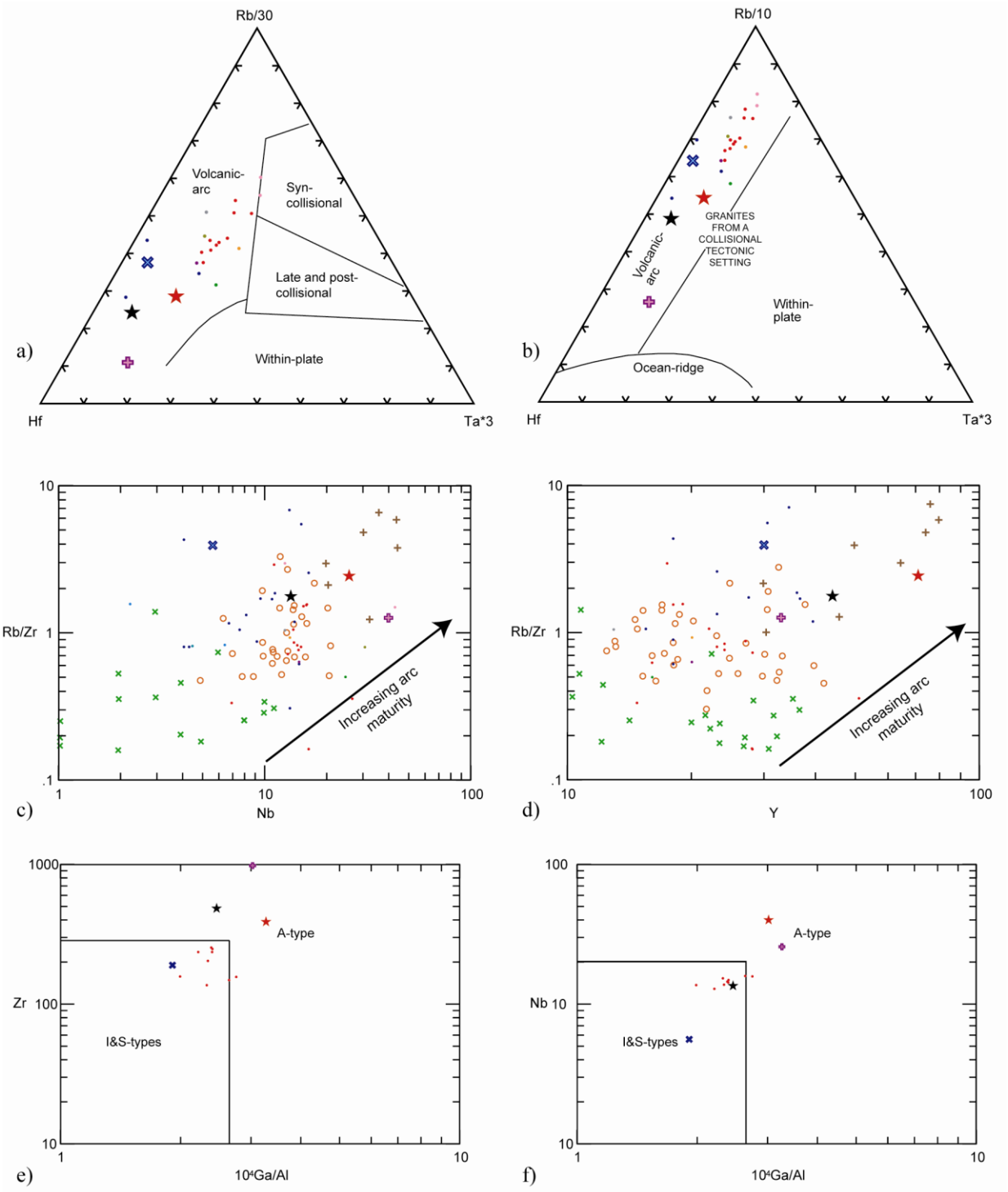

Figure 5-10. Tectonic discriminant diagrams: a & b) Hf-Rb/30-Ta*3 and Hf-Rb/10-Ta*3 (Harris et al., 1986); c) Rb/Zr-Nb and d) Rb/Zr-Y diagrams showing increasing arc maturity (Brown et al., 1984). Green x–primitive island arc and continental arcs; orange o–normal continental arc; brown + –mature continental arc. e) Zr-10^4Ga/Al and f) Nb-10^4Ga/Al (Whalen et al., 1987). Symbols same as in Fig 5-9.

plutons, except the Vale charnockite, suggest magmas were fairly water-rich (Mapes, 2002).

Zircon Geochronology

Methodology

Samples of the Vale charnockite and Walker Top Granite from the Vale outcrop were collected for geochronologic analysis. Zircon separation techniques were carried out at Vanderbilt University and the Stanford University–U. S. Geological Survey Micro Analysis Center (SUMAC). Initial crushing of the samples to gravel-sized fragments and smaller was done by hand. Samples were further crushed and sieved to <500 μm. Density sorting was done using a water table followed by heavy liquids to separate out less dense minerals. Magnetic minerals were removed using a Frantz magnetic separator. 20-30 zircon grains were hand-picked under a binocular microscope for analysis. At SUMAC, these grains were mounted in epoxy and polished to the average grain center. Cathodoluminescence (CL) images were taken using a Jeol 5600 LV scanning electron microscope equipped with a Hamamatsu photo multiplier. These with reflected light images, collected at SUMAC, were used to assess shape, zoning, morphology, and structural integrity (presence or absence of fractures and inclusions) of grains prior to analysis. The SHRIMP-RG was operated under standard operating conditions (Bream et al., 2004). U-Pb-Th, trace, and rare-earth element analyses were performed in sequential analytical sessions using a 15-20 μ spot and methods described by Mazdab and Wooden (2006). Data were obtained from eight Walker Top Granite zircons and nine Vale charnockite zircons. Core-rim pairs were measured for possible inherited cores as well as timing of metamorphic overgrowth. Standard R33 (~419 Ma), provided by SUMAC, was measured every fifth analysis. All data were reduced using the computer program SQUID v. 1.02 (Ludwig, 2001). Age calculations and plots to display data were made using Isoplot v. 3.0 (Ludwig, 2003).

Zircon Morphology

Walker Top Granite zircons range from 200-675 μm long, from 75-280 μm wide, and have aspect ratios between 1:2 and 1:5.9. The grains are commonly subhedral, acicular, doubly terminated when not broken. CL imaging reveals normally concentric to modified oscillatory zoning in the center of the zircons with minor metamorphic overgrowths (Fig. 5-11a). Metamorphic rims typically embay and truncate zoning in zircon cores. Some grains display convoluted zoning from having recrystallization transgressing in the grain driven by dissolution or regrowth along fractures.

Vale charnockite zircons very closely resemble those of the Walker Top Granite. Grains range from 175-550 μm long, from 75-175 μm wide, and have aspect ratios between 1:1.8 and 1:5. Reflected light images reveal that inclusions are more abundant in zircons from this sample than the Walker Top Granite zircons. Most zircons have normally concentric to modified oscillatory zoning with metamorphic overgrowths (Fig. 5-11b). Grains that are not zoned are fairly uniform in color, and may have been dissolved and reprecipitated during metamorphism. Shapes range from subhedral to anhedral, acicular to stubby, and are commonly doubly terminated.

Based on observed grain shape and morphology, the majority of zircons in both the Walker Top Granite and Vale charnockite are magmatic in origin. The few zircons described above that appeared to be metamorphic in origin were not analyzed.

Age Results

All grains analyzed yielded middle Paleozoic U-Pb ages ranging from Late Devonian to early Mississippian (Table 5-4). No inherited cores were observed or measured. Some rims returned older ages than the innermost part of the zircon. This could be interpreted as later recrystallization of zircon from a fracture that penetrated the zircon to its core, as indicated by CL images. Another explanation could be Pb loss or U enrichment in parts of the grains. Concordia and weighted average plots at 2σ error, and relative probability plots at 1σ error, were made using ^{207}Pb corrected $^{206}Pb/^{238}U$ ages at 95 percent confidence (Figs. 5-12, 5-13).

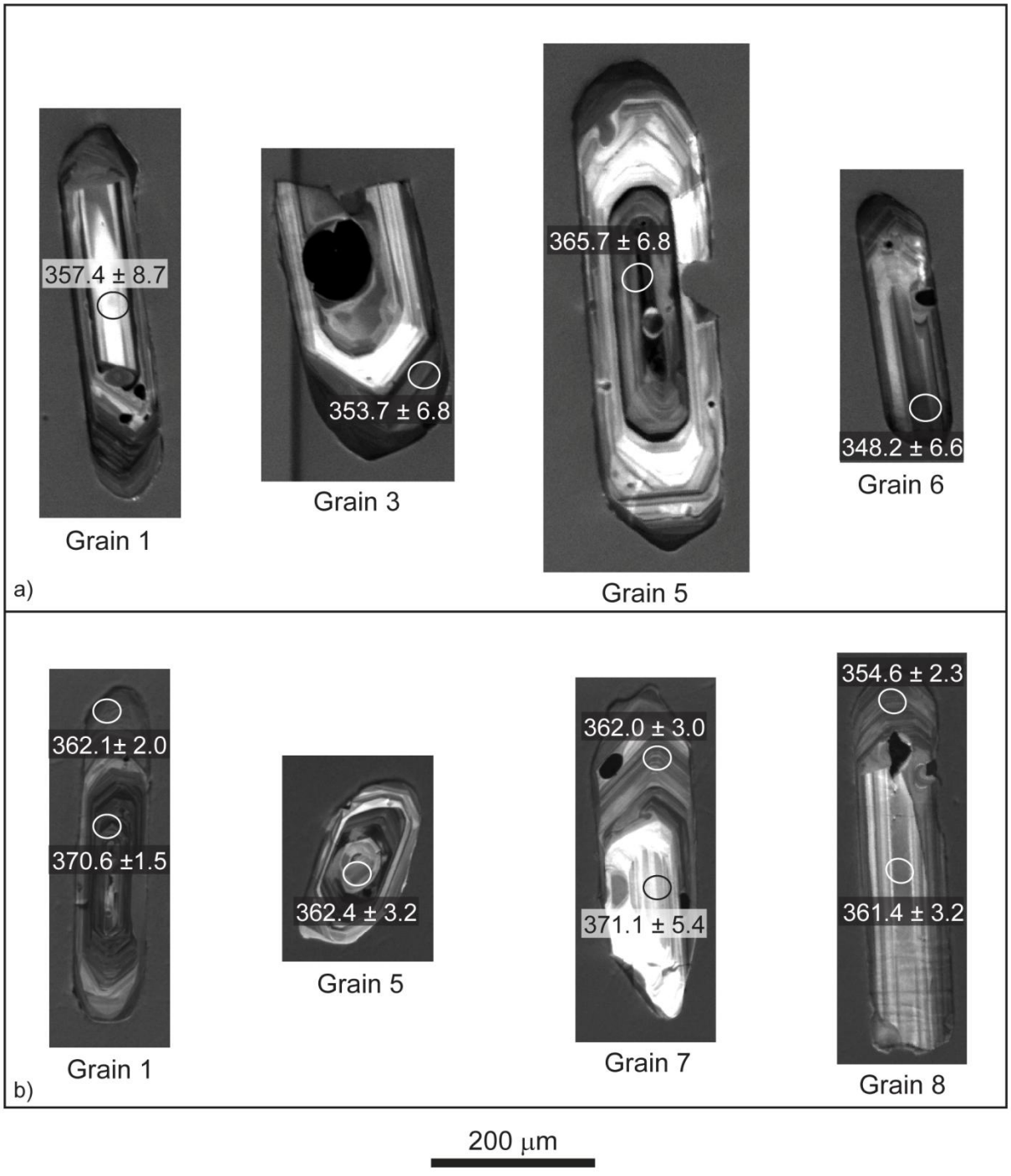

Figure 5-11. Cathodoluminescence images and ages of representative a) Walker Top Granite zircon grains and b) Vale charnockite zircon grains. Size and location of spot analyses are indicated on each zircon. Scale same for a and b.

Table 5-4. SHRIMP-RG U-Th-Pb analytical results for the Vale charnockite and Walker Top Granite.

					Total				Radiogenic Ratio							207-corrected		208-corrected		204-corrected ages (Ma)				
Analysis Number	Common ^{206}Pb (%)	U ppm	Th ppm	$^{232}Th/^{238}U$	$^{238}U/^{206}Pb$	error (%)	$^{207}Pb/^{206}Pb$	error (%)	$^{206}Pb/^{238}U$	error (%)	$^{207}Pb/^{206}Pb$	error (%)	$^{207}Pb/^{235}U$	error (%)	ρ	$^{206}Pb/^{238}U$	± 1σ	$^{206}Pb/^{238}U$	± 1σ	$^{206}Pb/^{238}U$	± 1σ	$^{207}Pb/^{206}Pb$	± 1σ	%Conc
Vale Charnockite																								
B9-8.2R	-0.23	268	93	0.36	17.72	0.6	.0518	1.9	.0563	0.7	.0503	2.7	0.39	2.7	.238	354.6	2.3	352.5	2.4	353.2	2.2	210	62	168
B9-6.1R	0.14	221	85	0.40	17.46	0.7	.0549	2.0	.0572	0.7	.0530	2.9	0.42	3.0	.249	358.6	2.6	359.3	2.8	358.3	2.6	329	65	109
B9-3.1R	0.09	300	48	0.16	17.37	0.5	.0544	1.5	.0577	0.5	.0556	1.8	0.44	1.9	.282	360.5	1.9	360.7	1.9	361.4	1.9	438	41	83
B9-8.1C	0.14	151	119	0.81	17.32	0.9	.0549	2.5	.0575	0.9	.0516	3.9	0.41	4.0	.225	361.4	3.2	362.4	3.7	360.5	3.2	270	90	134
B9-7.1C	0.16	166	87	0.54	17.29	0.8	.0551	2.4	.0576	0.9	.0516	4.0	0.41	4.1	.210	362.0	3.0	361.6	3.3	361.0	3.0	268	92	135
B9-1.1R	0.04	283	47	0.17	17.30	0.5	.0541	1.6	.0576	0.6	.0520	2.3	0.41	2.4	.233	362.1	2.0	361.8	2.0	361.3	2.0	286	53	127
B9-5.1C	-0.03	157	113	0.75	17.30	0.9	.0536	2.6	.0577	0.9	.0520	3.0	0.41	3.2	.282	362.4	3.2	363.5	3.6	361.6	3.1	286	69	127
B9-9.1C	0.00	452	208	0.48	17.24	0.5	.0538	1.4	.0581	0.5	.0552	1.9	0.44	2.0	.261	363.6	1.8	363.4	2.0	364.2	1.8	421	42	87
B9-3.2C	0.31	102	73	0.74	17.17	0.9	.0563	2.5	.0579	1.0	.0515	5.5	0.41	5.6	.172	363.7	3.3	360.3	3.8	362.7	3.4	262	126	138
B9-2.1C	0.02	587	160	0.28	17.08	0.4	.0540	1.1	.0585	0.4	.0531	1.4	0.43	1.4	.279	366.8	1.4	366.8	1.5	366.4	1.4	331	31	111
B9-9.2R	-0.02	208	81	0.40	16.91	0.7	.0539	2.1	.0589	0.7	.0501	3.6	0.41	3.7	.202	370.4	2.7	370.1	2.8	368.7	2.7	202	84	183
B9-1.2C	-0.06	483	262	0.56	16.91	0.4	.0535	1.2	.0591	0.4	.0530	1.3	0.43	1.3	.304	370.6	1.5	369.7	1.7	370.1	1.5	327	29	113
B9-7.1C2	-0.06	55	40	0.75	16.88	1.4	.0536	4.1	.0590	1.5	.0507	5.7	0.41	5.8	.250	371.1	5.4	371.6	6.0	369.7	5.2	229	131	161
B9-4.1R	-0.29	155	82	0.55	16.84	0.9	.0517	2.6	.0594	0.9	.0517	2.6	0.42	2.8	.324	372.9	3.3	371.8	3.6	371.9	3.2	273	60	136
Walker Top Granite																								
B9WT-8(	0.70	125	54	0.45	18.33	2.0	.0588	2.9	.0538	2.1	.0461	9.6	0.34	9.8	.215	336.7	6.8	337.1	7.3	337.7	6.9	6	230	5570
B9WT-7(	0.16	209	109	0.54	18.12	2.0	.0546	2.2	.0554	2.0	.0577	3.4	0.44	3.9	.502	342.1	6.7	342.3	7.2	347.4	6.7	518	75	67
B9WT-6(	0.18	242	186	0.79	17.79	1.9	.0549	1.9	.0562	1.9	.0549	1.9	0.43	2.7	.714	348.2	6.6	348.8	7.5	352.5	6.6	408	42	86
B9WT-2(	0.12	78	56	0.74	17.74	2.2	.0544	3.4	.0564	2.2	.0544	3.4	0.42	4.1	.543	349.3	7.6	347.8	8.6	353.4	7.6	390	77	91
B9WT-7F	0.31	293	52	0.18	17.61	1.9	.0560	1.6	.0568	1.9	.0560	1.6	0.44	2.5	.765	351.3	6.5	352.1	6.7	356.0	6.6	453	35	79
B9WT-3I	0.00	204	83	0.42	17.54	2.0	.0536	2.1	.0569	2.0	.0518	2.7	0.41	3.4	.583	353.7	6.8	353.4	7.2	356.7	6.8	276	63	129
B9WT-4(	-0.08	299	216	0.75	17.42	1.9	.0530	1.7	.0574	1.9	.0524	1.8	0.41	2.6	.725	356.4	6.7	355.2	7.5	359.7	6.6	304	41	118
B9WT-1C	-0.11	40	20	0.50	17.37	2.5	.0528	4.5	.0576	2.5	.0528	4.5	0.42	5.1	.482	357.4	8.7	355.8	9.4	360.8	8.7	321	102	112
B9WT-8I	0.34	223	102	0.47	17.21	2.0	.0564	2.0	.0578	2.0	.0519	4.2	0.41	4.6	.423	359.2	6.9	359.6	7.4	362.3	6.9	282	96	129
B9WT-2I	-0.25	178	49	0.29	17.11	1.9	.0518	2.1	.0584	1.9	.0509	2.4	0.41	3.1	.634	363.2	7.0	361.5	7.2	365.8	6.9	238	55	154
B9WT-5(	0.09	431	183	0.44	16.93	1.9	.0546	1.3	.0591	1.9	.0546	1.3	0.44	2.3	.825	365.7	6.8	366.5	7.2	369.9	6.8	395	29	94
B9WT-9I	0.05	121	63	0.54	16.93	2.2	.0543	3.1	.0590	2.2	.0528	3.6	0.43	4.2	.513	366.0	7.8	365.2	8.4	369.4	7.8	322	82	115

Note:Corrections for common Pb made using measured ^{204}Pb. See text for analytical details.

C = core; R = rim

%Conc = 100 x [($^{206}Pb/^{238}U$ age) / ($^{207}Pb/^{206}Pb$ age)].

ρ = error correlation of Ludwig (1998).

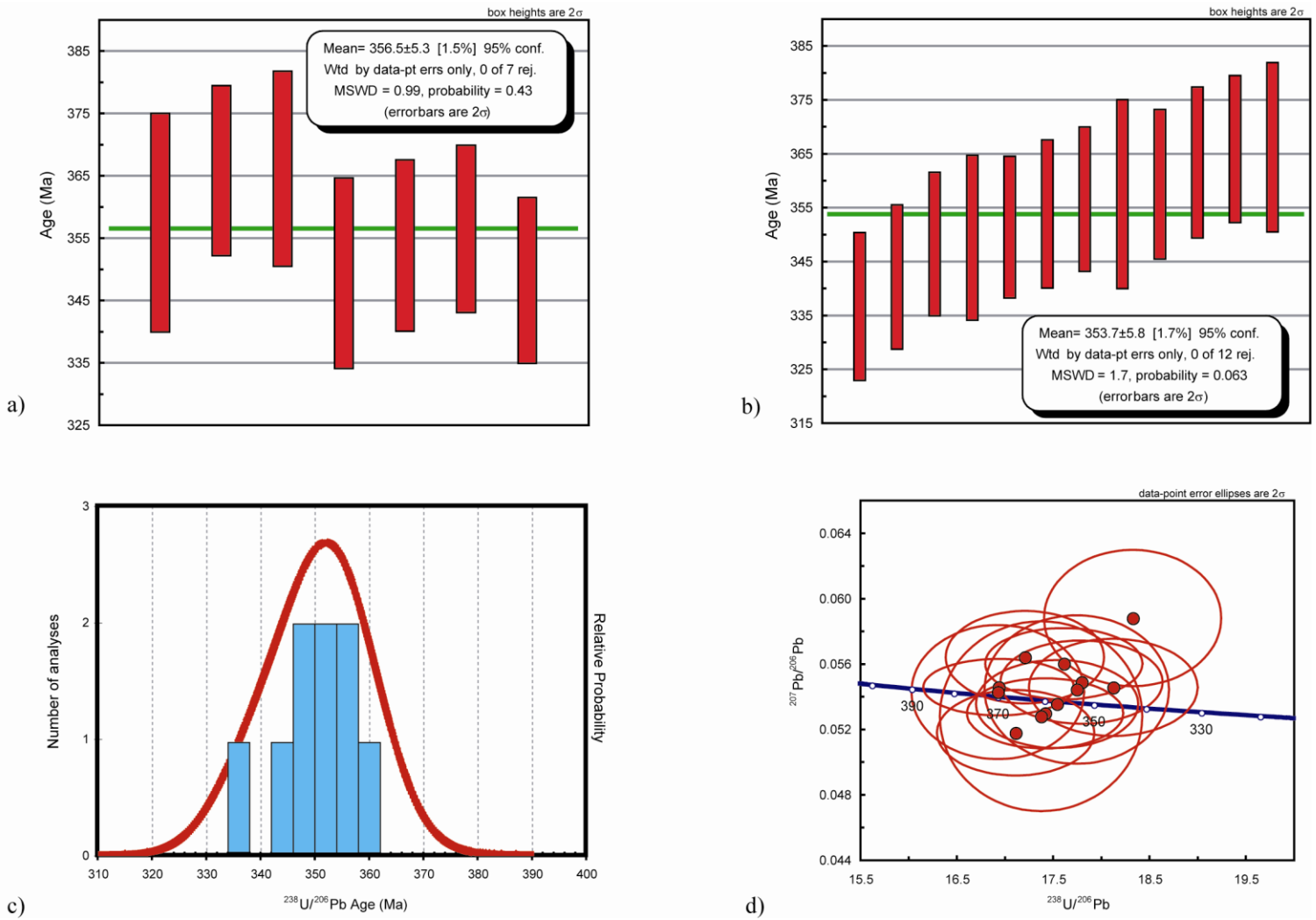

Figure 5-12. U-Pb SHRIMP results for the Walker Top Granite. a) Mean of seven data points thought to represent crystallization. b) Mean of all twelve data points. c) Relative probability plot of all data. d) Tera-Wasserburg concordia diagram of all data. Ages in Ma.

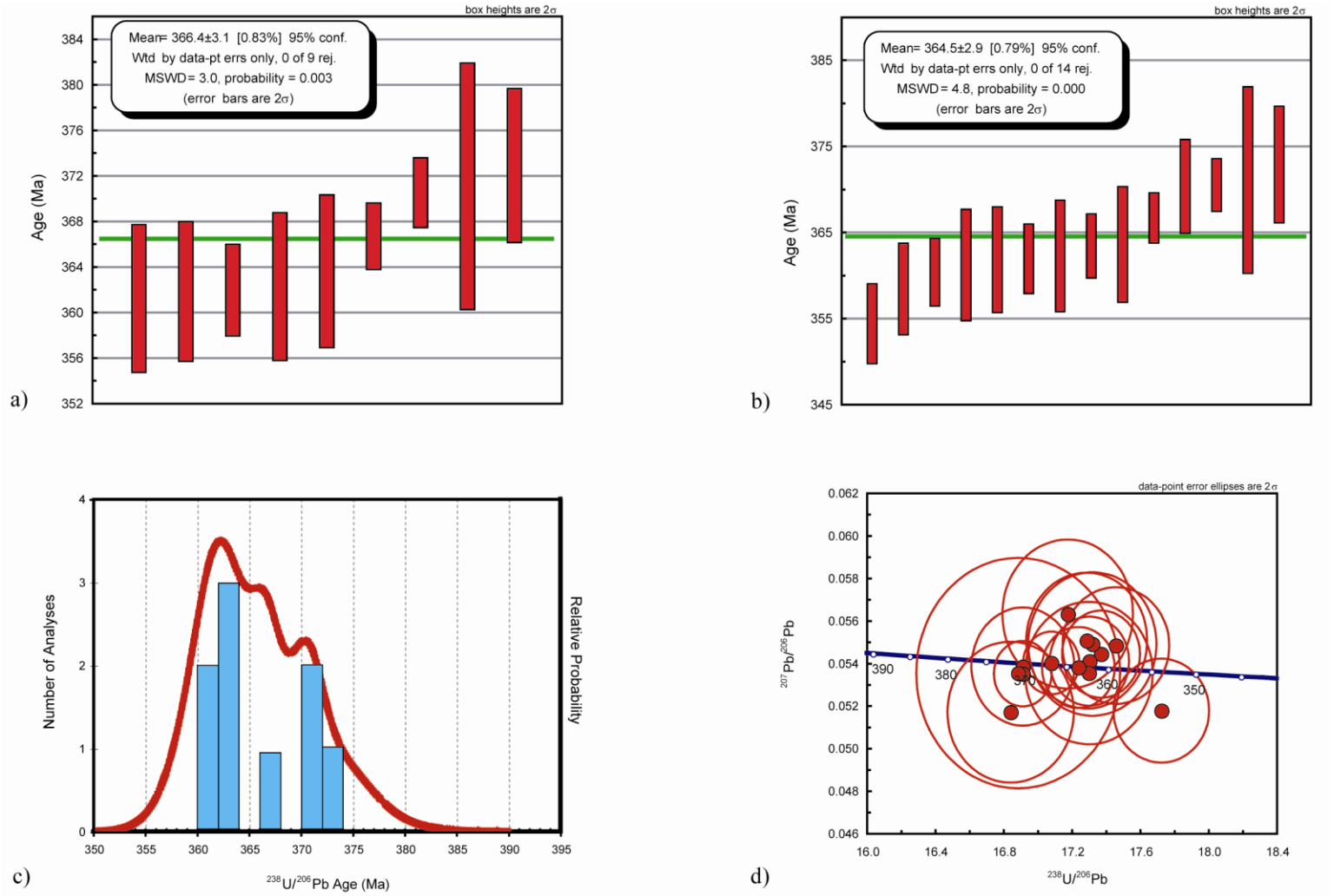

Figure 5-13. U-Pb SHRIMP results for the Vale charnockite. a) Mean of nine data points thought to represent crystallization. b) Mean of all fourteen data points. c) Relative probability plot of all data. d) Tera-Wasserburg concordia diagram of all data. Ages in Ma.

Metamorphic rim ages were separated based on CL images and not used to determine average crystallization ages.

The coherent group of seven Walker Top Granite zircons, interpreted to be magmatic cores, produced $^{206}Pb/^{238}U$ crystallization ages ranging from 348 to 366 Ma. Three points were not used because of elevated ^{204}Pb amounts, or because a younger age was analyzed in the core than the rim. A weighted mean for these seven grains gave an age 356 ± 5.3 Ma (MSWD = 0.99; Fig. 5-12a). When all twelve analyses are taken into consideration, a weighted mean gives an age of 355 ± 5.2 Ma (MSWD = 1.2) (Fig. 5-12b). Metamorphic rims, determined from zircon morphology, produced $^{206}Pb/^{238}U$ ages of ~342 Ma and ~351 Ma. Relative probability plots reveal a peak for crystallization at ~353 Ma (Fig. 5-12c). The data from all Walker Top zircons are concordant within 2σ error, mainly clustering between 350 and 365 Ma (Fig. 5-12d). Vale charnockite zircons produced concordant $^{206}Pb/^{238}U$ ages with crystallization ages ranging from 361-373 Ma from a coherent group of nine analyses. Metamorphic rims yielded ages at ~355 Ma, ~359 Ma, and ~361 Ma. Analyses from grain 9 were not used due to elevated amounts of ^{204}Pb and a reverse of core-rim ages. A weighted mean of the nine crystallization ages gave an age of 366.4 ± 3.1 Ma (MSWD = 3.0; Fig. 5-13a). Data for all fourteen analyses give a weighted mean of 364.5 ± 2.9 Ma (MSWD = 4.8) (Fig. 5-13b). Two peaks, at ~363 Ma and 371 Ma, are revealed from relative probability plots (Fig. 5-13c). Concordant data, within 2σ error, cluster between 360 and 370 Ma (Fig. 5-13d).

Zircon Rare Earth Element Concentrations

The use of zircon REE abundances is a recent venture in the realm of geochronology. Several correlations have been attempted in order to better understand magmatic evolution during zircon fractionation and to relate this to the tectonic environment in which plutons are emplaced. REE data from Vale charnockite and Walker Top Granite zircons have nearly identical condrite-normalized patterns (Figs. 5-14). The profiles exhibit strongly depleted light REE relative to heavy REE with pronounced positive Ce and negative Eu anomalies, suggested to be common to igneous zircons (Whitehouse and Platt, 2003). Elemental variations for the

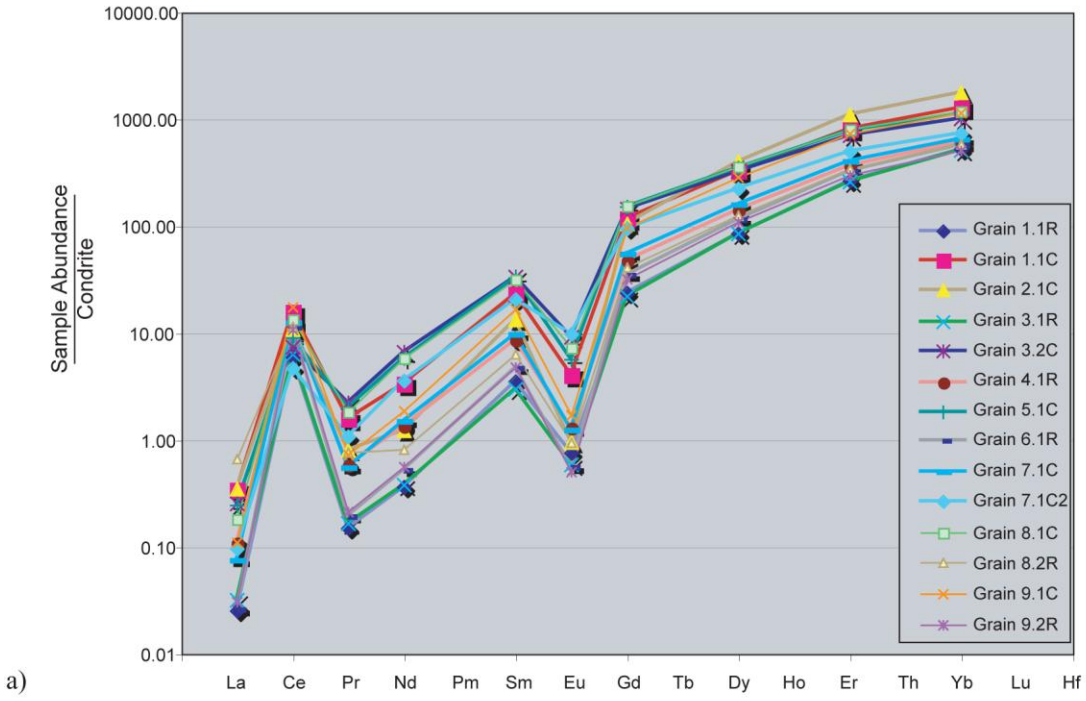

a)

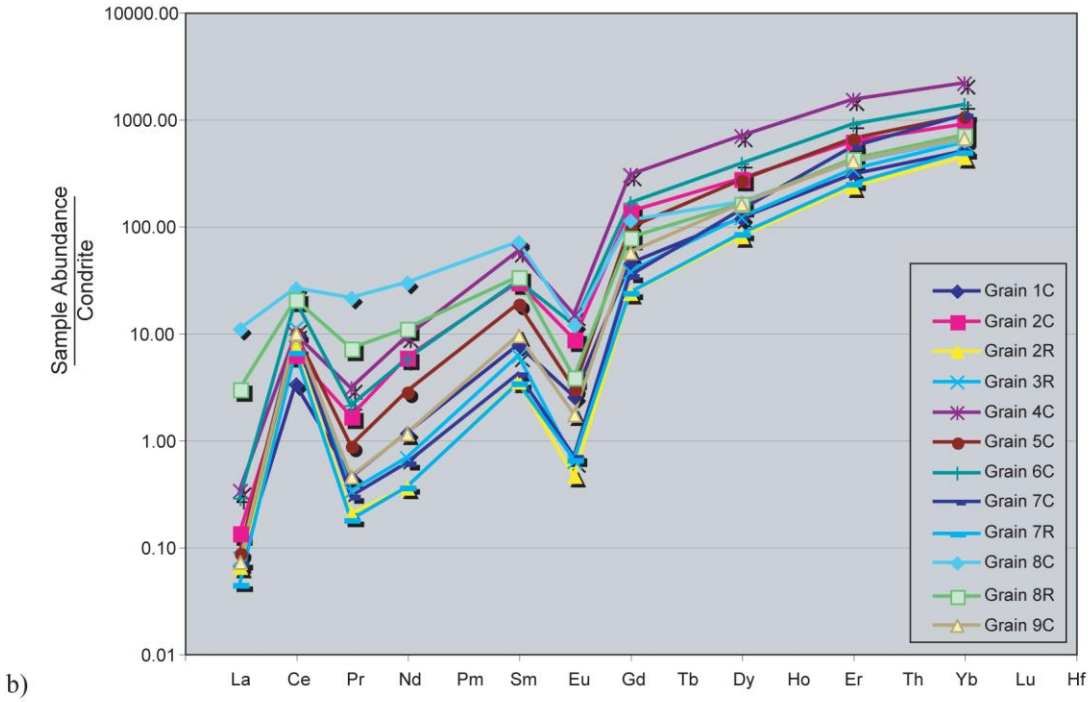

b)

Figure 5-14. Condrite-normalized REE plots from zircons of the a) Vale charnockite and b) Walker Top Granite.

Walker Top Granite zircons are slightly more expansive in concentrations than in the Vale charnockite zircons. A negative Eu anomaly suggests strong feldspar fractionation during zircon growth, while positive Ce anomaly is likely due to favorable conditions for incorporation of smaller amounts of Ce^{4+} in the zircon crystal lattice. The slight concave-down curvature of the heavy REE (Dy-Lu) has been suggested to be due to the heavy REE depletion of melt by crystallization of mafic phases such as orthopyroxene and clinopyroxene (Hoskin and Ireland, 2000). There is an enrichment in La and Pr in one of the Walker Top Granite zircons (grain 8; Fig. 5-14b). Overall, nearly identical patterns may suggest a similar source for zircons from the two granites.

Sourcing: Isotopic Compositions

Methodology

Splits of fragmented Vale charnockite and Walker Top Granite samples used for whole-rock geochemical analysis were employed for Rb-Sr and Sm-Nd analysis. These fragments were sent to the University of North Carolina – Chapel Hill's Isotope Geochemistry Lab for isotopic analysis using a Micromass VG Sector 54 thermal ionization mass spectrometer. Sm-Nd data were collected using the same analytical technique as outlined in Fullagar et al. (1997), while Rb-Sr data were collected using analytical techniques described by Fullagar and Butler (1979) and Kish (1983).

Results

Isotopic values collected for the Vale charnockite and Walker Top Granite are similar to Inner Piedmont plutonic and metasedimentary rocks (Mapes, 2002; Bream, 2003) (Tables 5-5, 5-6; Figs. 5-15, 5-16). Initial $^{87}Sr/^{86}Sr$ ratios for the Vale charnockite, Walker Top Granite, and other Cat Square terrane plutons have a slight correlation with the spatial distribution of the plutons across the Inner Piedmont: granitoids in the eastern portions of the Cat Square terrane have higher ratios, whereas ratios are lower in the western Cat Square terrane (Fig. 5-15a; see Fig. 2-16 for locations of Cat Square terrane granites). One of the few samples of Cat Square

Table 5-5. Rb/Sr isotopic data for the Vale charnockite and Walker Top Granite.

Sample	Rock Type	Age† (in Ma)	Rb (ppm)	Sr (ppm)	$^{87}Rb/^{86}Sr$	$^{87}Sr/^{86}Sr^{(0)}$§ (± 2σ)	$^{87}Sr/^{86}Sr^{(t)}$
B9CH	Vale Charnockite	356 Ma	99	221	1.298	0.716014 (06)	0.70925
B9WT	Walker Top Granite	355 Ma	150	184	2.363	0.720479 (07)	0.70850

† Age is measured U-Pb SHRIMP zircon crystallization age.

(0) Present day values.

§ $^{87}Rb/^{86}Sr$ measured ratios normalized to $^{86}Sr/^{88}Sr = 0.1194$. 2σ errors are reported as last two significant digits.

(t) Values calculated at age of sample.

Table 5-6. Sm/Nd isotopic data for the Vale charnockite and Walker Top Granite.

Sample	Rock Type	Age† (in Ma)	Sm (ppm)	Nd (ppm)	$^{147}Sm/^{144}Nd$	$^{143}Nd/^{144}Nd^{(0)}$§ (± 2σ)	$^{143}Nd/^{144}Nd^{(t)}$	$\varepsilon_{Nd}^{(0)}$‡	$\varepsilon_{Nd}^{(t)}$‡	$T_{(DM)}$* (in Ga)
B9CH	Vale Charnockite	356 Ma	11.8	58.5	0.12198	0.512387 (18)	0.512094	-4.90	-1.4	1.09
B9WT	Walker Top Granite	355 Ma	12.7	63.1	0.12171	0.512278 (24)	0.511995	-7.02	-3.6	1.27

† Age is measured U-Pb SHRIMP zircon age.

(0) Present day values.

§ $^{143}Nd/^{144}Nd$ measured ratios normalized to $^{146}Nd/^{144}Nd = 0.7219$. 2σ errors are reported as last two significant digits.

(t) Values calculated at age of sample.

‡ $\varepsilon_{Nd} = [\{^{143}Nd/^{144}Nd]_{Sample} - [^{143}Nd/^{144}Nd]_{Bulk\ Earth}\}/\{[^{143}Nd/^{144}Nd]_{Bulk\ Earth}\} \times 10^4$.

Bulk Earth present day parameters: $^{143}Nd/^{144}Nd = 0.512638$, $^{147}Sm/^{144}Nd = 0.1967$.

* T_{DM} age calculated according to DePaolo (1981), $\varepsilon_{Nd} = 0.25T^2 - 3T + 8.5$.

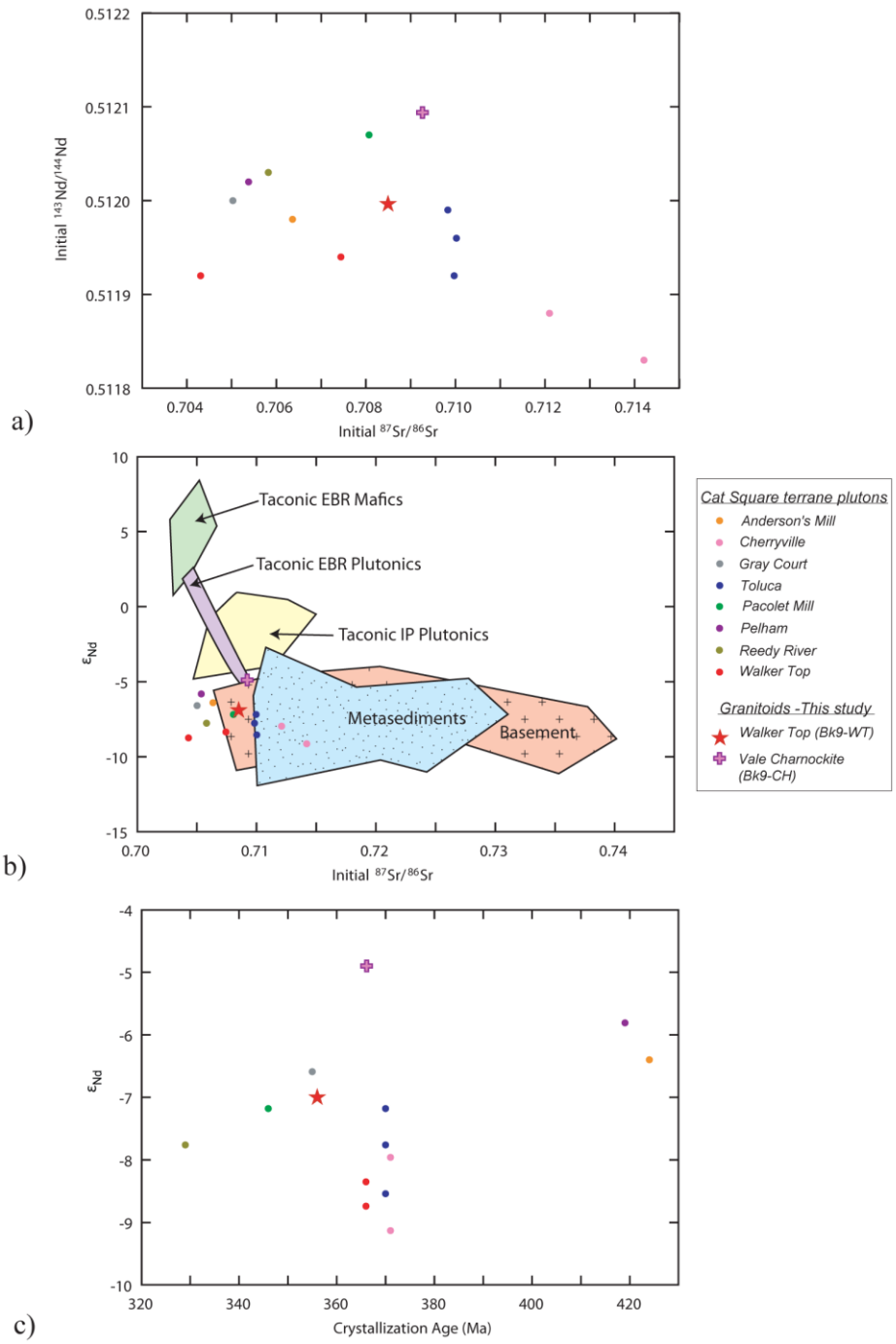

Figure 5-15. Plots comparing isotopic data of the Vale charnockite and Walker Top Granite to other Cat Square terrane plutons and possible source material. a) Initial $^{87}Sr/^{86}Sr$ versus initial $^{143}Nd/^{144}Nd$ showing similarities in values of different granites. b) Initial $^{87}Sr/^{86}Sr$ versus ε_{Nd} of Cat Square terrane plutons showing simlar isotopic values to metasedimentary and basement sources. Fields for Taconic eastern Blue Ridge (EBR) mafics, plutonics, Inner Piedmont (IP) plutonics, metasediments, and basement from Mapes (2002). c) Crystallization age versus εNd of Cat Square terrane granites. Data for Cat Square terrane plutons from Mapes (2002).

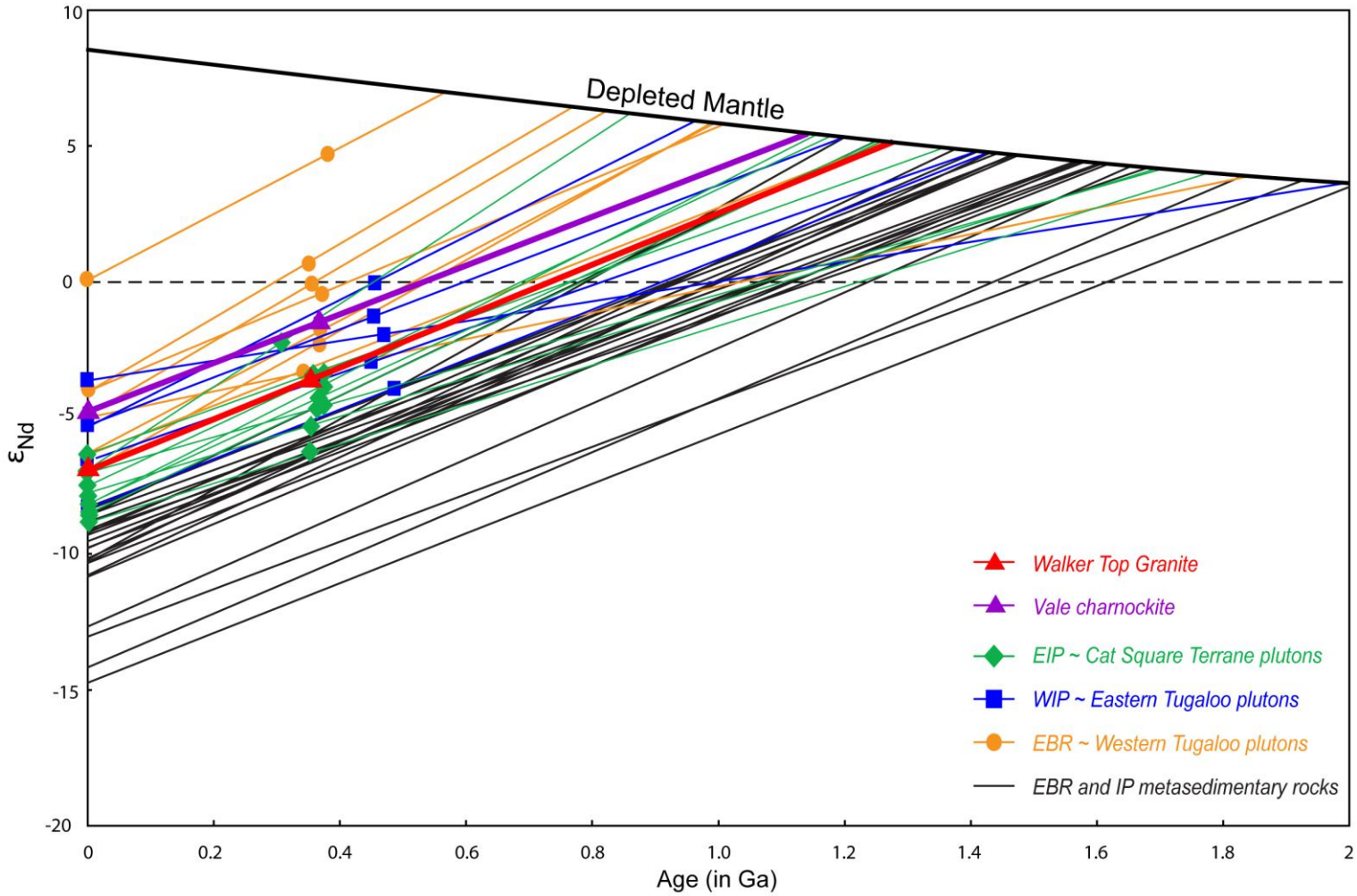

Figure 5-16. ε_{Nd} evolution with of Vale charnockite and Walker Top Granite compared with eastern Blue Ridge and Inner Piedmont granitoids and metasedimentary rocks. Depleted mantle model of DePaolo (1983). Data compiled from Mapes (2002) and Bream (2003). Figure modified from Wilson (2006), Bream et al. (2004) and sources therein.

terrane metasedimentary rocks, from the Benn Knob 7.5-minute quadrangle west of the study area, has an initial $^{87}Sr/^{86}Sr$ value nearly identical (0.709003; Bream, 2003) to the Vale charnockite. Most Cat Square terrane plutons plot near or within the fields for Inner Piedmont and Blue Ridge metasediments and basement rocks (Fig. 5-15b)

Initial ε_{Nd} values for the Vale granitoids are more evolved than most Cat Square terrane plutons (Figs. 5-15, 5-16). The Vale charnockite has the highest initial ε_{Nd} value (-4.90) while the Walker Top Granite initial ε_{Nd} value (-7.02) is higher than other Walker Top Granite samples but average for Cat square terrane plutons (Fig. 5-15c). Initial ε_{Nd} values of the Vale charnockite and Walker Top Granite correspond to depleted mantle model ages (T_{DM}) of 1.09 and 1.27 Ga, respectively (Table 5-6; Fig. 5-16). These data are slightly more evolved than eastern Blue Ridge and Inner Piedmont metasedimentary rocks and Grenville basement at the time of crystallization suggesting derivation from preexisting Grenville and older Laurentian crust. This trend has also been noted for western Inner Piedmont plutons (Fig. 5-16) (Bream, 2003).

Two-Pyroxene and Two-Feldspar Geothermometry

Methodology

A fresh, representative sample of the Vale charnockite was cut perpendicular to foliation, mounted with epoxy on a round slide and polished. The petrography of the sample was examined under reflected and transmitted light, as well as with the energy dispersive spectrometer on the Cameca SX 50 at the University of Tennessee–Knoxville Department of Earth and Planetary Sciences. The thick section was photographed under reflected light in order to make a map of the section, as well as take more detailed pictures of areas of interest for further study. Quantitative analyses were obtained using the wavelength-dispersive component of the Cameca SX 50 electron microprobe. Standard operating conditions for the electron microprobe were as follows: excitation potential of 15 KeV, 10 nA beam current for analyzing feldspars and 20 nA for all other minerals, 1μm spot size, and 20 seconds counting time. Raw data were processed using the PAP program. The main constituents of the charnockite sample were

analyzed to obtain modal compositions, determine if there were any compositional variations within the minerals, and calculate crystallization temperatures.

Mineral compositions

Chemical compositions of the feldspars, biotite, pyroxenes, hornblende, and ilmenite are fairly homogeneous, with only minor variations (Appendix B). Plagioclase grains range from An_{30} to An_{40} and alkali feldspars from Or_{85} to Or_{95} (Fig. 5-17a). Orthopyroxene grains exhibit rather low values of En composition ranging from En_{30} to En_{40}. Clinopyroxene compositions plot in the augite field, exhibiting the most variation of the minerals present in the sample (Fig. 5-17b).

Temperature Estimates

Based on the mineral assemblage present in thin section, a two-pyroxene thermometer (QUILF; Anderson et al., 1993) and a graphical two-feldspar thermometer (Fuhrman and Lindsley, 1988) were employed. The assemblage present in the section analyzed did not permit use of a geobarometer. Several traverses were made across orthopyroxene and clinopyroxene grains, as well as their grain boundaries where the two pyroxenes are in contact. The across-grain values were obtained for use in a two-pyroxene geothermometer (Table 5-7). Values collected on individual feldspar grains and across-grain boundaries were used in the two-feldspar thermometer (Table 5-8).

Several two-pyroxene thermometers were considered for use in this study (Wood and Banno, 1973; Wells, 1977; Lindsley and Anderson, 1983; Davison and Lindsley, 1985; Anderson et al., 1993). The two-pyroxene thermometer program QUILF (Anderson et al., 1993) was chosen based on its approach using a seven-component system (CaO-MgO-MnO-FeO-Fe_2O_3-TiO_2-SiO_2) compared to others thermometers that only incorporate three or four components (typically CaO-MgO-Al_2O_3-SiO_2 or CaO-FeO-SiO_2). Six traverses across clino- and orthopyroxene grain boundaries were used in the 2-pyroxene QUILF calculations (Table 5-7). Pressure and clinopyroxene compositions were treated as variables. A range of pressure

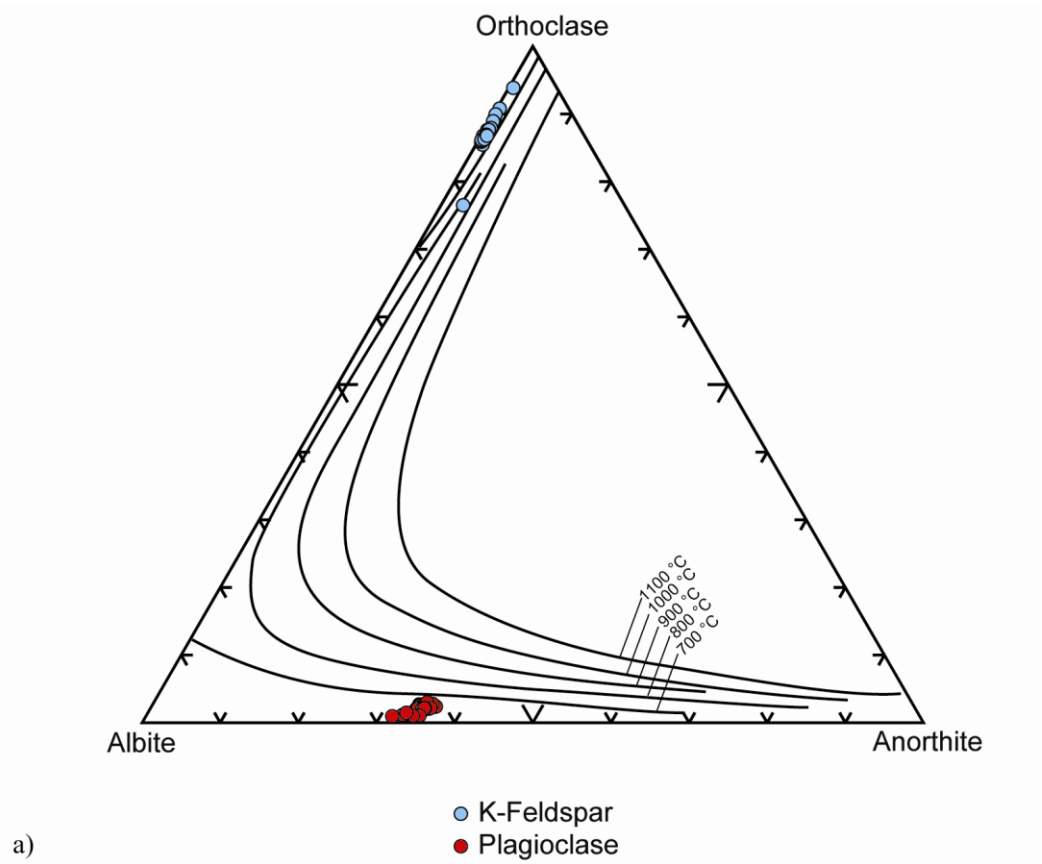

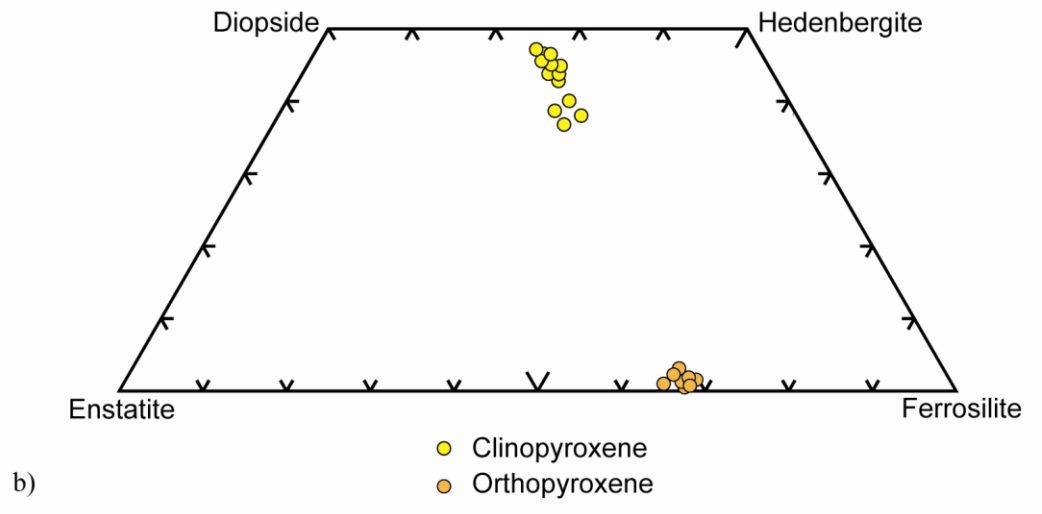

Figure 5-17. Microprobe results of mineral compositions for the Vale charnockite. a) Clino- and orthopyroxene compositions. b) Alkali feldspar and plagioclase compositions. Isotherms, at 1 kbar, from Fuhrman and Lindsley (1988).

Table 5-7. Microprobe data from across grain traverses of ortho- and clinopyroxenes used in the two pyroxene thermometer.

	Traverse 1		Traverse 2		Traverse 3		Traverse 4		Traverse 5		Traverse 6	
Oxides	Opx (15.16)	px (15.18)	Opx (22.58)	Cpx (22.60)	Opx (22.25)	Cpx (22.27)	Opx (15.6)	Cpx (15.8)	Opx (15.10)	px (15.13)	Opx (15.31)	px (15.32)
SiO_2	49.2	51.4	49.1	51.1	51.1	51.0	49.0	50.7	51.0	49.2	51.5	49.6
TiO_2	0.11	0.09	0.04	0.14	0.03	0.16	0.08	0.13	0.13	0.07	0.09	0.03
Al_2O_3	0.64	1.15	0.59	1.21	0.68	1.28	0.58	1.26	1.27	0.61	1.06	0.59
Cr_2O_3	0.00	0.01	0.03	0.03	0.00	0.00	0.03	0.01	0.01	0.03	0.00	0.01
MgO	10.6	8.58	10.4	8.65	9.36	8.50	10.51	8.66	8.39	10.5	8.86	10.8
CaO	0.83	20.7	0.52	20.8	0.68	21.4	0.77	20.4	20.5	0.55	21.4	0.74
MnO	1.02	0.38	0.98	0.34	0.96	0.37	0.95	0.48	0.40	0.95	0.36	1.01
FeO	38.4	18.5	38.5	18.0	37.0	17.3	38.7	18.3	17.8	39.1	16.5	37.9
Na_2O	0.02	0.36	0.00	0.41	0.03	0.40	0.04	0.44	0.36	0.02	0.36	0.01
K_2O	0.02	0.02	0.02	0.01	0.06	0.03	0.00	0.01	0.00	0.01	0.00	0.00
Total	100.76	101.13	100.18	100.69	99.93	100.45	100.69	100.37	99.85	101.00	100.15	100.66
Normalized to 4 Cations*												
Si	1.977	1.976	1.984	1.971	2.045	1.969	1.974	1.967	1.981	1.977	1.985	1.987
Ti	0.003	0.002	0.001	0.004	0.001	0.005	0.002	0.004	0.004	0.002	0.003	0.001
Al	0.03	0.052	0.028	0.055	0.032	0.058	0.028	0.057	0.058	0.029	0.048	0.028
Cr	0.00	0.00	0.001	0.001	0.000	0.000	0.001	0.000	0.000	0.001	0.000	0.000
Mg	0.634	0.492	0.627	0.497	0.558	0.490	0.631	0.501	0.486	0.627	0.509	0.647
Ca	0.036	0.854	0.022	0.861	0.029	0.887	0.033	0.846	0.854	0.024	0.886	0.032
Mn	0.035	0.012	0.033	0.011	0.032	0.012	0.033	0.016	0.013	0.032	0.012	0.034
Fe[a]	1.289	0.594	1.301	0.581	1.237	0.560	1.306	0.592	0.577	1.312	0.533	1.269
Na	0.002	0.027	0.00	0.031	0.003	0.030	0.003	0.033	0.027	0.002	0.027	0.001
K	0.001	0.001	0.001	0.00	0.003	0.001	0.000	0.001	0.000	0.001	0.000	0.000
Total	4.007	4.01	3.998	4.012	3.940	4.012	4.011	4.017	4.000	4.007	4.003	3.999
% En	32.36	25.36	32.15	25.63	30.59	25.30	32.03	25.84	25.35	31.94	26.40	33.21
% Wo	1.84	44.02	1.13	44.40	1.59	45.79	1.68	43.63	44.55	1.22	45.95	1.64
% Fs	65.80	30.62	66.72	29.96	67.82	28.91	66.29	30.53	30.10	66.84	27.65	65.14

Numbers in ( ) represent analysis number as found in Appendix B.

* Cations calculated based on 6 oxygens

[a] All Fe calculated as Fe^{2+}

(2.5 to 11 kbar) estimates calculated for other charnockites (Frost and Frost, 2008) was used for temperature estimates. The QUILF program yielded temperatures from 730-790° C. These temperatures may represent crystallization or metamorphic temperatures.

The two-feldspar thermometer chosen for this study is the graphical projection of isotherms on the feldspar ternary diagram suggested by Fuhrman and Lindsley (1988) (Fig. 5-17b). Plagioclase grains are andesine (An_{30-40}) in composition (Table 5-8). The alkali feldspars are very potassium-rich reflecting an end-member apex value indicating a lack of mixing between K and Na in the orthoclase-albite solid-solution series. These feldspar compositions fall below the 700° C isotherm at 1 kbar. As pressure increases, the isotherms shift to the right, so at higher pressures, the temperature estimate would be lower. These temperatures likely represent post-crystallization requilibration.

Limits on Timing and Emplacement

Outcrop relationships

Sharp and gradational contacts exist between the Vale charnockite and Walker Top Granite. The sharp contact may be a product of assimilation or, possibly, is an apparent contact based on observation on weathered surfaces. If the Vale charnockite is a single xenolith or multiple xenoliths, the gradational contact is likely a product of partial assimilation of the dehydrated charnockite into the hydrous magma of the Walker Top Granite. Another explanation is that the charnockite formed from an influx of CO_2-rich fluids that migrated through the Walker Top Granite, and possibly surrounding rocks, during metamorphism. These and other ideas will be discussed in more detail below.

Geochemistry

Based on whole-rock chemistries, there are slight compositional variations between the Vale granites. Both plot as A-type, ferroan, metaluminous granitoids with normal to mature volcanic-arc to within-plate granite affinities. The Vale charnockite is alkali-calcic while the

Table 5-8. Microprobe data of representative plagioclase and alkali feldspar analyses.

	Plagioclase traverse 1	K-feldspar inclusion	Plagioclase traverse 2	Plagioclase traverse 3	K-feldspar traverse 1	Plagioclase inclusion	K-feldspar traverse 2
# Analyses	7	1	10	7	7	1	11
SiO2	59.4 (2)	63.80	59.2 (2)	58.7 (1)	64.3 (2)	59.1	63.4 (4)
Al2O3	24.9 (2)	18.00	25.2 (2)	24.8 (4)	18.2 (1)	24.8	18.5 (2)
CaO	7.12(15)	0.08	7.31(10)	6.81(24)	0.06 (3)	6.95	0.12 (14)
FeO	0.05 (4)	-	0.05 (2)	0.44(60)	0.02 (3)	0.05	0.02 (1)
Na2O	7.22(10)	0.63	7.07 (9)	7.35(26)	1.25(19)	7.5	1.54 (27)
K2O	0.38(10)	15.60	0.42 (4)	0.18 (3)	15.0 (2)	0.2	14.4 (5)
Total	99.07	98.11	99.25	98.28	98.83	98.6	97.98
Normalized to 5 cations*							
Si	2.674	3.000	2.662	2.665	2.996	2.673	2.979
Al	1.321	1.000	1.334	1.328	1.001	1.321	1.022
Ca	0.343	0.004	0.353	0.332	0.003	0.337	0.006
Fe	0.002	0.000	0.002	0.017	0.001	0.002	0.001
Na	0.630	0.057	0.616	0.647	0.113	0.657	0.140
K	0.022	0.936	0.024	0.010	0.889	0.011	0.865
Total	4.992	4.997	4.991	5.000	5.004	5.001	5.013

All Fe calculated as Fe^{2+}

Units in ( ) represent one standard deviation of replicate analyses in terms of least units cited

* Cations calculated based on 8 oxygens

Walker Top Granite is calc-alkalic. Significant differences of major element compositions are seen in increased concentrations of Fe_2O_3(t), CaO, P_2O_5, TiO_2, MgO compared to other Cat Square terrane granitoids (Fig. 5-4). High amounts of Fe/(Fe+Mg) are thought to be a contributing factor to the formation of charnockite, because biotite is not stable under higher pressures with elevated amounts of iron. Instead, orthopyroxene is the primary crystallizing mineral (Frost et al., 2000). Trace and REE compositions between the Vale charnockite and Walker Top Granite, at the Vale outcrop, reflect nearly identical to moderately variant amounts and patterns. This may be indicative of minor changes in petrologic conditions during formation and crystallization.

Patiño-Douce (1997) attributed similarities in major and trace element compositions of isotopically different A-type granites to the fact that they all form in shallow crust. Zhao et al. (1997) noted that limited variations in chemical and isotopic signatures are consistent with crystal fractionation of dry, hot magmas, with pyroxenes, K-feldspar, plagioclase, apatite, zircon, ilmenite and magnetite as early-crystallizing phases.

Individual mineral analyses in charnockite minerals reveal moderately consistent compositions. The lack of Ca in the plagioclase could be explained by the more felsic composition of the charnockite, or that it was taken in by clinopyroxene and hornblende during crystallization. Because clinopyroxene and hornblende are not abundant in the charnockite, the former explanation is likely. No zoning or exsolution features, other than albite twinning and perthitic textures in feldspars, are observed in the feldspar or pyroxene grains. These data would suggest consistent petrologic conditions during the crystallization of the Vale charnockite.

Geochronology

U-Pb SHRIMP geochronology yielded Late Devonian to early Mississippian crystallization and metamorphic ages for the Vale outcrop granites. The Vale charnockite formed at ~366 Ma and records metamorphism at ~360 Ma. The Walker Top Granite crystallized at ~356 Ma followed by metamorphism from 351-340 Ma. Crystallization and metamorphism of the granites are pre- to syn-tectonic with the Neoacadian orogeny, forming prior to or during peak deformation and metamorphism. Although two distinct ages seem to be present between

zircons of the Vale charnockite and Walker Top Granite, several ages for both plutons are within 2σ error of each other. It could be argued that with a larger number of analyses, there would be more overlap in ages based on the rate of crystallization.

Zircons in the Vale granites contain no evidence of inheritance, which is consistent with other geochronologic studies of Walker Top Granite samples (Mapes, 2002; Gatewood, 2007). Mapes (2002) suggested the rarity of inherited cores indicate Inner Piedmont magmas were zircon undersaturated proposing magmatic temperatures ranging from a minimum of 830° C up to 950° C. Therefore, all potential inherited zircons present in the magma source would have been completely dissolved by hot, zircon undersaturated melts (Mapes, 2002), which is in agreement with findings of Miller and Meschter (2001).

REE data from Walker Top Granite and Vale charnockite zircons are nearly identical in pattern and concentrations. These data may be helpful in observing elemental partitioning during zircon crystallization, but are not an indicator for tectonic or petrologic environment. Hoskin and Ireland (2000) showed that, except for kimberlite and carbonatite, REE data in zircons show no systematic differences. For example, all zones of the Boggy Plain zoned pluton, ranging from pyroxene-rich and plagioclase-rich gabbroic cumulates, through pyroxene-bearing quartz monzodiorites and granodiorites to high-silica granites, which formed from fractional crystallization, have the same zircon REE pattern. Similarly, the Blind Gabbro and Mawson igneous charnockite, both in Australia, exhibit parallel patterns; but the Blind Gabbro formed above a subduction zone, while the Mawson charnockite represents an orogenic magma formed by melting of thickened crust (Hoskin and Ireland, 2000).

Isotopic compositions

Isotopic values for the Walker Top Granite and Vale charnockite reflect those of Cat Square terrane plutons with an evolved range of initial ε_{Nd} and $^{87}Sr/^{86}Sr$ values (-6.4 to -1.6 and 0.7050-0.7142; Mapes, 2002). These values closely resemble limited data for Cat Square terrane metasedimentary rocks and may indicate formation in the shallow crust (Mapes, 2002; Bream, 2003). The Vale granitoids have Mesoproterozoic T_{DM} ages suggesting derivation from Grenville

and older basement rocks. Since other data suggest these granitoids are anatectic melts, the ages may indicate Laurentian-dominated sourcing for Cat Square terrane sediments. Fullagar et al. (1997) concluded the occurrence of Meso- and Paleoproterozoic T_{DM} ages indicates contributions of source components from both Laurentian evolved crust and Carolina terrane volcanogenic materials.

$\delta^{18}O$ values for the Toluca and Cherryville Granitoids in the Cat Square terrane have above 10 percent $\delta^{18}O$ (Mapes, 2002). Mapes (2002) suggested these data reflect pluton generation from more evolved continental sources (9.5–11%), such as local metasediments with some input from juvenile crustal material, instead of mantle source (7–9.5%). Since $\delta^{18}O$ analyses have not been performed on Walker Top Granite or Vale charnockite, these data may not directly reflect the evolution of these magmas.

P-T-t evolution

Two-pyroxene and two-feldspar thermometers yielded results of 730-790° C and <700° C, respectively. These temperatures are >10° C to >100° C lower than minimum magmatic temperatures calculated using zircon saturation thermometry, but similar to estimates for metamorphic conditions. Therefore, temperatures based on two-pyroxene and two-feldspar thermometers may represent crystallization temperatures or metamorphic conditions at which the minerals requilibrated. Although pressure estimates were not obtained in this study, the temperature estimates can be compared to a P-T-t path for the Cat Square terrane from other studies (Fig. 5-18). Peak metamorphic conditions have been estimated at 700-850° C and 7-9 kbar (Merschat, 2003; Wilson, 2006; Gatewood, 2007; Fig. 5-18). Based on similarities in pyroxene temperatures with magmatic temperatures and igneous textures, the pyroxenes are believed to be primary minerals formed from melt instead of being a result of granulite metamorphism.

Pyroxene thermometry from other charnockites yielded crystallization (solidus) temperatures to range from 650-967° C, with estimates for liquidus temperatures in excess of 1100° C (Kilpatrick and Ellis, 1992; Frost and Frost, 2008). Such high temperatures are not

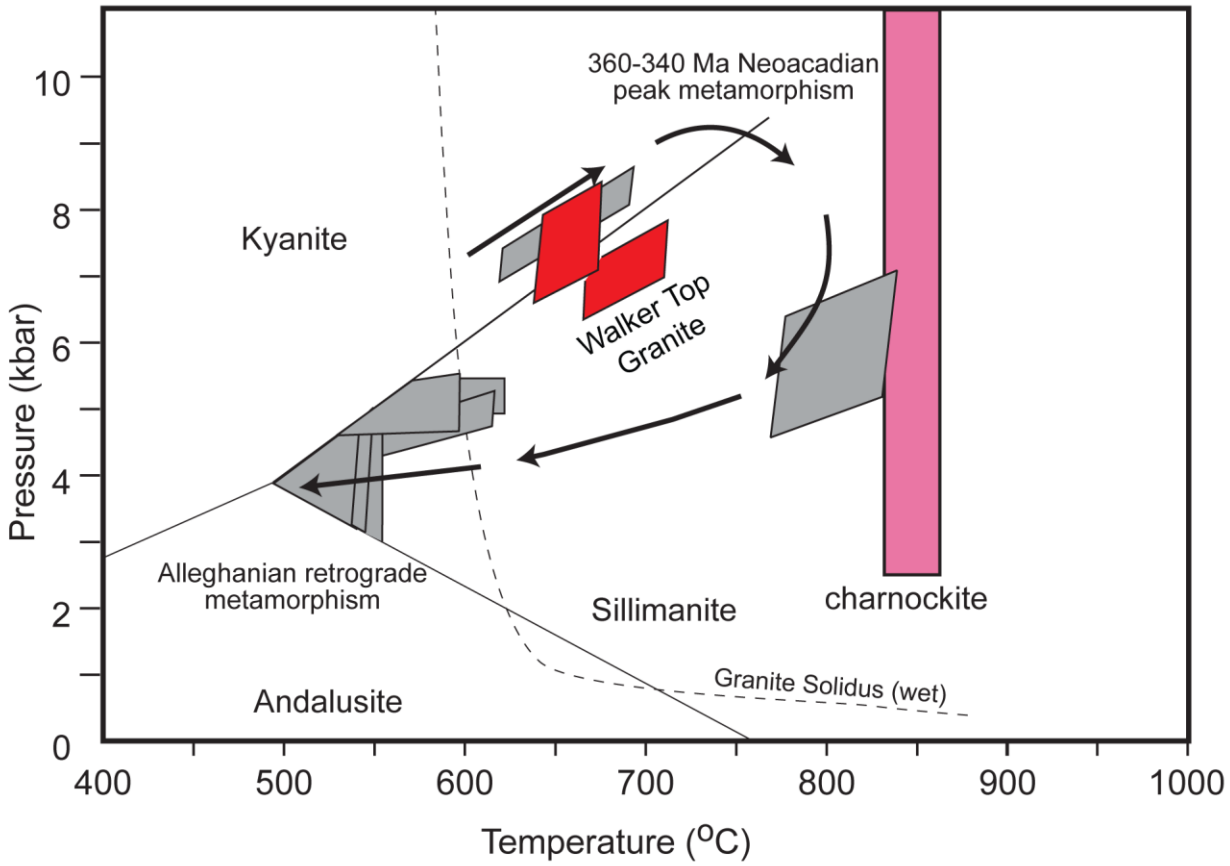

Figure 5-18. Pressure-temperature-time path of the Cat Square terrane. Gray boxes are estimates from previous studies in the Brushy and South Mountains (see Fig. 3-4 for sources). P-T range of Walker Top Granite (red boxes) from the Brushy Mountains (Gatewood, 2007). Range of calculated Vale charnockite temperatures from zircon saturation thermometry calculations is shown for reference with a permissible range of pressures (Frost and Frost, 2008). Figure modified from Gatewood (2007).

uncommon and are to be expected for anhydrous mineral assemblages found in charnockitic rocks. Barometry estimates from charnockites have been calculated to range from 2.5-11 kbars (Kilpatrick and Ellis, 1992; Frost and Frost, 2008).

Discussion

Formation of Charnockites: Overview

Four tectonic environments have been recognized for the formation of igneous charnockitic (pyroxene-bearing granitoid) rocks, as summarized by Frost and Frost (2008). One is a rift-related environment producing A-type, ferroan magmatism (e.g., Sherman, Thor Range, Bjerkreim; Table 5-1). These are generally direct differentiates of tholeiitic melts with little to no crustal components (Frost and Frost, 2008). A second, generating magnesian calcic to calc-alkalic metaluminous magmatism, is a subduction-related, cordilleran-type environment or melting of delaminated eclogitic crust (e.g., Ironside Mountain, Fiordland, Louis Lake, Utsalik, Desliens, Mawson; Table 5-1). These granitoids are associated with coeval thrusting of juvenile graywackes in arcs. Another, rarer environment is post-collisional delamination-related Caledonian-type magmatism where magnesian, alkali-calcic to alkali magmatism is observed (e.g., Ballachulish). Finally, charnockites are produced from deep crustal melting related to granulite metamorphism (dry crustal anatexis) or the emplacement of A-type magmas (e.g., Minto, Utsalik, Desliens).

Metamorphic charnockites are suggested to form from an influx of CO_2-rich fluids causing dehydration of hydrous assemblages or dehydration during granulite facies metamorphism. Dehydrations reactions responsible for the formation of metamorphic charnockites are:

$$\text{Biotite} + \text{Quartz} = \text{Orthopyroxene} + \text{K-feldspar} + H_2O \qquad (5\text{-}1)$$

$$\text{Garnet} + \text{Quartz} = \text{Orthopyroxene} + \text{Plagioclase} \qquad (5\text{-}2)$$

These charnockites are found in contact aureoles and granulite terranes often associated with biotite and hornblende granites (e.g., Kabbaldurga, Namaqualand; Wendlandt, 1981; Newton, 1992; van den Kerkhof and Grantham, 1999; Frost and Frost, 2008). Major sources for CO_2 may

have evolved from carbonates during metamorphism or from mantle degassing (Frost et al., 2000).

Petrogenetic models for the formation of the Vale charnockite

Any model for the formation and emplacement of the Vale charnockite and Walker Top Granite must take into account data presented in this study as well as tectonic models for the southern Appalachians. Petrogentic models are suggested and discussed below.

1.) Dehydration of the Walker Top Granite via CO_2-rich fluids or granulite metamorphism

Contact relationships support this model with the observed gradational contact. Similarities in the geochemical character between the two Vale granites would be identical, if the Vale charnockite was originally Walker Top Granite. The source of CO_2-rich fluids would have to be mantle-derived, because there is not a large presence of calc-silicate rocks in the study area. However, there is no evidence for vein or fluid flow. Although granulite facies metamorphism may have occurred in this study area based on modes of mafic complexes, there is no strong evidence for a metamorphic origin of the Vale charnockite. The Vale charnockite has igneous textures and zircon analyses reveal a distinctly older population of crystallization ages than the Walker Top Granite. The differences in elemental abundances cannot be explained by metamorphic processes. Based on these date, metamorphism by fluid influx or dehydration are not likely formation mechanisms.

2.) Fractionation within a pluton

This model is not a highly likely scenario for the formation of the Vale charnockite. Variations in whole-rock trace element and REE data are not significant enough to be accounted for by fractionation. Instead, differences in bulk REE plots can be accounted for by the presence of garnet in the Walker Top Granite and the differences in Hf, Th, and Zr could be from an extra zircon or two in the analyzed powder.

3.) Assimilation of previously crystallized charnockite into Walker Top Granite magma

The gradational nature of the contact between the two Vale granites supports assimilation as a valid emplacement mechanism. Crystallization and metamorphic ages of the Vale charnockite overlap with those of the Walker Top Granite, indicating the charnockite may or may not have been completely solid when incorporated into the magma. Because the geochemical signatures of the granites are so similar, the charnockite would have to be an autolith, an early crystallization of magma with higher Fe and Mg minerals derived from the same parent as the Walker Top Granite. After partial or full crystallization, it would have been incorporated into the Walker Top Granite magma body as it rose through the crust to final emplacement levels. To explain the anhydrous and hydrous natures of the two granites, the earlier magma would have been anhydrous with higher Fe # and crystallizing under higher pressures to explain the presence of pyroxene. Later pulses of magma began as or evolved into a hydrous melt with a lower Fe # at shallower crustal levels.

Mapes (2002) suggested there is a crustal component present in Inner Piedmont plutons. Contamination has been noted and mapped in several Walker Top Granite bodies. Within the study area, xenoliths of metagraywacke occur along-strike in the Walker Top Granite body containing the Vale charnockite. A mappable enclave of an orthopyroxene-bearing metagabbro, first thought to be a charnockite, has been recognized in another Walker Top Granite close to the western exposure of the Brindle Creek fault in the South Mountains (Giorgis, 1999). The lack of K-feldspar and quartz, in addition to a more mafic plagioclase content of An_{60}, confirms the rock type as a metagabbro.

4.) Deep crustal melting associated with an arc environment in which both granite types crystallize from the same magmatic body

Evidence for this can be seen in the geochemical signature of both Vale granitoids. The granitoids plot within the volcanic-arc field on most tectonic discriminant diagrams. Similarities in trace and REE trends as well as participation of a crust component could be explained by this model. The overlap of crystallization ages may be related to earlier crystallization of dehydrated charnockitic rocks, and later crystallization of the Walker Top Granite around it, because of its

hydrous nature. Isolated occurrences of charnockite could be explained by areas with a higher Fe/(Fe+ Mg) ratio within the magma, causing orthopyroxene to be the dominant mineral crystallizing in these areas, as opposed to biotite.

A similar model has been suggested for the Louis Lake and Ironside Mountain batholiths (Table 5-1) where charnockitic rocks occur as enclaves within larger, hydrated granitoids forming from volcanic-arc related magmatism (Frost and Frost, 2008). The Sherman batholith also contains isolated outcrops of dry, orthopyroxene-bearing granites within hydrated biotite granite, but is suggested to have formed from rift-related magmatism (Frost et al., 1999). Distribution of these enclaves and isolated outcrops is thought to suggest an increase in hydration (a_{H20}) moving from deeper to shallow levels within a magma until charnockitic rocks are represented only by these isolated occurrences (Frost et al., 2000).

Summary and Tectonic Synthesis

The model best explaining the formation and emplacement of the Vale charnockite of the latter two discussed is having the Vale charnockite be an autolith or xenolith, although autolith is favored. Magmas generating the Vale charnockite and Walker Top Granite were either derived from metasedimentary rocks of the Cat Square terrane or may have been arc-related with significant contamination in order to produce isotopic signatures similar to the metasedimentary rocks. With these considerations, the following tectonic model is adapted for the formation and emplacement of the Vale charnockite and Walker Top Granite.

Sediments of the Cat Square terrane were deposited in the remnant Rheic ocean basin, outboard from the eastern margin of Laurentia and western margin of Avalon (Carolina superterrane) (Merschat and Hatcher, 2007; Fig. 5-19a). Eastward subduction beneath Avalon and a northwest-directed transpressive collision between Laurentia and Avalon closed the Rheic ocean. Sediments were accreted and subducted by ~407 Ma when anatectic magmatism began in the Cat Square terrane (Fig. 5-19b). Heat from the mantle was a likely heat source driving the formation of these magmas. From 370-350 Ma, deep crustal anatectic melting produced an iron-rich pluton at temperatures ~850° C. Orthopyroxene the dominant iron-rich mineral crystallizing at lower to mid-crustal levels. As the same magma or a later pulse of magmatism, with the same

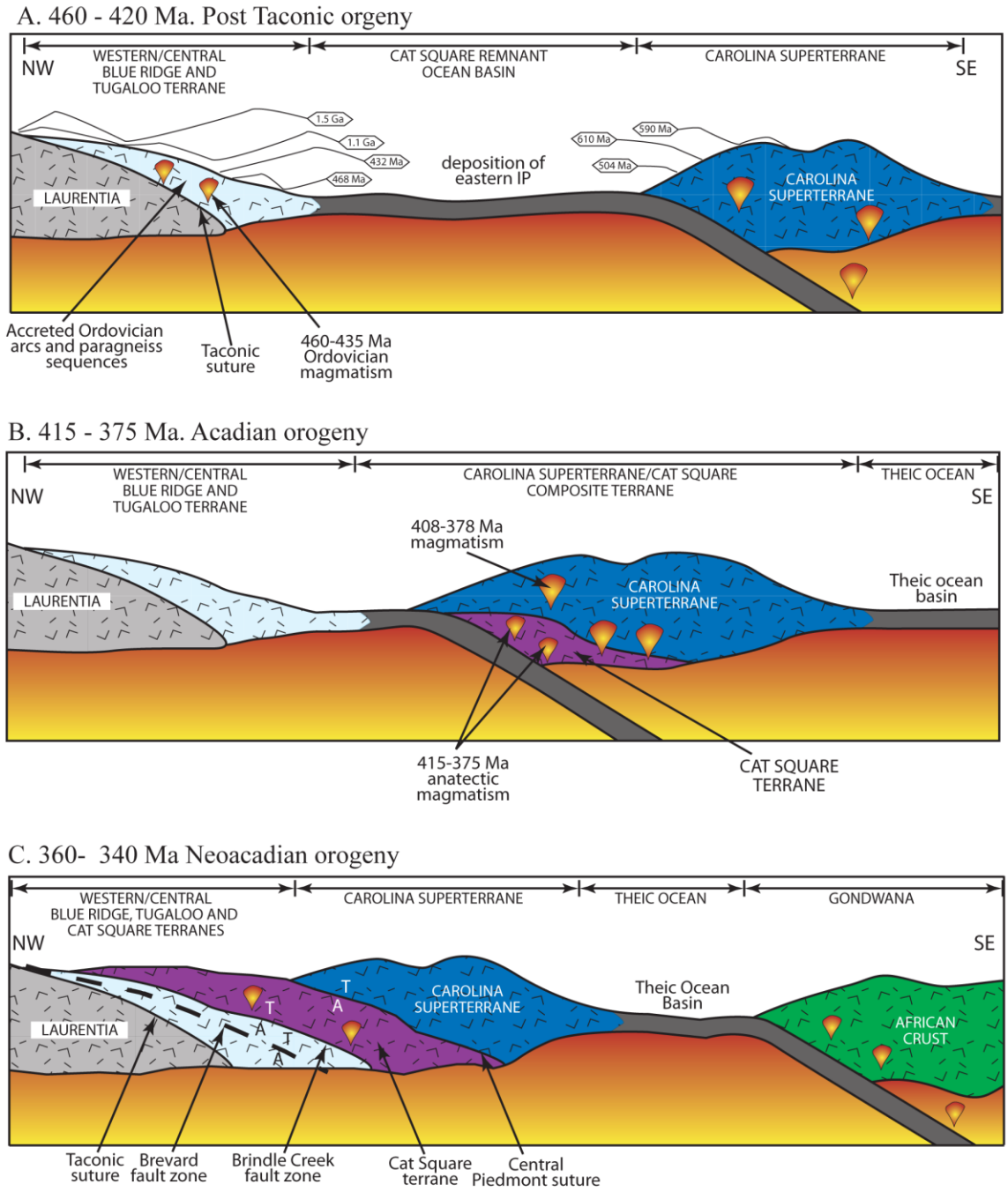

Figure 5-19. Generalized model for the development of the Cat Square terrane (from Gatewood, 2007). A.) Deposition of Cat Square terrane sediments. B.) Subduction of Cat Square terrane beneath the Carolina superterrane with initiation of Devonian anatectic magmatism in the Cat Square terrane. C.) Accretion of the composite Cat Square terrane and Carolina superterrane and movement on the Brindle Creek fault during the Neoacadian orogeny.

source, reached mid- to shallow crustal levels, water became the dominant fluid and biotite the dominant iron-rich mineral. Crystallization around the mid- to upper-crustal levels of the magma recorded this transition from an anhydrous to hydrous mineral-assemblage pluton.

With continued collision during the Neoacadian orogeny, the transition from B- to A-type subduction of Laurentia beneath the metasediments cut off the source for volcanic-arc type plutonism in the Cat Square terrane (Hatcher, in review; Fig. 5-19c). Rocks within the Cat Square terrane continued to undergo high-grade (sillimanite II to locally granulite) metamorphism until ~340 Ma as movement along the Brindle Creek fault emplaced and transported the terrane in a northwest- to southwest-directed flow pattern between Avalon and Laurentia (Hatcher and Merschat, 2006).

CHAPTER 6

GEOCHEMICAL EVIDENCE FOR THE FORMATION OF CAT SQUARE TERRANE MAFIC COMPLEX AND AMPHIBOLITE BODIES

Introduction

Mafic and ultramafic bodies are widely distributed in the Cat Square terrane, as documented by reconnaissance and detailed geologic mapping (Overstreet et al., 1963; Privett, 1984; Mittwede et al., 1987; Goldsmith et al., 1988; Giorgis, 1999; Merschat, 2003; Wilson, 2006; Byars et al., 2008b). The majority of map-scale mafic and ultramafic bodies are located in the eastern portions of the Cat Square terrane, near the Kings Mountain shear zone and Central Piedmont suture (Fig. 6-1). Noteworthy mafic and ultramafic bodies include the Turnersburg intrusive in North Carolina (Privett, 1984; Butler, 1988) and the Hammet Grove meta-igneous suite in South Carolina (Mittwede, 1986, 1989). The Turnersburg intrusive is composed of metamorphosed ultramafics suggested to have a pyroxenite or peridotite protolith (Privett, 1984). The Hammet Grove meta-igneous suite, consisting of altered metapyroxenite, metagabbro, and metabasalt, has been interpreted as a dismembered ophiolite (Mittwede, 1989). Multiple isolated occurrences of mafic and ultramafic bodies occur in the Cat Square terrane in Georgia and North and South Carolina (Griffin, 1979; Milton and Michie, 1987; Nelson et al., 1988; Whitney et al., 1987; Goldsmith et al., 1988; Maybin and Mittwede, 1988; Mittwede, 1989). Several of the aforementioned studies concluded these bodies are mélanges, or dismembered ophiolites, based on texture, mineralogy, chemistry, and field relationships, indicative of a terrane suture between the Inner Piedmont and Kings Mountain belt.

Eight discontinuous mafic complex and amphibolite bodies occur in the Cat Square terrane in the west-central portion of the study area (Fig. 6-2). Mafic complexes contain undifferentiated metagabbro, amphibolite, and metadiorite. Metabasite interlayers are commonly found in the pelitic schist and metagraywacke units. Sample and petrographic descriptions and modal analyses of these units were discussed in Chapter 2 (Figs 2-22 to 2-24; Table 2-4). Two metagabbro (samples Ch4, Ch5f), one amphibolite (sample Ch2), and one metadiorite (sample

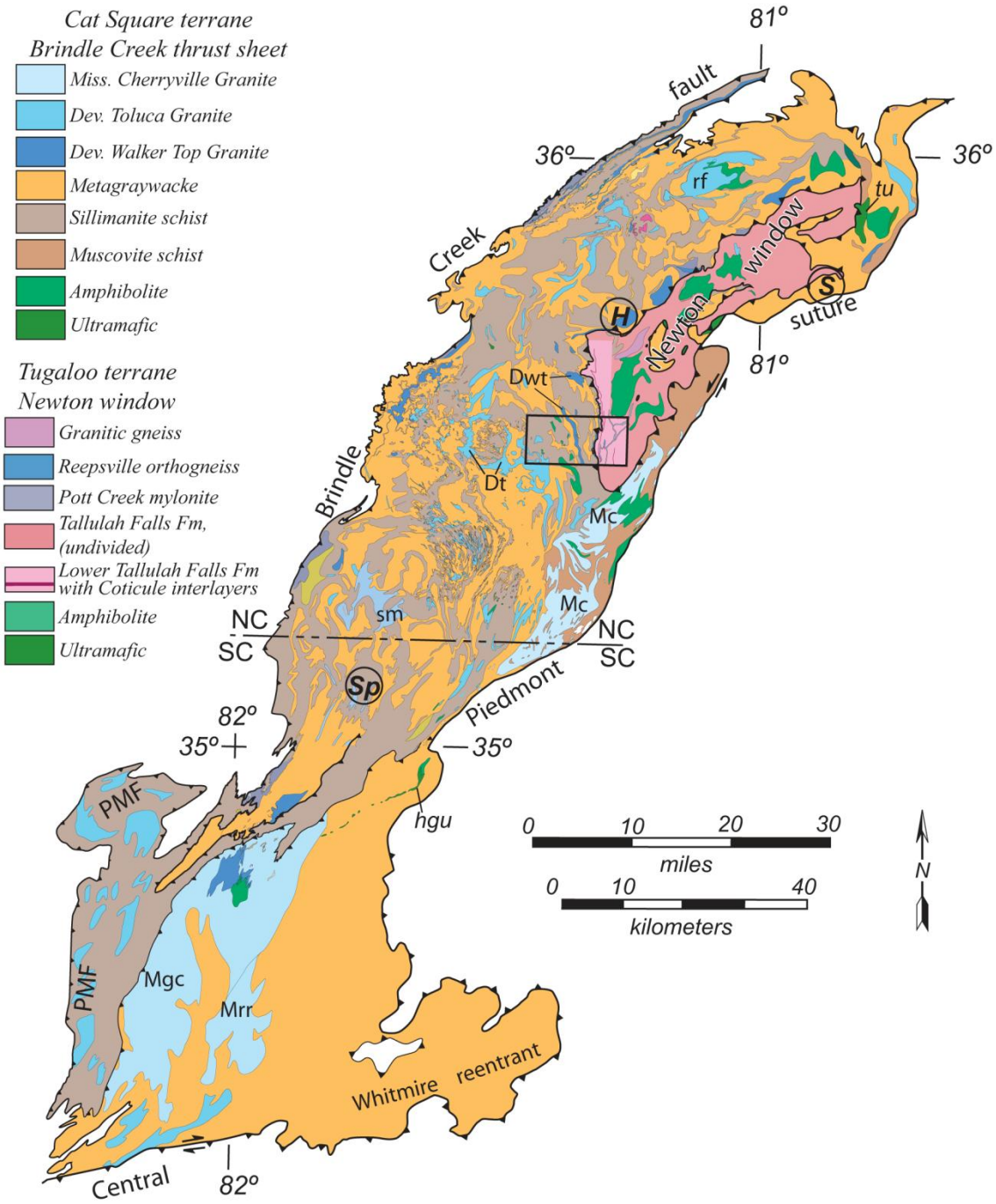

Figure 6-1. Simplified geologic map of the Cat Square terrane from its northern extent to near the Georgia-South Carolina border (from Merschat and Hatcher, 2007). Black box outlines study area. Dt -Toluca Granite. Dwt-Walker Top Granite. hgu-Hammett Grove metaigneous mafic-ultramafic body. Mc-Cherryville Granite. Mgc-Gray Court Granite. Mrr-Reedy River Granite. PMF-Paris Mountain thrust sheet, an out-of-sequence fault that broke through the Brindle Creek thrust sheet. rf-Rocky Face granite. sm-Sandy Mush granite. tu-Turnersberg ultramafic. H-Hickory. S-Statesville. Sp-Spartanburg.

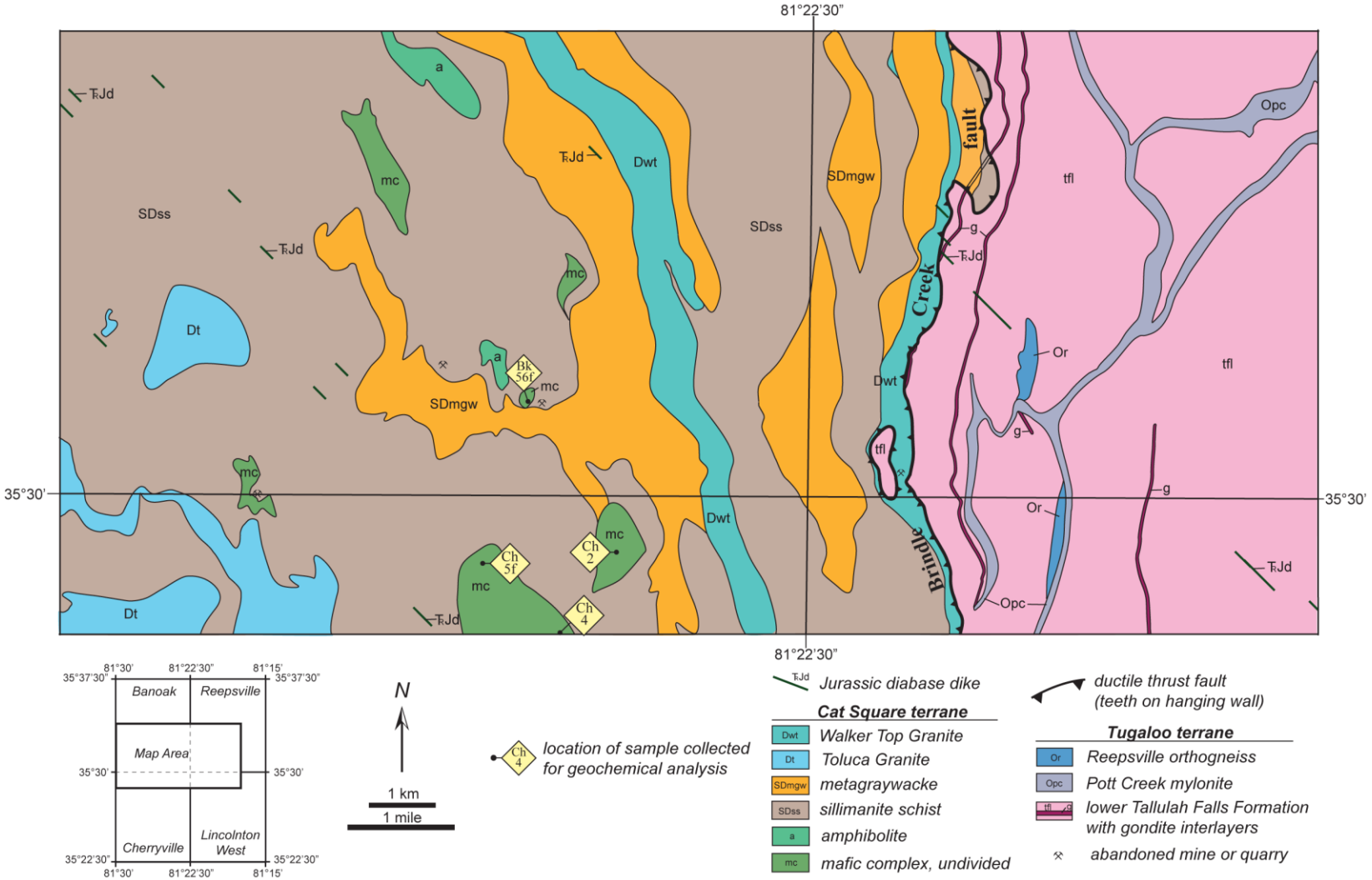

Figure 6-2. Simplified geologic map of study area showing location of mafic complex and amphibolite samples collected for geochemical analysis.

Bk56f) were analyzed for whole-rock geochemistry. These data are discussed with other Cat Square amphibolite studies of Wilson (2006) and Merschat (2009) in order to determine if they represent vestiges of oceanic crust, as proposed by Merschat and Hatcher (2007), and, if so, in what tectonic environment they were formed. Other data from Cat Square terrane amphibolite samples discussed in this chapter include three samples (HA-Hiddenite amphibolite, WTxeno-Walker Top Granite xenolith, RFxeno-Rocky Face pluton [Toluca Granite equivalent?] xenolith) from the Brushy Mountains (Wilson, 2006) and one (Ha10 of Merschat, 2009) from an amphibolite body (Goldsmith et al., 1988) adjacent to the Turnersburg ultramafic body (Privett, 1984). Mafic complex and amphibolite samples will be collectively referred to as metabasites herein.

Whole-rock Geochemistry

Methodology

Four fresh representative samples were collected from three mafic complex bodies in the Cherryville and Banoak 7.5-minute quadrangles (Fig. 6-2). Each sample was cut into three or more thin (5.0 cm x 3.0 cm x 1.0 cm) representative slabs on a diamond bit trim saw, rinsed with isopropyl alcohol, and dried. Slabs were broken into 1.0 cm x 0.5 cm or smaller fragments. Fragments were sent to Activation Laboratories in Ancaster, Ontario, to be powdered and analyzed for bulk rock geochemistry. Major elements, and Ba, Be, Sr, V, and Y, were determined using inductively coupled plasma (ICP) emission spectroscopy employing lithium metaborate/tetraborate fusion (FUS-ICP). Total digestion (TD-ICP) methods were used to determine Ag, Cd, Cu, Ni, Pb, S, and Zn. Trace- and rare-earth elements (REE) were determined by fusion methods (FUS-MS) and instrumental neutron activation analysis (INAA) (Table 6-1). Data plots were constructed using Igpet05 and CIPW norms were calculated using the CIPW application.

Table 6-1. Whole-rock oxide weight percents and trace element (ppm-ppb) concentrations for Cat Square terrane mafic complex samples from the Banoak and Cherryville 7.5-minute quadrangles.

	Sample ID	Ch2	Ch4	Ch5f	Bk56f
	Rock Unit	Amphibolite	Metagabbro	Metagabbro	Metadiorite
Analysis Type	Detection Limit				
FUS-ICP					
SiO_2	0.01%	55.76	46.85	45.85	54.94
Al_2O_3	0.01%	16.35	17.98	17.17	15.36
Fe_2O_3(T)	0.01%	8.14	15.4	13.87	10.1
MnO	0.001%	0.15	0.174	0.199	0.18
MgO	0.01%	2.65	4.7	5.6	7
CaO	0.01%	6.17	9.21	8.95	8.72
Na_2O	0.01%	2.74	2.3	1.74	1.21
K_2O	0.01%	1.97	1.34	1.02	1.06
TiO_2	0.001%	0.863	1.729	1.921	0.946
P_2O_5	0.01%	0.2	0.19	0.12	0.13
LOI		0.62	0.16	0.23	0.13
	TOTAL %	95.61	100	96.67	99.77
Ba	1 ppm	272	197	199	209
Be	1 ppm	4	2	2	2
Sr	2 ppm	237	340	350	180
V	5 ppm	144	403	332	231
Y	1 ppm	46	44	35	27
INAA					
Au	1 ppb	< 1	< 1	< 1	< 1
As	1 ppm	< 1	< 1	< 1	< 1
Br	0.5 ppm	< 0.5	< 0.5	< 0.5	< 0.5
Co	0.1 ppm	18	41	49	40
Cr	0.5 ppm	46	10	9	268
Hg	1 ppm	< 1	< 1	< 1	< 1
Ir	1 ppb	< 1	< 1	< 1	< 1
Sb	0.1 ppm	< 0.1	0.2	0.1	0.1
Sc	0.01 ppm	26.6	41.7	35.7	36.1
Se	0.5 ppm	< 0.5	< 0.5	< 0.5	< 0.5
W	1 ppm	< 1	< 1	< 1	< 1

Table 6-1. *continued.*

	Sample ID	Ch2	Ch4	Ch5f	Bk56f
	Rock Unit	Amphibolite	Metagabbro	Metagabbro	Metadiorite
Analysis Type	Detection Limit				
FUS-MS					
Bi	0.1 ppm	5.7	< 0.1	0.8	< 0.1
Cs	0.1 ppm	3.8	2.7	2.5	1.7
Ga	1 ppm	19	24	20	18
Ge	0.5 ppm	1.8	1.4	1.8	1.8
Hf	0.1 ppm	5.8	3.7	3.2	3
In	0.1 ppm	0.1	0.1	< 0.1	0.1
Mo	2 ppm	< 2	< 2	< 2	< 2
Nb	0.2 ppm	10.7	7.4	6.5	6
Rb	2 ppm	93	66	47	64
Sn	1 ppm	3	3	1	1
Ta	0.1 ppm	0.8	0.5	0.4	0.4
Th	0.05 ppm	4.96	1.83	0.43	3.84
U	0.05 ppm	0.57	0.83	0.24	0.75
Zr	1 ppm	231	128	91	119
La	0.05 ppm	27.1	15.9	12.1	17.9
Ce	0.1 ppm	63.6	39.9	28.6	38.3
Pr	0.02 ppm	8.6	5.31	4.33	5.32
Nd	0.05 ppm	35.1	24.8	19	19.5
Sm	0.01 ppm	8.36	7.04	5.15	4.46
Eu	0.005 ppm	1.91	2.1	2.06	1.26
Gd	0.02 ppm	8.89	8	6.04	4.28
Tb	0.01 ppm	1.5	1.3	1.05	0.75
Dy	0.02 ppm	9.09	7.59	6.52	4.73
Ho	0.01 ppm	1.82	1.54	1.35	1
Er	0.01 ppm	5.61	4.6	3.95	2.95
Tl	0.05 ppm	0.41	0.67	0.16	0.43
Tm	0.005 ppm	0.819	0.652	0.561	0.433
Yb	0.01 ppm	4.64	3.94	3.45	2.81
Lu	0.002 ppm	0.624	0.574	0.5	0.431
TD-ICP					
Ag	0.5 ppm	< 0.5	< 0.5	< 0.5	< 0.5
Cd	0.5 ppm	< 0.5	0.5	< 0.5	< 0.5
Cu	1 ppm	25	61	31	21
Ni	1 ppm	11	6	13	69
Pb	5 ppm	10	8	5	7
S	0.001%	0.064	0.262	0.218	0.008
Zn	1 ppm	91	107	102	84

Major Element Compositions

Normative Mineralogy

Normative mineralogy was calculated using major elements obtained in whole-rock analyses (Table 6-2). $FeO/(FeO + Fe_2O_3)$ was assumed to equal 0.85 (Thompson, 1984), because total (T) iron was measured as Fe_2O_3(T) during analysis. Normative olivine is present in metagabbro samples, although olivine is rarely present in modes (Table 2-4). These samples lack normative quartz. The opposite is true for the amphibolite and metadiorite samples: normative quartz is present, normative olivine is not. A disadvantage of normative mineralogy is that the presence or amount of amphibole and biotite is not calculated due to the nature of their crystal structure, and because H_2O is not measured or used in the calculation. For instance, clinopyroxene and orthopyroxene are not present in sample Ch2, although greater than 40 percent of the norm is pyroxene.

Variation Diagrams

Variation diagrams of select major-element oxides and trace elements were constructed using magnesium number (Mg #) and zirconium (Zr) as the differentiation index (Figs. 6-3, 6-4, 6-5). Magnesium number (MgO/(MgO+FeO)) is a good indicator of igneous processes because iron and magnesium ratios change significantly with the early fractionation of mafic magmas (Rollinson, 1993). Zr was chosen as the differentiation index, because it is highly incompatible and increases in concentration as fractionation proceeds (Wilson, 1989).

Overall, samples in this study reflect trends in the Mg # variation diagrams previously discussed in Wilson (2006), whereas trends in the Zr plots are not readily distinguishable due to the lack of variation in Zr between samples.. Fe_2O_3, Al_2O_3, V, Sr, and Y have distinct, decreasing trends in the Mg # plots (Figs. 6-3, 6-4). Strong increasing trends are present in MgO, Ni, and Cr plots. Three of four samples from this study have similar amounts of Zr, whereas the fourth has a significantly higher amount of Zr. If these samples are treated as having the same parental material, an increasing trend of Nb and decreasing trends of MgO and V become apparent in Zr plots (Fig. 6-5).

Although trends seem apparent in some of the variation diagrams when looking at

Table 6-2. CIPW normative mineralogy of analyzed metabasite samples.

	Sample ID	Ch2	Ch4	Ch5f	Bk56f
	Rock Unit	Amphibolite	Metagabbro	Metagabbro	Metadiorite
Normative mineralogy					
Quartz		12.0	—	—	11.7
Orthoclase		11.6	7.9	6.0	6.3
Albite		23.2	19.5	14.7	10.2
Anorthite		26.5	34.8	36.0	33.4
Diopside		2.3	8.1	6.3	7.4
	wollastonite	1.2	4.0	3.2	3.8
	enstatite	0.5	1.6	1.5	2.2
	ferrosilite	0.7	2.4	1.6	1.5
Hypersthene		14.7	10.8	23.7	25.5
	enstatite	6.1	4.4	11.4	15.3
	ferrosilite	8.6	6.4	12.3	10.2
Olivine		—	10.4	1.5	—
	forsterite	—	4.0	0.7	—
	fayalite	—	6.5	0.8	—
Magnetite		1.8	3.3	3.0	2.2
Ilmenite		1.6	3.3	3.6	1.8
Apatite		0.5	0.5	0.3	0.3

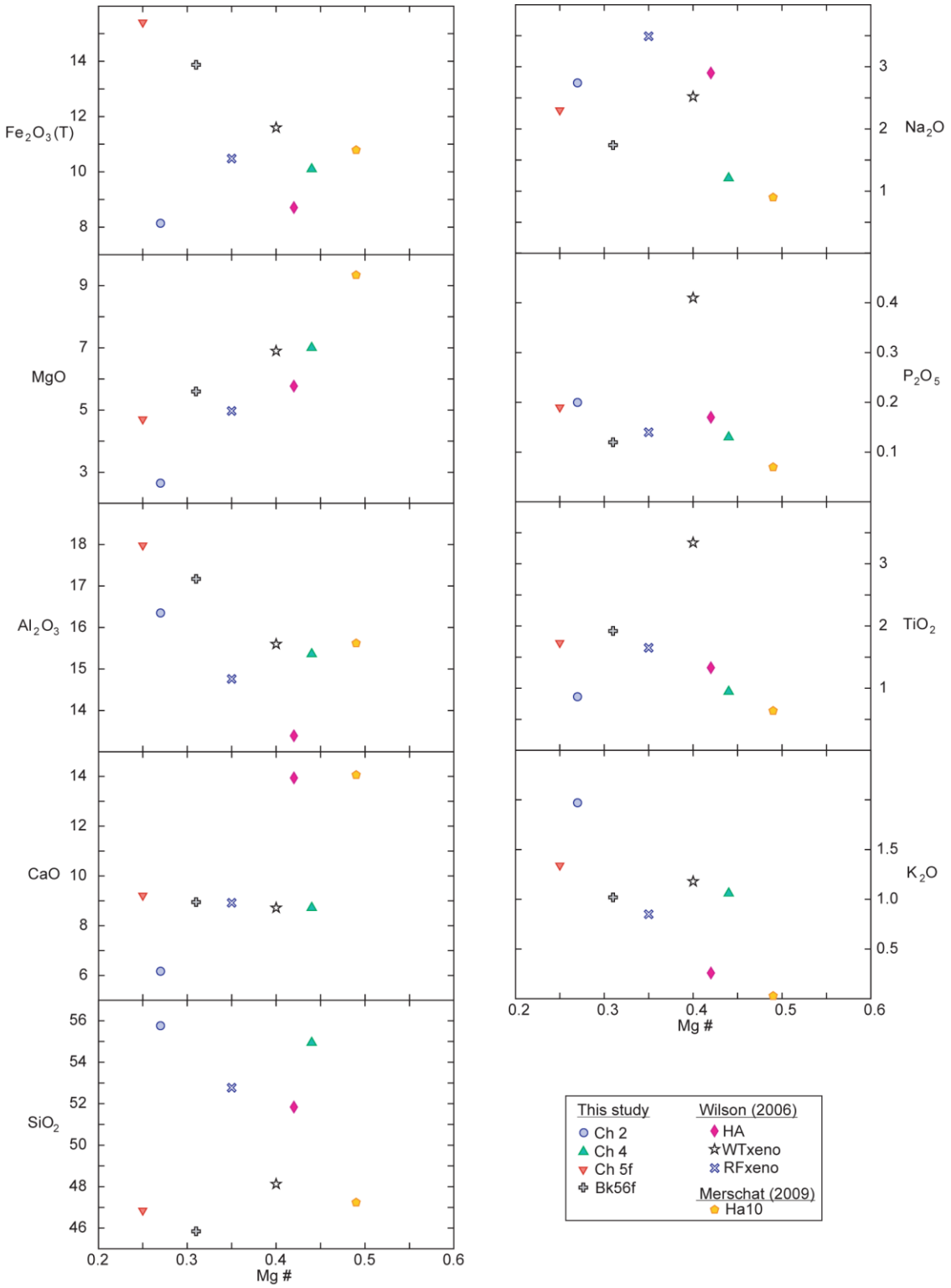

Figure 6-3. Variation diagrams of major element oxides versus Mg # for Cat Square terrane metabasites.

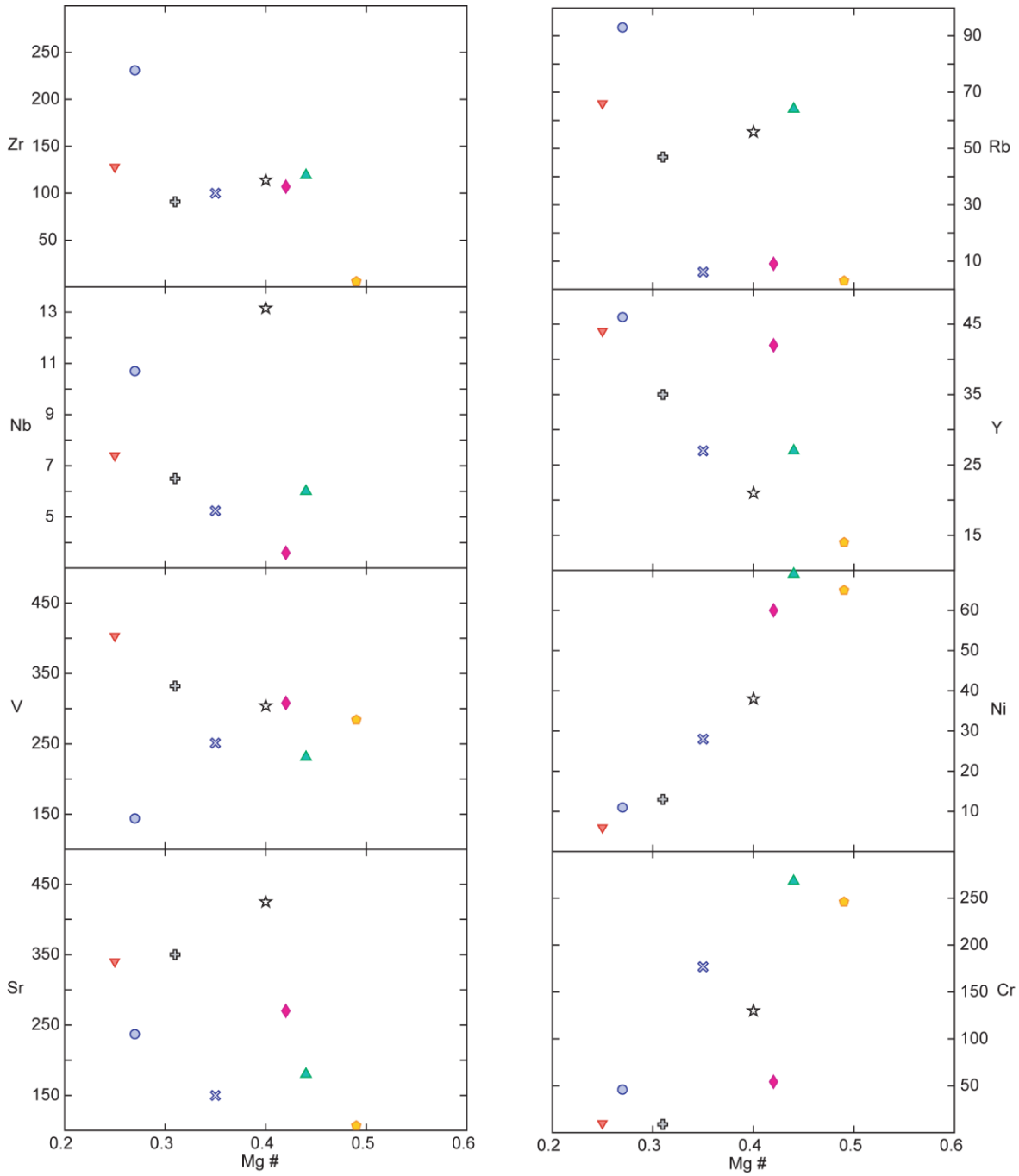

Figure 6-4. Variation diagrams of select trace elements versus Mg # for Cat Square terrane metabasites. Symbols same as in Fig. 6-3.

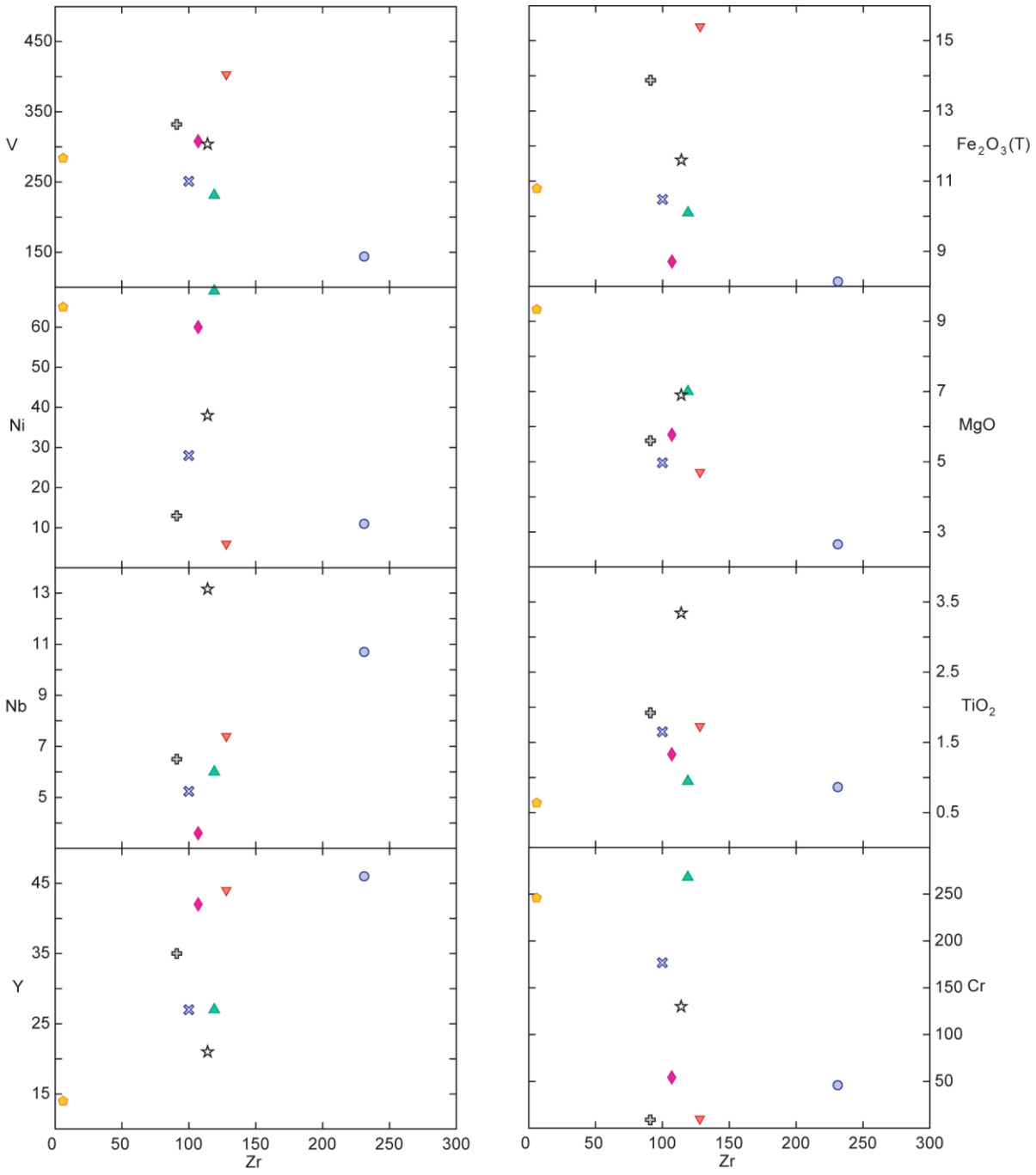

Figure 6-5. Variation diagrams of select major-element oxides and trace elements versus Zr for Cat Square terrane metabasites. Symbols same as in Fig. 6-3.

samples from all three studies, these may be artificial, because samples were collected over a wide area of northeastern portions of the Cat Square terrane. Trends from samples in the study area are not likely to be artificial since they were collected from mafic bodies in close proximity to each other. These mafic bodies may have once been a uniform body separated during accretion and subsequent deformation during the Neoacadian orogeny. Trends are more evident where Mg # and Zr are plotted against immobile elements, such as Ni, Cr, and V, indicative of the rocks being affected by alteration, causing mobile element concentrations, such as Ba, Rb, and K, to be affected.

Igneous Versus Sedimentary Origin

An igneous origin for the samples in this study was determined using an *mg–(al-alk)–c* ternary diagram of Niggli values (Fig. 6-6a). The following equations were used to calculate end member apex values:

$$mg = 100 \times (Mg/[FeO + MnO + 2Fe_2O_3 + MgO]) \quad (6\text{-}1)$$

$$al\text{-}alk = Al_2O_3 - (Na_2O + K_2O) \quad (6\text{-}2)$$

$$c = CaO \quad (6\text{-}3)$$

Most data points plot along the middle of the basic igneous trend line. Three samples, all from this study, plot slightly right of the trend line toward typical pelite and semipelite compositions. Samples in this study and from previous studies will be treated as metaigneous rocks and further subdivided with discriminant plots discussed below.

Alkaline Versus Subalkaline Basalts

The total alkali–silica diagram, invented by Cox et al. (1979), was used to obtain a general classification of the igneous protolith for the metabasite samples (Fig. 6-6b). This diagram, however, is used with caution because alkalis are highly mobile elements. All samples range from basaltic to andesitic compositions. Inconsistencies exist between different plots with samples spanning the alkaline and subalkaline series (Fig. 6-6b), and the calc-alkaline and tholeiite series (Figs. 6-6c, d). On the AFM diagram (Irvine and Baragar, 1971), all but one sample reveal a tholeiite trend (Fig. 6-6c). Subdividing the subalkaline series in Fig. 6-6b using the K_2O versus silica diagram (Rickwood, 1989), sample Ch2 is high-K calc-alkaline while

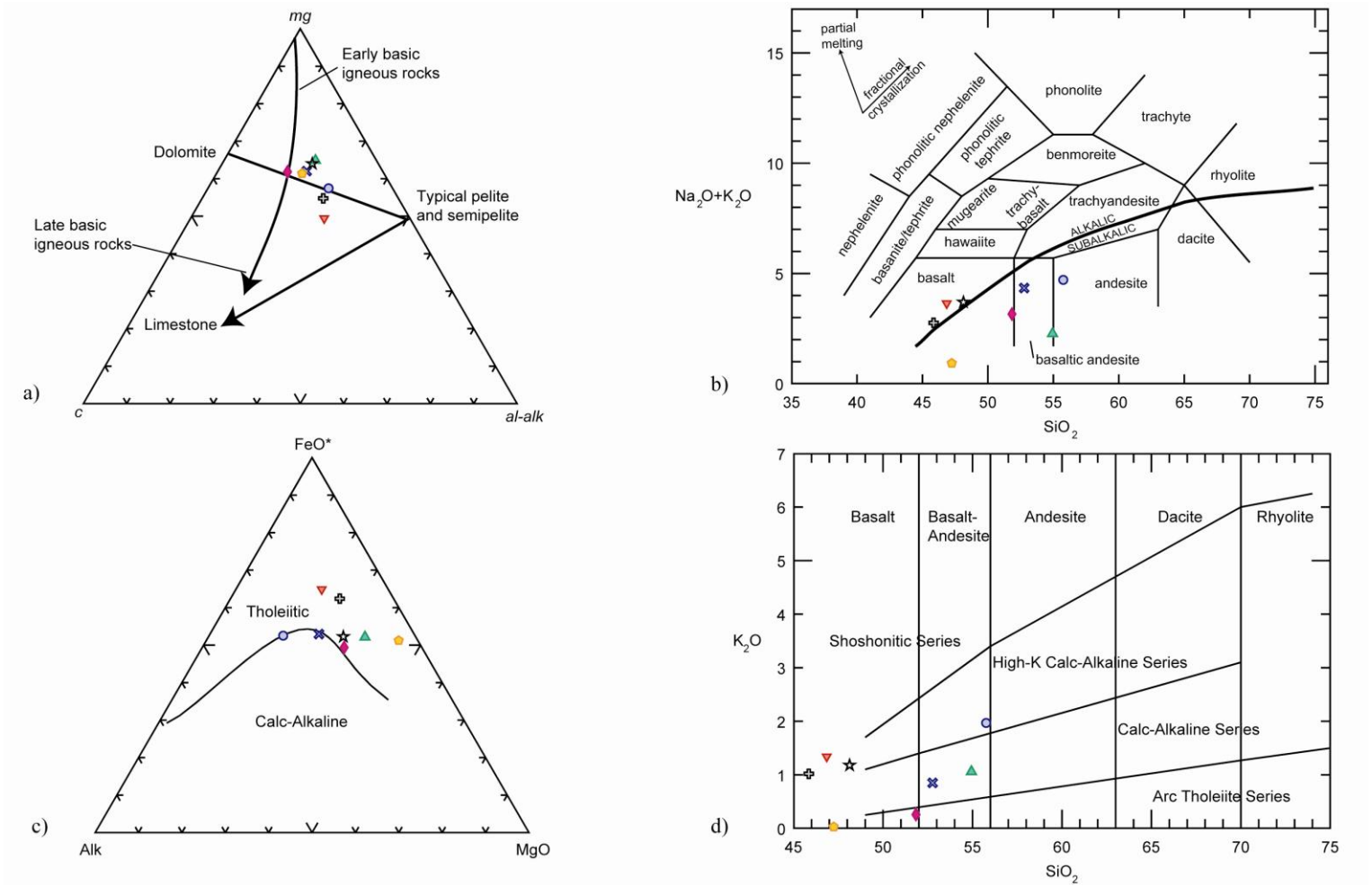

Figure 6-6. Major element oxide plots for Cat Square terrane metabasites. a) *mg–(al-alk)–c* diagram of Niggli values. *mg* = 100 x (MgO/[FeO + MnO + $2Fe_2O_3$+ MgO]); *al-alk* = Al2O3 – (Na_2O +K_2O); *c* = CaO. b) Total alkali–silica (TAS) diagram (Cox et al., 1979) showing volcanic-rock equivalents metabasites. Alkaline and subalkaline magma series dividing line from Miyashiro (1978). c) AFM diagram (Irvine and Baragar, 1971). d) K_2O versus SiO_2 diagram and nomenclature of Rickwood (1989) indicating the subdivision of subalkalic rocks. Symbols same as in Fig. 6-3.

Bk56f is calc-alkaline (Fig. 6-6d). These differences are somewhat resolved when using less mobile trace elements as discussed below.

Rare Earth and Trace Element Compositions

Rare earth element (REE) and trace element spider diagrams were used to determine igneous processes that parental magmas of the metabasites underwent during or post-crystallization, such as fractionation, partial melting, assimilation, and hydrothermal or metamorphic alteration. Negatively sloping patterns of samples from this study very closely resemble each other with slight variations (Fig. 6-7a). Light REE concentrations are higher than heavy REE concentrations (25-100 x condrite and 5-45 x condrite, respectively). Two samples (Ch2 and Ch4) have small negative Eu anomalies; one sample (Ch5f) has a small positive Eu anomaly, and one sample (Bk56f) has no Eu anomaly. Compared to previous studies of Wilson (2006) and Merschat (2009), samples from this study have higher concentrations of rare earth elements (Fig. 6-7b). Sample Ha10 does not reflect a pattern of any sample. Retrograde hydration reactions are prominent in this sample, which may be affecting its bulk chemistry.

Trace element data normalized to condrite, primitive mantle, and mid-ocean ridge basalt (MORB) values are less consistent than REE data, but, overall, patterns have a negative slope (Fig. 6-8). Sample Ch2 has slightly elevated values compared to samples Ch4, Ch5f, and Bk56f from this study. Significant differences between samples are observed in the amounts of Th, U, Zr, and Ti. Samples are enriched in the compatible and mobile large ion lithophile (LIL) elements of Cs, Rb, Ba, K, and Pb, based on which normalizing values are used. These positive anomalies likely indicate post-crystallization alteration. Values for immobile high field strength (HFS) elements are close to normalizing values for MORB (Fig. 6-8e). This supports a MORB rather than primitive mantle source for mafic complex and amphibolite bodies in the study area. Trends of samples from Wilson (2006) and Merschat (2009) indicate a similar MORB source (Fig. 6-8f).

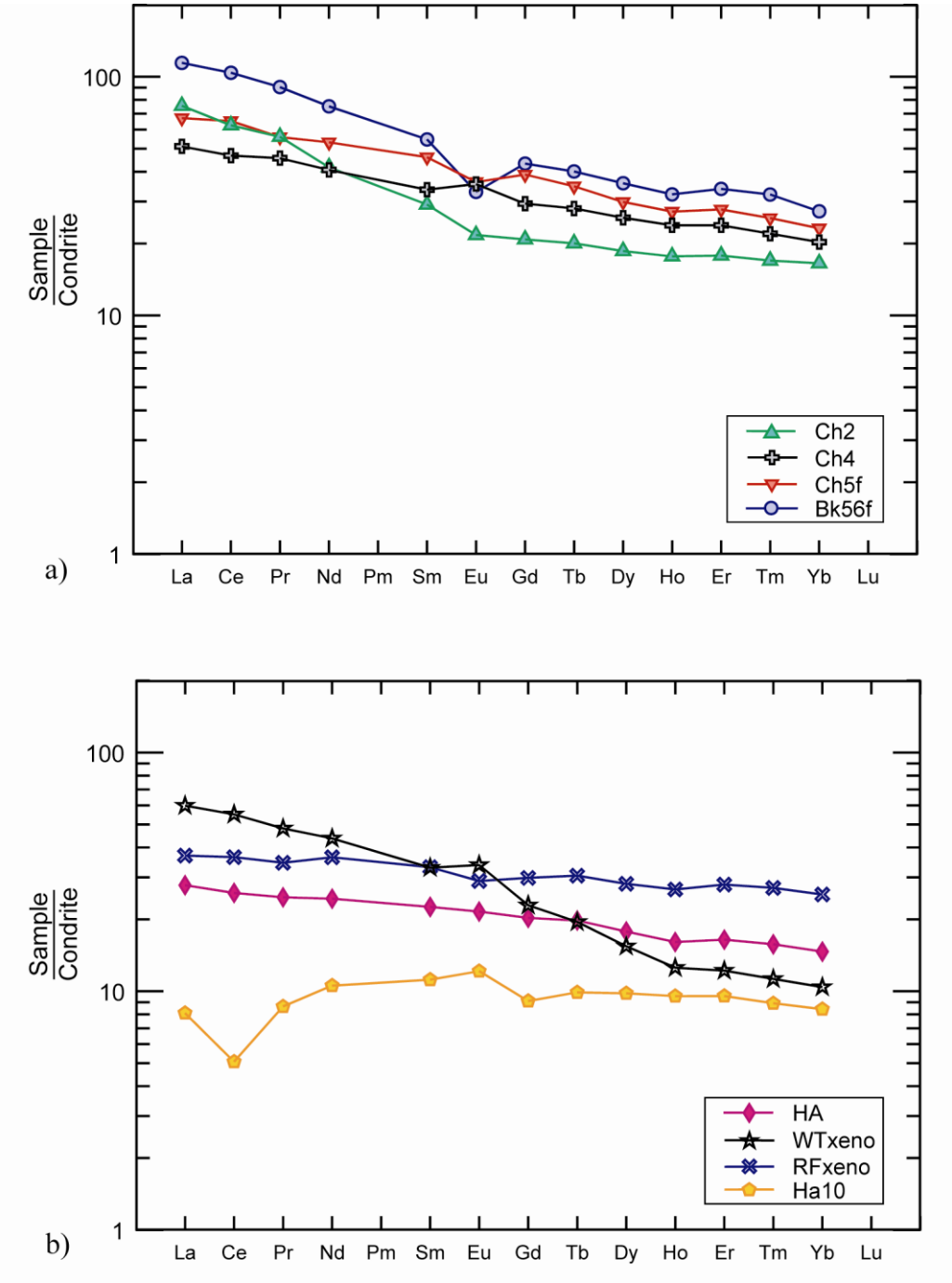

Figure 6-7. REE data from a) this study and b) other studies normalized to condrite (Sun and McDonough, 1989). Symbols same as in Fig. 6-3.

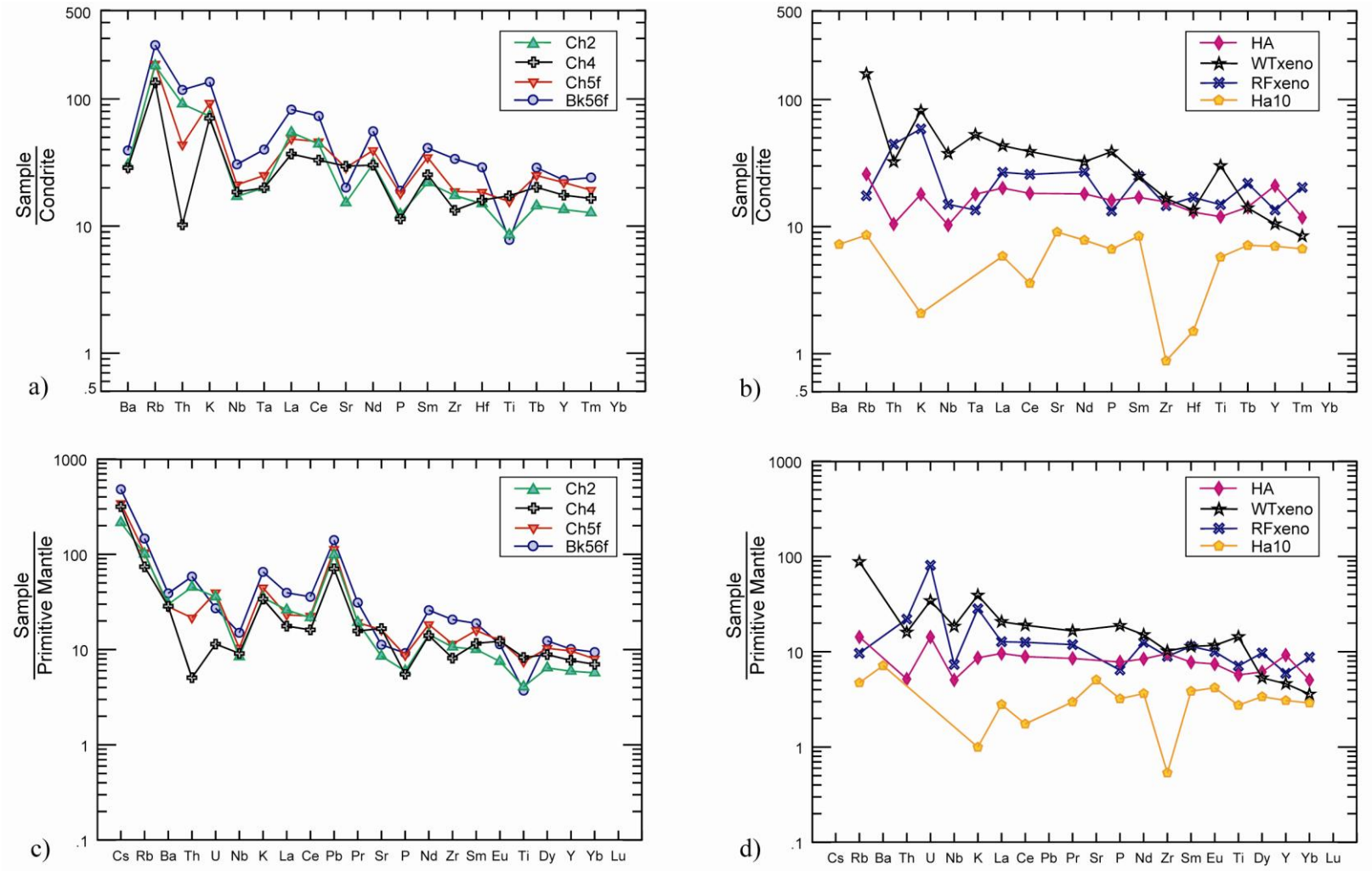

Figure 6-8. Trace element data spider plots. Data from this study (a, c, e) and other studies (b, d, f) normalized to: a, b) condrite (Thompson, 1982); c, d) primitive mantle (Sun and McDonough, 1989); e, f) MORB (Pearce, 1983). Symbols same as in Fig. 6-3.

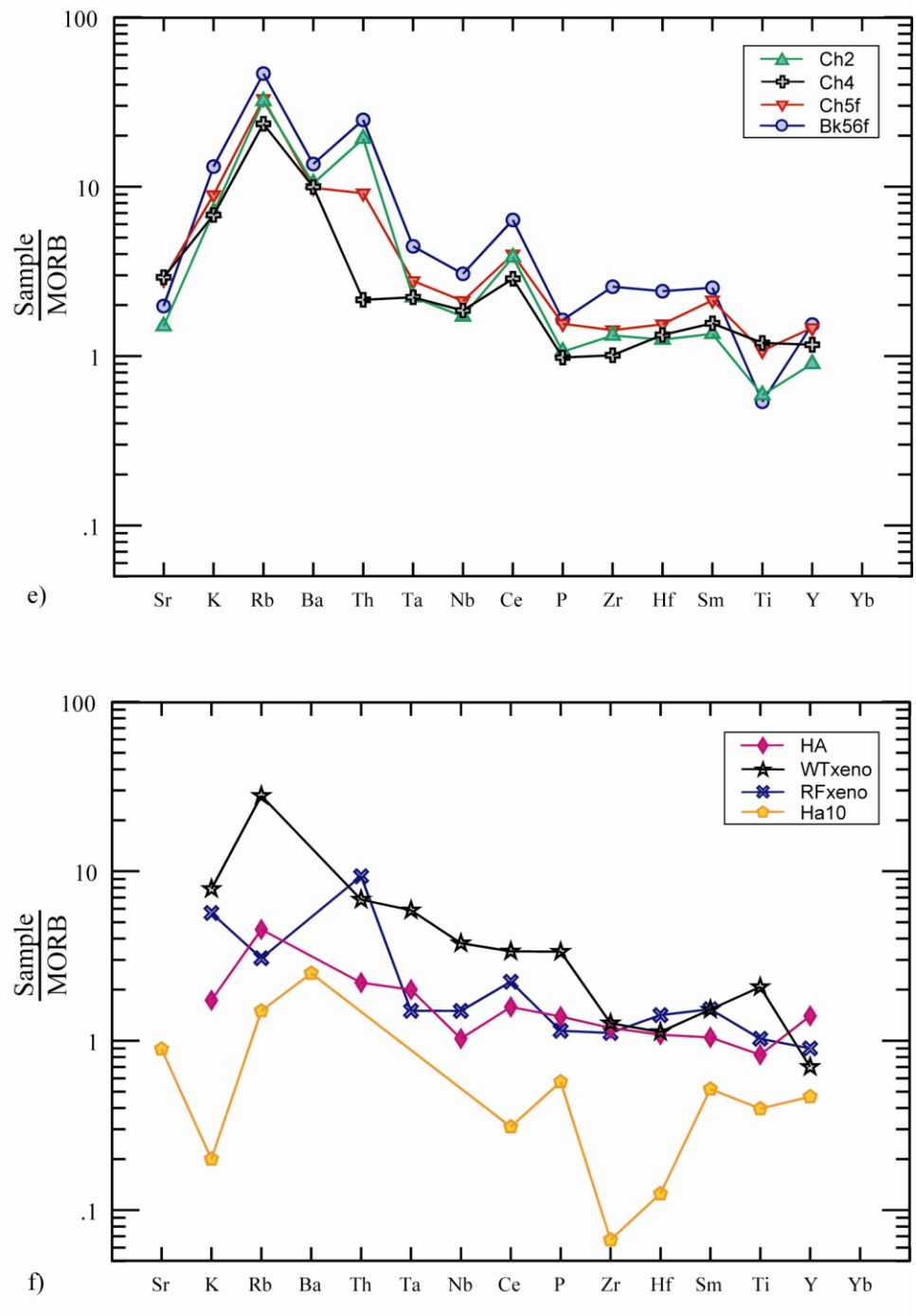

Figure 6-8. *continued*.

Tectonic Discrimination Diagrams

Tectonic discrimination diagrams were utilized to postulate former tectonic environments for the formation of Cat Square terrane metabasites. The Ti–Zr–Y plot (Pearce and Cann, 1973) was first used to identify within-plate basalts (Fig. 6-9a). Since no samples plotted in this field, the Ti–Zr diagram (Pearce and Cann, 1973) was used to identify other types of basalts (Fig. 6-9b). Half of the samples plot in the MORB and calc-alkali basalt fields, while the rest have Ti and Zr values outside of the fields represented in the diagram. The Zr/Y–Zr diagram (Pearce and Norry, 1979), using the fractionation of Zr as an indicator of environments, shows more variability than the previous two diagrams with samples in the within-plate, volcanic-arc, and MORB fields (Fig. 6-9c). Using the Nb/Y–Ti/Y diagram (Pearce, 1982), samples again plot in the MORB and volcanic-arc basalt fields, which have significant overlap (Fig. 6-9d). Pearce and Norry (1979) noted that variations within Ti–Zr–Y–Nb diagrams reflect differences in the mantle source regions (e.g., higher Zr/Y values for within-plate basalts versus other basalt types). Island-arc basalts and MORB basalts may have the same source, but have different values based on the degree of partial melting (Pearce and Norry, 1979).

In an attempt to separate out different types of MORB and volcanic-arc magma series, diagrams based on immobile HFS elements, such as Ti, V, Y, Zr, Nb, La, Yb, Hf, Ta, and Th, are used. The Y/15–La/10–Nb/8 diagram (Cabanis and Lecolle, 1989), useful for distinguishing MORB from volcanic-arc basalts based on depletion of Nb, shows more variation between samples than other discriminant diagrams (Fig. 6-10a). Sample Ch5f now plots as continental basalt near the volcanic-arc boundary where Ch4 plots. Both Ch2 and Bk56f plot as calc-alkali basalt. Trivariate plots of Wood (1980) and Meschede (1986) were also proposed for subdividing MORB and volcanic-arc type magmas. Ch5f plots as N-type (normal) MORB (N-MORB) while all other samples from this study plot as arc-basalts on the Hf/3–Th–Ta diagram (Wood, 1980) (Fig. 6-10b). The Nb*2–Zr/4–Y diagram (Meschede, 1986) has overlap of N-MORB and volcanic-arc basalt fields, which is not helpful for distinguishing between the two, but illustrates that no samples plot as E-type (enriched) MORB (E-MORB) (Fig. 6-10c).

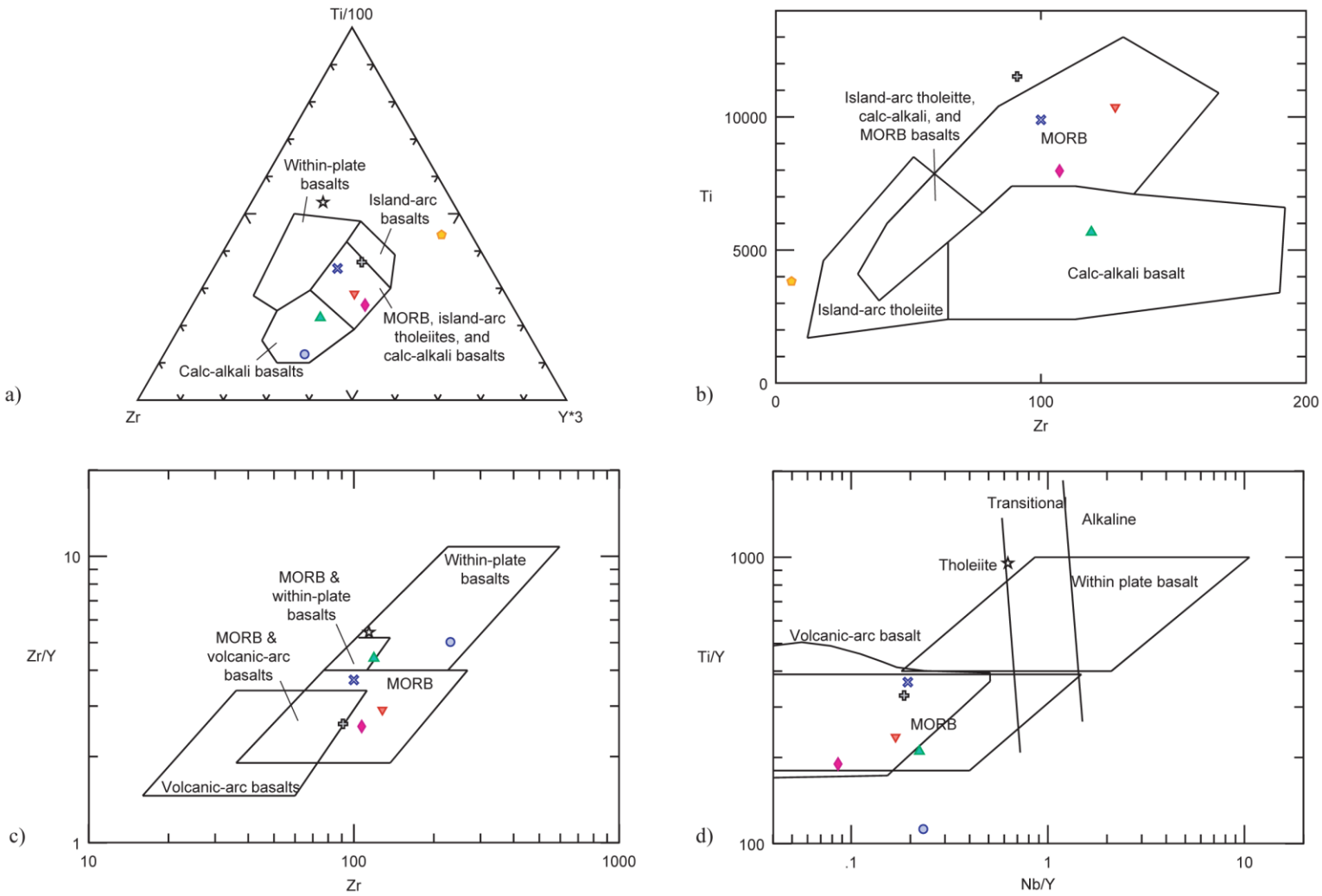

Figure 6-9. Ti-Zr-Y-Nb based tectonic discrimination diagrams for Cat Square terrane metabasites. a) Ti/100–Zr–Y*3 diagram (Pearce and Cann, 1973). b) Ti–Zr diagram (Pearce and Cann, 1973) c) Zr/Y–Zr diagram (Pearce and Norry, 1979). d) Nb/Y–Ti/Y diagram (Pearce, 1982). Symbols same as in Fig. 6-3.

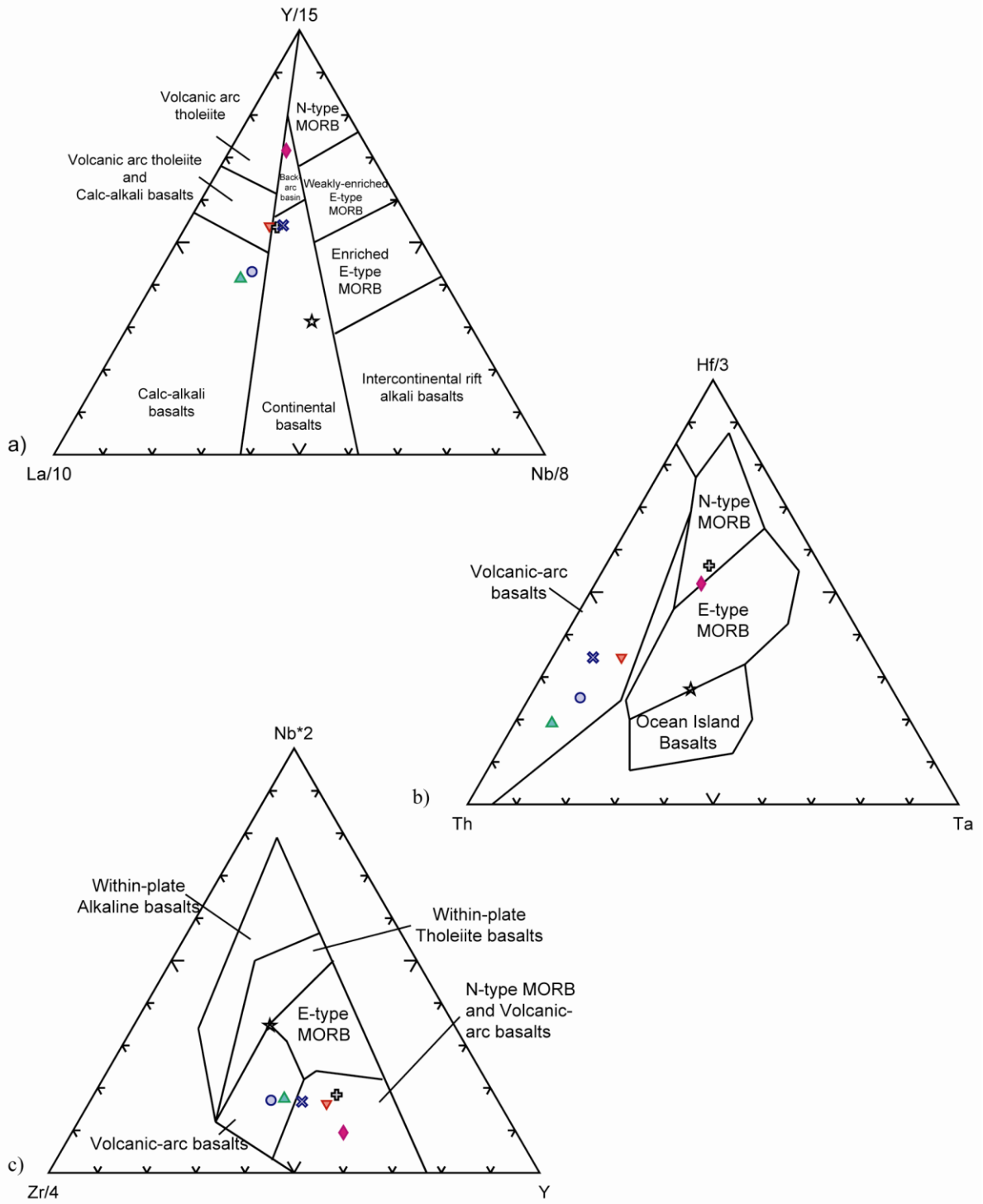

Figure 6-10. Y-La-Nb-Hf-Th-Ta-Zr based tectonic discrimination diagrams for Cat Square terrane metabasites. a) Y/15–La/10–Nb/8 diagram (Cabanis and Lecolle, 1989). b) Hf/3–Th–Ta diagram (Wood, 1980). c) Nb*2–Zr4–Y diagram (Meschede, 1986). Symbols same as in Fig. 6-3.

Two bivariate plots based on HFS elements listed above also indicate a MORB and volcanic-arc affinity for metabasites of this and other studies. The Ta/Yb–Th/Yb diagram (Pearce, 1983) is useful for showing contribution of subduction versus mantle components (Fig. 6-11a); rocks formed from the mantle will plot along the mantle array, whereas rocks formed in a subduction zone or that have crustal contamination will shift to the left of the array. Ch5f is the only sample from this study that plots on the mantle array while the others plot as calc-alkaline basalts, indicative of a convergent margin trend. The V–Ti/1000 diagram (Shervais, 1982) uses elements highly immobile under hydrothermal alteration and medium- to high-grade metamorphism (Rollinson, 1993). This diagram measures the oxygen activity of magmas and crystal fractionation processes taking place to indicate the environment of eruption for basalts (Rollinson, 1993). All samples of this study plot within the MORB and back-arc basin MORB field (Fig. 6-11b).

Summary and Discussion

Composite data between three studies do not consistently plot in same field for all discriminant diagrams, although the majority of time samples plot in the calc-alkaline volcanic arc and MORB fields. When they do not plot in the MORB field, samples plot as back-arc basin basalts, continental basalts, and tholeiitic arc-basalts. Only in the Th–Hf/3–Ta diagram do two samples plot on the edges of the E-MORB field. Samples Ch2 and Bk56f consistently plot near each other in the MORB and calc-alkaline basalt fields on most diagrams. Although these samples are from separate map bodies, similar chemical signatures indicate a similar source and environment of formation. Samples Ch4 and Ch5f, from the same map body, also plot near each other on some diagrams in the MORB and arc-basalts fields. Wilson (2006) suggested Walker Top Granite and Rocky Face pluton xenoliths were likely contaminated by the host granites, causing them to inconsistently plot in MORB and within plate and continental basalt fields. The Hiddenite amphibolite has a dominant MORB signature with some arc-like traits (Wilson, 2006). Sample Ha10 sometimes did not plot on the discriminant diagrams presented here, because values were outside of the axes of the diagram. As previously mentioned, retrograde metamorphic reactions observed in thin section of this sample likely account for this disparity.

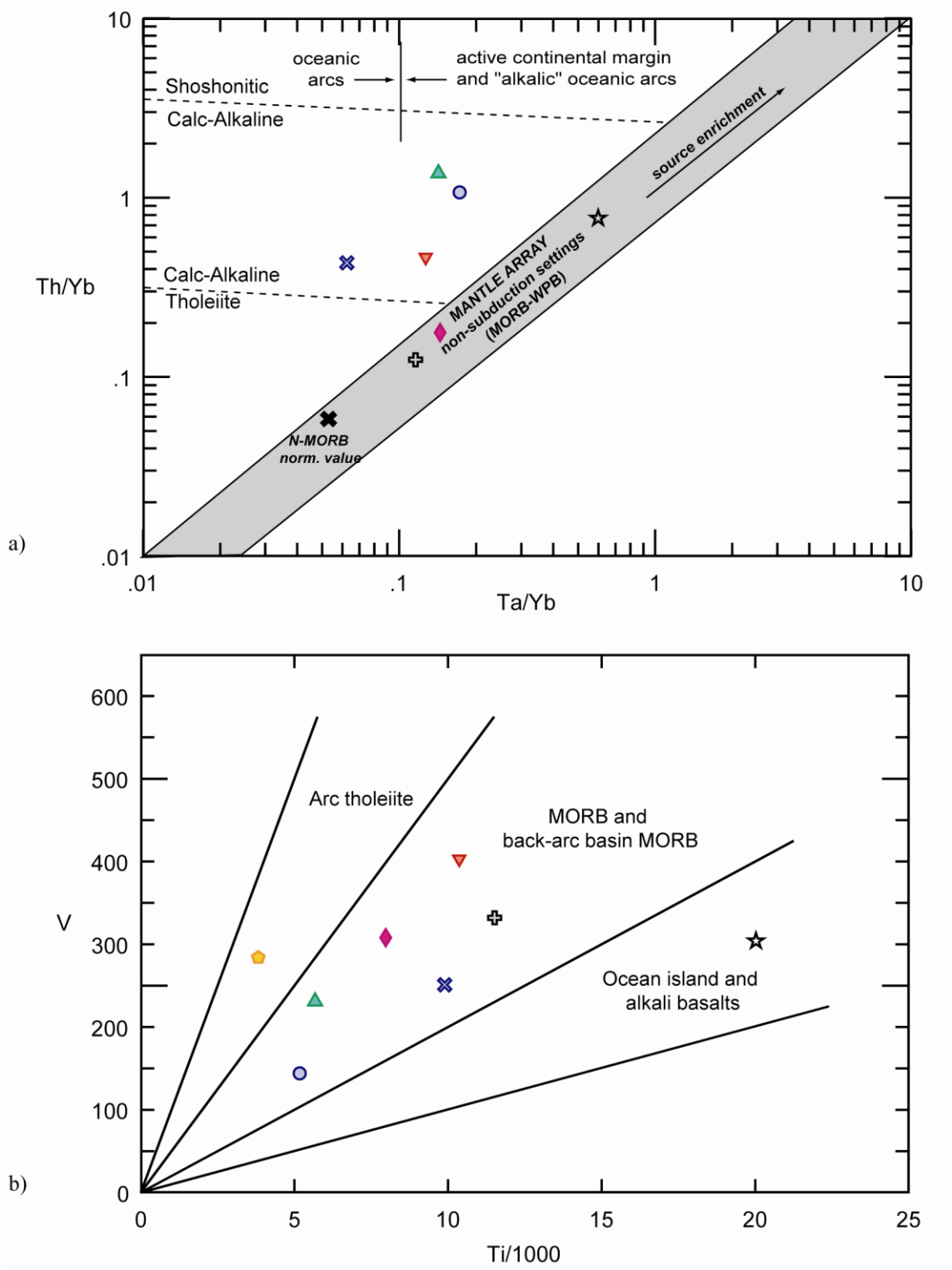

Figure 6-11. Th-Ta-Yb-V-Ti based tectionic discrimination diagrams for Cat Square terrane metabasites. a) Th/Yb–Ta/Yb diagram (Pearce, 1983). b) V–Ti/1000 diagram (Shervais, 1982). Symbols same as in Fig. 6-3.

The mixed MORB and calc-alkaline basalt signatures from samples in this study may be a result of mixed input from MORB and volcanic arc sources, or may represent basalts underlying a back-arc basin. Similar chemical characteristics have been reported in back-arc basins: characteristics that are dependent on the stage of subduction zone development (Saunders and Tarney, 1984; Taylor and Martinez, 2003). At the early stages of subduction, volcanic arcs, produced from hydrated mantle material, record calc-alkaline signatures. When a spreading center has fully developed and is sufficiently separated from the volcanic front where it is no longer affected by hydration, basalts have a NMORB-like composition. The transition between these two end-member stages records a progressive evolution of chemical characteristics from the mixing of calc-alkaline and MORB sources (Taylor and Martinez, 2003).

Tectonic Synthesis: Origin and Evolution of Mafic Complex and Amphibolite Bodies

The Cat Square terrane was proposed to have been a short-lived shrinking remnant ocean basin that closed between Laurentia and the approaching Carolina superterrane (Merschat and Hatcher, 2007). Palinspastic restoration of the Cat Square terrane, prior to its emplacement during the Neoacadian orogeny, places the Cat Square basin in the Pennsylvania embayment, between the New York and Virginia promontories. Preserved from the basin is a deformed, mixed affinity (Laurentian and peri-Gondwanan), flysh facies sequence of metapsammite and pelitic schist, along with ocean floor assemblages of mafic and ultramafic bodies (Merschat and Hatcher, 2007). Most mafic and ultramafic bodies occur along the eastern boundary of the Cat Square terrane (Fig. 6-1).

Previous studies of mafic and ultramafic bodies have concluded that these are dismembered ophiolite sequences and mélanges emplaced during an accretionary event. Misra and Keller (1978) suggested two possible tectonic models for the emplacement of Inner Piedmont ultramafics: a two-stage emplacement, initially in the lower crust and later into the upper crust during subduction; or in a back-arc basin closed by subduction. Based on these two models, Privett (1984) suggested the emplacement of the Turnersburg ultramafic in North Carolina was the result of back-arc basin subduction. The Hammet Grove Suite in South Carolina has been interpreted by Mittwede (1989) as either a thrust slice caught between the

accreting terranes or as a fore-arc ophiolite obducted during initiation of east-dipping subduction beneath the Carolina superterrane. Other amphibolite samples from the Cat Square terrane in South Carolina are reported to have a distinct MORB affinity, while amphibolites of the Kings Mountain belt have chemistries suggesting an island-arc environment (Misra et al., 1990). Samples presented in this study, which plot as both MORB and arc-type basalts, range between the reported values of major element oxide and trace amounts reported by Misra et al. (1990) for the Piedmont and Kings Mountain belt samples. Mittwede (1989) reported the Kings Mountain belt is an ancient arc-trench gap sequence, containing calc-alkaline metavolcanics.

Based on the aforementioned data, one of the following two tectonic models could explain the development of the Cat Square basin and the emplacement of mafic and ultramafic bodies in the Cat Square terrane. Relative locations are discussed based on present- day orientations and directions.

One or more volcanic arcs developed off the eastern Laurentian margin during the Cambrian-Ordovician. A back-arc basin subsequently developed as subduction progressed and the overriding plate remained stationary or moved away from the trench. This back-arc basin probably developed in a pre-existing ocean basin. During this time, upwelling and mantle convection caused the mixing of sources, which produced mixed chemical signatures in the basalts at the spreading center. Since there is no evidence for the subduction of a mid-ocean ridge beneath the western margin of the Carolina superterrane in the Silurian-Devonian, the ridge likely went extinct with a change in plate motion, resulting in a lack of strain accumulated in the basin. Collision of the volcanic arcs with Laurentia during the Taconic orogeny may have affected plate motion. A modern-day example of relict mid-ocean ridge is the Japan Sea, where the basin initially formed in an extensional setting but later became a stable back-arc basin. The basin is now experiencing shortening accompanied by strike-slip deformation (Fournier et al., 1994).

East-dipping subduction, if not already taking place during this time, likely initiated in the Carolina superterrane with back-arc basin development. Significant amounts of sediment, sourced from both Laurentia and the Carolina superterrane, were being deposited into the basin. Deposition continued until post-430 Ma, as recorded by the youngest detrital zircon age from the

Cat Square terrane (Bream, 2003). Southwest-directed oblique collision of the Carolina superterrane with Laurentia began incrementally closing the Theic ocean and, ultimately, the Cat Square basin (Merschat and Hatcher, 2007). Preservation of such an expansive amount of the basin may be a result of the subduction zone becoming choked with sediments if this remnant ocean basin contained large amounts of sediments as proposed by Merschat and Hatcher (2007). Back-arc basin crust could have been preserved with the initiation of subduction or the eventual subduction of younger, warmer crust, or it may have been scraped off and later subducted with pelitic and psammitic sediments. By ~407 Ma, northern portions of the basin were subducted to depths of 15-20 km beneath the Carolina superterrane (Hatcher and Merschat, 2006; Merschat and Hatcher, 2007). Initiation of arc plutonism of the Concord and Salisbury suites at ~407 Ma is suggested to mark the beginning of a mid-Paleozoic event (McSween and Harvey, 1997) with the onset of Neoacadian deformation. The Cat Square terrane became sandwiched between the Carolina superterrane and Laurentia with continued collision during the Neoacadian orogeny and transition from B- to A-type subduction. Slab break-off likely occurred after portions of Laurentia were subducted beneath the Carolina superterrane, possibly causing additional magmatism prior to the onset of the Alleghanian orogeny.

An unconstrained factor affecting this model is the timing of formation of the oceanic crust. Since mafic and ultramafic body ages are unknown, it is difficult to postulate when their oceanic crust protolith formed. The back-arc basin model presented here suggests the basin formed during the Cambrian-Ordivician east of a volcanic arc that was accreted during the Taconic orogeny. It is possible this oceanic crust may have formed in a similar environment, but at a different time.

Timing of accretion of mafic and ultramafic bodies is potentially poorly constrained by the variant ages of granitic bodies in both the Cat Square terrane and the Carolina superterrane. Merschat and Hatcher (2007) suggested the basin was buried to 15-20 km by ~407 Ma, the U-Pb zircon age of the Walker Top Granite (a possible anatectic granitoid) in the Brushy Mountains. However, ages of all other granites in the Cat Square terrane range from 383 to 355 Ma, with a few younger at 325 Ma and 305 Ma (Fig. 2-16). Timing of arc plutonism in the Carolina superterrane is correlative with emplacement of the mafic Concord and Salisbury plutonic suites

with Nd-Sm and Rb-Sr ages ranging from 408-378 Ma (McSween and Harvey, 1997, and references therein). It is difficult to reconcile having the Cat Square terrane fully subducted beneath the Carolina superterrane by ~407 Ma with the initiation of mafic arc magmatism in the overriding plate, unless the arc-trench gap was large enough so that the volcanic arc was not affected by subduction. Different dating techniques could contribute to lack of age correspondence when trying to make a viable tectonic model.

CHAPTER 7

CONCLUSIONS

1. Detailed geologic mapping of the west-central Newton window in portions of the Banoak, Reepsville, Lincolnton West, and Cherryville 7.5-minute quadrangles shows the north-south trending Brindle Creek fault is folded by early tight folding and late open folding, which produces the small Howards Creek window, and larger Newton window, respectively. The Brindle Creek fault has a gentle to moderate, westward dip. Shear-sense indicators along the trace of the fault suggest the Brindle Creek fault is north-directed.

2. The Pott Creek mylonite and Reepsville orthogneiss, located in the Newton window, are deformed Ordovician-Silurian plutons as indicated by zircons with Grenville-aged xenocrystic cores, Ordovician-Silurian oscillatory zoned overgrowths, and Devonian-Mississippian metamorphic rims. The Pott Creek mylonite has an anastomosing outcrop pattern attributed to a tabular, sill-like emplacement and Neoacadian and Alleghanian folding events. The Reepsville orthogneiss occurs as two map-scale bodies and may have been emplaced as dikes or localized bodies of melt.

3. Metamorphic mineral assemblages indicate this portion of the Inner Piedmont experienced sillimanite I and likely up to sillimanite II grade metamorphism during the Neoacadian orogeny. The sillimanite II isograd is approximated to trend northeast-southwest across the central portion of the study area.

4. Map patterns and trends of dominant structural elements, such as S_2 foliation, L_2 mineral lineations, F_2 fold axes, and shear-sense indicators, suggest portions of at least three, and possibly four, map-scale sheath folds occur in the Cat Square terrane of the study area. These sheath folds, cored by sillimanite schist and outlined by metagraywacke, ~356 Ma Walker Top Granite, and ~378 Ma Toluca Granite, may have caused extension within and dismemberment of

mafic complex, amphibolite, metagraywacke and Walker Top Granite bodies. Involvement of these plutons limits timing of deformation to post 356 Ma. Structural data confirms this portion of the Inner Piedmont was involved in north-northwest directed flow during Neoacadian deformation.

5. U-Pb SHRIMP zircon geochronology yielded concordant Devonian-Mississippian crystallization ages for the Vale charnockite (366.4 ± 3.1 Ma) and Walker Top Granite (356 ± 5.3 Ma) at the Vale, North Carolina outcrop. Geochemical signatures indicate the granitoids are A-type, ferroan, metaluminous granitoids with normal to mature volcanic-arc to within-plate granite affinities. Initial ε_{Nd} and $^{87}Sr/^{86}Sr$ values of the Vale granitoids (-4.90 and -7.02; 0.70925 and 0.7085) are similar to those of other Cat Square terrane plutonic and metasedimentary rocks (-6.4 to -9.05; 0.70431 to 0.71421). The Vale charnockite ε_{Nd} value is slightly higher than other Cat Square terrane plutons, plotting towards the mantle array, which may indicate it was influenced more by a mafic source. Isotopic data and retained volcanic-arc signature suggests the granites were derived from a subduction related source. Based on zircon saturation thermometry, minimum magmatic temperatures were calculated at ~840° C for the Vale charnockite and ~800° C for the Walker Top Granite. Two-pyroxene and two-feldspar thermometers yielded crystallization and requilibration temperatures of 730 to 790° C and <700° C, respectively. These data best support a formation model in which the Vale charnockite is an autolith that was incorporated into the Walker Top Granite. The charnockite autoliths represent an early, Fe-rich crystallization of a melt derived from the same parent magma as the Walker Top Granite.

6. Eight map-scale mafic complex and amphibolite bodies, seven of which were previously unrecognized in reconnaissance mapping, range in composition from metagabbro to metadiorite with coarse-grained to schistose textures. Mixed MORB and volcanic-arc basalt geochemical signatures suggest these metabasites formed from MORB and volcanic-arc input or in a back-arc basin setting. The basin may have developed from east-dipping subduction prior to the Taconic orogeny. These bodies likely represent remnant oceanic crust that was dismembered during accretion and possibly the development of F_2 map-scale sheath folds.

REFERENCES CITED

Aftalion, M., Bibikova, E. V., Bowes, D. R., Halliday, A. N., Hopgood, A. M., and Perchuk, L. L., 1991, U-Pb, Rb-Sr, and Sm-Nd isotopic study of the Sharyzhalgay granulite-gneiss-charnockite-granite complex, Lake Baikal region, Siberia, USSR: Journal of Geology, v. 99, p. 851-862.

Aftalion, M., Bowes, D. R., Dash, B., and Dempster, T. J., 1988, Late Proterozoic charnockites in Orissa, India: a U-Pb and Rb-Sr study: Journal of Geology, v. 96, p. 663-676.

Allmendinger, R. W., 2003, Stereonet v.6.3.3.

Albee, A. I., 1965, Distribution of Fe, Mg, and Mn between garnet and biotite in natural mineral assemblages: Journal of Geology, v. 73, p. 155-164.

Anderson, D. J., Lindsley, D. H., and Davidson, P. M., 1993, QUILF: A Pascal program to assess equilibria among Fe-Mg-Mn-Ti oxides, pyroxenes, olivine, and quartz: Computers and Geosciences, v. 19, no. 9, p. 1333-1350.

Barker, F., 1979, Trondhjemite: Definition, environment and hypothesis of origin, *in* Barker, F., ed., Trondhjemites, dacites, and related rocks: Amsterdam, Elsevier, p. 1-12.

Barnes, C. G., Mars, E. V., Swapp, S., and Frost, C. D., 2006, Petrology and geochemistry of the Middle Jurassic Ironside Mountain batholith: evolution of potassic magmas in a primitive arc setting: Geological Society of America Special Paper 410, p. 199-221.

Battacharya, S., and Sen, S. K., 2000, New insights into the origin of Kabbaldurga charnockites, Karnataka, South India: Gondwana Research, v. 3, p. 489-506.

Beaumont, C., Jamieson, R. A., Nguyen, M. H., and Medvede, S., 2004, Crustal channel flows: 1. Numerical models with applications to the tectonics of the Himalayan- Tibetan orogen: Journal of Geophysical Research, v. 109, B06406, doi:10.1029/2003JB002809.

Bentley, R. D., and Neathery, T. N., 1970, Geology of the Brevard zone and related rocks of the Inner Piedmont of Alabama: Alabama Geological Society, Eighth Annual Field Trip Guidebook, 80 p.

Berquist, P. J., Fisher, C. M., Miller, C. F., Wooden, J. L., Fullagar, P. D., and Loewy, S. L., 2005; Geochemistry and U-Pb zircon geochronology of Blue Ridge basement, western North Carolina and eastern Tennessee: implications for tectonic assembly, *in* Hatcher, R. D., Jr., and Merschat, A. J., ed., Blue Ridge geology geotraverse east of the Great Smoky Mountains National Park, western North Carolina: Carolina Geological Society Field Trip Guidebook, p. 33-43.

Bier, S. E., 2001, Geology of the southeastern South Mountains, North Carolina [M.S. thesis]: Knoxville, University of Tennessee, 162 p.

Bier, S. E., Bream, B. R., and Giorgis, S. D., 2002, Inner Piedmont stratigraphy, metamorphism, and deformation in the Marion-South Mountains area, North Carolina, *in* Hatcher, R. D., Jr., and Bream, B. R., eds., Inner Piedmont geology in the South Mountains-Blue Ridge Foothills and southwestern Brushy Mountains, central-western North Carolina: North Carolina Geological Survey, Carolina Geological Society annual field trip guidebook, p. 65-99.

Bream, B. R., 1999, Geology of the Glenwood and Sugar Hill quadrangles, North Carolina, and the structure of the northeast end of the Henderson Gneiss [M.S. thesis]: Knoxville, University of Tennessee, 155 p.

Bream, B. R., 2002, The southern Appalachian Inner Piedmont: new perspectives based on recent detailed mapping; Nd isotopic evidence and zircon geochronology, *in* Hatcher, R. D., Jr., and Bream, B. R., eds., Inner Piedmont geology in the South Mountains-Blue Ridge foothills and the southwestern Brushy Mountains, central western North Carolina: North Carolina Geological Survey, Carolina Geological Society annual field trip guidebook, p. 45-63.

Bream, B. R., 2003, Tectonic implications of geochronology and geochemistry of para- and orthogneisses from the southern Appalachian crystalline core [Ph.D. dissertation]: Knoxville, University of Tennessee, 296 p.

Bream, B. R., Hatcher, R. D., Jr., Miller, C. F., and Fullagar, P.D., 2001, Geochemistry and provenance of Inner Piedmont paragneisses, NC and SC: Evidence for an internal terrane boundary?: Geological Society of America Abstracts with Programs, v. 33, no. 2, p. 65.

Bream, B. R., Hatcher, R. D., Jr., Miller, C. F., and Fullagar, P. D., 2004, Detrital zircon ages and Nd isotopic data from the southern Appalachian crystalline core, Georgia, South Carolina, North Carolina, and Tennessee: New provenance constraints for part of the Laurentian margin, *in* Tollo, R. P., Corriveau, L., McLelland, J., and Bartholomew, M. J., eds., Proterozoic tectonic evolution of the Grenville orogen in North America: Boulder, Colorado, Geological Society of America Memoir 197, p. 459–475.

Bridgwater, D., Sutton, J., and Watterson, J., 1974, Crustal downfolding associated with igneous activity: Tectonophysics, v. 21, p. 57-77.

Brown, G. C., Thorne, R. S., and Webb, P. C., 1984, The geochemical characteristics of granitoids in contrasting arcs and comments on magma sources: Journal of the Geological Society, v. 141, p. 401-426.

Bucher, K., and Frost, B. R., 2006, Fluid transfer in high-grade metamorphic terrains intruded by anorogenic granites: the Thor Range, Antarctica: Journal of Petrology, v. 47, p. 567–593.

Buhl, D., Grauert, B., and Raith, M., 1983, U-Pb zircon dating of Archean rocks from the South India Craton: results from the amphibolite to granulite facies transition zone at Kabbal Quarry, southern Karnataka: Fortschritte der Mineralogie, v. 61, p. 43-45.

Butler, J. R., 1972, Geologic map and mineral resources summary of the Black Mountain quadrangle, North Carolina: North Carolina Department of Natural and Economic Resources Map GM 201–SE, scale 1:24,000.

Butler, J. R., 1988, Review and classification of ultramafic bodies in the Piedmont of the Carolina, *in* Mittwede, S. K., and Stoddard, E. F., eds., Ultramafic rocks of the Appalachian Piedmont: Geological Society of America Special Paper 231, p. 19-31.

Butler, J. R., 1991, Metamorphism, *in* Horton, J. W., Jr., and Zullo, V. A., eds., The geology of the Carolinas: Knoxville, University of Tennessee Press, p. 127-141.

Butler, J. R., and Fullagar, P. D., 1978, Petrochemical and geochronological studies of plutonic rocks in the southern Appalachians: III. Leucocratic adamellites of the Charlotte belt near Salisbury, North Carolina: Geological Society of America Bulletin, v. 89, p. 460-466.

Byars, H., Merschat, A. J., Hatcher, R. D., Jr., and Wooden, J., 2008a, Timing and implications for the emplacement of Paleozoic Vale (Cat Square) charnockite and Walker Top Granite, eastern Inner Piedmont: Geological Society of America Abstracts with Programs, v. 40, no. 4, p. 18.

Byars, H. E., Gilliam, W. G., Hatcher, R. D., Jr., Merschat, A. J., and Bier, S. E., 2008b, Tectonic evolution of the Appalachian Inner Piedmont from a new detailed geologic map from the Brevard fault into the Newton window: Geological Society of America Abstracts with Programs, v. 40, no. 6, p. 157.

Cabanis, B., and Lecolle, M., 1989, Le diagramme La/10-Y/15-Nb/8: on outil pour la discrimination des series volcaniques et la mise en evidence des processus de mélange et/ ou de contamination crustale: C.R. Academy of Science Ser. II, v. 309, p. 2023-2029.

Carpenter, R. H., 1970, Metamorphic history of the Blue Ridge province of Tennessee and North Carolina: Geological Society of America Bulletin, v. 81, p. 749-762.

Carrigan, C. W., Bream, B. R., Miller, C. F., and Hatcher, R. D., Jr., 2001, Ion microprobe analyses of zircon rims from the eastern Blue Ridge and Inner Piedmont, NC-SC-GA: Implications for the timing of Paleozoic metamorphism in the southern Appalachians: Geological Society of America Abstracts with Programs, v. 33, no. 2, p. A7.

Carrigan, C. W., Miller, C. F., Fullagar, P. D., Bream, B. R., Hatcher, R. D., Jr., and Coath, C. D., 2003, Ion microprobe age and geochemistry of southern Appalachian basement, with implications for Proterozoic and Paleozoic reconstructions: Precambrian Research, v. 120, p. 1-36.

Chatterjee, N. D., and Johannes, W., 1974, Thermal stability and standard thermodynamic properties of synthetic $2M_1$ muscovite, $KAl_2AlSi_3O_{10}(OH)_2$: Contributions to Mineralogy and Petrology, v. 48, p. 119-126.

Christoffel, C. A., Connelly, J. N., and Åhåll, K. I., 1999, Timing and characterization of recurrent pre-Sveconorwegian metamorphism and deformation in the Varberg-Halmstad region of SW Sweden: Precambrian Research, v. 98, p. 173–195.

Connelly, J. B., and Dallmeyer, R. D., 1993, Polymetamorphic evolution of the western Blue Ridge; evidence from $^{40}Ar/^{39}Ar$ whole-rock slate/phyllite and muscovite ages: American Journal of Science, v. 293, p. 322-359.

Corfu, F., Hanchar, J. M., Hoskin, P. W. O., and Kinny, P., 2003a, Atlas of zircon textures, *in* Hanchar, J. M., and Hoskin, P. W. O., eds., Reviews in Mineralogy & Geochemistry: Zircon: Mineralogical Society of America, v. 53, p. 468-500.

Corfu, F., Armitage, P. E. B., Kullerud, K., and Bergh, S. G., 2003b, Preliminary U-Pb geochronology in the West Troms Basement Complex, North Norway: Archean and Paleoproterozoic events and younger overprints: Geological Survey of Norway Bulletin, v. 441, p. 61-72.

Corrie, S. L., and Kohn, M. J., 2007, Resolving the timing of orogenesis in the western Blue Ridge, southern Appalachians, via *in situ* ID-TIMS monazite geochronology: Geology, v. 35, no. 7, p. 627-630.

Cox, K. G., Bell, J. D., and Pankhurst, R. J., 1979, The interpretation of igneous rocks: London, Allen and Urwin, 450 p.

Curl, D. C., 1998, Stratigraphy and structure of Wellford and Reidville Quadrangles in part of the eastern Inner Piedmont, near Spartanburg, South Carolina [M.S. thesis]: Knoxville, University of Tennessee, 129 p.

Dallmeyer, R. D., 1988, Late Paleozoic tectonothermal evolution of the western Piedmont and eastern Blue Ridge, Georgia: Controls on the chronology of terrane accretion and transport in the southern Appalachian orogen: Geological Society of America Bulletin, v. 100, no. 5, p. 702-713.

Dallmeyer, R. D., 1989, Late Paleozoic thermal evolution of crystalline terranes within portions of the U.S., Appalachian orogen, *in* Hatcher, R. D., Jr., Thomas, W.A., and Viele, G. W., eds., The Appalachian–Ouachita orogen in the United States: Boulder, Colorado, Geological Society of America, The Geology of North America F-2, p. 417-444.

Dallmeyer, R. D., Wright, J. E., Secor, D. T., and Snoke, A. W., 1986, Character of the Alleghanian Orogeny in the southern Appalachians; Part II, Geochronological constraints on the tectonothermal evolution of the eastern Piedmont in South Carolina: Geological Society of America Bulletin, v. 97, no. 11, p. 1329-1344.

Davidson, P. A., and Lindsley, D. H., 1985, Thermodynamic analysis of quadrilateral pyroxene: Part II: Model calibration from experiments and applications to geothermometry: Contributions to Mineralogy and Petrology, v. 91, p. 390-404.

Davis, B. A., 2009, Tectonic evolution of the southern Appalachian Inner Piedmont: Identification and interpretation of crustal features from aeromagnetic data and detailed geologic mapping in central Georgia [M.S. thesis]: Knoxville, University of Tennessee, xxx p.

Davis, B. A., Huebner, M. T., and Hatcher, R. D., Jr., 2009, Detailed geologic mapping and structural analysis of a portion of the central Georgia Inner Piedmont and a possible fault identified with aeromagnetic data: Geological Society of America Abstracts with Programs, v. 41, no. 3, p. 29.

Davis, T. L., 1993, Lithostratigraphy, structure, and metamorphism of a crystalline thrust terrane, western Inner Piedmont, North Carolina [Ph.D. dissertation]: Knoxville, University of Tennessee, 245 p.
Dennis, A. J., 2007, Cat Square basin, Catskill clastic wedge: Silurian-Devonian orogenic events in the central Appalachians and the crystalline southern Appalachians, *in* Sears, J. W., Harms, T. A., and Evenchick, C. A., eds., Whence the Mountains? Inquiries into the evolution of orogenic systems: A volume in honor of Raymond A. Price: Geological Society of America Special Paper 433, p. 313-329.
Dennis, A. J., and Wright, J. C., 1997a, Middle and late Paleozoic monazite U-Pb ages, Inner Piedmont, South Carolina: Geological Society of America Abstracts with Programs, v. 29, no. 3, p. 12.
Dennis, A. J., and Wright, J. C., 1997b, The Carolina terrane in northwestern South Carolina, U.S.A: Late Precambrian-Cambrian deformation and metamorphism in a peri-Gondwanan oceanic arc: Tectonics v. 16, p. 460-473.
DePaolo, D., 1983, The mean life of continents: estimates of continent recycling rates from Nd and Hf isotopic data and implications for mantle structure: Geophysical Research Letters, v. 10, p. 705-708.
DePaolo, D., 1981, Neodymium isotopes in the Colorado Front Range and crust-mantle evolution in the Proterozoic: Nature, v. 291, p. 193-196.
Duchesne, J. C., and Wilmart, E., 1997, Igneous charnockites and related rocks from the Bjerkreim-Sokndal layered intrusion (southwest Norway): a Jotunite (hypersthene monzodiorite)-derived A-type granitoid suite: Journal of Petrology, v. 38, p. 337–369.
Eckert, J. O., Hatcher, R. D., Jr., and Mohr, D. W., 1989, The Wayah granulite-facies metamorphic core, southwestern North Carolina: High grade culmination of Taconic metamorphism in the southern Blue Ridge: Geological Society of America Bulletin, v. 101, p. 1434-1447.
Espenshade, G. H., Rankin, D. W., Shaw, K. W., and Neuman, R. B., 1975, Geologic map of the west half of the Winston-Salem quadrangle, North Carolina–Virginia: U.S. Geological Survey Map I–709–B, scale 1:250,000.
Fournier, M., Jolivet, L., Huchon, P., Sergeyev, K. F., and Oscorbin, L. S., 1994, Neogene strike-slip faulting in Sakhalin and the Japan Sea opening: Journal of Geophyical Research, v. 99, no. B2, p. 2701-2725.
Frost C. D., Frost, B. R., Chamberlain, K. R., and Edwards, B. R., 1999, Petrogenesis of the 1.43 Ga Sherman batholiths, SE Wyoming: a reduced rapikivi-type anorogenic granite: Journal of Petrology, v. 40, p. 1771-1802.
Frost, B. R., Frost, C. D., Hulsebosch, T. P., and Swapp, S. M., 2000, Origin of the charnockites of the Louis Lake batholiths, Wind River Range, Wyoming: Journal of Petrology, v. 41, 1759-1776.
Frost, B. R., Arculus, R. J., Barnes, C. G., Collins, W. J., Ellis, D. J., and Frost, C. D., 2001, A geochemical classification of granitic rocks: Journal of Petrology, v. 42, p. 2033-2048.
Frost, B. R., and Frost, C. D., 2008, On charnockites: Gondwana Research, v. 13, p. 30-44.
Fullagar, P. D., and Butler, J. R., 1979, 325 to 265 M.Y.-old granitic plutons in the Piedmont of the southeastern Appalachians: American Journal of Science, v. 279, p.161-185.
Fullagar, P. D., Goldberg, S. A., and Butler, J. R., 1997, Nd and Sr isotopic characterization of crystalline rocks from the southern Appalachian Piedmont and Blue Ridge, North and South Carolina, *in* Sinha, A., K., Whalen, J. B., and Hogan, J. P., eds., The Nature of Magmatism in the Appalachian Orogen: Boulder Colorado, Geological Society of America Memoir 191, p. 165-179.
Fuhrman, M. L., and Lindsley, D. H., 1988, Ternary-feldspar modeling and thermometry: American Mineralogist, v. 73, p. 201-215.
Gatewood, M. P., 2007, Structure and tectonics of the northeastern Inner Piedmont from detailed geologic mapping, geochronologic, geochemical, and petrologic studies with macro-, meso-, and

microstructural analyses of ductile fault zones [M.S thesis]: Knoxville, University of Tennessee, 279 p.
Gilliam, W. G., in progress, Detailed geologic mapping of the western Newton window: Evidence for Neoacadian ductile thrusting [M.S. thesis]: Knoxville, University of Tennessee, xxx p.
Gilliam, W. G., Byars, H. E., Hatcher, R. D., Jr., and Merschat, A. J., 2008, Tectonic implications of geologic mapping in the western Newton window, Inner Piedmont, NC: Geological Society of America Abstracts with Programs, v. 40, no. 4, p.18.
Giorgis, S. D., 1999, Inner Piedmont geology of the northwestern South Mountains near Morganton, North Carolina [M.S. thesis]: Knoxville, University of Tennessee, 191 p.
Giorgis, S. D., Mapes, R. W., and Bream, B. R., 2002, The Walker Top Granite: Acadian granitoid or eastern Inner Piedmont basement?, *in* Hatcher, R. D., Jr., and Bream, B. R., eds., Inner Piedmont geology in the South Mountains-Blue Ridge Foothills and southwestern Brushy Mountains, central-western North Carolina: North Carolina Geological Survey, Carolina Geological Society annual field trip guidebook, p. 33-43.
Goldberg, S. A., and Dallmeyer, R. D., 1997, Chronology of Paleozoic metamorphism and deformation in the Blue Ridge thrust complex, North Carolina and Tennessee: American Journal of Science, v. 297, p. 488-526.
Goldsmith, R., 1981, Structural patterns in the Inner Piedmont of the Charlotte and Winston-Salem 2-degree quadrangles, North Carolina and South Carolina, *in* Horton, J. W., Jr., Butler, J. R., and Milton, D. M., eds., Geological investigations of the Kings Mountain belt and adjacent areas in the Carolinas: Carolina Geological Society Field Trip Guidebook, p. 9-27.
Goldsmith, R., Milton, D. J., and Horton, J. W., Jr., 1988, Geologic map of the Charlotte 1° X 2° quadrangle, North Carolina and South Carolina: U.S. Geological Survey Map I–1251–E, scale 1:250,000.
Grew, E. S., and Manton, W. I., 1984, Age of allanite from Kabbaldurga Quarry, Karnataka: Journal of the Geological Society of India, v. 25, p. 193-195.
Griffin, V. S., Jr., 1967, Geology of the Six Mile quadrangle, South Carolina: South Carolina Division of Geology, Geology Notes, v. 13, p. 87-104.
Griffin, V. S., Jr., 1969, Inner Piedmont tectonics in the vicinity of Walhalla, South Carolina: South Carolina Division of Geology, Geology Notes, v. 13, p. 15-28.
Griffin, V. S., Jr., 1971, The Inner Piedmont belt of the southern crystalline Appalachians: Geological Society of America Bulletin, v. 82, p. 1885-1898.
Griffin, V.S., Jr., 1974, Analysis of the Piedmont in northwest South Carolina: Geological Society of America Bulletin, v. 85, p. 1123-1138.
Griffin, V. S., Jr., 1979, Geology of the Abbeville East, Abbeville West, Latimer, and Lowndesville quadrangles, South Carolina: South Carolina Geological Survey Map Series 24, 58 p. and maps.
Griffitts, W. C., and Overstreet, W. C., 1952, Granitic rocks of the western Carolina Piedmont: American Journal of Science, v. 250, p. 777-789.
Hadley, J. B., and Goldsmith, R., 1963, Geology of the eastern Great Smoky Mountains, North Carolina: U.S. Geological Survey Map I-654, scale 1:250,000.
Hadley, J. B., and Nelson, A. E., 1971, Geology of the Knoxville quadrangle, North Carolina, Tennessee, South Carolina: U.S. Geological Survey Map I-654, scale 1:250,000.
Hames, W. E., Renne, P. R., and Ruppel, C., 2000, New evidence for geologically instantaneous emplacement of the earliest Jurassic Central Atlantic magmatic province basalts on the North American margin: Geology, v. 28, no. 9, p. 859-862.

Hamilton, M. A., McLelland, J., and Selleck, B., 2004, SHRIMP U-Pb zircon geochronology of the anorthosite-mangerite-charnockite-granite suite, Adirondack Mountains, New York: ages of emplacement and metamorphism: Geological Society of America Memoir 197, p. 337-355.

Hansen, E. C., and Stuk, M. A., 1989, Devolitization reactions in the amphibolite to granulite facies transitional terrane around Lone Peak, Santa Lucia Range, California: Geological Society of America Abstracts with Programs, v. 21, p. A277.

Harris, N. B. W., Pearce, J. A., and Tindle, A. G., 1986, Geochemical characteristics of collision-zone magmatism, *in* Coward, M. P. and Reis, A. C., eds., Collision tectonics: Geological Society of America Special Publication, v. 19, p. 67-81.

Harrison, T. M., and Watson, E. B., 1983, Kinetics of zircon dissolution and zirconium diffusion in granitic melts of variable water content: Contributions to Mineralogy and Petrology, v. 84, p. 66-72.

Hatcher, R. D., Jr., 1987, Tectonics of the southern and central Appalachian internides: Annual Review of Earth and Planetary Sciences, v. 15, p. 337-362.

Hatcher, R. D., Jr., 1993, Perspectives on the tectonics of the Inner Piedmont, southern Appalachians, *in* Hatcher, R. D., Jr., and Davis, T. L., eds., Studies of Inner Piedmont geology with a focus on the Columbus Promontory: Carolina Geological Society Guidebook, p. 17-43.

Hatcher, R. D., Jr., 2001, Rheological partitioning during multiple reactivation of the Paleozoic Brevard fault zone, southern Appalachians, USA, *in* Holdsworth, R. E., Strachan, R. A., Magloughlin, J. F., and Knipe, R. J., eds., The nature and tectonic significance of fault zone weakening: London, Geological Society of London Special Publication 186, p. 255-269.

Hatcher, R. D., Jr., 2002, An Inner Piedmont primer, *in* Hatcher, R. D., Jr., and Bream, B. R., eds., Inner Piedmont geology in the South Mountains-Blue Ridge Foothills and the southwestern Brushy Mountains, central-western North Carolina: North Carolina Geological Survey, Carolina Geological Society annual field trip guidebook, p. 1-18.

Hatcher, R. D., Jr., 2004, Southern Appalachian Crustal Transect: Day 2, The Neoacadian metamorphic core, large ductile thrust sheets, and a multiply reactivated crustal scale shear zone, *in* Merschat, A. J., and Hatcher, R. D., Jr., eds., Trans Appalachian Internides Geotraverse: 17th International Basement Tectonics Association Field Trip Guidebook, p. 29-60.

Hatcher, R. D., Jr., 2006, Juxtaposed Mesozoic diabase dikes and siliceous cataclasite fault zones in the Carolinas and the mechanics of dike emplacement: Geological Society of America Abstracts with Programs, v. 38, no. 3, p. 8.

Hatcher, R. D., Jr., in press, Developmental history of the Appalachian Orogen: A brief summary, *in*, Tollo, R. P., Bartholomew, M. J., and Hibbard, J. P., Geological Society of America Memoir.

Hatcher, R. D., Jr., and Butler, J. R., 1979, Guidebook for southern Appalachian field trip in the Carolinas, Tennessee, and northeastern Georgia: University of North Carolina, Chapel Hill, International Geological Correlation Program Project 27, 117 p.

Hatcher, R. D., Jr., and Goldberg, S. A., 1991, The Blue Ridge Geologic province, *in* Horton, J. W., Jr., and Zullo, V. A., eds., The geology of the Carolinas: Knoxville, University of Tennessee Press, p. 11-37.

Hatcher, R. D., Jr., and Merschat, A. J., 2006, The Appalachian Inner Piedmont: An exhumed strike-parallel, tectonically forced orogenic channel, *in* Law, R. D., Searle, M., and Godin, L., eds., Channel flow, ductile extrusion and exhumation of lower-mid crust in continental collision zones: London, Geological Society of London Special Publication 268, p. 517-540.

Hatcher, R. D., Jr., and Steltenpohl, M. G., in preparation, Geologic map of the Pine Mountain window: Geological Society of America Maps and Charts Series.

Hatcher, R. D., Jr., Bream, B. R., and Merschat, A. J., 2007, Tectonic map of the southern and central Appalachians: A tale of three orogens and a complete Wilson cycle, *in* Hatcher, R. D., Jr., Carlson, M. P., McBride, J. H., and Martínez Catalán, J. R., eds., 4-D Framework of Continental Crust: Geological Society of America Memoir 200, p. 595-632.

Hatcher, R. D., Jr., Merschat, A. J., and Thigpen, J. R., 2005, Blue Ridge primer, *in* Hatcher, R. D., Jr. and Merschat, A. J., eds., Blue Ridge geology geotraverse east of the Great Smoky Mountains National Park, western North Carolina: Carolina Geological Society Guidebook, p. 1-24.

Heaman, L. M., Erdmer, P., and Owen, J. V., 2002, U-Pb geochronologic constraints on the crustal evolution of the Long Range Inlier, Newfoundland: Canadian Journal of Earth Sciences, v. 35, no. 5, p. 845-865.

Hibbard, J. P., Tracy, R. J., and Henika, W. S., 2003, Smith River allochthon; a southern Appalachian peri-Gondwanan terrane emplaced directly on Laurentia?: Geology, v. 31, p. 215-218.

Higgins, M. W., Crawford, T. J., Atkins, R. L., and Crawford, R. F., 2003, Geologic map of the Atlanta 30° x 60° quadrangle, Georgia: U.S. Geological Survey, Geologic Investigations Series Map I-2602, scale 1:250,000.

Hill, J. C., 1999, Geology of the Marion East quadrangle, North Carolina and the stratigraphy of the Tallulah Falls Formation in the Chauga belt [M. S. thesis]: Knoxville, University of Tennessee, 188 p.

Holdaway, M. J., 1971, Stability of andalusite and the aluminum silicate phase diagram: American Journal of Science, v. 271, p. 97-131.

Holdaway, M. J., and Lee, S. M., 1977, Fe-Mg cordierite stability in high-grade pelitic rocks based on experimental, theoretical, and natural observation: Contributions to Mineralogy and Petrology, v. 63, p. 175-198.

Holland, T. H., 1900, The charnockite series, a group of Archean hypersthenic rocks in Peninsular India: Memoirs of the Geological Survey of India, v. 28, p. 130-149.

Hopson, J. L., 1994, Structure of part of the Blue Ridge, northeastern Georgia and North Carolina [Ph.D. dissertation]: Knoxville, University of Tennessee, 454 p.

Hopson, J. L., and Hatcher, R. D., Jr., 1988, Structural and stratigraphic setting of the Alto allochthon, NE Georgia: Geological Society of America Bulletin, v. 100, p. 339-350.

Hopson, J. L., Hatcher, R. D., Jr., and Stieve, A. L., 1989, Geology of the eastern Blue Ridge, northeastern Georgia and the adjacent Carolinas, *in* Fritz, W. J., Hatcher, R. D., Jr., and Hopson, J. L., eds., Geology of the eastern Blue Ridge of northeast Georgia and the adjacent Carolinas: Georgia Geological Society Guidebooks, v. 9, p. 1-40.

Horton, J. W., 2008, Geologic Map of the Kings Mountain and Grover Quadrangles, Cleveland and Gaston Counties, North Carolina, and Cherokee and York Counties, South Carolina: U.S. Geological Survey Scientific Investigations Map 2981, scale 1:24,000.

Horton, J. W., and McConnell, K. I., 1991, The western Piedmont, *in* Horton, J. W., and Zullo, V. A., eds., The geology of the Carolinas: Knoxville, Tennessee, University of Tennessee Press, p. 36-58.

Hoskin, P. W. O., and Ireland, T. R., 2000, Rare earth element chemistry of zircon and its use as a provenance indicator: Geology, v. 28, p. 627–630.

Hubbard, F. H., and Whitley, J. E., 1979, REE in charnockite and associated rocks, southwest Sweden: Lithos, v. 12, p. 1–11.

Irvine, T. N., and Baragar, W. R. A., 1971, A guide to the chemical classification of common rocks: Canadian Journal of Earth Science, v. 8, p. 523-548.

Irwin, J. J., Kirschbaum, C., Lim, T., Glassley, W., Ryerson, F. J., Shaw, H. F., Niemeyer, S., and Abeysinghe, P. B., 1987, Laser-microprobe ^{39}Ar-^{40}Ar ages of high grade metamorphic rocks from Sri Lanka: EOS, v. 68, p. 431.

Jordt-Evangelista, H., 1997, Igneous charnockites in the southeastern transition zone between the São Francisco Craton and the Costeiro Mobile Belt, Brazil: Revista Brasileira Geociências, v. 26, no. 2, p. 93–102.

Kagami, H., Owada, M., Osanai, Y., and Hiroi, Y., 1990, Preliminary geochronological study of Sri Lankan rocks, *in* Hiroi, Y., and Motoyoshi, Y., eds., International Report of Japan-Sri Lanka Joint Research: Japanese Ministry of Education, Science, and Culture, p. 55-70.

Kalbas, J. L., 2003, Geology of part of the southwestern Brushy Mountains, Inner Piedmont [M.S. thesis]: Knoxville, University of Tennessee, 208 p.

Kalbas, J. L., Bream, B. R., Hatcher, R. D., Jr., and Maybin, A. H., 2002, Evidence for mafic Ordovician magmatism in the Brushy Mountains, western Inner Piedmont of North Carolina: Geological Society of America Abstracts with Programs, v. 34, no. 2, p. 119.

Keith, A., and Sterrett, D. B., 1931, Description of the Gaffney and Kings Mountain quadrangles, S. C.-N. C.: U. S. Geological Survey Folio 222, 18 p.

Kilpatrick, J. A., and Ellis, D. J., 1992, C-type magmas: igneous charnockites and their extrusive equivalents: Transactions of the Royal Society of Edinburgh: Earth Sciences, v. 83, p. 155-164.

Kish, S. A., 1983, A geochronological study of deformation and metamorphism in the Blue Ridge and Piedmont of the Carolinas [Ph.D. dissertation]: Chapel Hill, University of North Carolina, 220 p.

Kish, S. A., 1997, The Cat Square charnockite ─ a Paleozoic charnockite in the Inner Piedmont of North Carolina: Geological Society of America Abstracts with Programs, v. 29, no. 3, p. 28.

Kish, S. A., and Odom, A. L., 1999, In search of Precambrian basement in the Piedmont of the southern Appalachian – all that is granulite is not Grenville: Geological Society of America Abstracts with Programs, v. 31, no. 3, p. 26.

Kohn, M. J., 2001, Timing and accretion in the southern Appalachians: perspectives from the Laurentian margin: Geological Society of America Abstracts with Programs, v. 33, no. 6, p. A262.

Lemmon, R. E., and Dunn, D. E., 1973a, Geologic map and mineral resources of the Fruitland quadrangle, North Carolina: North Carolina Department of Natural Resources and Community Development GM 202-NW, scale 1:24,000.

Lemmon, R. E., and Dunn, D. E., 1973b, Geologic map and mineral resources of the Bat Cave quadrangle, North Carolina: North Carolina Department of Natural Resources and Community Development GM 203-NW, scale 1:24,000.

Lindsley, D. H., and Anderson, D. J., 1983, A two-pyroxene thermometer: Journal of Geophysical Research, v. 88, p. A887-A906.

Ludwig, K. R., 1998, On the treatment of concordant uranium-lead ages: Geochimica et Cosmochimica Acta, v. 62, p. 315-318.

Ludwig, K. R., 2001, SQUID v. 1.02, computer program.

Ludwig, K. R., 2003, Isoplot v. 3.00, computer program.

Luth, W. D., Jahns, R. H., and Tuttle, O. F., 1964, The granite system at pressures of 4 to 10 kilobars: Journal of Geophysical Research, v. 69, p. 759-773.

Malm, O. A., and Ormaasen, D. E., 1978, Mangerite–charnockite intrusives in the Lofoten-Vesterålen Area, North Norway: petrography, chemistry, and petrology: Geological Survey of Norway Bulletin, v. 338, p. 83–114.

Mapes, R. W., 2002, Geochemistry and geochronology of mid-Paleozoic granitic plutonism in the southern Appalachian Piedmont terrane, North Carolina-South Carolina-Georgia [M.S. thesis]: Nashville, TN, Vanderbilt University, 150 p.

Mapes, R. W., Maybin, A. H., III, Miller, C. F., Fullagar, P. D., and Bream, B. R., 2002, Geochronology and geochemistry of mid-Paleozoic granitic magmatism, central and eastern Inner Piedmont, North Carolina and South Carolina: Geological Society of America Abstracts with Programs, v. 34, no. 2, p. A92.

Mapes, R. W., Miller, C. F., Fullagar, P. D., and Bream, B. R., 2001, Nature and origin of Acadian plutonism, Piedmont terrane, NC-GA: Geological Society of America Abstracts with Programs, v. 33. no. 6, p. A92.

May, P. R., 1971, Pattern of Triassic-Jurassic diabase dikes around the North Atlantic in the context of predrift position of the continents: Geological Society of America Bulletin, v. 82, p. 1285-1292.

Maybin, A. H., III, and Mittwede, S. K., 1988, The Enoree mélange, Laurens County, South Carolina: Geological Society of America Abstracts with Programs, v. 20, no. 4, p. 278.

Mazdab, F. K., and Wooden, J. L., 2006, Trace element analysis in zircon by ion microprobe (SHRIMP-RG): technique and applications: 6th Annual V.M. Goldschmidt Conference.

McConnell, K. I., 1990, Geology and geochronology of the Sauratown Mountains anticlinorium, northwestern North Carolina [PhD. Dissertation]: Columbia, University of South Carolina, 300 p.

McGregor, V. R., and Friend, C. R. L., 1992, Late Archean prograde amphibolite- to granulite-facies relations in the Fiskenaesset region, southern west Greenland: Journal of Geology, v. 100, p. 207-219.

McSween, H.Y., Jr., and Harvey, R. P., 1997, Corcord plutonic suite: Pre-Acadian gabbro-syenite in the southern Appalachains, *in* Sinha, A. K., Whalen, J. B., and Hogan, J. P., eds., The nature of magmatism in the Appalachian orogen: Boulder, Colorado, Geological Society of America Memoir 191, p. 221-234.

McSween, H. Y., Jr., Sando, T. W., Clark, S. R., Harden, J. T., and Strange, E. A., 1984, The gabbro-metagabbro association of the southern Appalachian Piedmont: American Journal of Science, v. 284, p. 437-461.

Merschat, A. J., 2003, Inner Piedmont tectonics in the southwestern Brushy Mountains, North Carolina Inner Piedmont: field and laboratory data revealing 3-D crustal flow and sillimanite I and II metamorphism [M.S. thesis]: Knoxville, University of Tennessee, 198 p.

Merschat, A. J., 2009, Assembling the Blue Ridge and Inner Piedmont: Insights into the nature and timing of terrane accretion in the southern Appalachian orogen from geologic mapping, stratigraphy, kinematic analysis, petrology, geochemistry, and modern geochronology [Ph.D. dissertation]: Knoxville, University of Tennessee, 455 p.

Merschat, A. J., and Hatcher, R. D., Jr., 2007, The Cat Square terrane: Possible Siluro-Devonian remnant ocean basin in the Inner Piedmont, southern Appalachians, USA, *in* Hatcher, R. D., Jr., Carlson, M. P., McBride, J. H., and Martínez Catalán, J. R., eds., The 4D Framework of Continental Crust: Geological Society of America Memoir 200, p. 553-565.

Merschat, A. J., and Kalbas, J. L., 2002, Geology of the southwestern Brushy Mountains, *in* Hatcher, R. D., Jr., and Bream, B. R., eds., Inner Piedmont geology in the South Mountains-Blue Ridge Foothills and the southwestern Brushy Mountains, central-western North Carolina: Carolina Geological Society annual field trip guidebook, North Carolina Geological Survey, p. 101-126.

Merschat, A. J., Gatewood, M. P., Fisher, C. M., Miller, C. F., Hatcher, R. D., Jr., Wooden, J. L., and Stahr, D. W., III, 2005a, The Newton antiform, NC: A previously unrecognized window through the allochthonous Inner Piedmont thrust stack: Geological Society of America Abstracts with Programs, v. 37, no. 7, p. 20.

Merschat, A. J., Hatcher, R. D., Jr., and Davis, T. L., 2005b, The northern Inner Piedmont, southern Appalachians, USA: kinematics of transpression and SW-directed mid-crustal flow: Journal of Structural Geology, v.27, p.1252-1281.

Merschat, A. J., Hatcher, R. D., Jr., Byars, H. E., and Gilliam, W. G., 2008, Inner Piedmont geotraverse from the Brushy Mountains to Lincolnton, North Carolina: Architecture of the Cat Square and Tugaloo terranes: Geological Society of America Southeastern Section Meeting Field Trip Guidebook, 62 p.

Merschat, C. E., and Wiener, L. S., 1988, Geology of the Sandymush and Canton quadrangles, North Carolina: North Carolina Geological Survey Bulletin, v. 90, p. 66.

Meschede, M., 1986, A method of discriminating between different types of mid-ocean ridge basalts and continental tholeiites with the Nb–Zr–Y diagram: Chemical Geology, v. 56, p. 207-218.

Miller, B. V., Fetter, A. H., and Stewart, K. G., 2006, Plutonism in three orogenic pulses, Eastern Blue Ridge province, southern Appalachians: Geological Society of America Bulletin, v. 118, no. 1-2, p. 171-184.

Miller, C. F., and Meschter, S. M., 2001, Zircon saturation temperatures and preservation of inheritance: Implications for contrasting mechanisms of felsic magma generation: 11th Annual V.M. Goldschmidt Conference.

Miller, C. F., McDowell, S. M., and Mapes, R. W., 2003, Hot and cold granites? Implications of zircon saturation temperatures and preservation of inheritance: Geology, v. 31, no. 6, p. 529-532.

Miller, C. F., Hatcher, R. D., Jr., Ayers, J. C., Coath, C. D., and Harrison, T. M., 2000, Age and zircon inheritance of eastern Blue Ridge plutons, southwestern North Carolina and northeastern Georgia, with implications for magmatic history and evolution of the southern Appalachian orogen: American Journal of Science, v. 300, p. 142-172.

Miller, J. S., Santosh, M., Pressley, R. A., Clemens, A. S., Rogers, J. J. W., 1996, A Pan-African thermal event in southern India: Journal of Southeast Asian Earth Sciences, v. 14, p. 127–136.

Milton, D. J., and Michie, J., 1987, Muscovite two-plagioclase amphibolite in the Inner Piedmont, Catawba County, North Carolina: Geological Society of America Abstracts with Programs, v. 19, p. 118.

Mirante, D. C., and De La Rosa, J., 2001, Geochemistry of migmatites for NE Georgia—The Athens Gneiss (AG): Geological Society of America Abstracts with Programs, v. 33, no. 2, p. 50.

Mirante, D. C., and Patiño-Douce, A. E., 2000, Melting and migmatization in the southern Appalachian Inner Piedmont of northeast Georgia; the Athens gneiss: Geological Society of America Abstracts with Programs, v. 33, no. 7, p. 297.

Misra, K. C., and Keller, F. B., 1978, Ultramafic bodies in the Southern Appalachian; a review: American Journal of Science, v. 278, p. 389-418.

Misra, K. C., Mittwede, S. K., and Conte, J. A., 1990, Amphibolite geochemistry as evidence of a terrane suture in the central Piedmont of South Carolina: Geological Society of America Abstracts with Programs, v. 22, no. 4, p. 51.

Mittwede, S. K., 1986, The Hammet Grove complex: Oceanic crust in the Piedmont of northwestern South Carolina: Geological Society of America Abstracts with Programs, v. 18, p. 256.

Mittwede, S. K., 1989, The Hammet Grove meta-igneous suite; A possible ophiolite in the northwestern South Carolina Piedmont, *in* Mittwede, S. K., and Stoddard, E. F., eds., Ultramafic rocks of the Appalachian Piedmont: Geological Society of America Special Paper 231, p. 45-62.

Mittwede, S. K., Ødegård, M., and Sharp, W. E., 1987, Major chemical characteristics of the Hammett Grove meta-igneous suite, northwestern South Carolina: Southeastern Geology, v. 28, p. 49-63.

Miyashiro, A., 1978, Nature of alkalic volcanic rock series: Contributions to Mineralogy and Petrology, v. 66, p. 91-104.

Moecher, D. P., Massey, M. A., and Tracy, R. J., 2005, Timing and pattern of metamorphism in the western and central Blue Ridge, TN and NC: Status and outstanding problems, *in* Hatcher, R. D., Jr., and Merschat, A. J., eds., Blue Ridge Geology Geotraverse East of the Great Smoky

Mountains National Park, Western North Carolina: North Carolina Geological Survey, Carolina Geological Society Field Trip Guidebook, 2005 Annual Meeting, p. 57-66.
Moecher, D. P., Samson, S. D., and Miller, C. F., 2004, Precise time and conditions of peak Taconian granulite facies metamorphism in the southern Appalachian orogen, U.S.A., with implications for zircon behavior during crustal melting events: Journal of Geology, v. 112, p. 289-304.
Mora, C. I., and Valley, J. W., 1985, Ternary feldspar thermometry in granulites from the Oaxacan Complex, Mexico: Contributions to Mineralogy and Petrology, v. 89, p. 215-225.
Naeser, C. W., Naeser, N. D., Kunk, M. J., Morgan, B. A., III, Schultz, A. P., Southworth, C. S., and Weems, R. E., 2001, Paleozoic through Cenozoic uplift, erosion, stream capture, and deposition history in the Valley and Ridge, Blue Ridge, Piedmont, and Coastal Plain provinces of Tennessee, North Carolina, Virginia, Maryland, and District of Columbia: Geological Society of America Abstracts with Programs, v. 33, no. 6, p. A-312.
Neilson, M. J., 1988, The structure and stratigraphy of the Tallassee synform, Dadeville Belt, Alabama: Southeastern Geology, v. 29, p. 41-50.
Nelson, A. E., Horton, J. W., and Clarke, J. W., 1988, Geologic map of the Greenville 1° x 2° quadrangle, Georgia, South Carolina, and North Carolina: U.S. Geological Survey Map I-2175, scale 1:250,000.
Nesse, W. D., 2004, Introduction to optical mineralogy: New York, New York, Oxford University Press, 348 p.
Newton, R. C., 1992, Charnockitic alteration: evidence for CO_2 infiltration in granulite facies metamorphism: Journal of Metamorphic Geology, v. 10, p. 383-400.
Nijland, T. G., and Senior, A., 1991, Granulite facies metamorphism of polyphase migmatites and basic dikes, South Norway: Journal of Geology, v. 99, p. 515-526.
Ormaasen, D. E., 1977, Petrology of the Hopen mangerite–charnockite intrusion, Lofoten, north Norway: Lithos, v. 10, p. 291–310.
Ownby, S. E., Miller, C. F., Berquist, P. J., Carrigan, C. W., Wooden, J. L., and Fullagar, P. D., 2004, U-Pb geochronology and geochemistry of a portion of the Mars Hill terrane, North Carolina-Tennessee: Constraints on origin, history, and tectonic assembly: Geological Society of America Memoir 197, p. 609-632.
Overstreet, W. C., Yates, R. G., and Griffits, W. R., 1951, Geologic map of the Shelby 15-minute quadrangle: U.S. Geological Survey 1:62,500.
Overstreet, W. C., Whitlow, J. W., White, A. W., and Griffits, W. R., 1963, Geologic map of the southern part of the Caesar quadrangle, Cleveland, Lincoln, and Burke counties, North Carolina showing areas mined for monazite and mica: U.S. Geological Survey, scale 1:24,000.
Patiño-Douce, A. E., 1997, Generation of metaluminous A-type granites by low-pressure melting of calc-alkaline granitoids: Geology, v. 25, n. 8, p. 743-746.
Patiño-Douce, A. E., 1996, Effects of pressure and H_20 content on the compositions of primary crustal melts: Transactions of the Royal Society of Edinburgh, v. 87, no. 1/2, p. 11-22.
Patiño-Douce, A. E., and Beard, J. S., 1995, Dehydration-melting of biotite gneiss and quartz amphibolite from 3 to 15 kbar: Journal of Petrology, v. 36, no. 3, p. 707-738.
Pattison, D. R. M., 1991, Infiltration-driven dehydration and anatexis in granulite facies metagabbro, Grenville Province, Ontario, Canada: Journal of Metamorphic Geology, v. 9, p. 315-332.
Paul, D. K., Barman, T. R., McNaughton, N. J., Fletcher, R., Potts, P. J., Ramakrishnan, M., and Augustine, P. F., 1990, Archean-Proterozoic evolution of Indian charnockites: isotopic and geochemical evidence from granulites of the Eastern Ghats Belt: Journal of Geology, v. 98, p. 253-263.

Pearce, J. A., 1982, Trace element characteristics of lavas from destructive plate boundaries, *in* Thorpe, R. S., ed., Andesites: orogenic andesites and related rocks: Chichester, Wiley, p. 525-548.
Pearce, J. A., 1983, Role of the sub-continental lithosphere in magma genesis at active continental margins, *in* Hawkesworth, C. J., and Norry, M. J., eds., Continental basalts and mantle xenoliths: Nantwich, Shiva, p. 230-249.
Pearce, J. A., and Cann, J. R., 1973, Tectonic setting of basic volcanic rocks determined using trace element analysis: Earth and Planetary Science Letters, v. 19, p. 290-300.
Pearce, J. A., and Norry, M. J., 1979, Petrogenetic implications of Ti, Zr, Y and Nb variations in volcanic rocks: Contributions to Mineralogy and Petrology, v. 69, p. 33-37.
Pearce, J. A., Harris, N. B. W., and Tindle, A. G., 1984, Trace element discrimination diagrams for the tectonic interpretation of granitic rocks: Journal of Petrology, v. 25, p. 956-983.
Percival, J. A., Stern, R. A, Rayner, N., 2003, Archean adakites from the Ashuanipi complex, eastern Superior province, Canada: geochemistry, geochronology and tectonic significance: Contributions to Mineralogy and Petrology, v. 145, p. 265–280.
Pettinghill, H. S., Sinha, A. K., and Tatsumoto, M., 1984, Age and origin of anorthosites, charnockites, and granulites in the central Virginia Blue Ridge: Nd and Sr isotopic evidence: Contributions to Mineralogy and Petrology, v. 85, p. 279-291.
Peucat, J. J., Vidal, P., Bernard-Griffiths, J., and Condie, K. C., 1989, Sr, Nd, and Pb isotopic systematic in the Archean low- to high-grade transition zone of southern India: Journal of Geology, v. 97, p. 537-550.
Pigage, L. C., and Greenwood, H. J., 1982, Internally consistent estimates of pressure and temperature: The staurolite problem: American Journal of Science, v. 282, p. 943-969.
Post, N. J., 2000, Unravelling Gondwana fragments: An integrated structural, isotopic and petrographic investigation of the Windmill Islands, East Antarctica [Ph.D. dissertation]: Sydney, University of New South Wales.
Presnell, L., 1999, Mines, miners, and minerals of western North Carolina's mountain empire: Alexander, North Carolina, Worldcomm, 256 p.
Privett, D. R., 1984, The Turnersburg intrusive: Petrogenesis of a metamorphosed Alpine ultramafite in the eastern Inner Piedmont, Iredell County, North Carolina: Southeastern Geology, v. 25, no. 1, p. 55-60.
Quinn, M. J., 1991, Two lithotectonic boundaries in western North Carolina: Geologic interpretation of a region surrounding Sylva, Jackson County [M.S. thesis]: Knoxville, University of Tennessee, 223 p.
Ragland, P. C., Hatcher, R. D., Jr., and Whittington, D., 1983, Juxtaposed Mesozoic diabase dike sets from the Carolinas: A preliminary assessment: Geology, v. 11, p. 394-399.
Raith, M., Klatt, E., Spiering, B., Srikantappa, C., and Stähle, H. J., 1988, Gneiss-charnockite transformation at Kottavattam, southern Kerala (India): Journal of the Geological Society of India, v. 31, p. 114-115.
Rankin, D. W., Espenshade, G. J., and Neuman, R. B., 1972, Geologic map of the west half of the Winston-Salem quadrangle, North Carolina, Virginia, and Tennessee: U.S. Geological Survey Map I-709-A, scale 1:250,000.
Ranson, W. A., Williams, I. S., and Garihan, J. M., 1999, SHRIMP zircon U-Pb ages of granitoids from the Inner Piedmont of South Carolina; evidence for Ordovician magmatism involving Mid- to Late Proterozoic crust: Geological Society of America Abstracts with Programs, v. 31, no. 7, p. 167.
Rickwood, P. C., 1989, Boundary lines within petrologic diagrams which use oxides of major and minor elements: Lithos, v. 22, p. 247-263.

Rollinson, H., 1993, Using geochemical data: evaluation, presentation, interpretation: Essex, England, Longman Group UK Limited, 352 p.
Saunders, A. D., and Tarney, J., 1984, Geochemical characteristics of basalt volcanism within back-arc basins, *in* Kokelaar, B. P., and Howell, M. F., eds., Marginal basin geology: Volcanic and associated sedimentary and tectonic processes in modern and ancient marginal basin: London, Backwell, p. 57-76.
Settles, D. J., 2002, Defining the Hayesville-Soque River and Allatoona faults and an Ordovician arc assemblage within the central Blue Ridge northwest of Dahlonega, Georgia [M.S. thesis]: Knoxville, University of Tennessee, 148 p.
Sheraton, J. W., Black, L. P., and Tindle, A. G., 1992, Petrogenesis of plutonic rocks in a Proterozoic granulite-facies terrane–the Bunger Hills, East Antarctica: Chemical Geology, v. 97, p. 163-198.
Shervais, J. W., 1982, Ti–V plots and the petrogenesis of modern and ophiolitic lavas: Earth and Planetary Science Letters, v. 59, p. 101-118.
Spear, F. S., 1993, Metamorphic phase equilibria and pressure-temperature-time paths: Chelsea, Michigan, Book Crafters, Inc., 799 p.
Stahr, D. W., Miller, C. F., Hatcher, R. D., Jr., Wooden, J., and Fisher, C. M., 2005, Evidence for high-temperature ductile Alleghanian deformation in the eastern Blue Ridge: Implications of new structural, petrologic, and geochronologic data from southwestern North Carolina: Geological Society of America Abstracts with Programs, v. 37, no. 7, p. 72.
Steltenpohl, M. G., Hatcher, R. D., Jr., Mueller, P. A., Heatherington, A. H., in press, Tectonic history of the Pine Mountain window, *in* Tollo, R. P., Bartholomew, M. J., and Hibbard, J. P., Geological Society of America Memoir.
Stern, R. A., Percival, J. A., and Mortensen, J. K., 1994, Geochemical evolution of the Minto block: a 2.7 Ga continental magmatic arc built on the Superior protocraton: Precambrian Geology, v. 65, p. 115–153.
Stormer, J. C., 1975, A practical two feldspar geothermometer: American Mineralogist, v. 670, p. 667-674.
Streckeisen, A., 1976, To each plutonic rock its proper name: Earth Science Reviews, v. 12, p. 1-33.
Stuckey, J. L., 1965, North Carolina: Its geology and mineral resources: Raleigh North Carolina, North Carolina State University Print Shop, 550 p.
Sun, S. S., and McDonough, W. F., 1989, Chemical and isotopic systematic of oceanic basalts: implications for mantle composition and processes, *in* Saunders, A. D., and Norry, M. J., eds., Magmatism in ocean basins: Geological Society of London Special Publication 42, p. 313-345.
Taylor, B., and Martinez, F., 2003, Back-arc basin basalt systematic: Earth and Planetary Sciences Letters, v. 210, p. 481-497.
Taylor, P. N., Chadwick, B., Friend, C. R. L., Ramakrishnan, M., and Viswanatha, M. N., 1988, New age data on the geological evolution of southern India: Journal of the Geological Society of India, v. 31, p. 155-157.
Taylor, S. R., and McLennan, S., M., 1985, The continental crust: its composition and evolution: Blackwell Scientific Publications, Oxford, 312 p.
Thomas, C. W., 2001, Origins of mafic-ultramafic complexes of the eastern Blue Ridge province, southern Appalachians: Geochronological and geochemical constraints [M.S. thesis]: Nashville, Vanderbilt University, 154 p.
Thompson, R. N., 1982, British Tertiary volcanic province: Scottland Journal of Geology, v. 18, p. 49-107.
Thompson, R. N., 1984, Dispatches from the basalt front. I: Experiments: Proceedings of the Geologists' Association, v. 95, p. 249-262.

Tollo, R. P., 2001, Timing of Grenville-age magmatism and deformation, Blue Ridge Province, central Virginia: Geological Society of America Abstracts with Programs, v. 33, no. 2, p. 7.
Tull, J. F., 2007, Tectonics of the Georgia Blue Ridge: Basement/cover rift architecture, important aspects of overlying drift and clastic wedge facies, and the westernmost accretionary terrane: Georgia Geological Society Guidebook, v. 27, no. 1, 203 p.
Tull, J. F., and Holm, C. S., 2005, Structural evolution of a major Appalachian salient-recess junction: consequences of oblique collisional convergence across a continental margin transform fault: Geological Society of America Bulletin, v. 117, no. 3/4, p. 482-499.
van Breemen, O., and Dallmeyer, R. D., 1984, The scale of Sr isotopic diffusion during post-metamorphic cooling of gneisses in the Inner Piedmont of Georgia, southern Appalachians: Earth and Planetary Science Letters, v. 68, p. 141-150.
van den Kerkhof, A. M., and Grantham, G. H., 1999, Metamorphic charnockite in contact aureoles around intrusive enderbite from Natal, South Africa: Contributions to Mineralogy and Petrology, v. 137, p. 11-132.
Van Reenen, D. D., Roering, C., Smit, C. A., Barton, J. M., and Van Schalkwyk, J. F., 1988, The high-grade margin of the northern Kaapvaal Craton, South Africa: Journal of Geology, v. 96, p. 549-560.
Varnell, M. G., Hatcher, R. D., Jr., Merschat, A. J., and Wooden, J., 2008, Limits on timing of deformation and plutonism in the eastern Blue Ridge, southwestern North Carolina, from geologic mapping and U-Pb zircon geochronology: Geological Society of America Abstracts with Programs, v. 40, no. 4, p. 28.
Vinson, S., 1999, Ion probe geochronology of granitoid gneisses of the Inner Piedmont, North Carolina and South Carolina [M.S. thesis]: Nashville, Tennessee, Vanderbilt University, 84 p.
Weiss, S., and Troll, G., 1989, The Ballachulish Igneous Complex, Scotland: petrography, mineral chemistry and order of crystallization in the monzodiorite–quartz diorite suite and in the granite: Journal of Petrology, v. 30, p. 1069–1115.
Welin, E., and Gorbatschev, R., 1978, The Rb-Sr age of the Varberg charnockite, Sweden: Geological Society of Stockholm Bulletin, v. 100, p. 225-227.
Wells, R. R. A., 1977, Pyroxene thermometry in simple and complex systems: Contributions to Mineralogy and Petrology, v. 62, p. 129-139.
Wendlandt, R. F., 1981, Influence of CO_2 on melting of model granulite facies assemblages: a model for the genesis of charnockites: American Mineralogist, v. 66, p. 1164-1174.
Whalen, J. B., Currie, K. L., and Chappell, B. W., 1987, A-type granites; Geochemical characteristics, discrimination and petrogenesis: Contributions to Mineralogy and Petrology, v. 95, p. 407-419.
Whitehouse, M. J., and Platt, J. P., 2003, Dating high-grade metamorphism–constraints from rare-earth elements in zircon and garnet: Contributions to Mineralogy and Petrology, v. 145, p. 61-74.
Whitney, J. A., Herz, N., and Legato, J. M., 1987, Allochthonous mafic and ultramafic lithologies from near the Russell Reservoir, eastern Georgia: evidence for late Paleozoic thrust emplacement of a dismembered ophiolite: Geological Society of America Abstracts with Programs, v. 19, p. 137.
Williams, S. T., 2000, Structure, stratigraphy, and migmatization in the southwestern South Mountains, North Carolina [M.S. thesis]: Knoxville, University of Tennessee, 111 p.
Wilson, C. G., 2006, Origin and tectonic evolution of the southern Appalachian Neoacadian crystalline core: Evidence from the geology of the Gilreath 7.5-minute quadrangle, North Carolina [M.S. thesis]: Knoxville, University of Tennessee, 200 p.
Wilson, M., 1989, Igneous petrogenesis: London, Unwin Hyman, 466 p.
Wood, B., and Banno, S., 1977, Pyroxene thermometry in simple and complex system: Contributions to Mineralogy and Petrology, v. 62, p. 129-139.

Wood, D. A., Joron, J. L., Treuil, M., Norry, M., and Tarney, J., 1979, Elemental and Sr isotope variations in basic lavas from Iceland and the surrounding ocean floor: Contributions to Mineralogy and Petrology, v. 70, p. 319-339.

Wood, D. A., 1980, The application of a Th-Hf-Ta diagram to problems of tectonomagmatic classification and to establishing the nature of crustal contamination of basaltic lavas of the British Tertiary volcanic province: Earth and Planetary Science Letters, v. 50, p. 11-30.

Yanagihara, G. M., 1994, Structure, stratigraphy, and metamorphism of a part of the Columbus Promontory, North Carolina [M.S. thesis]: Knoxville, University of Tennessee, 214 p.

Young, D. N., and Black, L. P., 1991, U-Pb zircon dating of Proterozoic igneous charnockites from the Mawson Coast, east Antarctica: Antarctic Science, v. 3, no. 2, p. 205-216.

Zhao, J., Ellis, D. J., Kilpatrick, J. A., and McCulloch, M. T., 1997, Geochemical and Sr-Nd isotopic study of charnockites and related rocks in the northern Prince Charles Mountains, East Antarctica: implications for charnockite petrogenesis and Proterozoic crustal evolution: Precambrian Research, v. 81, p. 37-66.

Zhou, X. Q., Bingen, B., Demaiffe, D., Liegois, J. P., Hertogen, J., Weis, D., and Michot, J., 1995, The 1160 Ma Hidderskog meta-charnockite: implications of this A-type pluton for the Sveconowegian belts in Vest Agder (SW Norway): Lithos, v. 36, p. 51–66.

APPENDICES

APPENDIX A

							Foliation		Lineation		Fold Axis		Joint	
Quad	Station	Rock Type 1(RT2)	RT 1 Minerals	Rock Type 2 (RT2)	RT2 Minerals	Modifier	Strike	Dip	Trend	Plunge	Trend	Plunge	Strike	Dip
Bk	1	Biotite Gneiss	bt,grt				155	44						
Bk	2	Biotite Gneiss	bt,grt				150	21						
Bk	3	Biotite Gneiss					172	22						
Bk	4	Biotite Gneiss	bt,grt				138	35						
Bk	5	Biotite Gneiss	bt,grt				145	49						
Bk	6	Migmatitie												
Bk	7	Metagraywacke	grt				207	15						
Bk	8	Schist	sll, gt, bt				175	42						
Bk	9	Granitic Orthogneiss	bt,kspr				348	18						
Bk	10	Schist	sil,grt			Migmatitic	180	52						
Bk	11	Schist	gt, ms			Migmatitic	170	27						
Bk	12	Hornblende Gneiss					90	42						
Bk	13	Amphibolite	amp				10	75						
Bk	14	Biotite Gneiss				Migmatitic	190	59						
Bk	15	Metagraywacke	grt				205	20						
Bk	16	Metagraywacke	grt	Amphibolite			167	50						
Bk	17	Metagraywacke		Schist	sil, gt		178	48						
Bk	18	Schist	sil,grt				156	18						
Bk	19	Amphibolite		Schist	sil		145	12						
Bk	20	Biotite Gneiss		Schist	sil,gt	Migmatitic	174	61						
Bk	21	Schist	grt,sil				192	40						
Bk	22	Schist	sil,grt				183	21						
Bk	23	Biotite Gneiss					175	33						
Bk	24	Biotite Gneiss					160	44						
Bk	25	Biotite Gneiss					185	28						
Bk	26	Amphibolite	amp, grt				190	69						
Bk	27	Amphibolite	amp, grt				25	61						
Bk	28	Amphibolite	amp, grt				165	35						
Bk	29	Amphibolite	amp, grt				165	31						
Bk	30	Amphibolite	amp, grt				165	35						
Bk	31	Amphibolite	amp, grt				165	55						
Bk	32	Biotite Gneiss				Migmatitic	180	28						
Bk	33	Biotite Gneiss				Migmatitic					171	43		
Bk	34	Biotite Gneiss				Migmatitic	165	35						
Bk	35	Biotite Gneiss	bt,grt				160	47						
Bk	36	Biotite Gneiss				Migmatitic	149	30						
Bk	37	Biotite Gneiss					150	40						
Bk	40	Biotite Gneiss				Migmatitic	254	20						
Bk	41	Biotite Gneiss				Migmatitic	172	12						
Bk	42	Biotite Gneiss				Migmatitic	178	27						
Bk	43	Biotite Gneiss				Migmatitic	180	40						
Bk	44	Biotite Gneiss				Migmatitic	200	39						
Bk	45	Biotite Gneiss					15	31						
Bk	46	Amphibolite	amp, grt				216	68						
Bk	47	Amphibolite	amp, grt				180	18						
Bk	48	Amphibolite	amp				351	71						
Bk	49	Amphibolite	amp, grt				194	16						
Bk	50	Amphibolite	amp, grt				198	38						
Bk	51	Amphibolite	amp, grt				169	65						
Bk	52	Amphibolite	amp, grt				202	40						
Bk	53	Schist	sil,grt				160	19						
Bk	54	MICA MINE												
Bk	55	Pegmatite					185	12						
Bk	56	Amphibolite	amp				223	74						
Bk	57	Amphibolite	amp				235	46						
Bk	58	Amphibolite	amp				185	60						
Bk	59	Schist	sil,grt				248	39						
Bk	60	Granitic Orthogneiss	bt,kspr				148	44						
Bk	61	Granitic Orthogneiss	bt,kspr				346	20						
Bk	62	Granitic Orthogneiss	bt,kspr				154	85						
Bk	63	Metasandstone					165	34						
Bk	64	Metasandstone					345	22						
Bk	65	Metasandstone					120	45						
Bk	66	Granitic Orthogneiss	bt,kspr				329	25						
Bk	67	Granitic Orthogneiss	bt,kspr				173	54						
Bk	68	Metadiorite					45	28						

							Foliation		Lineation		Fold Axis		Joint	
Quad	Station	Rock Type 1(RT2)	RT 1 Minerals	Rock Type 2 (RT2)	RT2 Minerals	Modifier	Strike	Dip	Trend	Plunge	Trend	Plunge	Strike	Dip
Bk	69	Metadiorite					54	40						
Bk	70	Metadiorite	amp,bt				348	30						
Bk	71	Metadiorite	amp,bt				170	20						
Bk	72	Amphibolite	amp				135	30						
Bk	73	Metadiorite	amp,bt				198	40						
Bk	74	Hornblende Gneiss					198	40						
Bk	75	Schist	sil,grt				170	45						
Bk	76	Schist	sil,grt				110	15						
Bk	77	Schist	sil,grt				7	33						
Bk	78	Schist	sil,grt				12	15						
Bk	79	Schist	sil,grt				115	32						
Bk	80	Metagraywacke				Migmatitic	170	12						
Bk	81	Hornblende Gneiss	amp,bt				145	89						
Bk	82	Schist	sil,grt				155	47						
Bk	83	Schist	sil,grt				120	35						
Bk	84	Schist	sil,grt				313	47						
Bk	85	Layered Metagraywacke	grt	Schist	sil		170	12						
Bk	86	Layered Metagraywacke		Schist	sil		140	15						
Bk	87	Layered Metagraywacke		Schist	sil		166	9						
Bk	88	Layered Metagraywacke		Schist	sil		166	20						
Bk	89	Layered Metagraywacke		Schist	sil		195	41						
Bk	90	Layered Metagraywacke	grt	Schist	sil		178	22						
Bk	91	Layered Metagraywacke		Schist	sil		200	40						
Bk	92	Metagraywacke				Migmatitic	157	60						
Bk	93	Metagraywacke					170	16						
Bk	94	Metagraywacke					164	24						
Bk	95	Metagraywacke					160	22						
Bk	96	Metagraywacke					170	5						
Bk	97	Granitic Orthogneiss	bt,kspr				177	46						
Bk	98	Granitic Orthogneiss	bt,kspr				150	15						
Bk	99	Biotite Gneiss					210	18						
Bk	100	Biotite Gneiss					135	30						
Bk	101	Biotite Gneiss				Migmatitic	137	53						
Bk	102	Biotite Gneiss				Migmatitic	38	35						
Bk	103	Biotite Gneiss				Migmatitic	190	30						
Bk	104	Biotite Gneiss				Migmatitic	5	11						
Bk	105	Biotite Gneiss									343	15		
Bk	105	Biotite Gneiss				Migmatitic	180	12						
Bk	106	Biotite Gneiss				Migmatitic	177	20						
Bk	107	Biotite Gneiss				Migmatitic	190	27						
Bk	108	Biotite Gneiss				Migmatitic	210	20						
Bk	109	Biotite Gneiss					234	23						
Bk	110	Biotite Gneiss				Migmatitic	164	23						
Bk	111	Biotite Gneiss				Migmatitic	115	15						
Bk	112	Biotite Gneiss					136	40						
Bk	113	Biotite Gneiss				Migmatitic	120	17						
Bk	113	Biotite Gneiss				Migmatitic							270	77
Bk	113	Biotite Gneiss				Migmatitic							351	89
Bk	114	Metagraywacke				Migmatitic	38	33						
Bk	115	Biotite Gneiss				Migmatitic	355	45						
Bk	116	Biotite Gneiss					185	22						
Bk	117	Biotite Gneiss				Migmatitic	345	11						
Bk	118	Amphibolite					19	19						
Bk	119	Biotite Gneiss	grt,bt			Migmatitic	10	34						
Bk	120	Layered Metagraywacke		Calc-silicate		Migmatitic	150	36						
Bk	121	Layered Metagraywacke		Calc-silicate		X-Bedded	175	25						
Bk	122	Layered Metagraywacke		Calc-silicate		Weathered	150	30						
Bk	123	Pegmatite	grt,ms				25	62						
Bk	124	Layered Metagraywacke	grt			Migmatitic	185	45						
Bk	125	Metagraywacke				Migmatitic	345	85						
Bk	126	Metagraywacke				Migmatitic	105	25						
Bk	127	Metagraywacke				Migmatitic	95	35						
Bk	128	Metagraywacke				Migmatitic	196	34						
Bk	129	Calc-silicate					185	15						
Bk	130	Calc-silicate				Migmatitic	336	20						
Bk	131	Calc-silicate		Metagraywacke		Migmatitic	238	13						
Bk	132	Calc-silicate		Metagraywacke		Migmatitic	345	17						
Bk	133	Metagraywacke		Calc-silicate		Migmatitic	120	18						
Bk	134	Metagraywacke		Calc-silicate		Migmatitic	345	24						

							Foliation		Lineation		Fold Axis		Joint	
Quad	Station	Rock Type 1(RT2)	RT 1 Minerals	Rock Type 2 (RT2)	RT2 Minerals	Modifier	Strike	Dip	Trend	Plunge	Trend	Plunge	Strike	Dip
Bk	135	Metagraywacke		Calc-silicate		Migmatitic	214	19						
Bk	136	Metagraywacke		Calc-silicate		Migmatitic	200	24						
Bk	137	Calc-silicate				Migmatitic	225	20						
Bk	138	Metagraywacke		Calc-silicate			170	20						
Bk	139	Calc-silicate				Migmatitic	176	14						
Bk	140	Calc-silicate				Migmatitic	175	22						
Bk	141	Calc-silicate					187	66						
Bk	142	Calc-silicate					166	29						
Bk	143	Calc-silicate					174	18						
Bk	144	Calc-silicate					185	25						
Bk	145	Calc-silicate				Migmatitic	198	22						
Bk	146	Layered Metagraywacke		Calc-silicate		Migmatitic	160	20						
Bk	147	Metagraywacke					93	37						
Bk	148	Metagraywacke				Migmatitic	170	40						
Bk	149	Layered Metagraywacke				Migmatitic	195	45						
Bk	150	Layered Metagraywacke		Calc-silicate		Migmatitic	135	23						
Bk	151	Layered Metagraywacke				Migmatitic	155	23						
Bk	152	Layered Metagraywacke				Migmatitic					165	15		
Bk	153	Layered Metagraywacke				Migmatitic	340	8						
Bk	154	Layered Metagraywacke				Migmatitic	155	23			194	14		
Bk	155	Layered Metagraywacke				Migmatitic								
Bk	156	Layered Metagraywacke				Migmatitic	25	13						
Bk	157	Layered Metagraywacke				Migmatitic	143	64						
Bk	158	Layered Metagraywacke				Migmatitic	70	2						
Bk	159	Layered Metagraywacke				Migmatitic	15	7						
Bk	160	Layered Metagraywacke				Migmatitic	171	12						
Bk	161	Layered Metagraywacke				Migmatitic	178	46						
Bk	162	Layered Metagraywacke				Migmatitic	68	5						
Bk	163	Hornblende Gneiss	amp,bt,gt				140	53						
Bk	164	Hornblende Gneiss	amp,bt				345	20						
Bk	165	Hornblende Gneiss	amp,bt			Migmatitic	315	44						
Bk	166	Hornblende Gneiss	amp,bt			Migmatitic	330	25						
Bk	167	Hornblende Gneiss	amp,bt			Migmatitic	325	23						
Bk	168	Hornblende Gneiss	amp,bt,gt				198	52						
Bk	169	Metagraywacke				Migmatitic	142	31						
Bk	170	Metagraywacke				Migmatitic	138	48						
Bk	171	Metagraywacke				Migmatitic					183	42		
Bk	172	Metagraywacke				Migmatitic	25	25						
Bk	173	Metagraywacke				Migmatitic	180	44						
Bk	174	Metagraywacke				Migmatitic	189	33						
Bk	175	Metagraywacke				Migmatitic	10	32						
Bk	176	Metagraywacke				Migmatitic	195	20						
Bk	177	Metagraywacke				Migmatitic	195	45						
Bk	178	Metagraywacke				Migmatitic	195	40						
Bk	179	Metagraywacke				Migmatitic	175	25						
Bk	180	Metagraywacke				Migmatitic	31	20						
Bk	181	Metagraywacke				Migmatitic	172	30						
Bk	182	Metagraywacke	grt			Migmatitic	156	22						
Bk	183	Metagraywacke									20	42		
Bk	183	Metagraywacke				Migmatitic	195	55						
Bk	184	Metagraywacke				Migmatitic	160	25						
Bk	185	Metagraywacke				Migmatitic	195	16						
Bk	186	Metagraywacke				Migmatitic	184	40						
Bk	187	Metagraywacke	grt			Migmatitic	155	32						
Bk	188	Metagraywacke				Migmatitic	130	16						
Bk	189	Metagraywacke				Migmatitic	174	26						
Bk	190	Granitic Orthogneiss	grt			Mylonitic	325	34						
Bk	191	Schist	sil,grt	Grt-Mica Schist		Migmatitic	161	29						
Bk	192	Schist	sil,grt	Calc-silicate			167	30						
Bk	193	Schist	sil,grt	Calc-silicate			167	20						
Bk	194	Schist	sil,grt				150	26						
Bk	195	Amphibolite		Calc Silicate			150	30						
Bk	196	Calc-silicate		Schist	sil,grt		175	25						
Bk	197	Layered Metagraywacke	kspr			Migmatitic	165	34						
Bk	198	Schist	sil,grt	Calc-silicate		Migmatitic	130	14						
Bk	199	Migmatite	qtz,kspr	Schist		Migmatitic	125	25						
Bk	200	Schist		Calc-silicate		Migmatitic	65	25						
Bk	201	Migmatite		Schist		Migmatitic	15	15						

							Foliation		Lineation		Fold Axis		Joint	
Quad	Station	Rock Type 1(RT2)	RT 1 Minerals	Rock Type 2 (RT2)	RT2 Minerals	Modifier	Strike	Dip	Trend	Plunge	Trend	Plunge	Strike	Dip
Bk	202	Migmatite		Schist		Migmatitic	10	15						
Bk	203	Migmatite		Schist		Migmatitic	105	13						
Bk	204	Calc-silicate		Amphibolite		Migmatitic	307	27						
Bk	205	Migmatite		Metasandstone		Migmatitic	45	20						
Bk	206	Calc-silicate		Migmatite		Migmatitic	140	19						
Bk	207	Migmatite				Migmatitic	105	13						
Bk	208	Migmatite				Migmatitic	213	25						
Bk	209	Calc-silicate		Migmatite		Migmatitic	75	22						
Bk	210	Calc-silicate				Migmatitic	15	30						
Bk	211	Migmatite		Schist	sil,grt	Migmatitic	52	44						
Bk	212	Migmatite	kspr,qtz	Schist	sil,grt	Migmatitic	346	32						
Bk	213	Calc-silicate					346	36						
Bk	214	Metagraywacke	bt,grt	Migmatite		Migmatitic	330	21						
Bk	215	Migmatite					0	30						
Bk	216	Schist	sil,grt			Migmatitic	150	20						
Bk	217	Schist	sil,grt			Migmatitic	113	47						
Bk	218	Amphibolite		Layered Metagraywacke			150	57						
Bk	219	Layered Metagraywacke		Migmatite		Migmatitic	173	19						
Bk	220	Amphibolite		Layered Metagraywacke			172	61						
Bk	221	Hornblende Gneiss	amp,grt			Migmatitic	166	29						
Bk	221	Hornblende Gneiss	amp,grt			Migmatitic			177	14				
Bk	222	Hornblende Gneiss	amp,grt			Migmatitic	150	5						
Bk	223	Hornblende Gneiss	amp,grt			Migmatitic	325	37						
Bk	223	Hornblende Gneiss	amp,grt			Migmatitic			340	14				
Bk	224	Biotite Gneiss		Hornblende Gneiss		Migmatitic	143	43						
Bk	225	Calc-silicate		Schist	sil,grt	Migmatitic	172	37						
Bk	226	Hornblende Gneiss	amp,grt			Migmatitic	237	34						
Bk	227	Hornblende Gneiss	amp,grt				195	70						
Bk	228	Metagraywacke		Calc-silicate		Migmatitic	120	20						
Bk	229	Schist	sil,grt				135	32						
Bk	230	Granitic Orthogneiss	plg,grt				145	42						
Bk	230	Granitic Orthogneiss	plg,grt						320	17				
Bk	231	Granitic Orthogneiss	kspr,grt				150	26						
Bk	232	Granitic Orthogneiss	kspr,grt				160	40						
Bk	233	Schist		Calc-silicate		Migmatitic	147	43						
Bk	234	Schist					170	50						
Bk	235	Migmatite		Schist		Migmatitic	185	24						
Bk	236	Biotite Gneiss		Calc-silicate		Migmatitic	198	25						
Bk	237	Hornblende Gneiss	amp,qtz	Amphibolite			145	21						
Bk	238	Hornblende Gneiss		Layered Metagraywacke		Migmatitic	150	30						
Bk	239	Hornblende Gneiss		Layered Metagraywacke			164	40						
Bk	240	Granitic Orthogneiss					335	27						
Bk	241	Granitic Orthogneiss	kspr			Mylonitic	165	55						
Bk	242	Metagraywacke		Hornblende Gneiss			325	50						
Bk	243	Calc-silicate				Migmatitic	165	40						
Bk	244	Metagraywacke	grt,bt			Migmatitic	156	29						
Bk	245	Schist	sil,grt			Migmatitic	145	25						
Bk	246	Biotite Gneiss	grt,bt				152	46						
Bk	247	Metagraywacke	grt,bt			Mylonitic	130	61						
Bk	248	Metagraywacke	grt,bt			Migmatitic	156	45						
Bk	249	Hornblende Gneiss	amp,bt	Layered Metagraywacke			200	28						
Bk	250	Metagraywacke					150	35						
Bk	251	Metagraywacke	bt,grt				155	77						
Bk	252	Calc-silicate		Schist		Migmatitic	160	40						
Bk	253	Schist	sil,grt	Migmatite		Migmatitic	144	40						
Bk	254	Calc-silicate		Schist		Migmatitic	155	30						
Bk	255	Metagraywacke	bt,grt				180	76						
Bk	256	Metagraywacke	bt,grt	Migmatite		Migmatitic	145	84						
Bk	257	Metasandstone		Calc-silicate			150	34						
Bk	258	Biotite Gneiss				Migmatitic	127	29						
Bk	259	Metasandstone		Metagraywacke		Migmatitic	144	24						
Bk	260	Migmatite				Migmatitic	328	19						
Bk	261	Pegmatite	kspr,qtz				80	28						
Bk	262	Granitic Orthogneiss	kspr				20	32						
Bk	263	Granitic Orthogneiss	grt,kspr			Mylonitic	335	37						
Bk	264	Granitic Orthogneiss	grt,kspr			Mylonitic	220	50						
Bk	265	Granitic Orthogneiss	grt,kspr			Mylonitic			315	30				
Bk	266	Biotite Gneiss				Migmatitic	185	35						

							Foliation		Lineation		Fold Axis		Joint	
Quad	Station	Rock Type 1 (RT2)	RT 1 Minerals	Rock Type 2 (RT2)	RT2 Minerals	Modifier	Strike	Dip	Trend	Plunge	Trend	Plunge	Strike	Dip
Bk	267	Granitic Orthogneiss	kspr				195	34						
Bk	268	Granitic Orthogneiss				Mylonitic	313	47						
Bk	269	Granitic Orthogneiss	kspr,grt			Mylonitic	150	30						
Bk	270	Granitic Orthogneiss	kspr,grt			Mylonitic	165	30						
Bk	270	Granitic Orthogneiss	kspr,grt			Mylonitic			260	42				
Bk	271	Granitic Orthogneiss	grt,kspr			Mylonitic	145	52						
Bk	272	Metagraywacke				Migmatitic	143	21						
Bk	273	Granitic Orthogneiss	kspr,grt				35	39						
Bk	274	Granitic Orthogneiss	kspr,bt				154	32						
Bk	274	Granitic Orthogneiss	kspr,bt						165	15				
Bk	275	Metagraywacke					165	45						
Bk	276	Granitic Orthogneiss	kspr,bt			Mylonitic	145	32						
Bk	277	Metagraywacke		Biotite Gneiss		Migmatitic	102	36						
Bk	278	Biotite Gneiss	bt,qtz				178	19						
Bk	279	Granitic Orthogneiss	kspr	Metagraywacke	bt,qtz	Mylonitic	140	30						
Bk	280	Granitic Orthogneiss				Mylonitic	192	24						
Bk	281	Granitic Orthogneiss	kspr,bt	Metagraywacke		Mylonitic	110	40						
Bk	282	Granitic Orthogneiss	kspr,bt			Mylonitic	198	21						
Bk	283	Granitic Orthogneiss	kspr,bt			Mylonitic	190	42						
Bk	284	Granitic Orthogneiss					192	35						
Bk	285	Metagraywacke					205	45						
Bk	286	Granitic Orthogneiss		Metagraywacke			150	24						
Bk	287	Granitic Orthogneiss				Mylonitic	220	47						
Bk	288	Granitic Orthogneiss		Metagraywacke			217	41						
Bk	289	Schist	grt,sil			Migmatitic	140	33						
Bk	290	Schist	grt,sil			Migmatitic	145	48						
Bk	291	Biotite Gneiss		Amphibolite		Migmatitic	350	37						
Bk	292	Biotite Gneiss		Metagraywacke	qtz,bt	Migmatitic	70	33						
Bk	293	Schist	grt,sil	Metagraywacke		Mylonitic					193	20		
Bk	294	Metagraywacke				Migmatitic	213	16						
Bk	295	Biotite Gneiss				Migmatitic	352	22						
Bk	296	Biotite Gneiss		Metagraywacke			165	15						
Bk	297	Metagraywacke					135	22						
Bk	298	Schist		Metagraywacke			145	32						
Bk	299	Migmatite				Migmatitic	165	40						
Bk	300	Schist		Metagraywacke		Migmatitic	185	37						
Bk	301	Metagraywacke		Schist	grt,sil		40	40						
Bk	302	Schist	grt,sil			Migmatitic	150	45						
Bk	303	Schist	grt,sil			Migmatitic	194	20						
Bk	304	Schist	grt,sil			Migmatitic	50	35						
Bk	305	Schist	grt,sil			Migmatitic	13	20						
Bk	306	Schist	sil,grt			Migmatitic	175	17						
Bk	307	Schist	sil,grt			Migmatitic	160	30						
Bk	308	Schist	sil,grt			Migmatitic	198	35						
Bk	309	Schist	sil,grt			Migmatitic	240	27						
Bk	310	Schist	sil,grt			Migmatitic	150	64						
Bk	311	Metagraywacke				Migmatitic	212	35						
Bk	312	Metagraywacke				Migmatitic	200	55						
Bk	313	Metagraywacke		Amphibolite			125	14						
Bk	314	Amphibolite		Migmatite			45	20						
Bk	315	Amphibolite		Metagraywacke		Migmatitic	55	20						
Bk	316	Metagraywacke					189	20						
Bk	317	Biotite Gneiss				Migmatitic	128	40						
Bk	318	Metagraywacke		Schist			160	31						
Bk	319	Schist	grt,sil			Migmatitic	160	14						
Bk	320	Metagraywacke	bt,qtz			Migmatitic	193	38						
Bk	321	Schist	grt,sil				210	24						
Bk	322	Schist	grt,sil			Migmatitic	138	70						
Bk	323	Schist	grt,sil				150	52						
Bk	324	Amphibolite					125	24						
Bk	325	Schist	grt,sil				38	53						
Bk	326	Schist	grt,sil				193	42						
Bk	327	Schist	grt,sil			Migmatitic	195	13						
Bk	328	Schist					95	20						
Bk	329	Metagraywacke					265	34						
Bk	330	Metagraywacke		Schist	sil,grt	Migmatitic				136	32			
Bk	331	Metagraywacke		Schist	sil,grt	Migmatitic	144	44						
Bk	332	Metagraywacke		Schist	sil,grt	Migmatitic	144	38						

							Foliation		Lineation		Fold Axis		Joint	
Quad	Station	Rock Type 1(RT2)	RT 1 Minerals	Rock Type 2 (RT2)	RT2 Minerals	Modifier	Strike	Dip	Trend	Plunge	Trend	Plunge	Strike	Dip
Bk	333	Metagraywacke				Migmatitic	120	59						
Bk	334	Schist	grt,sil			Migmatitic	122	48						
Bk	335	Biotite Gneiss	bt,kspr			Mylonitic	152	25						
Bk	336	Biotite Gneiss					130	21						
Bk	337	Schist	grt,sil			Migmatitic	61	30						
Bk	338	Schist	grt,bt	Schist	sil	Migmatitic	190	18						
Bk	339	Schist	sil,grt			Migmatitic	129	33						
Bk	340	Schist	sil,grt	Metagraywacke		Migmatitic	154	38						
Bk	341	Schist	grt,sil				152	67						
Bk	342	Schist	grt,sil	Quartzite			123	21						
Bk	343	Schist	grt,sil				60	27						
Bk	344	Granitic Orthogneiss	grt,kspr				175	12						
Bk	345	Granitic Orthogneiss	grt,kspr				196	11						
Bk	346	Granitic Orthogneiss	grt,kspr				170	17						
Bk	347	Schist	grt,sil				330	18						
Bk	348	Schist	grt,sil				204	29						
Bk	349	Schist	grt,sil				126	21						
Bk	350	Schist	sil,grt				150	26						
Bk	351	Schist	sil,grt	Metagraywacke		Migmatitic	35	28						
Bk	352	Schist	sil,grt	Metagraywacke		Migmatitic	60	18						
Bk	353	Schist		Metagraywacke		Migmatitic	235	16						
Bk	354	Schist		Metagraywacke		Migmatitic	95	16						
Bk	355	Metagraywacke		Schist		Migmatitic	230	33						
Bk	356	Schist					215	17						
Bk	357	Schist		Amphibolite			165	13						
Bk	358	BT Schist		Schist	sil,grt		155	14						
Bk	359	Schist	sil,grt				118	16						
Bk	360	Granitic Orthogneiss				Mylonitic	142	40						
Bk	361	Granitic Orthogneiss					70	22						
Bk	362	Schist	grt,sil				265	29						
Bk	363	Schist					127	35						
Bk	364	Schist		Metagraywacke							235	60		
Bk	365	Schist		Metagraywacke		Migmatitic	218	12						
Bk	366	Metagraywacke		Schist		Migmatitic	146	23						
Bk	367	Biotite Gneiss	bt,grt	Metagraywacke		Migmatitic	152	14						
Bk	368	Biotite Gneiss	bt,grt	Metagraywacke		Migmatitic	140	20						
Bk	369	Schist				Migmatitic	305	25						
Bk	370	Schist		Metagraywacke			60	20						
Bk	371	Biotite Gneiss	bt,kspr			Migmatitic	207	27						
Bk	372	Metagraywacke		Schist		Migmatitic	165	52						
Bk	373	Metagraywacke		Schist		Migmatitic	135	15						
Bk	374	Metagraywacke		Schist		Migmatitic	325	32						
Bk	375	Granitic Orthogneiss	bt,kspr				230	11						
Bk	376	Schist					80	15						
Bk	377	Schist	grt,sil				145	24						
Bk	378	BT Schist	bt,kspr				106	50						
Bk	379	BT Schist	bt,grt				165	20						
Bk	380	BT Schist	bt,grt				340	35						
Bk	381	Biotite Gneiss		Hornblende Gneiss			173	18						
Bk	382	Hornblende Gneiss	bt,amp			Migmatitic	195	24						
Bk	383	Metagraywacke		Schist			23	21						
Bk	384	Metagraywacke		Schist			220	12						
Bk	385	Metagraywacke		Schist			340	22						
Bk	386	Schist				Migmatitic	140	42						
Bk	387	Schist				Migmatitic	105	20						
Bk	388	Schist		Metagraywacke		Migmatitic	216	22						
Bk	389	Diabase Dike					135	90						
Bk	390	Metagraywacke		Schist			25	37						
Bk	391	Metagraywacke		Schist			146	22						
Bk	392	Metagraywacke		Schist			130	18						
Bk	393	Metagraywacke		Schist			140	40						
Bk	394	Metagraywacke		Schist		Migmatitic	130	32						
Bk	395	Metagraywacke		Schist		Migmatitic	342	22						
Bk	396	Metagraywacke		Schist		Migmatitic	312	17						
Bk	397	Metagraywacke		Schist		Migmatitic	220	37						
Bk	398	Metagraywacke		Schist		Migmatitic	172	34						
Bk	399	Metagraywacke		Schist		Migmatitic	150	29						
Bk	400	Schist	sil,ms				238	37						

							Foliation		Lineation		Fold Axis		Joint	
Quad	Station	Rock Type 1 (RT2)	RT 1 Minerals	Rock Type 2 (RT2)	RT2 Minerals	Modifier	Strike	Dip	Trend	Plunge	Trend	Plunge	Strike	Dip
Bk	401	Schist	sil,ms	Metagraywacke			318	21						
Bk	402	Schist	sil,ms	Metagraywacke			157	28						
Bk	403	Metagraywacke		Granitic Orthogneiss		Migmatitic	137	17						
Bk	404	Schist					209	35						
Bk	405	Schist	sil,grt	Diabase Dike			139	25						
Bk	406	Schist		Metagraywacke			0	23						
Bk	407	Schist	sil,grt				152	8						
Bk	408	Schist	sil,grt	Metagraywacke			170	27						
Bk	409	Schist		Metagraywacke		Migmatitic	65	15						
Bk	410	Schist		Metagraywacke		Migmatitic	145	23						
Bk	411	Schist		Metagraywacke		Migmatitic	122	20						
Bk	412	Schist		Metagraywacke		Migmatitic	28	24						
Bk	413	Schist		Metagraywacke		Migmatitic	137	19						
Bk	414	Schist		Metagraywacke		Migmatitic	137	45						
Bk	415	Schist		Metagraywacke		Migmatitic	297	28						
Bk	416	Schist		Metagraywacke		Migmatitic	50	22						
Bk	417	Schist		Metagraywacke		Migmatitic	148	27						
Bk	418	Schist		Metagraywacke		Migmatitic	132	16						
Bk	419	Pegmatite		Migmatite			327	27						
Bk	420	Metagraywacke		Schist		Migmatitic	140	65						
Bk	421	Biotite Gneiss					126	54						
Bk	422	Metagraywacke					334	48						
Bk	423	Metagraywacke					320	52						
Bk	424	Metagraywacke				migmatitic			130	27				
Bk	425	Metagraywacke					185	10						
Bk	426	Metagraywacke				Migmatitic	323	21						
Bk	427	Metagraywacke				Migmatitic	122	41						
Bk	428	Metagraywacke				Migmatitic	117	14						
Bk	429	Metagraywacke		Schist		Migmatitic	191	40						
Bk	430	Schist	sil,ms			Migmatitic	197	17						
Bk	431	Schist	sil,ms			Migmatitic	124	47						
Bk	432	Metagraywacke		Biotite Gneiss		Migmatitic	145	27						
Bk	433	Metagraywacke		Biotite Gneiss		Migmatitic	125	23						
Bk	434	Diabase Dike					315	90						
Bk	435	Metagraywacke		Schist		Migmatitic	142	44						
Bk	436	Metagraywacke		Schist		Migmatitic	55	13						
Bk	437	Metagraywacke		Schist		Migmatitic	165	30						
Bk	438	Metagraywacke		Schist		Migmatitic	132	16						
Bk	439	Schist	sil,grt				60	30						
Bk	440	Schist	sil,grt	Metagraywacke		Migmatitic	329	28						
Bk	441	Schist	sil,grt	Metagraywacke		Migmatitic	320	42						
Bk	442	Schist	sil,grt	Metagraywacke		Migmatitic	322	34						
Bk	443	Schist	sil,grt	Metagraywacke		Migmatitic	300	30						
Bk	444	Schist	sil,grt	Metagraywacke		Migmatitic	320	25						
Bk	445	Schist	sil,grt	Metagraywacke		Migmatitic	128	28						
Bk	446	Biotite Gneiss				Migmatitic	95	20						
Bk	447	Metagraywacke					223	15						
Bk	448	Metagraywacke					160	25						
Bk	62a	Granitic Orthogneiss	bt,kspr						330	72				
Bk	66a	Granitic Orthogneiss	bt,kspr						331	35				
Ch	1	Biotite Gneiss	bt,grt			Migmatitic	358	48						
Ch	2	Hornblende Gneiss	amp,bt	Biotite Gneiss		Migmatitic	60	88						
Ch	3	Migmatite				Weathered	170	40						
Ch	4	Amphibolite		Hornblende Gneiss		Migmatitic	220	32						
Ch	5	Amphibolite		Hornblende Gneiss		Migmatitic	353	58						
Ch	6	Amphibolite	grt,amp				142	22						
Ch	7	Amphibolite	grt,amp											
Ch	8	Amphibolite	grt,amp			Migmatitic	346	38						
Ch	9	Amphibolite	grt,amp				10	32						
Ch	10	Amphibolite	grt,amp				175	40						
Ch	11	Amphibolite	grt,amp				170	16						
Ch	12	Amphibolite	grt,amp				8	5						
Ch	13	Amphibolite	grt,amp				198	18						
Ch	13	Amphibolite	grt,amp										90	88
Ch	14	Amphibolite	grt,qtz				160	42						
Ch	15	Amphibolite	grt,amp			Migmatitic	155	25						
Ch	16	Amphibolite	amp,grt				85	48						
Ch	17	Amphibolite	amp,grt			Migmatitic	20	48						
Ch	18	Amphibolite					65	42						

							Foliation		Lineation		Fold Axis		Joint	
Quad	Station	Rock Type 1 (RT2)	RT 1 Minerals	Rock Type 2 (RT2)	RT2 Minerals	Modifier	Strike	Dip	Trend	Plunge	Trend	Plunge	Strike	Dip
Ch	19	Amphibolite	bt,grt				117	42						
Ch	20	Amphibolite	bt,grt				210	27						
Ch	21	Amphibolite	bt,grt			Migmatitic	217	19						
Ch	22	Metagraywacke		Schist			142	32						
Ch	23	Metagraywacke		Amphibolite			165	37						
Ch	24	Diabase Dike					135	90						
Ch	25	Diabase Dike					135	90						
Ch	26	Metagraywacke		Schist			160	28						
Ch	27	Schist		Metagraywacke			185	23						
Ch	28	Schist	grt,sil				190	45						
Ch	29	Schist	grt,sil	Metagraywacke			132	44						
Ch	30	Metagraywacke		Schist		Migmatitic	170	55						
Ch	31	Metagraywacke					24	28						
Ch	32	Metagraywacke	bt,qtz				155	21						
Ch	33	Metagraywacke	bt,qtz				145	30						
Ch	34	Metagraywacke				Migmatitic	170	21						
Ch	35	Biotite Gneiss	bt,grt	Metagraywacke		Migmatitic	180	56						
Ch	36	Metagraywacke		Schist		Migmatitic	187	44						
Ch	37	Schist					183	33						
Ch	38	Metagraywacke		Schist			193	65						
Ch	39	Metagraywacke		Schist			195	42						
Ch	40	Biotite Gneiss					203	32						
Ch	41	Biotite Gneiss					208	32						
Ch	42	biotite gneiss									238	32		
Ch	43	Schist		Metagraywacke			145	15						
Ch	44	Metagraywacke		Schist			135	30						
Ch	45	Layered Metagraywacke	bt,grt				208	30						
Ch	46	Layered Metagraywacke	bt,grt				183	23						
Ch	47	Layered Metagraywacke	bt,grt				188	47						
Ch	48	Layered Metagraywacke	bt,grt				171	39						
Ch	49	Layered Metagraywacke	bt,grt	Schist							237	44		
Ch	50	Layered Metagraywacke	bt,grt	Schist			174	32						
Ch	51	Schist	sil,grt				172	23						
Ch	52	Schist	sil,grt				155	26						
Ch	53	Schist	sil,grt	Metagraywacke			170	15						
Ch	54	Metagraywacke		Schist		Migmatitic					290	44		
Ch	55	Metagraywacke		Schist		Migmatitic	143	24						
Ch	56	Metagraywacke		Schist		Migmatitic	124	35						
Ch	57	Metagraywacke		Schist		Migmatitic	125	23						
Ch	58	Pegmatite		Granitic Orthogneiss			170	33						
Ch	59	Metagraywacke	bt			Migmatitic	150	27						
Ch	60	Schist					160	17						
Ch	61	Metagraywacke				Migmatitic	130	20						
Ch	62	Metagraywacke				Migmatitic	125	16						
Ch	63	Layered Metagraywacke	qtz				122	39						
Ch	64	Layered Metagraywacke		Schist			102	38						
Ch	65	Migmatite		Metagraywacke			191	37						
Ch	66	Layered Metagraywacke		Schist		Migmatitic	120	17						
Ch	67	Layered Metagraywacke		Schist		Migmatitic	310	23						
Ch	68	Schist	sil,grt	Layered Metagraywacke		Migmatitic	227	35						
Ch	69	Schist	sil,grt	Layered Metagraywacke		Migmatitic	155	20						
Ch	70	Hornblende Gneiss					23	58						
Ch	71	Hornblende Gneiss	amp,bt				18	20						
Ch	72	Hornblende Gneiss		Biotite Gneiss			190	31						
Ch	73	Schist	grt,sil			Migmatitic	153	29						
Ch	74	Hornblende Gneiss					110	57						
Ch	75	Hornblende Gneiss					125	51						
Ch	76	Metagraywacke		Schist			133	34						
Ch	77	Migmatite					203	37						
Ch	78	Granitic Orthogneiss	grt,kspr			Mylonitic	98	20						
Ch	79	Granitic Orthogneiss	grt,kspr			Mylonitic	117	7						
Ch	80	Granitic Orthogneiss	grt,kspr			Mylonitic	37	22						
Ch	81	Granitic Orthogneiss	grt,kspr			Mylonitic	340	68						
Ch	82	Granitic Orthogneiss	grt,kspr			Mylonitic	70	19						
Ch	82	Granitic Orthogneiss	grt,kspr			Mylonitic	205	22						
Ch	83	Granitic Orthogneiss	grt,kspr			Mylonitic	2	22						
Ch	84	Granitic Orthogneiss	bt,kspr			Mylonitic	46	55						
Ch	85	Granitic Orthogneiss	bt,kspr			Mylonitic	149	43						
Ch	86	Granitic Orthogneiss	bt,kspr			Mylonitic	240	40						

							Foliation		Lineation		Fold Axis		Joint	
Quad	Station	Rock Type 1 (RT2)	RT 1 Minerals	Rock Type 2 (RT2)	RT2 Minerals	Modifier	Strike	Dip	Trend	Plunge	Trend	Plunge	Strike	Dip
Ch	87	Amphibolite	amp,grt				50	27						
Ch	88	Schist		Layered Metagraywacke		Migmatitic	167	40						
Ch	89	Schist		Layered Metagraywacke		Migmatitic	197	24						
Ch	90	Schist		Layered Metagraywacke		Migmatitic	148	37						
Ch	91	Schist		Layered Metagraywacke		Migmatitic	20	44						
Ch	92	Metagraywacke					166	20						
Ch	93	Metagraywacke		Schist		Migmatitic	152	47						
Ch	94	Metagraywacke		Schist		Migmatitic	171	45						
Ch	95	Metagraywacke		Schist		Migmatitic	161	46						
Ch	96	Metagraywacke		Schist		Migmatitic	180	47						
Ch	97	Amphibolite					138	62						
Ch	98	Schist	sil,grt				20	29						
Ch	99	Granitic Orthogneiss	qtz,kspr	Schist			116	21						
Ch	100	Metagraywacke		Schist			125	35						
Ch	101	Schist					136	24						
Ch	102	Gondite	grt,qtz	Schist	bt,plg		140	28						
Ch	103	BT Schist	bt				123	14						
Ch	104	Gneiss	bt,plg			Mylonitic	135	17						
Ch	105	Biotite Gneiss					47	31						
Ch	106	Biotite Gneiss				Migmatitic	137	27						
Ch	107	Biotite Gneiss				Migmatitic	38	33						
Ch	108	Biotite Gneiss		Layered Metagraywacke		Migmatitic	152	38						
Ch	109	Biotite Gneiss		Metagraywacke		Migmatitic	15	50						
Ch	110	Granitic Orthogneiss	qtz,grt				75	5						
Ch	111	Granitic Orthogneiss	qtz,grt				73	22						
Ch	112	Granitic Orthogneiss	qtz,grt				141	34						
Ch	113	Granitic Orthogneiss	grt,kspr				35	75						
Ch	114	Granitic Orthogneiss	grt,kspr				44	12						
Ch	115	Granitic Orthogneiss	grt,kspr				105	37						
Ch	116	Schist	sil,grt				335	36						
Ch	117	Granitic Orthogneiss	grt,kspr				50	10						
Ch	118	Granitic Orthogneiss	grt,kspr				196	16						
Ch	118	Granitic Orthogneiss	grt,kspr										70	66
Ch	118	Granitic Orthogneiss	grt,kspr										340	74
Ch	118	Granitic Orthogneiss	grt,kspr										24	59
Ch	119						175	12						
Ch	120	Granitic Orthogneiss	grt,kspr				208	6						
Ch	121	Biotite Gneiss					55	13						
Ch	122	Schist					160	47						
Ch	123	Schist		Layered Metagraywacke		Migmatitic	115	17						
Ch	124	Biotite Gneiss		Schist		Migmatitic	150	30						
Ch	125	Pegmatite		Granitic Orthogneiss			95	35						
Ch	126	Metagraywacke				Migmatitic	120	24						
Ch	127	Granitic Orthogneiss		Pegmatite			316	16						
Ch	128	Schist	sil,grt	Metagraywacke		Migmatitic	170	20						
Ch	129	Granitic Orthogneiss	ms,grt				164	14						
Ch	130	Granitic Orthogneiss	grt,qtz				5	11						
Ch	131	Granitic Orthogneiss	grt,qtz	Schist			185	40						
Ch	132	Granitic Orthogneiss					225	46						
Ch	133	Granitic Orthogneiss					132	15						
Ch	134	Granitic Orthogneiss	qtz,kspr				330	19						
Ch	135	Granitic Orthogneiss	qtz,kspr				120	11						
Ch	136	Granitic Orthogneiss	qtz,kspr				205	14						
Ch	137	Granitic Orthogneiss	qtz,kspr				191	11						
Ch	138	Granitic Orthogneiss					243	13						
Ch	139	Granitic Orthogneiss	grt,qtz				51	31						
Ch	140	Granitic Orthogneiss					85	20						
Ch	141	Granitic Orthogneiss	grt,kspr				100	29						
Ch	142	Granitic Orthogneiss	grt,kspr	Schist			80	40						
Ch	143	Hornblende Gneiss	bt,amp			Migmatitic	15	28						
Ch	144	Hornblende Gneiss					57	21						
Ch	145	Hornblende Gneiss					180	41						
Ch	146	Biotite Gneiss	bt	Hornblende Gneiss			168	22						
LW	2	Biotite Gneiss	bt,grt			Migmatitic	173	32						
LW	3	Biotite Gneiss	bt,grt			Migmatitic	163	32						
LW	4	Biotite Gneiss	bt,grt			Migmatitic	180	55						
LW	5	Biotite Gneiss	bt,grt			Migmatitic	120	27						
LW	6	Biotite Gneiss	bt,grt			Migmatitic	170	28						
LW	7	Granitic Orthogneiss					170	54						

							Foliation		Lineation		Fold Axis		Joint	
Quad	Station	Rock Type 1 (RT2)	RT 1 Minerals	Rock Type 2 (RT2)	RT2 Minerals	Modifier	Strike	Dip	Trend	Plunge	Trend	Plunge	Strike	Dip
LW	8	Biotite Gneiss					170	50						
LW	9	Granitic Orthogneiss				Mylonitic	185	67						
LW	10	Layered Metagraywacke				Mylonitic	170	45						
LW	11	Amphibolite	amp,grt				188	42						
LW	12	Biotite Gneiss	grt,grt			Mylonitic	171	56						
LW	13	Metagraywacke	grt,bt			Mylonitic	188	44						
LW	14	Metagraywacke	grt,bt			Mylonitic	185	49						
LW	15	Gondite				Migmatitic	160	29						
LW	16	Gondite					198	44						
LW	17	Biotite Gneiss					180	24						
LW	18	Biotite Gneiss	bt			Migmatitic	170	33						
LW	19	Biotite Gneiss	grt,bt			Migmatitic	191	58						
LW	20	Biotite Gneiss					160	68						
LW	21	Biotite Gneiss	grt,bt								275	77		
LW	21	Biotite Gneiss	grt,bt				155	67						
LW	22	Biotite Gneiss	grt,bt				145	68						
LW	23	Biotite Gneiss	grt,bt				110	47						
LW	24	Biotite Gneiss	grt,bt				185	42						
LW	25	Biotite Gneiss	grt,kspr			Mylonitic	165	55						
LW	26	Biotite Gneiss	grt,kspr			Mylonitic	125	47						
LW	27	Biotite Gneiss				Migmatitic	127	32						
LW	28	Biotite Gneiss	bt			Mylonitic	138	42						
LW	29	Granitic Orthogneiss	kspr,grt			Mylonitic	358	18						
LW	30	Granitic Orthogneiss	kspr,grt			Mylonitic	135	60						
LW	31	Layered Metagraywacke	bt,grt	Amphibolite			196	66						
LW	32	Biotite Gneiss		Metagraywacke			170	50						
LW	33	Biotite Gneiss		Metagraywacke			225	52						
LW	34	Biotite Gneiss		Metagraywacke			165	62						
LW	35	Biotite Gneiss		Amphibolite			5	30						
LW	36	Biotite Gneiss		Hornblende Gneiss			359	45						
LW	37	Biotite Gneiss		Amphibolite		Migmatitic	5	45						
LW	38	Biotite Gneiss		Amphibolite			183	48						
LW	39	Biotite Gneiss		Amphibolite			355	47						
LW	40	Biotite Gneiss					160	25						
LW	41	Amphibolite	garnet				200	40						
LW	42	Amphibolite		Biotite Gneiss			150	22						
LW	43	Hornblende Gneiss					115	85						
LW	44	Hornblende Gneiss					133	75						
LW	45	Biotite Gneiss		Amphibolite			190	55						
LW	46	Biotite Gneiss	grt,bt				220	20						
LW	47	Biotite Gneiss	grt,bt	Hornblende Gneiss	grt,bt	Mylonitic	185	40						
LW	48	Layered Metagraywacke		Biotite Gneiss		Mylonitic	182	28						
LW	49	Biotite Gneiss	grt,bt			Mylonitic	166	30						
LW	50	Biotite Gneiss	grt	Granitic Orthogneiss		Mylonitic	147	25						
LW	51	Biotite Gneiss	grt	Granitic Orthogneiss		Mylonitic	178	30						
LW	52	Biotite Gneiss	grt	Granitic Orthogneiss	quartz	Mylonitic	190	50						
LW	53	Gondite					200	20						
LW	53	Gondite											280	63
LW	53	Gondite											20	57
LW	54	Biotite Gneiss				Migmatitic	175	35						
LW	55	Amphibolite					208	74						
LW	56	Hornblende Gneiss									15	75		
LW	57	Biotite Gneiss		Amphibolite			190	37						
LW	58	Hornblende Gneiss		Biotite Gneiss			195	31						
LW	59	Amphibolite									200	75		
LW	60	Amphibolite					10	54						
LW	61	Biotite Gneiss					120	25						
LW	62	Hornblende Gneiss					206	66						
LW	63	Granitic Orthogneiss				Mylonitic	220	45						
LW	64	Biotite Gneiss	garnet	Hornblende Gneiss		Migmatitic	147	35						
LW	65	Granitic Orthogneiss				Mylonitic	217	32						
LW	66	Amphibolite		Biotite Gneiss			175	52						
LW	67	Hornblende Gneiss	amp,bt				158	72						
LW	68	Hornblende Gneiss					223	43						
LW	69	Hornblende Gneiss				Migmatitic	170	33						
LW	70	Amphibolite		Biotite Gneiss			195	67						
LW	71	Pegmatite					220	44						
LW	72	Biotite Gneiss		Metagraywacke			135	49						
LW	73	Biotite Gneiss	grt,bt			Migmatitic	153	32						

							Foliation		Lineation		Fold Axis		Joint	
Quad	Station	Rock Type 1 (RT2)	RT 1 Minerals	Rock Type 2 (RT2)	RT2 Minerals	Modifier	Strike	Dip	Trend	Plunge	Trend	Plunge	Strike	Dip
LW	74	Biotite Gneiss	grt,bt			Migmatitic	156	32						
LW	75	Biotite Gneiss	grt,bt	Amphibolite		Migmatitic	145	40						
LW	76	Granitic Orthogneiss	bt			Mylonitic	165	25						
LW	77	Metagraywacke					166	38						
LW	78	Metagraywacke				Migmatitic	174	26						
LW	79	Metagraywacke				Migmatitic	173	35						
LW	80	Biotite Gneiss		Metagraywacke		Migmatitic	207	43						
LW	81	Biotite Gneiss		Metagraywacke		Migmatitic	165	37						
LW	82	Biotite Gneiss	bt,grt	Metagraywacke		Migmatitic	167	17						
LW	83	Layered Metagraywacke	bt,grt				117	39						
LW	84	Amphibolite					147	26						
LW	85	Biotite Gneiss					142	27						
LW	86	Gondite		Schist			292	84						
LW	87	Diabase Dike					135	90						
LW	88	Metagraywacke	qtz,kspr	Schist	sil,grt		208	31						
Rp	1	Metagraywacke					173	41						
Rp	2	Metagraywacke					172	39						
Rp	3	Metagraywacke					156	28						
Rp	3a	Metagraywacke							191	9				
Rp	4	Metagraywacke					194	40						
Rp	5	Metagraywacke					177	20						
Rp	6	Metagraywacke					170	25						
Rp	7	Metagraywacke					160	45						
Rp	8	Metagraywacke					150	30						
Rp	9	Metagraywacke					177	34						
Rp	10	Metagraywacke					350	9						
Rp	11	Metagraywacke					169	26						
Rp	12	Metagraywacke					168	49						
Rp	13	Metagraywacke					175	40						
Rp	14	Gondite					195	73						
Rp	15	Metagraywacke					97	71						
Rp	16	Metagraywacke					169	64						
Rp	17	Metagraywacke					175	54						
Rp	18	Schist	grt, sil				328	41						
Rp	19	Schist	grt, sil			Migmatitic	339	49						
Rp	20	Biotite Gneiss	grt				152	12						
Rp	21	Biotite Gneiss	grt				134	46						
Rp	22	Metagraywacke	ksp,qtz			Migmatitic	166	60						
Rp	23	Metagraywacke	ksp,qtz			Migmatitic	134	61						
Rp	24	Hornblende Gneiss	amp,bt				5	58						
Rp	25	Granitic Orthogneiss	ksp,grt			Mylonitic	158	31						
Rp	26	Granitic Orthogneiss	ksp,grt			Mylonitic	288	25						
Rp	26a	Granitic Orthogneiss	kspr,grt						1	20				
Rp	27	Granitic Orthogneiss	kspr,grt			Mylonitic	254	32						
Rp	28	Granitic Orthogneiss	kspr,grt			Mylonitic	270	1						
Rp	29	Granitic Orthogneiss	kspr,grt			Mylonitic	245	65						
Rp	30	Granitic Orthogneiss	kspr,grt			Mylonitic	260	16						
Rp	30a	Granitic Orthogneiss	kspr,grt			Mylonitic			341	14				
Rp	31	Granitic Orthogneiss	kspr,grt			Mylonitic	288	22						
Rp	32	Granitic Orthogneiss	kspr,grt			Mylonitic	174	57						
Rp	32a	Granitic Orthogneiss	kspr,grt			Mylonitic			6	16				
Rp	33	Granitic Orthogneiss	kspr,grt			Mylonitic	207	45						
Rp	34	Granitic Orthogneiss	kspr,grt			Mylonitic	210	46						
Rp	35	Granitic Orthogneiss	kspr,grt			Mylonitic	215	42						
Rp	36	Schist	grt				167	78						
Rp	37	Metagraywacke					190	45						
Rp	38	Metagraywacke					206	61						
Rp	39	Metagraywacke					210	65						
Rp	40	Metagraywacke					166	40						
Rp	41	Metagraywacke	grt,bt				182	30						
Rp	42	Metagraywacke	grt,bt				158	34						
Rp	43	Metagraywacke					183	36						
Rp	44	Metagraywacke					178	51						
Rp	45	Metagraywacke					186	48						
Rp	46	Metagraywacke					208	25						
Rp	47	Metagraywacke					195	35						
Rp	48	Granitic Orthogneiss		Metagraywacke		Mylonitic	165	44						
Rp	49	Metagraywacke					55	25						

							Foliation		Lineation		Fold Axis		Joint	
Quad	Station	Rock Type 1 (RT2)	RT 1 Minerals	Rock Type 2 (RT2)	RT2 Minerals	Modifier	Strike	Dip	Trend	Plunge	Trend	Plunge	Strike	Dip
Rp	50	Granitic Orthogneiss				Mylonitic	180	54						
Rp	51	Metagraywacke					185	62						
Rp	52	Granitic Orthogneiss	kspr			Mylonitic	203	45						
Rp	53	Granitic Orthogneiss	kspr			Mylonitic	185	38						
Rp	54	Granitic Orthogneiss	kspr,grt			Mylonitic	256	64						
Rp	54a	Granitic Orthogneiss	kspr,grt			Mylonitic			355	24				
Rp	55	Granitic Orthogneiss	kspr			Mylonitic	206	34						
Rp	56	Granitic Orthogneiss	kspr			Mylonitic	95	45						
Rp	56a	Granitic Orthogneiss	kspr			Mylonitic			168	8				
Rp	57	Granitic Orthogneiss	kspr			Mylonitic	255	18						
Rp	58	Granitic Orthogneiss	kspr			Mylonitic	238	24						
Rp	59	Granitic Orthogneiss	kspr			Mylonitic	285	22						
Rp	60	Granitic Orthogneiss	kspr			Mylonitic	190	36						
Rp	61	Amphibolite					156	8						
Rp	62	Granitic Orthogneiss	kspr			Mylonitic	185	44						
Rp	63	Granitic Orthogneiss	kspr			Mylonitic	315	18						
Rp	64	Pegmatite	qtz				110	35						
Rp	65	Biotite Gneiss	grt,kspr,bt				205	42						
Rp	66	Biotite Gneiss	grt,bt,kspr				191	64						
Rp	67	Biotite Gneiss					180	42						
Rp	68	Biotite Gneiss				Mylonitic	185	42						
Rp	69	Biotite Gneiss	bt,qtz,kspr				175	80						
Rp	70	Biotite Gneiss				Mylonitic	235	25						
Rp	71	Biotite Gneiss					215	64						
Rp	72	Biotite Gneiss					192	60						
Rp	73	Biotite Gneiss				Migmatitic	191	63						
Rp	74	Metagraywacke	grt,bt				168	79						
Rp	75	Hornblende Gneiss	amp,bt,kspr				153	24						
Rp	76	Metagraywacke					237	45						
Rp	77	Biotite Gneiss					192	33						
Rp	78	Biotite Gneiss	bt,qtz				176	52						
Rp	79	Hornblende Gneiss	amp,bt				320	84						
Rp	80	Metagraywacke					165	47						
Rp	81	Metagraywacke					176	38						
Rp	82	Biotite Gneiss					142	26						
Rp	83	Metagraywacke					180	54						
Rp	84	Hornblende Gneiss		Biotite Gneiss		Migmatitic	185	45						
Rp	85	Biotite Gneiss	grt,bt,kspr				190	41						
Rp	86	Biotite Gneiss				Migmatitic	204	34						
Rp	87	Biotite Gneiss				Migmatitic	210	33						
Rp	88	Biotite Gneiss				Migmatitic	190	32						
Rp	89	Biotite Gneiss	grt,bt	Schist	grt,ms		196	48						
Rp	90	Metagraywacke					193	33						
Rp	91	Metagraywacke	grt,bt				210	32						
Rp	92	Biotite Gneiss	grt,bt			Migmatitic	105	54						
Rp	93	Granitic Orthogneiss	grt,kspr				240	39						
Rp	93a	Granitic Orthogneiss	grt,kspr						0	14				
Rp	94	Schist	grt,sill				150	47						
Rp	95	Biotite Gneiss				Mylonitic	177	34						
Rp	96	Biotite Gneiss				Migmatitic	140	38						
Rp	97	Biotite Gneiss					146	22						
Rp	98	Biotite Gneiss				Migmatitic	195	55						
Rp	99	Biotite Gneiss				Migmatitic	190	36						
Rp	100	Biotite Gneiss				Migmatitic	176	53						
Rp	100b	Biotite Gneiss				Migmatitic							130	39
Rp	100c	Biotite Gneiss				Migmatitic							359	53
Rp	101	Granitic Orthogneiss	kspr,bt			Mylonitic	135	60						
Rp	101a	Granitic Orthogneiss	kspr,bt			Mylonitic			315	19				
Rp	101b	Granitic Orthogneiss	kspr,bt			Mylonitic							248	51
Rp	102	Granitic Orthogneiss	kspr,bt			Mylonitic	185	38						
Rp	103	Granitic Orthogneiss	kspr,bt			Mylonitic	200	28						
Rp	104	Granitic Orthogneiss	kspr,bt			Mylonitic	186	10						
Rp	105	Granitic Orthogneiss	kspr,bt			Mylonitic	185	15						
Rp	106	Gondite	grt,qtz	Biotite Gneiss			210	26						
Rp	107	Biotite Gneiss	grt,bt				190	34						
Rp	108	Biotite Gneiss	grt,bt				215	57						
Rp	109	Biotite Gneiss	grt,bt				180	41						
Rp	110	Biotite Gneiss	grt,bt				184	34						
Rp	111	Biotite Gneiss	grt,bt				177	15						

							Foliation		Lineation		Fold Axis		Joint	
Quad	Station	Rock Type 1 (RT2)	RT 1 Minerals	Rock Type 2 (RT2)	RT2 Minerals	Modifier	Strike	Dip	Trend	Plunge	Trend	Plunge	Strike	Dip
Rp	112	Biotite Gneiss	grt,bt				180	23						
Rp	113	Biotite Gneiss	grt,bt				190	36						
Rp	114	Biotite Gneiss	grt,bt	Amphibolite	amp,bt		190	47						
Rp	115	Biotite Gneiss					160	67						
Rp	116	Biotite Gneiss					155	50						
Rp	117	Biotite Gneiss					175	62						
Rp	118	Biotite Gneiss					160	49						
Rp	119	Biotite Gneiss					155	53						
Rp	120	Biotite Gneiss	grt,bt				175	50						
Rp	121	Diabase Dike					155	46						
Rp	122	Biotite Gneiss	grt,bt				220	19						
Rp	123	Granitic Orthogneiss				Mylonitic	205	50						
Rp	123a	Granitic Orthogneiss				Mylonitic			350	24				
Rp	124	Granitic Orthogneiss				Mylonitic	194	40						
Rp	125	Biotite Gneiss					180	17						
Rp	126	Biotite Gneiss					180	42						
Rp	127	Granitic Orthogneiss				Mylonitic	135	85						
Rp	128	Granitic Orthogneiss	grt,kspr,bt			Mylonitic	194	40						
Rp	128a	Granitic Orthogneiss				Mylonitic			346	5				
Rp	129	Granitic Orthogneiss	grt,fspr,bt			Mylonitic	151	14						
Rp	130	Schist	grt,sil				190	25						
Rp	131	Schist	grt,sil				140	37						
Rp	132	Schist	grt,sil				190	22						
Rp	133	Biotite Gneiss					165	36						
Rp	134	Biotite Gneiss					200	16						
Rp	135	Biotite Gneiss	grt,bt				325	42						
Rp	136	Biotite Gneiss	grt,bt				160	25						
Rp	137	Schist	grt,sil	Biotite Gneiss		Migmatitic	208	27						
Rp	138	Schist	grt,sil				201	55						
Rp	138a	Schist	grt,sil						5	25				
Rp	139	Schist	grt,sil	Biotite Gneiss		Migmatitic	214	42						
Rp	139	Schist	grt,sil	Biotite Gneiss		Migmatitic							218	85
Rp	140	Schist	grt,sil	Biotite Gneiss		Migmatitic					358	13		
Rp	140b	Schist	grt,sil	Biotite Gneiss		Migmatitic							73	68
Rp	141	Granitic Orthogneiss					140	23						
Rp	141b	Granitic Orthogneiss											241	23
Rp	142	Biotite Gneiss				Migmatitic	170	33						
Rp	143	Biotite Gneiss				Migmatitic	162	45						
Rp	144	Metagraywacke				Mylonitic	175	39						
Rp	144a	Metagraywacke				Mylonitic			161	23				
Rp	145	Metagraywacke				Mylonitic	169	36						
Rp	145b	Metagraywacke				Mylonitic							305	82
Rp	146	Biotite Gneiss				Migmatitic	162	31						
Rp	147	Biotite Gneiss				Migmatitic	169	46						
Rp	148	Biotite Gneiss				Migmatitic	120	33						
Rp	149	Granitic Orthogneiss					169	33						
Rp	150	Granitic Orthogneiss					185	50						
Rp	151	Granitic Orthogneiss					160	24						
Rp	152	Granitic Orthogneiss					172	51						
Rp	152b	Granitic Orthogneiss											245	86
Rp	152c	Granitic Orthogneiss											271	86
Rp	153	Biotite Gneiss				Migmatitic	169	32						
Rp	154	Metagraywacke				Mylonitic	182	59						
Rp	154a	Metagraywacke				Mylonitic			194	17				
Rp	155	Biotite Gneiss					168	51						
Rp	155b	Biotite Gneiss				Migmatitic							95	72
Rp	156	Metagraywacke				Migmatitic	222	18						
Rp	157	Metagraywacke				Migmatitic	188	16						
Rp	157a	Metagraywacke				Migmatitic			316	13				
Rp	158	Amphibolite					164	72						
Rp	158a	Amphibolite							206	43				
Rp	159	Schist	grt,sil	Metagraywacke			159	33						
Rp	162	Metagraywacke		Schist	grt,ms,sil		228	32						
Rp	163	Diabase Dike					315	90						
Rp	163b	Diabase Dike											301	65
Rp	164	Granitic Orthogneiss	grt,bt,plag			Mylonitic	161	31						
Rp	166	Granititc Orthogneiss	grt,bt,kspr				190	50						
Rp	167	Biotite Gneiss					65	18						
Rp	168	Biotite Gneiss					185	74						

							Foliation		Lineation		Fold Axis		Joint	
Quad	Station	Rock Type 1 (RT2)	RT 1 Minerals	Rock Type 2 (RT2)	RT2 Minerals	Modifier	Strike	Dip	Trend	Plunge	Trend	Plunge	Strike	Dip
Rp	169	Hornblende Gneiss					227	50						
Rp	170	Biotite Gneiss					185	70						
Rp	171	Biotite Gneiss					175	50						
Rp	172	Biotite Gneiss					173	56						
Rp	173	Biotite Gneiss					170	33						
Rp	174	Biotite Gneiss					175	64						
Rp	175	Biotite Gneiss				Migmatitic	170	34						
Rp	176	Biotite Gneiss				Migmatitic	182	30						
Rp	177	Biotite Gneiss				Migmatitic	185	29						
Rp	178	Granitic Orthogneiss	grt,bt			Mylonitic	211	40						
Rp	178a	Granitic Orthogneiss	grt,bt			Mylonitic			350	12				
Rp	178b	Granitic Orthogneiss	grt,bt			Mylonitic							41	55
Rp	178c	Granitic Orthogneiss	grt,bt			Mylonitic							90	85
Rp	179	Granitic Orthogneiss	grt,bt,plag			Mylonitic	68	24						
Rp	180	Schist	grt,sil				168	28						
Rp	181	Biotite Gneiss				Migmatitic	187	11						
Rp	182	Biotite Gneiss				Migmatitic	192	56						
Rp	183	Biotite Gneiss				Migmatitic	5	24						
Rp	184	Biotite Gneiss					188	35						
Rp	185	Biotite Gneiss				Migmatitic	185	16						
Rp	186	Biotite Gneiss				Migmatitic	345	42						
Rp	187	Granitic Orthogneiss					180	33						
Rp	188	Granitic Orthogneiss					163	17						
Rp	189	Granitic Orthogneiss					150	23						
Rp	190	Biotite Gneiss				Migmatitic	132	55						
Rp	191	Biotite Gneiss					150	73						
Rp	192	Schist	grt,sil				185	51						
Rp	193	Biotite Gneiss	grt			Mylonitic	200	60						
Rp	194	Biotite Gneiss					145	40						
Rp	195	Biotite Gneiss	grt			Migmatitic	203	45						
Rp	196	Biotite Gneiss				Migmatitic	195	15						
Rp	196b	Biotite Gneiss				Migmatitic							255	64
Rp	197	Biotite Gneiss				Migmatic	195	25						
Rp	198	Biotite Gneiss					140	6						
Rp	199	Biotite Gneiss					185	14						
Rp	200	Biotite Gneiss					145	52						
Rp	201	Granitic Orthogneiss	grt,plag,bt				200	35						
Rp	202	Biotite Gneiss					175	40						
Rp	203	Gondite	grt,qtz				192	43						
Rp	204	Metagraywacke	grt				192	42						
Rp	205	Granitic Orthogneiss	grt,plag,bt			Mylonitic	187	25						
Rp	206	Granitic Orthogneiss	grt,plag,bt				185	31						
Rp	207	Granitic Orthogneiss	grt,plag,bt			Mylonitic	175	57						
Rp	208	Granitic Orthogneiss	grt,plag,bt			Mylonititc	175	84						
Rp	209	Schist	grt,sil				175	42						
Rp	210	Granitic Orthogneiss				Mylonitic	229	57						
Rp	211	Granitic Orthogneiss	bt,plag			Mylonitic	178	54						
Rp	212	Granitic Orthogneiss	grt,bt			Mylonitic	185	26						
Rp	213	Granitic Orthogneiss				Mylonitic	195	17						
Rp	214	Gondite	qtz,grt				200	46						
Rp	215	Biotite Gneiss					213	24						
Rp	216	Granitic Orthogneiss	grt			Mylonitic	240	40						
Rp	217	Granitic Orthogneiss					205	30						
Rp	217b	Granitic Orthogneiss											93	66
Rp	218	Granitic Orthogneiss					248	40						
Rp	219	Biotite Gneiss					190	45						
Rp	220	Biotite Gneiss					170	65						
Rp	221	Biotite Gneiss					193	67						
Rp	222	Biotite Gneiss					180	64						
Rp	223	Metasandstone		Schist	grt,sill		170	30						
Rp	224	Biotite Gneiss				Migmatitic	200	58						
Rp	225	Biotite Gneiss					205	45						
Rp	226	Biotite Gneiss					178	52						
Rp	227	Biotite Gneiss				Mylonitic	165	29						
Rp	228	Biotite Gneiss	grt,bt			Migmatitic	185	41						
Rp	229	Biotite Gneiss					166	43						
Rp	230	Biotite Gneiss					165	35						
Rp	231	Biotite Gneiss	grt,bt				165	22						
Rp	232	Biotite Gneiss				Mylonitic	175	18						

							Foliation		Lineation		Fold Axis		Joint	
Quad	Station	Rock Type 1 (RT2)	RT 1 Minerals	Rock Type 2 (RT2)	RT2 Minerals	Modifier	Strike	Dip	Trend	Plunge	Trend	Plunge	Strike	Dip
Rp	233	Biotite Gneiss				Migmatitic	285	26						
Rp	234	Biotite Gneiss				Migmatitic	155	23						
Rp	235	Biotite Gneiss				Migmatitic	150	40						
Rp	236	Biotite Gneiss				Migmatitic	150	42						
Rp	237	Biotite Gneiss				Migmatitic	125	16						
Rp	238	Biotite Gneiss				Migmatitic	143	43						
Rp	239	Biotite Gneiss				Migmatitic	163	32						
Rp	240	Biotite Gneiss				Migmatitic	170	27						
Rp	241	Biotite Gneiss				Migmatitic	180	49						
Rp	242	Granitic Orthogneiss				Mylonitic	180	57						
Rp	243	Granitic Orthogneiss				Mylonitic	190	43						
Rp	243a	Granitic Orthogneiss				Mylonitic			5	26				
Rp	244	Biotite Gneiss		Amphibolite			180	32						
Rp	245	Amphibolite	amp,bt				175	22						
Rp	246	Biotite Gneiss				Migmatitic	162	38						
Rp	247	Biotite Gneiss				Migmatitic	155	28						
Rp	248	Hornblende Gneiss					165	67						
Rp	249	Biotite Gneiss				Mylonitic	145	45						
Rp	250	Biotite Gneiss	grt,bt			Mylonitic	191	63						
Rp	251	Biotite Gneiss				Mylonitic	195	64						
Rp	252	Biotite Gneiss	grt,bt			Mylonitic	185	51						
Rp	253	Biotite Gneiss				Mylonitic	185	65						
Rp	254	Granitic Orthogneiss	grt,plag,bt			Mylonitic	205	41						
Rp	255	Granitic Orthogneiss	grt			Mylonitic	180	48						
Rp	256	Granitic Orthogneiss	grt			Mylonitic	210	32						
Rp	256	Granitic Orthogneiss	grt			Mylonitic							90	64
Rp	257	Granitic Orthogneiss				Mylonitic	215	31						
Rp	258	Granitic Orthogneiss	grt			Mylonitic	180	60						
Rp	259	Granitic Orthogneiss				Mylonitic	205	23						
Rp	259	Granitic Orthogneiss				Mylonitic							70	70
Rp	259	Granitic Orthogneiss				Mylonitic							143	80
Rp	260	Granitic Orthogneiss				Mylonitic	220	16						
Rp	261	Granitic Orthogneiss				Mylonitic	200	18						
Rp	262	Amphibolite	amp			Weathered	255	62						
Rp	263	Biotite Gneiss	bt,grt			Mylonitic	230	33						
Rp	264	Amphibolite	amp				230	24						
Rp	265	Layered Metagraywacke	grt	Calc-silicate		Migmatitic	190	50						
Rp	266	Metagraywacke	grt,bt				215	38						
Rp	267	Migmatite				Mylonitic	190	47						
Rp	268	Gondite		Metagraywacke	grt		150	47						
Rp	269	Granitic Orthogneiss	kspr,grt			Mylonitic	166	57						
Rp	270	Granitic Orthogneiss	grt			Mylonitic	164	55						
Rp	271	Metagraywacke	grt				166	45						
Rp	272	Amphibolite		Metagraywacke			165	14						
Rp	273	Biotite Gneiss				Migmatitic	160	19						
Rp	274	Biotite Gneiss	bt,grt				180	30						
Rp	275	Biotite Gneiss	bt,grt			Mylonitic	195	30						
Rp	276	Biotite Gneiss				Migmatitic	144	22						
Rp	277	Biotite Gneiss	garnet			Migmatitic	220	42						
Rp	278	Granitic Orthogneiss	grt,bt			Mylonitic	155	42						
Rp	279	Granitic Orthogneiss	kspr,grt			Mylonitic	172	31						
Rp	280	Granitic Orthogneiss	grt,kspr			Mylonitic	142	38						
Rp	281	Biotite Gneiss	grt			Migmatitic	140	22						
Rp	282	Granitic Orthogneiss		Mylonite		Mylonitic	155	22						
Rp	283	Granitic Orthogneiss					10	40						
Rp	284	Granitic Orthogneiss	kspr,grt				168	55						
Rp	285	Biotite Gneiss		Migmatite			155	20						
Rp	286	Biotite Gneiss	grt,bt	Hornblende Gneiss			135	50						
Rp	287	Biotite Gneiss	grt,bt			Mylonitic	155	58						
Rp	288	Biotite Gneiss					320	50						
Rp	289	Biotite Gneiss					170	43						
Rp	290	Biotite Gneiss	bt,grt				181	61						
Rp	291	Pegmatite	qtz				340	19						
Rp	292	Biotite Gneiss					125	16						
Rp	293	Biotite Gneiss	grt,qtz				163	22						
Rp	294	Biotite Gneiss	grt,qtz	Hornblende Gneiss			166	60						
Rp	295	Biotite Gneiss	grt,bt				310	72						
Rp	296	Biotite Gneiss	grt,bt				173	26						
Rp	297	Biotite Gneiss	grt,bt	Amphibolite			177	43						

							Foliation		Lineation		Fold Axis		Joint	
Quad	Station	Rock Type 1(RT2)	RT 1 Minerals	Rock Type 2 (RT2)	RT2 Minerals	Modifier	Strike	Dip	Trend	Plunge	Trend	Plunge	Strike	Dip
Rp	298	BT Schist				Migmatitic	165	30						
Rp	299	Biotite Gneiss	grt,bt	Schist		Migmatitic	195	37						
Rp	300	Layered Metagraywacke		Biotite Gneiss		Migmatitic	187	30						
Rp	301	Biotite Gneiss					185	35						
Rp	302	Schist	grt,sil				178	15						
Rp	303	Schist	grt,sil				192	26						
Rp	304	Gondite					183	54						
Rp	305	Gondite					195	27						
Rp	306	Biotite Gneiss					230	14						
Rp	307	Granitic Orthogneiss				Mylonitic	155	45						
Rp	308	Pegmatite	grt,ms		bt,qtz		260	14						
Rp	309	Granitic Orthogneiss					196	19						
Rp	310	Pegmatite					215	17						
Rp	311	BT Schist		Granitic Orthogneiss			120	23						
Rp	312	Biotite Gneiss		Amphibolite			196	50						
Rp	313	Amphibolite		Biotite Gneiss			202	50						
Rp	314	Amphibolite		Biotite Gneiss			160	32						
Rp	315	Biotite Gneiss	bt,grt	Metagraywacke			220	24						
Rp	316	Metagraywacke	bt,grt	Hornblende Gneiss	amp,bt		180	43						
Rp	317	Layered Metagraywacke	bt				185	39						
Rp	318	Amphibolite					173	42						
Rp	319	Biotite Gneiss		Metagraywacke			232	42						
Rp	320	Biotite Gneiss		Metagraywacke			218	50						
Rp	321	Biotite Gneiss		Metagraywacke			202	30						
Rp	322	Biotite Gneiss		Metagraywacke		Migmatitic					354	30		
Rp	323	Schist		Biotite Gneiss			175	30						
Rp	324	Pegmatite	qtz				220	42						
Rp	325	Biotite Gneiss					205	36						
Rp	326	Biotite Gneiss					173	40						
Rp	327	Biotite Gneiss					162	39						
Rp	328	Biotite Gneiss					183	22						
Rp	329	Biotite Gneiss		Metagraywacke			187	36						
Rp	330	Biotite Gneiss		Metagraywacke			193	37						
Rp	331	Biotite Gneiss		Metagraywacke			190	25						
Rp	332	Layered Metagraywacke					180	49						
Rp	333	Layered Metagraywacke		Biotite Gneiss		Migmatitic	190	17						
Rp	334	Pegmatite					105	40						
Rp	335	Metagraywacke		Schist		Migmatitic	184	40						
Rp	336	Gondite		Biotite Gneiss			170	58						
Rp	337	Biotite Gneiss		Amphibolite			240	53						
Rp	338	Gondite					165	33						
Rp	339	Biotite Gneiss				Migmatitic	175	44						
Rp	340	Biotite Gneiss				Migmatitic	187	47						
Rp	341	Diabase Dike					314	47						
Rp	342	Amphibolite					190	45						
Rp	343	Biotite Gneiss				Migmatitic	193	24						
Rp	344	Biotite Gneiss				Migmatitic	166	32						
Rp	345	Biotite Gneiss	bt,plg				53	38						
Rp	346	Biotite Gneiss	bt,qtz				310	18						
Rp	347	Biotite Gneiss	bt,qtz				190	35						
Rp	348	Biotite Gneiss					325	47						
Rp	349	Biotite Gneiss					217	21						
Rp	350	Metagraywacke		Amphibolite			170	42						
Rp	351	Granitic Orthogneiss	grt,bt			Mylonitic	170	30						
Rp	352	Biotite Gneiss		Amphibolite			220	48						
Rp	353	Schist	grt,sil	Metagraywacke		Migmatitic	175	50						
Rp	354	Schist	grt,sil	Metagraywacke		Migmatitic	152	43						
Rp	355	Schist	grt,sil	Metagraywacke		Migmatitic	170	46						
Rp	356	Schist	grt,sil	Metagraywacke		Migmatitic	135	60						
Rp	357	Granitic Orthogneiss				Mylonitic	208	25						
Rp	358	Granitic Orthogneiss				Mylonitic	210	42						

APPENDIX B

Representative feldspar analyses.

	Plagioclase traverse 1	K-feldspar inclusion	Plagioclase traverse 2	Plagioclase traverse 3	K-feldspar traverse 1	Plagioclase inclusion	K-feldspar traverse 2
# Analyses	7	1	10	7	7	1	11
SiO2	59.4 (2)	63.8	59.2 (2)	58.7 (1)	64.3 (2)	59.1	63.4 (4)
Al2O3	24.9 (2)	18.0	25.2 (2)	24.8 (4)	18.2 (1)	24.8	18.5 (2)
CaO	7.12(15)	0.08	7.31(10)	6.81(24)	0.06 (3)	6.95	0.12 (14)
FeO	0.05 (4)	-	0.05 (2)	0.44(60)	0.02 (3)	0.05	0.02 (1)
Na2O	7.22(10)	0.63	7.07 (9)	7.35(26)	1.25(19)	7.50	1.54 (27)
K2O	0.38(10)	15.6	0.42 (4)	0.18 (3)	15.0 (2)	0.20	14.4 (5)
S	99.07	98.11	99.25	98.28	98.83	98.60	97.98
Cations based on 8 oxygens							
Si	2.674	3.000	2.662	2.665	2.996	2.673	2.979
Al	1.321	1.000	1.334	1.328	1.001	1.321	1.022
Ca	0.343	0.004	0.353	0.332	0.003	0.337	0.006
Fe	0.002	0.000	0.002	0.017	0.001	0.002	0.001
Na	0.630	0.057	0.616	0.647	0.113	0.657	0.140
K	0.022	0.936	0.024	0.010	0.889	0.011	0.865
S	4.992	4.997	4.991	5.000	5.004	5.001	5.013

[a] All Fe calculated as Fe^{2+}

[b] Units in ( ) represent one standard deviation of replicate analyses in terms of least units cited

Representative orthopyroxene analyses.

	Traverse 1	Traverse 2	Traverse 3	Traverse 4	Traverse 5
# Analyses	10	10	6	10	6
SiO2	49.2 (1)	49.2 (2)	48.6 (3)	48.1 (3)	47.3 (2)
TiO2	0.09(2)	0.07(3)	0.09(2)	0.08(1)	0.11(3)
Al2O3	0.64(5)	0.67(9)	0.67(9)	0.66(4)	0.64(4)
Cr2O3	0.02(7)	0.01(2)	0.01(1)	0.03(3)	0.03(2)
MgO	10.7 (1)	10.4 (1)	10.4 (2)	10.4 (7)	10.3 (1)
CaO	0.96(2)	0.79(3)	0.93(5)	0.91(9)	0.53(5)
MnO	0.92 (4)	0.90(4)	0.94(5)	0.91(5)	1.03(6)
FeO	38.2 (3)	38.4 (6)	38.4 (6)	38.5 (4)	38.7 (5)
Na2O	0.02(2)	0.02(3)	0.04(2)	0.02(1)	0.03(1)
K2O	0.01(1)	0.02(2)	0.02(2)	0.01(1)	0.00(1)
S	100.76	100.48	100.08	99.62	98.67
Cations based on 6 oxygens					
Si	1.9773	1.982125	1.970	1.964	1.957
Ti	0.0027	0.002	0.003	0.0025	0.004
Al	0.0304	0.03175	0.032	0.0316	0.031
Cr	0.0006	0.000375	0.000	0.0008	0.001
Mg	0.6379	0.624625	0.628	0.6312	0.636
Ca	0.0414	0.033875	0.041	0.0399	0.023
Mn	0.0315	0.03075	0.032	0.0313	0.036
Fe	1.2823	1.29275	1.303	1.3154	1.337
Na	0.0013	0.00175	0.003	0.0017	0.002
K	0.0003	0.001	0.001	0.0003	0.000
S	4.0057	4.001	4.014	4.0187	4.025

[a] All Fe calculated as Fe^{2+}

[b] Units in ( ) represent one standard deviation of replicate analyses in terms of least units cited

Representative clinopyroxene analyses.

	Traverse 1	Grain 1	Grain 2	Grain 3	Grain 4
# Analyses	10	3	3	3	3
SiO2	51.5 (5)	51.3 (1)	50.9 (3)	51.2 (2)	51.1 (1)
TiO2	0.10(2)	0.13(2)	0.13(1)	0.13(1)	0.13(3)
Al2O3	1.41(82)	1.26(1)	1.21(3)	1.20(1)	1.24(4)
Cr2O3	0.03(2)	0.04(3)	0.03(1)	0.02(2)	0.01(2)
MgO	8.91(32)	8.60(25)	8.63(23)	8.62(9)	8.58(7)
CaO	20.7 (10)	20.9 (1)	19.7 (10)	20.8 (7)	21.4 (3)
MnO	0.40(5)	0.43(3)	0.40(5)	0.39(7)	0.38(5)
FeO	17.1 (12)	17.4 (6)	18.9 (10)	18.1 (1)	16.9(4)
Na2O	0.49(28)	0.40(3)	0.40(2)	0.39(2)	0.41(4)
K2O	0.01(1)	0.06(5)	0.03(1)	0.01(1)	0.02(2)
S	100.65	100.52	100.33	100.86	101.42
Cations based on 6 oxygens					
Si	1.977	1.977	1.974	1.974	1.974
Ti	0.003	0.004	0.004	0.004	0.004
Al	0.064	0.057	0.055	0.054	0.056
Cr	0.001	0.001	0.001	0.001	0.000
Mg	0.510	0.494	0.499	0.495	0.495
Ca	0.853	0.865	0.820	0.857	0.888
Mn	0.013	0.014	0.013	0.013	0.012
Fe	0.549	0.562	0.613	0.583	0.548
Na	0.036	0.030	0.030	0.029	0.031
K	0.001	0.003	0.001	0.000	0.001
S	4.006	4.006	4.010	4.010	4.009

[a] All Fe calculated as Fe^{2+}

[b] Units in ( ) represent one standard deviation of replicate analyses in terms of least units cited

Representative biotite and ilmenite analyses.

	Biotite 1	Biotite 2	Biotite 3	Biotite 4	Ilmenite 1	Ilmenite 2	Ilmenite 3
# Analyses	10	8	10	8	8	8	5
SiO2	34.1 (9)	34.5 (2)	35.1 (3)	35.0 (3)	0.34(59)	0.02(1)	0.02(1)
TiO2	4.87(14)	4.39(12)	5.09(34)	4.56(40)	50.5 (10)	50.8 (2)	51.2 (2)
Al2O3	14.0 (5)	14.3 (2)	14.0 (2)	14.1 (2)	0.10(15)	0.01(1)	0.01(2)
Cr2O3	0.04 (2)	0.04 (4)	0.03 (2)	0.03 (2)	0.01(1)	0.02(2)	0.02(2)
MgO	7.06(29)	7.20 (9)	7.03 (3)	7.15(14)	0.21(11)	0.16(2)	0.16(2)
CaO	0.02 (2)	0.01 (1)	0.05 (7)	0.02 (3)	0.02(2)	0.01(2)	0.04(5)
MnO	0.10 (4)	0.08 (3)	0.10 (3)	0.12 (4)	0.94(7)	0.67(5)	0.68(2)
FeO	25.6 (3)	26.0 (2)	25.5 (4)	26.0 (4)	46.0 (3)	47.2 (2)	46.9 (4)
Na2O	0.15 (7)	0.07 (3)	0.08 (3)	0.07 (2)	0.02(2)	0.01(1)	0.01(1)
K2O	9.21(16)	9.34 (6)	9.30(15)	9.29(27)	0.01(1)	0.00(1)	0.00 (1)
H2O	3.82 (8)	3.85 (1)	3.83 (2)	3.83 (3)	-	-	-
S	98.97	99.78	100.11	100.17	98.15	98.90	98.89
Cation basis	22	22	22	22	6	6	6
Si	5.515	5.518	5.487	5.485	0.018	0.001	0.038
Ti	0.576	0.514	0.599	0.538	1.957	1.963	1.962
Al	2.594	2.618	2.591	2.606	0.006	0.001	0.001
Cr	0.005	0.005	0.004	0.004	0.000	0.001	0.001
Mg	1.611	1.670	1.640	1.671	0.016	0.012	0.013
Ca	0.003	0.003	0.009	0.004	0.001	0.001	0.002
Mn	0.013	0.010	0.013	0.016	0.041	0.029	0.029
Fe	3.355	3.381	3.334	3.412	1.983	2.026	1.952
Na	0.032	0.021	0.026	0.022	0.002	0.001	0.001
K	1.844	1.854	1.857	1.857	0.001	0.000	0.000
H	0.000	0.000	0.000	0.000	-	-	-
S	15.548	15.594	15.558	15.613	4.024	4.035	3.998

[a] All Fe calculated as Fe^{2+}

[b] Units in ( ) represent one standard deviation of replicate analyses in terms of least units cited

Representative hornblende analyses.

	Grain 1	Grain 2	Grain 3	Grain 4
# Analyses	6	7	11	3
SiO2	39.5 (11)	41.0 (1)	40.3 (9)	40.3 (2)
TiO2	2.09(45)	2.17(27)	1.85(27)	0.29(4)
Al2O3	12.8 (7)	12.1 (4)	12.3 (5)	14.6 (3)
Cr2O3	0.03(2)	0.04(3)	0.06(2)	0.05(2)
MgO	5.47(19)	5.78(9)	5.79(20)	5.34(22)
CaO	11.0 (2)	11.1 (1)	11.1 (1)	11.1 (5)
MnO	0.22(2)	0.22(2)	0.18(5)	0.15(1)
FeO	23.0 (6)	22.7 (2)	22.9 (3)	22.9 (3)
Na2O	1.33(8)	1.39(5)	1.43(11)	1.24(3)
K2O	1.75(9)	1.75(9)	1.67(23)	1.64(2)
H2O	1.91(4)	1.94(1)	1.92(2)	1.93(1)
S	99.10	100.19	99.50	99.54
Cations based on 23 oxygens				
Si	6.197	6.339	6.286	6.248
Ti	0.248	0.252	0.216	0.034
Al	2.362	2.203	2.256	2.667
Cr	0.004	0.004	0.007	0.006
Mg	1.280	1.331	1.347	1.237
Ca	1.847	1.831	1.851	1.851
Mn	0.029	0.029	0.024	0.020
Fe	3.028	2.935	2.995	2.968
Na	0.405	0.417	0.433	0.373
K	0.352	0.345	0.332	0.325
H	0.000	0.000	0.000	0.000
S	15.751	15.686	15.748	15.729

[a] All Fe calculated as Fe^{2+}

[b] Units in ( ) represent one standard deviation of replicate analyses in terms of least units cited

VITA

Heather Elizabeth Byars was born in the great state of Kentucky on July, 2, 1984, to Glenn and Mary Byars. After graduation from Union County High School in 2002, she attended DePauw University in Greencastle, Indiana, in pursuit of a science major. After testing the waters with biology and physics, she unintentionally found geology to be her perfect major. Heather participated in the National Science Foundation's Research Experience for Undergraduates at the University of Southern Maine during the summer of 2005, where she mapped deformed metamorphic and igneous rocks on islands in Muscongus Bay, Maine. Heather graduated from DePauw University in May, 2006, with a B.A. in Geology. Although born and bred to bleed Kentucky blue, Heather dared to take her unbridled spirit behind enemy lines into "Big Orange Country" for graduate school at the University of Tennessee, all for the sake of her education and love of rocks. Although she never became *fully* immersed in the Rocky Top culture, Heather survived her mission with the scars and degree to prove it. Upon completion of her Master's degree, Heather is headed to Houston, Texas, where she will begin her career as a geologist working for Southwestern Energy Company.